Hydrated Clusters of Nucleic Acid Bases in Supersonic Beams Probed by Multiphoton Ionization (MPI) Mass Spectrometry

Thesis

UNRESTRICTED

Hydrated clusters of nucleic acid bases in supersonic beams probed by multi-photon ionization (MPI) mass spectrometry

Bartłomiej Barć (M. Sci.)

A Thesis submitted in partial fulfilment of the requirements for the Degree of Doctor of Philosophy

The Open University

Department of Physical Sciences

Milton Keynes

21-st of March 2012

Date of Submission: 21 March 2012
Date of Award: 13 July 2012

Abstract

In the present thesis clusters of nucleic acid bases and water are used as model systems of cellular DNA to investigate UV induced radiation damage in the gas phase. A new experimental system has been designed and commissioned to perform multiphoton ionization experiments on hydrogen bonded clusters of the nucleic acid bases: adenine, thymine and uracil, as well as on the related chromophores: 5-fluorouracil and hypoxanthine. As the result of pulsed nanosecond laser irradiation in the wavelength range of 220-230 nm, cluster, monomer and fragment ions were detected using a time-of-flight mass spectrometer. Possible multiphoton ionization pathways of clustered and isolated molecules including the role played by short (singlet) and long-lived (triplet) excited states as well as excited state tautomeric transitions are discussed.

Signal intensities as a function of laser pulse fluence were measured. The slope of a logarithmic plot of the signal intensity versus fluence yields the so-called 'photon order' and provides information on the number of photons leading to the production of cluster, monomer and fragment ions. The results indicate two-photon ionization for uracil and thymine in dry molecular beams (i.e. photon orders equal to 1.9±0.2 and 1.4±0.1, respectively). An interesting result in the form of photon order equal to 3.0±0.5 has been measured for adenine in a dry molecular beam irradiated with an unfocused laser beam. This suggests a three photon ionization process, however further experimental work is required in order to exclude factors related to stability of the laser beam spatial profile.

Hydrated cluster ions with up to 7 water molecules attached to a single uracil and 4 water molecules attached to adenine were unambiguously identified after adding water vapour to the molecular beam source. A maximum of 7 water molecules attached to adenine-uracil base pairs were detected. Possible ionization pathways of such hydrated clusters mediated by excited states tautomeric transitions are discussed. On the basis of photon orders measured under hydrated conditions, it is proposed that sequential MPI processes with 2, 3, and 4 photon absorption lead to production of cluster ions, cluster fragment ions (including protonated monomers), and molecular fragment ions, respectively.

Table of Contents

List of Tables

Table of Figures

1 Introduction

1.1 Overview of the research field

In this thesis the technology of supersonic expansion is coupled with multi-photon ionization in the research on hydrated *clusters* of nucleic acid bases and related chromophores as model systems for biological environments. The formation of clusters and radiation-induced processes in these simple models of living matter are the major subjects of investigation. From an applied perspective, the results of this research can contribute to the characterization of DNA damage on the molecular scale. Indeed, this work forms part of a wide international effort reflected in a number of interrelated conference series, for example *Radiation Damage in Biomolecular Systems (RADAM)*[1-10] and *International Workshop on Radiation Damage to DNA*[11-14]. The major processes on the molecular scale which can be probed in cluster studies are reviewed in the current section (**1.1**), while the wider picture of DNA damage and related phenomena is presented in section **1.2**. Molecular structures of DNA/RNA molecular building blocks (adenine, thymine, and uracil) and related chromophores (5-fluorouracil, hypoxanthine) examined in this thesis are presented in section **1.3**. In addition, the literature describing their behaviour in experimental conditions of increased temperature (200 - 300 °C) and their ionization potentials is briefly summarized.

The interest in radiation-induced processes in DNA at the molecular level[15, 16] in biological model systems has led to numerous studies of clusters in the literature[17-21]. This thesis focuses on the interactions of UV photons with isolated gas phase molecules and with weakly bound molecular complexes in vacuum. Gas phase studies enable investigation of the intrinsic properties of single DNA building blocks[22], as well as elementary reactive processes related to DNA radiation damage[23]. However radiation damage to DNA has to be considered together with the environmental influence and radiation-induced intermolecular processes have to be identified in order to establish the description of DNA damage at the molecular level[24]. The study of nucleobases (adenine, thymine, uracil,

cytosine, and guanine) in molecular complexes (clusters) as opposed to in isolation represents a step towards the conditions in cellular DNA/RNA. Studying clusters can be justified by early research[25, 26] indicating that energy and charge transfer processes between the hydrogen-bonded components within DNA are important from the radiation damage standpoint and that the distribution of damage in the DNA is not necessarily directly related to the distribution of ionizing events (track structure). The damage distributions might be related to the specific physico-chemical properties of the DNA.

Cluster systems represent an intermediate state of matter between the gas phase and the condensed phase, and their energetics and dynamics are an extensive subject of investigation[27]. Weakly bound atomic and molecular clusters can be viewed as finite-size "pieces" of the condensed phases of matter[28]. Therefore there is a central objective of cluster science to 'bridge the gap' between properties characteristic of individual atoms or molecules, and the behaviour of those same substances when in the condensed phase[29].

Topics of interest in clusters research include:

- creation and structures of clusters containing nucleobases[17, 30-32];
- changes of ionization energies upon clustering[18, 33-35];
- intermolecular charge and energy transfer in clusters[36-44];
- cluster dissociation[21, 45, 46];
- characteristic properties of cluster-assembled materials[47-49];
- microscopic aspects of nucleation phenomena[50].

In this thesis, clusters are used as model systems to investigate radiation damage and the first four effects are considered carefully in the data interpretations. However the analytical limitations of the experimental apparatus used in this work often do not allow the unambiguous separation of these potential effects to explain observations.

Hydrated DNA/RNA base clusters can be considered as simplified model systems of irradiated cell nuclei in cancer radiotherapies, currently dominated by treatments using X-rays and accelerated electron beams in the energy range 4-25 MeV[51]. The major

motivation and challenge in studying the molecular mechanisms of DNA damage in radiation therapy is the ability to characterise and potentially manipulate the different kinds of radiation effects (caused by electrons, photons, or heavy ions, as well as by secondary species) on the nanoscale – for example by developing DNA 'radiosensitizers'[52]. Cluster studies may help to gain the knowledge of the molecular mechanisms responsible for radio-sensitization.

Another interesting research subject which can be explored using the experimental system assembled in this work is the intrinsic photo-physics (excited states dynamics) of isolated DNA bases. This is essential for a mechanistic understanding of the UV photochemistry[53] and the complex molecular-level processes leading to DNA radiation damage[54]. Moreover, it has been suggested that the photostability of DNA bases was critical to early life on Earth, exposed to much more intense UV irradiation than we currently experience[55]. It is generally understood that ultrafast excited-state deactivation in nucleic acid bases contributes to the photochemical stability of DNA by minimising the formation of mutagenic photochemical products[56], however further research is necessary to elucidate the detailed dynamics across the UV spectral range.

UV absorption by DNA triggers photochemical reactions which can induce mutations leading to skin cancer. Assessing UV interactions with DNA is particularly important as depletion of the stratospheric ozone layer has increased the level of ultraviolet radiation at the Earth's surface. Despite extensive research in the field, the fate of excitation energy within the double helix structure is far from being clear[57]. Sinha et al.[58] reviewed UV-induced DNA damage and the associated repair mechanisms. The effects of solar light on cellular DNA are mostly explained by direct excitation of nucleobases and photosensitized reactions that are mediated by UVB and UVA radiation (280 – 315 nm and 315-400 nm, respectively[23, 59]). The laser wavelengths applied in the present research (220 nm – 230 nm) belong to the UVC spectral range (100 – 280 nm)[59]. Relatively low intensities of this radiation can be found in the Standard Solar Spectrum for Space Applications and this wavelength range is not included in the Standard Spectra for Terrestrial Use[60]. However

naturally occurring solar light is not the only source of radiation being considered from the radiation damage point of view. The study of laser damage to DNA is also the topic of extensive research. For example D'Souza et al. have studied the effects of intense, ultrashort laser pulses on DNA plasmids[61]. Furthermore, intense laser irradiation is a powerful tool to understand DNA repair in living cells, since specific local induction of DNA strand breaks can be followed[62]. Indeed, the generation of DNA photolesions by two-photon absorption of a frequency-doubled (400 nm) Ti:sapphire laser, which is equivalent to one photon absorption of 200 nm, has been investigated by Tycon et al.[63]. Three photons of 750 nm laser radiation are energetically equivalent to one 250 nm photon, and they can produce DNA damage characteristic for one UVC photo-absorption[64]. The present wavelength range (220-230 nm) lies within 200-250 nm limits established by those studies[63, 64]. Therefore, elucidating laser induced processes in DNA constituents and their clusters can help to link molecular scale processes to experimental results observed on the macromolecular and cellular scale.

In addition to providing information about the lowest electronic excited states of biomolecules and their relaxation pathways, studies of laser-induced photophysical and photochemical processes in DNA-related molecules in gaseous, liquid and solid phases can be relevant to processes in the field of radiation chemistry. In particular, multiphoton ionization can probe superexcited states (neutral electronic excited states above the lowest ionization thresholds) which may play a role in high-energy radiation damage. Indeed, Platzman first identified superexcited states by theoretical analysis of the interaction of ionizing radiation with matter[65]. This particular case is just one example of the numerous interfaces of radiation chemistry with other fields in basic science[66].

The potential use of DNA in nanoelectronic sensors and devices opens new possible applications for the present research in assessing radiation damage in these devices. In this case, the link between functionality and fundamental radiation-induced processes can be expected to be more direct than in biological environments due to the absence of concomitant repair mechanisms.

The research carried out within the framework of this thesis adds to our understanding of the effects of clustering on the multiphoton ionization of DNA/RNA bases on ns-timescales. Ns timescale MPI depends strongly on the lifetimes and relaxation pathways of the valence electronic states accessed so the measurements provide an indirect window into these characteristics and dynamics. In particular new measurements of ionization effectiveness as a function of laser intensity for DNA bases in isolated and clustered conditions have been performed and clustering effects on fragment ion production have been studied. Several previously unstudied cluster types (notably containing the RNA base uracil) have been created in a molecular expansion for the first time.

1.2 Understanding DNA damage

The DNA bases investigated in this research are only small fragments of the DNA double helix in living organisms, while complexes of bases are used as model systems representing a step closer towards conditions within a biological cell (subsection **1.2.1**). Detailed effects of radiation action on clusters can be followed using analytical methods; mass spectrometry has been applied in this research. The significant differences between the experimental environment (molecules and clusters in vacuum) and the cellular medium must be taken into account when experimental results are used to predict effects of radiation in condensed biological material. As with present gas phase and cluster work, related investigations carried out on surfaces[67-71], in solution[72, 73], or in crystal[74-77]conditions do not reflect the natural DNA environment. Whole biological cells[78-81] or DNA extracted directly from them[82-88] are more appropriate from this point of view, however it is extremely challenging to follow processes on a molecular scale in such complex structures. Radiation damage to DNA is investigated in many model systems, starting from gas phase studies and ending on biological objects, like living cells. The major subject of this thesis is the characterisation and comparison of UV multiphoton ionization in gas phase and clustered nucleobases. All of the test cases mentioned above have important roles to play in developing a molecular-scale understanding of radiation damage in biological material. Further subsections of this chapter discuss the highly challenging nature of DNA damage studies due to the large number and diverse sources of potential reaction products (**1.2.2**)

in irradiated material, while the range of time-scales (**1.2.3**), non-linear effects, and DNA repair processes add even more complexity. Strand breaks and clustered DNA damage (**1.2.4**) are among the most frequent types of radiation effects. Although DNA lesions cannot be studied directly in the present experiments, the investigation of intrinsic properties of nucleic acid bases and their complexes with water is an important step in the "bottom-up" approach.

1.2.1 DNA (Deoxyribonucleic acid) in a living cell

The first description of the DNA molecular structure was made by Watson and Crick in 1953[89, 90]. They proposed that DNA consists of two strands coiled as a right-handed helix around a common axis. The two strands are held together by hydrogen bonds between the bases, where a single base from one strand is hydrogen bonded with a single base from the other strand. The base pairs for DNA are adenine – thymine and guanine – cytosine. Each base is linked to a sugar forming a nucleoside, which are interconnected by phosphates in each strand[24]. Water molecules at the surface of DNA are critical to the structure and to the recognition of other molecules, proteins and drugs[91]. From 2 (thymine, cytosine) to 4 hydration sites (guanine) are possible for a single base in the most hydrated B-DNA conformation double helix[92]. Higher order conformations and structures of DNA within cell nuclei are discussed in references[24, 93].

1.2.2 Primary and secondary ionizing radiation effects

The physical processes leading to DNA damage are traditionally grouped into two categories: "primary interactions" comprise direct ionization of DNA and the transfer of electrons and holes to the DNA from excited water molecules associated with DNA; "secondary interactions" refer to reactions in DNA initiated by radicals and electrons released from excited bulk water molecules[94] (**Fig. 1.1**). In the early radiobiology literature, secondary effects of ionizing radiation were considered to be more biologically relevant than primary effects. Accordingly, Douki et al.'s experiments on DNA samples and human monocytes exposed to γ-rays and heavy ions suggest that ionization in primary interactions has a relatively minor contribution to DNA base damage induced by heavy ions, and that

the final radiation-induced DNA base degradation products arise primarily from the attack of OH• radicals[95]. Further studies using radical scavengers[96, 97] have indicated that the contribution of secondary radical-driven processes to DNA damage by ionizing radiation is approximately 70% in cells containing oxygen. In these studies, the medium in which the cells are prepared was substituted prior to irradiation with a medium containing various concentrations of chemical radiosensitizers or radioprotectors (various alcohols or dimethyl sulfoxide).

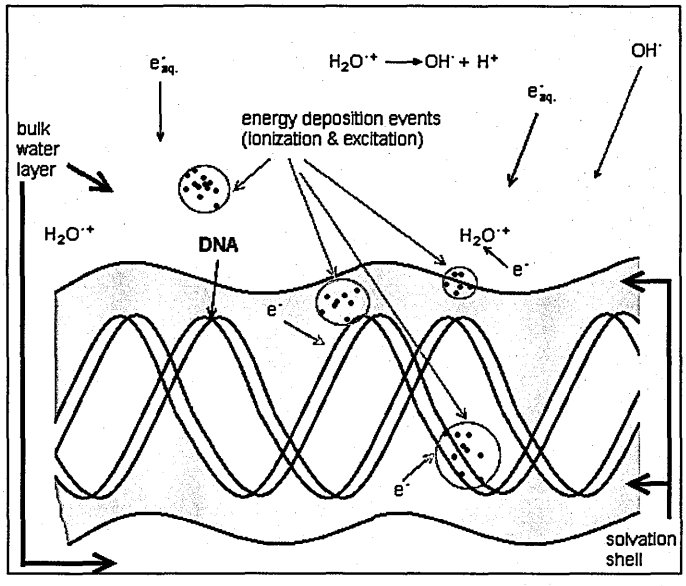

Fig. 1.1: Schematic representation of DNA in aqueous solution showing energy deposition events, the solvation shell of DNA, and the bulk water in the vicinity of DNA. Ionization events in DNA and its solvation shell result in primary-type damage. The DNA solvation shell consists of up to ~20 to 22 water molecules per nucleotide[98].

A number of recent studies, however, suggest that primary-type damage processes are of comparable importance to secondary-type damage from radiation-induced water radicals[98]. In particular, the yields of radiation-induced strand breaks measured in plasmid DNA irradiated as a 'dry film' are similar to those measured in DNA irradiated in a cellular environment[99]. This suggests a common dominant mechanism, namely primary excitation of DNA[100]. Krisch[101] estimated that primary-type effects contribute about 50% to cellular DNA damage. It is significant to note that DNA is tightly packed in the cell nucleus, hence a large fraction of the DNA damage may be due to primary-type process in view of the relative scarcity of local *bulk* water[94]. Both primary and secondary effects of ionizing

radiation are widely investigated with special emphasis on the structural characterization of the final decomposition products of nucleic acid components[102]. Primary and secondary interactions with DNA damage in solution phase can be monitored in real time on ultrafast time scales using picosecond vibrational spectroscopy[103]. The water molecules in the clusters studied in the present work form solvation shells around a nucleobase[104, 105]; hence the experiments are most relevant to enhancing our understanding of primary-type radiation damage processes.

1.2.3 Timescales of radiation action

The timescale of radiation effects in biological material can be divided into three domains: physical, chemical and biological[106] (see **Table 1.1**).

Table 1.1: Time domains of radiation action[107].

Domain	Time	Event
Physical stage: Energy transfer	10^{-18} s	Ionizing particle traverses a molecule
	10^{-15} s	Excitation and Ionization
	10^{-14} s	Molecular vibration and dissociation, electron thermalization
Chemical stage: Formation of radicals and other molecular products	10^{-12} s	Diffusion of free radicals
	10^{-10} s	Free radical reactions with the solute
	10^{-8} s	Formation of molecular products
	10^{-5} s	Chemical reactions
Biological stage	1s – 1hr	Enzymatic reactions, repair processes
	1 hr – 100 yrs	Genomic instability, aberration, mutation, cell killing
	days – months	Early effects: stem cell killing, normal-tissue damage and loss of cell proliferation
	days – years	Late effects: fibrosis, telengiectasia, skin damage, spinal cord damage, blood vessel damage
	many years	Carcinogenesis: appearance of tumours & secondary tumours

The physical stage of radiation action occurs at 10^{-18} – 10^{-14} s, during which time the ionizing particle traverses a molecule and excitation / ionization takes place. The creation of hydrated electrons (free electrons in water) is regarded as the start of the chemical stage of the interaction of radiation with matter[107]. The laser pulse width used in the present experiments is 7 ns and the flight times of molecular and cluster ions in the mass spectrometer tube are tens of μs. Comparison with **Table 1.1** indicates that these times cover the physical stage of radiation action on DNA, as well as partially covering the chemical stage. Hence the present research provides information that contributes to understanding certain processes in these stages, although the high probability of rapid cluster dissociation (complete or partial) following any molecular dissociation events limits the possibility of observing the chemical stage effects.

1.2.4 Strand breaks, clustered damage and other types of radiation-induced processes within DNA

DNA radiation damage is initiated by physical events: ionizations and neutral electronic excitations. **Fig. 1.2** shows simple schematic representations of the most common types of radiation induced damage in DNA.

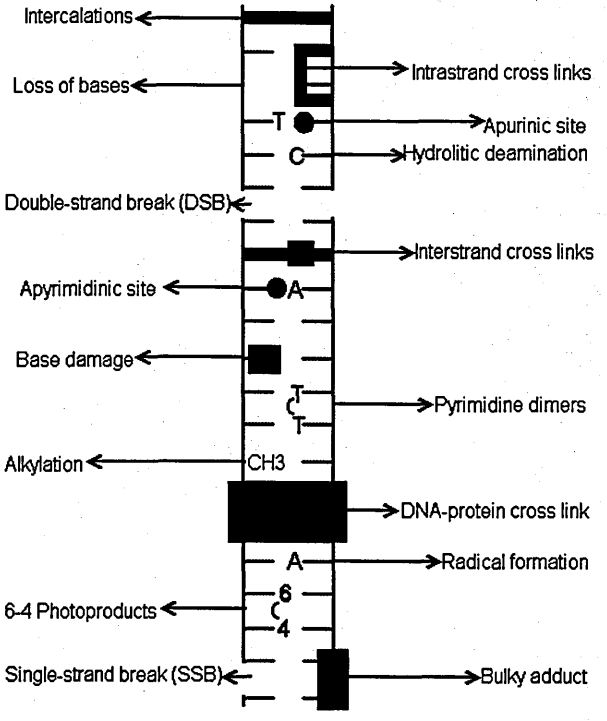

Fig. 1.2: Different types of DNA radiation damage[108].

Elucidating radiation damage of cellular DNA on the molecular scale is challenging due to the large variety and large numbers of types of DNA damage produced[109, 110]. In the case where many of the damage types are of comparable importance it is extremely difficult to understand their roles or to manipulate them[111]. Biophysical analyses demonstrate a wide spectrum of initial physical damage mechanisms and that the chemical, biochemical, and cellular consequences differ considerably across this spectrum[109].

There is a strong effort to determine the chemical mechanism for different classes of DNA damage presented in **Fig. 1.2**. The yields of single-strand breaks (SSB), double-strand breaks (DSB), base lesions, and clustered damage can be measured using the agarose gel electrophoresis method[112]. Theoretical analysis and experimental evidence suggest that complex DNA damages are more likely to occur for high-LET (linear energy transfer) radiation such as protons. When lesions are separated by distances of the order of intermolecular distances (i.e. nm, forming a cluster of lesions) misrepair is more likely, resulting in destabilization of the genome[98].

The various aspects of formation and repair of radiation-induced DSB have been summarized previously[113]. The different mechanisms for their formation can be presented as follows[114]:

1) single radical production,
2) soliton production (nonlinear mechanical excitation of the DNA double helix)[115],
3) the production of a pair of radical ions,
4) two radicals produced within an ionization cluster,
5) dissociative electron capture;

where 4) or a combination of 3) and 4) are considered to be the dominant mechanism[116, 117].

Among complex DNA lesions, the induction of highly repair-resistant bipolar clusters has been suggested as the underlying molecular mechanism for the higher levels of biological damage[118]. It has been shown that ionizing radiation induces clustered DNA damages containing abasic sites (apyrimidinic and apurinic sites in **Fig. 1.2**), oxidized purines or

pyrimidines represent only about 20 % of complex damages, with other clustered damages and SB constituting about 80 %[119].

AFM (atomic force microscopy) visualization of DSBs induced in plasmid supercoiled DNA by low- and high-LET radiation has been presented by Psonka et al.[120] and discussed in the context of the Local Effect Model (LEM) for predicting DNA fragment formation[120]. The LEM is a semi-empirical model originally developed within the tumour therapy project at GSI (Gesellschaft für Schwerionenforschung, Darmstadt) to predict cell inactivation probabilities by heavy ions. The model can also be used to calculate DSB induction in DNA. Furthermore, the induction of clustered DNA damage has been investigated in cells with emphasis on the influence of structural differences in the chromatin organization[121]. The damage yields increased with decreasing compactness of chromatin, and the chromatin effect was larger for clustered lesions than for DSBs.

Quantum calculations on duplex DNA trimers (DNA fragments with three base pairs) were used to model the changes in structure, hydrogen bonding, stacking properties, and electrostatic potential induced by oxidized purine bases and abasic sites[122]. The repair resistant OCDLs (oxidative clustered DNA lesions) could serve as a common indicator of oxidative stress in human malignant cells or tissues; indeed they have potential as a cancer biomarker[123]. A nanodosimetric model for predicting the yield of double strand breaks and non-DSB clustered damages induced in irradiated DNA has been presented[124]. This model contains only those parameters which can be directly measured by a nanodosimeter, i.e. conditional cluster-ion size distribution (the probability of generating an ion cluster n_{ion} normalized to all events with at least one ion, where n_{ion} is the number of ions in a cluster). A new generation of Monte Carlo models of radiation damage incorporating calculations and experimental measurements of fundamental molecular radiation induced processes (notably ionization, dissociation, and scattering cross sections) is currently under development[125, 126].

There is some experimental evidence supporting the hypothesis that the majority of DNA strand breaks produced by direct-type effects are due to sugar free radical precursors and

that these radicals are produced by direct ionization of the sugar-phosphate backbone or by hole transfer (see below) to the sugar from tightly bound water[94]. A correlation has been found between the dose response profiles of sugar-trapped radicals and strand breaks in crystalline DNA samples irradiated at 4 K with doses from 0 to 1800 kGy, where 1 Gy is the unit of absorbed radiation dose defined as 1 Joule of energy per 1 kilogram of mass (J/kg) These kinds of processes in sugar-phosphate backbone and water are initiated by high-energy ionizing particles.

DNA sugar-phosphate damage is less relevant for UV irradiation. Neither single water molecules nor DNA backbone constituents absorb light in the range of 220-230 nm[127]. Ribose phosphate and deoxyribose absorb light below 190 nm[128]. The present work focuses on the UVC absorbing DNA chromophores, i.e. nucleic acid bases and their resonant ionization in laser fields. The major types of DNA damage which can be caused by single photon absorption are pyrimidine dimers and 6-4 photoproducts[129] (**Fig. 1.2**). Moreover UV-type DNA damage occurs for visible and infra-red femtosecond laser pulses irradiating biological material as the result of multi-photon absorption[64].

DNA has efficient hole-conducting properties and may be considered as a building block for nanoelectronic sensors and devices[130]. A hole migrates along DNA through the highest occupied molecular orbital of the guanine bases[130] (guanine has the lowest ionization potential of the four DNA bases[131]); the conductivity of DNA decreases as the adenine – thymine base pair content increases. It has been shown that replacing adenine bases with diaminopurine[132] or 7-deazaadenine[130] increases DNA charge transfer efficiency. Total internal reflection fluorescence microscopy has been used to observe charge transfer in DNA at the single-molecule level[133]. The distance of hole migration through DNA determines the degree to which radiation-induced lesions are clustered[134] and is governed by the competition between hole transfer and irreversible trapping reactions. Hole transfer in DNA is of interest in predicting the health risk associated with the formation of DNA damage by ionizing radiation.

1.3 Creation of molecular targets

In order to achieve the ambitious target of an accurate, predictable assessment of the initial stages of radiation damage in biological objects on the basis of molecular data, sophisticated technologies have to be applied. This thesis is particularly focused on the development of one type of such a technology: the production of molecular model systems (clusters) in an experimental environment. A detailed description of the technique can be found in chapter 3. The data presented in the experimental results chapters (5-7) provide many interesting indications how the technology should be developed further in the future, and also demonstrate effects that require theoretical calculations beyond the scope of this thesis for a definitive elucidation of the underlying dynamics. Construction and optimization of the experimental system based on multiphoton ionization of isolated molecules and their complexes followed by the detection of ionized species was the first major objective of the present research programme. The experiment can be divided into three parts: the supersonic jet (molecular target), the laser (probe), and the mass-spectrometer (analysis). Formed by a gaseous mixture of argon and vaporized molecules flowing through a nozzle into a pumped chamber, the jet passes through a skimmer and crosses a pulsed UV laser beam. The resulting ions and cluster ions are detected and analyzed using a high-resolution *reflectron* time-of-flight (TOF) mass spectrometer. This new experimental system was successfully applied to study the multiphoton ionization of DNA/RNA bases. The key characteristics of the investigated DNA bases and their possible behaviour in the conditions of the thermally generated molecular target applied in the present research are presented in the subsection below.

1.3.1 Investigated molecules and their ionization energies

Different tautomeric forms of DNA/RNA bases and related chromophores are presented in **Fig. 1.3**, **Fig. 1.4**, **Fig. 1.5** and **Fig. 1.6**. The lowest energy tautomers of thymine and uracil are the diketo forms[135-137], whereas for adenine it is the amino 9-H tautomer[138-140]. It is important to identify tautomers present in a given experiment, since their physical properties are different. For example, different tautomers of the DNA base guanine

generated in the gas phase by two different methods (thermal vaporization and laser desorption) have different photoionization efficiencies for a given laser energy[141].

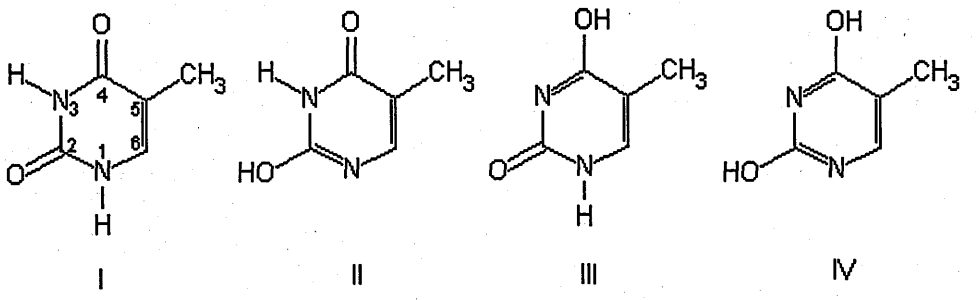

I II III IV

Fig. 1.3: Thymine tautomers I – diketo (reported as most abundant in the gas phase[135, 136, 142]), II – O2H1, III – O4H3, IV– dienol.

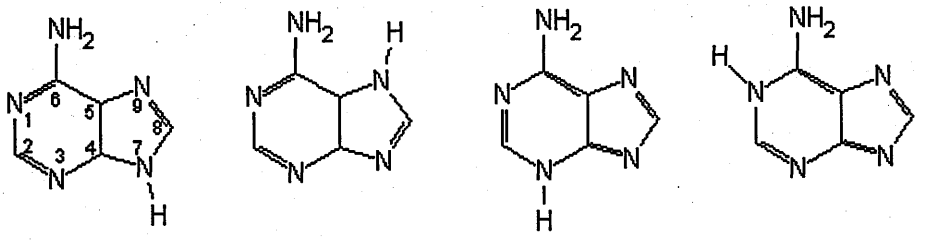

Fig. 1.4: Adenine amine tautomers 9-H (reported as most abundant in the gas phase[138-140]), 7-H, 3-H and 1-H (from left to right).

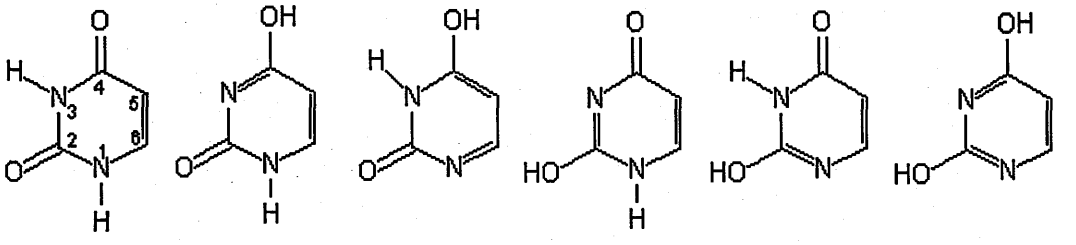

Fig. 1.5: Uracil tautomers, from left to right: I – diketo (reported as most abundant in the gas phase[135-137]), II – O4H3, III – O4H1, IV – O2H3, V – O2H1, VI - dienol.

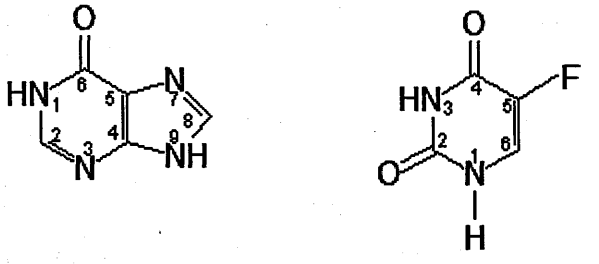

Fig. 1.6: N(1)–H/N(9)–H hypoxanthine tautomeric form[143] (on the left) and diketo tautomer of 5-fluorouracil[144] (on the right).

The nomenclature of different tautomers are such that U (T)-enol represents the dienol tautomer, while U(T)-OmHn represents the mono enol tautomer in which the Hn hydrogen atom attached to the Nn site of the keto form of the uracil (thymine) ring is attached to the Om carbonyl oxygen.

The infrared spectra of adenine, thymine and uracil (the bases studied in this thesis) were recorded in heated cell experiment at 10 - 15 Torr of argon as a buffer gas and temperature range 200 – 325 °C[136]. The infrared spectra[136] presented were measured at 325 °C for uracil and adenine, and at 300 °C for thymine, while mass spectra indicated that no appreciable decomposition occurred. Attempts to record the gas phase spectra of guanine and cytosine were unsuccessful, due to low vapour pressure and decomposition when heated[136]. Accordingly, no attempts have been made to record mass spectra of cytosine and guanine in the present work. Colarusso et al.[136] have not observed any evidence of the tautomerization of uracil or thymine to the enol form or of adenine to the imino form. However minor tautomers could be present in concentrations below the detection threshold (on the order of 1%) for their experimental conditions.

Infrared cavity ringdown spectroscopy experiments of jet-cooled uracil and thymine at 210 – 220 °C confirmed that the only gas-phase tautomeric structure observed for thymine and uracil is the diketo form[105]. However, the IR absorption spectrum of adenine taken at 280 °C in the gas cell and without jet cooling, points to a large portion of the 7-H-amino adenine tautomer in the mixture[145]. On the basis of the literature summarized above it can be assumed that tautomers dominating in a dry (without water reservoir attached) molecular beam for temperatures below 260 °C applied in this work are diketo forms of uracil and thymine, as well as amino-9H adenine tautomer. These tautomers are also the lowest energy forms present in natural DNA/RNA.

The photon energies used in our experiment are within the range of 5.39 – 5.64 eV. The values of ionization energy for adenine, uracil and thymine monomers are presented below

(**Table 1.2**); the energy of two photons from the laser beam used in the present experiments is sufficient to ionize each of these molecules in the target.

Table 1.2: Experimentally and theoretically derived Ionization Energies (IE) of isolated DNA bases.

Molecule	Experimental IE [eV]	Calculated IE [eV]
Adenine	8.20[146]	8.28 (adiabatic)[147] 8.13 (adiabatic)[148] 8.43 (vertical)[147]
Thymine	8.9178[149] 8.95+/-0.05[148]	8.89[148] (adiabatic)
Uracil	9.3411 +/- 0.0008[150] 9.59+/-0.08[151]	9.11[152] (vertical)

1.4 Summary

Gaining knowledge of basic physical processes (excitations and ionizations) occurring in model biomolecular systems upon laser irradiation is the major aim of this work. The new multi-photon ionization experiment has been developed to probe the results of the sequential absorption of UV photons by DNA/RNA related chromophores (adenine, thymine, uracil, 5-fluorouracil and hypoxanthine). Modelling and manipulation of the radiation-response by tailoring the radiation sources and the molecular properties of the irradiated medium are challenging tasks with potential applications in many fields. The core physical rules governing photophysical and photochemical characteristics of single molecules and their complexes are presented in the following chapter.

2 Theoretical concepts

This chapter presents the basic theoretical concepts of photon interactions with molecules and their aggregates. The photo-absorption phenomenon is reviewed on the basis of molecular orbital theory and common transitions between electronic states in organic molecules are summarized. The range of intermolecular forces responsible for the creation of weakly bound molecular clusters is discussed with examples. Knowledge of the relaxation processes leading to energy dissipation following photo-absorption within an isolated molecule or a cluster, as well as ionization-induced chemical reactivity is required to interpret the experimental data presented in the forthcoming chapters. In particular, it is important to consider the timescales of the processes described in this chapter in comparison with the nanosecond-order laser pulse width in our experiment as this has a major influence on the recorded mass spectra.

2.1 The molecular orbital model

The molecular orbital model describes the geometrical arrangement of polyatomic molecules and the changes of their electronic structure brought about by the absorption of electromagnetic radiation. The molecular orbital wavefunction Φ is treated as linear combinations of atomic orbitals ϑ_n. The wave function Φ is expressed as a sum of individual atomic orbitals multiplied by appropriate weighting factors (atomic coefficients)[153]:

$$\Phi = c_1\vartheta_1 + c_2\vartheta_2 + \ldots + c_n\vartheta_n \qquad \textbf{2-1}$$

ϑ_n - wave functions of atomic orbitals;

c_n - weighting factors. These coefficients are the weights of the contributions of the n atomic orbital wavefunctions to the molecular orbital wavefunction.

This method of representing the molecular orbital wave function in terms of combinations of atomic orbital wave functions is known as the linear combination of atomic orbitals approximation (LCAO)[153]. The combination of atomic orbitals chosen is called the basis set[153].

In a polyatomic molecule, interactions between atoms occur, causing deformation of atomic

orbitals. A linear combination of at least two atomic orbitals results in the final (hybridized) molecular orbital. An extensive description of the molecular orbital model and examples of sp, sp^2 and sp^3 hybridizations are given in[154].

2.1.1 π, n and σ orbitals

Molecular orbitals[155] which are completely symmetrical about the internuclear axis are designated **σ** if bonding or **σ*** if antibonding. The sideways overlap of two adjacent p-orbitals results in orbitals called **π** if bonding or **π*** if antibonding[156]. Delocalized electrons play an essential role in aromatic molecules, where alternating single and double bonds (with one or two pairs of electrons shared between atoms, respectively) between the carbon atoms occur. Electron delocalization occurs when molecular orbitals encompass more than two atomic centres. Larger delocalization corresponds to lower energy of the electrons. A third type of molecular orbital is the non-bonding **n** orbital, which makes no contribution to the binding energy of the molecule. Orbitals of this kind accommodating lone-pair electrons localised on nitrogen and / or oxygen atoms occur in nucleobases.

2.2 Intermolecular interactions

Six types of intermolecular forces are generally recognized (according to the classification given in[157]):

1. Repulsion forces

These are short range interactions which occur when two atoms or molecules approach one other. The repulsion between closed electron shells is mainly due to the Pauli exclusion principle. The repulsion energy is represented by the following function:

$$E(R)(repulsion) = \beta_r \exp\left(-\frac{R}{\rho_r}\right) \qquad \text{2-2}$$

$$E(R)(repulsion) = \beta_r \exp\left(-\frac{R}{\rho_r}\right)$$

β_r and ρ_r - empirical factors;

R - the distance between the two interacting atoms or groups of atoms.

2. Orientation forces

These forces are a result of Coulombic attraction or repulsion of the net charges or electric dipole moments carried by two interacting atoms or molecules. The interaction energy between two charged ions q and q' is given by the relation:

$$E(R)(ion\text{-}ion) = \frac{qq'}{\varepsilon R} \qquad \textbf{2-3}$$

ε - effective value for the dielectric constant of the medium surrounding the two charges. Higher order Coulombic interactions are ion-dipole and dipole-dipole interactions.

3. Polarization forces

These forces arise from the polarization of one atom or molecule by an approaching atom or molecule. In the case of a charge q interacting with a spherical group of isotropic polarizability α_p, the polarization energy is:

$$E(R)(ion\text{-}induceddipole) = -\frac{q^2\alpha_p}{2\varepsilon^2 R^4} \qquad \textbf{2-4}$$

4. Dispersion (London) forces

These are attractive forces of purely quantum mechanical nature that arise even between neutral, non-polar molecules or atoms. They are due to the average interaction of instantaneous dipole moments brought about by charge density fluctuations. A pair of isotropic groups of polarizability α has a dispersion interaction energy given by the following equation:

$$E(R)(dispersion) = -\frac{3\,\Delta E\,\alpha^2}{4R^6} \qquad \textbf{2-5}$$

ΔE - average electronic energy related to the difference between electronic energies of separated atoms (or molecules) and their energies in the complex.

5. Mulliken charge transfer forces

When an electron donor molecule *(D:)* approaches an electron acceptor molecule *(A)*, an electron can be transferred from *D:* to *A*. The total wavefunction for the ground state of the system $\Psi_{(S_0)}$ will depend on the weighting factors *a* and *b* for the two different contributions: a non-bonded form *(:D, A)* and a bound form $(D^+ - A^-)$:

$$\Psi_{(S_0)} = a\Psi(:D,A) + b\Psi(D^+ - A^-) \qquad \textbf{2-6}$$

6. Hydrogen bonding

The most important contributions for the hydrogen bond are electrostatic and repulsion forces (see **Table 2.1**)[158]. In the hydrogen bond A–H···B, A and B are both electronegative, so the charge distribution is $A^- - H^+ \cdots B^-$, and there is a strong electrostatic attraction between H and B and an electrostatic repulsion between A and B which tends to keep the hydrogen bond linear (**Fig. 2.1**). Atom A in the hydrogen bond shown in the **Fig. 2.1** is electronegative, therefore the electron density on the H atom is relatively small, and the repulsion between A and B is not very strong. The example of water's hydrogen bond (O – H ··· O) is given in **Fig. 2.2**[159], its parameters depend on temperature[160].

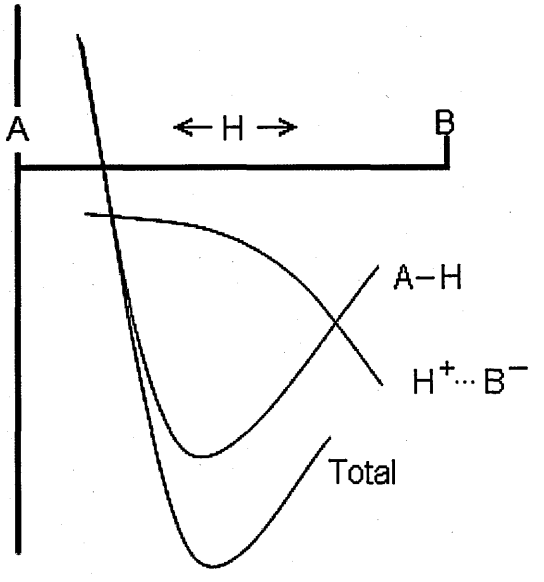

Fig. 2.1: Hydrogen bond potentials[158].

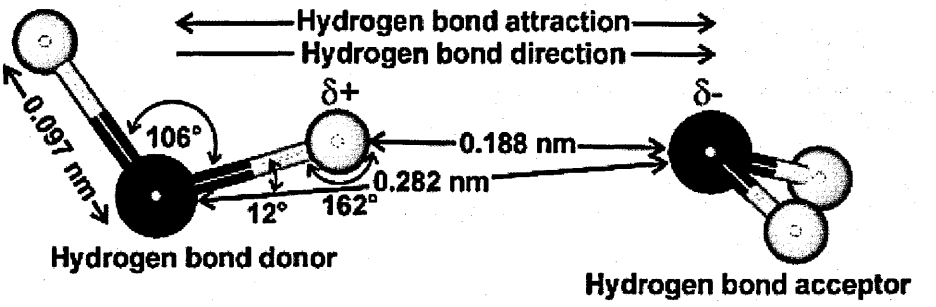

Fig. 2.2: The average parameters for the hydrogen bonds in liquid water (0 - 80°C)[159, 160].

For a water dimer (a hydrogen-bonded complex) in its equilibrium geometry, **Table 2.1** lists the binding energy contributions calculated using two alternative methods [158].

Table 2.1: Calculated binding energy contributions for a water dimer[158].

Intermolecular interaction	Calculated energy contribution [kJmol^{-1}] (negative for binding)	
	IMPT *	SAPT †
Electrostatic	-25.8	-31.6
Repulsion	21.3	35.4
Dispersion	-9.2	-11.1
Induction	-4.5	-11.4 (total contribution from induction and charge transfer intermolecular interactions)
Charge transfer	-3.7	
Higher-order corrections		-3.2
Total	-21.9 (-0.227 eV)	-20.9 (-0.217 eV)

* IMPT (InterMolecular Perturbation Theory)[161] was the first successful method for calculating intermolecular interactions *ab initio*.

† SAPT (Symmetry Adapted Perturbation Theory)[162] is a later, more accurate, method that includes electron correlation effects.

The overall attractive or repulsive interaction depends on the sum of all the interactions. Examples of intermolecular potential energy surfaces for weakly bonded and structurally

diverse groups (clusters) of molecules are presented in[28], including van der Waals complexes of argon and H_2O[28], hydrogen bonded planar structures of nucleobases[163], π-electron hydrogen bonded benzene-H_2O complexes[45]; open shell complexes[164]; T-shaped structures like benzene dimers[165]; and stacked π-π complexes[166, 167].

2.3 Excited states of isolated molecules

2.3.1 Photoabsorption process

The Schrodinger equation of a molecule of energy E in an initial stationary state described by the wavefunction $\Psi_k(\tau)$ is:

$$H_0\Psi_k(\tau)=E\Psi_k(\tau) \qquad \textbf{2-7}$$

where τ stands for all spatial and spin coordinates. Exposure of the system to electromagnetic radiation induces oscillating forces on the charged particles of a molecule[168]. Hence the static Hamiltonian operator H_0 is replaced by (H_0+H'), where H' is the perturbation operator, which takes into account the effect of the radiation field:

$$(H_0+H')\Psi(\tau,t)=E\Psi(\tau,t) \qquad \textbf{2-8}$$

As the radiation field changes with time, the new wavefunctions $\Psi(\tau,t)$ are also functions of time and can be expanded in terms of the wavefunctions of the unperturbed system:

$$\Psi(\tau,t)=\sum a_k(t)\Psi_k(\tau), \qquad \textbf{2-9}$$

There is a probability that at a time t, when the perturbation is suddenly removed, the system will be found in some final state (Ψ_f) other than the initial one. This probability is given by the square of the corresponding coefficient $a_f(t)$:

$$[a_f(t)]^2=\frac{8\pi^3}{3h^2}\langle\Psi_i|\mu|\Psi_f\rangle^2\rho(\nu_{if})t; \qquad \textbf{2-10}$$

where:

$\rho(\nu_{if})$ - the radiation density (energy per unit volume) at the frequency ν_{if} corresponding to the transition;

t - the time of irradiation;

$\langle \Psi_i | \mu | \Psi_f \rangle$ - the transition moment, *T.M.* (can also be written as $\int \Psi_i . \mu . \Psi_f d\tau$ [†], where τ represents all electronic and nuclear coordinates including spin coordinates of the electrons, $d\tau$ indicates that the integral is taken over all space);

μ - the dipole moment operator $\sum_j q_j r_j$ where q_j is charge and r_j is the position vector (location) of the j-th charged particle in relation to an arbitrary reference origin.

h - Planck's constant.

The probability of a given transition is proportional to the square of a transition moment. The relation between the square of the transition moment $\langle T.M. \rangle^2$ and the oscillator strength f is presented below:

$$f = \frac{8\pi^2 \nu_{if} m_e \langle \Psi_i | \mu | \Psi_f \rangle^2}{3he^2} \qquad \textbf{2-11}$$

m_e - electron mass.

2.3.2 Born-Oppenheimer approximation

For most molecules, the transition moment cannot be evaluated because the exact form of the wavefunction is not known. The problem can be simplified by applying the Born-Oppenheimer approximation[168], whereby the wavefunction Ψ is essentially divided into separate electronic ψ, vibrational θ and rotational ω components: $\Psi = \psi . \theta . \omega$. It is assumed that ψ can be represented as the product of one-electron wavefunctions (orbitals) Φ (which may themselves be linear combinations of atomic orbitals), and that only one electron is promoted during a transition. Indeed, the approximation of looking at the overlap of a single orbital rather than the whole electronic wavefunction is introduced. The final approximation is that the orbitals can be factorized into a product of space (φ) and spin (S) wavefunctions: $\Phi = \varphi . S$.

[†] It is assumed in the discussion presented in this thesis that wavefunctions are real. For complex wavefunctions $T.M. = \int \Psi_i^* . \mu . \Psi_f d\tau$, the asterisk denotes the complex conjugate.

Under the assumptions mentioned above and with the rotational component neglected, the transition moment (T.M.) in the Born-Oppenheimer approximation is given by the equation[168]:

$$T.M. = \int \theta_i \theta_f d\tau_N \cdot \int S_i S_f d\tau_s \cdot \int \varphi_i . \mu_e . \varphi_f d\tau_{e\text{-}orb}; \qquad \textbf{2-12}$$

where:

$\int \theta_i \theta_f d\tau_N$ - the overlap integral of the wavefunctions for nuclear vibrations, it embodies a quantum mechanical formulation of the Franck-Condon principle (see section **2.2.4**); τ_N represents spatial coordinates of the nuclei.

$\int S_i S_f d\tau_S$ - the spin overlap integral, its value depends on the initial and final spin states of the promoted electron; τ_S represents spin coordinates of the electrons.

$\int \varphi_i . \mu_e . \varphi_f d\tau_{e\text{-}orb}$ - the electronic transition moment, the value of which depends on the symmetries and the degree of spatial overlap of the initial (i) and final (f) orbitals; $\tau_{e\text{-}orb}$ represents spatial coordinates of a single orbital; μ_e is the electronic dipole moment operator.

The rotational part of the transition moment (T.M.) has been neglected in the equation **2-12** for simplicity, experimental work often provides spectra, which are not rotationally resolved.

Within the Born-Oppenheimer approximation, the Schrodinger equation $H\Psi=E\Psi$, can be split into simpler equations with Hamiltonians and wavefunctions which depend on subsets of coordinates, for example[169]:

$$H_e \psi = E_e \psi \qquad \textbf{2-13}$$

$$H_{rv} \chi = E_{rv} \chi \qquad \textbf{2-14}$$

where $\chi = \theta.\omega$ is the rovibrational wavefunction, H_e - the electronic Hamiltonian, H_{rv} - the rovibrational Hamiltonian. E, E_e, E_{rv} are the energies of Ψ, ψ *and* χ states, respectively.

The total molecular energy can be expressed as the sum of electronic (E_e), vibrational (E_v), rotational (E_r) and translational (E_{tr}) energies; the term E_{others} includes nuclear spin energy levels, and may also be used to include the interactions between the first four terms[170]:

$$E = E_e+E_{rv}+E_{tr}+E_{others}=E_e+E_v+E_r+E_{tr}+E_{others} \quad \textbf{2-15}$$

The Born-Oppenheimer approximation breaks down near degeneracies, i.e. where potential energy surfaces cross and a small change in nuclear coordinates can produce a large change in the electronic component of the wavefunction. It also fails to account for the non-zero intensities observed for forbidden transitions (see section **2.2.6**).

2.3.3 Potential energy surface

A potential energy surface is derived by solving Schrodinger's equation for a variety of nuclear configurations and plotting the electronic energy as a function of these nuclear configurations. The differences between wavefunctions obtained in this way and the true wavefunctions are usually significant where potential surfaces cross. A cartoon representing potential energy surfaces with various possible crossing points, including conical intersections between two potential energy surfaces, is presented below.

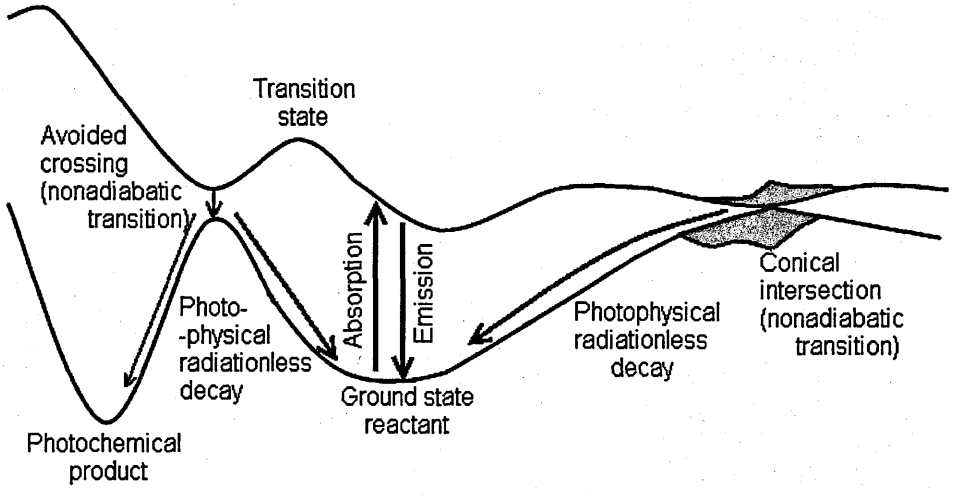

Fig. 2.3: Cartoon of ground and excited state potential energy surfaces, indicating points where nonadiabatic transitions can occur, adapted from[171].

2.3.4 Vibrational overlap integral (Franck-Condon principle)

Electronic transitions take place over such a short timescale that, according to the Franck-Condon principle[168], nuclear positions (the motion of which is described as vibration) can be assumed to be unchanged from the initial to the final state. The transition may be

represented by a vertical line connecting the two potential energy surfaces, and the most probable transition from a vibrationally-cold electronic state will be to the vibrational level with the same internuclear distance at the turning point of oscillation (when the kinetic energy is zero and the system is momentarily at rest), as shown in **Fig. 2.4**. Thus state of motion is preserved as well as nuclear separation during the transition and the most probable transition is known as vertical. Once the electronic transition is complete the molecule begins to vibrate at an energy corresponding to the destination vibrational state[172]. In order to evaluate the vibrational overlap integral according to the quantum mechanical version of the Franck-Condon principle, the individual values of wavefunctions (θ_i and θ_f) for each internuclear separation are multiplied, and the infinitesimal contributions summed ($\theta_i\theta_f d\tau_N$)[168].

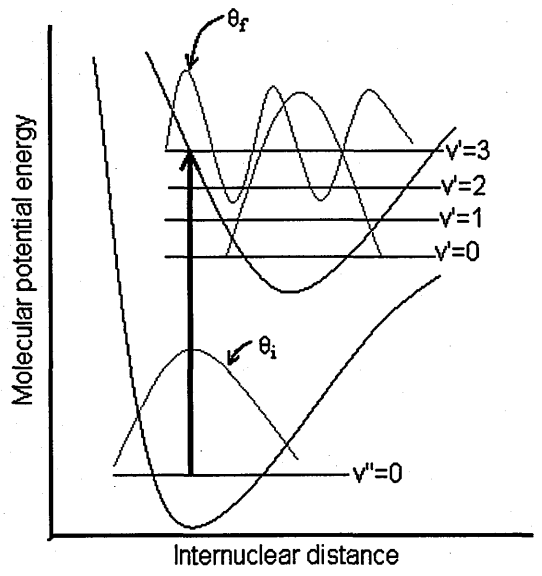

Fig. 2.4: A transition between two electronic states illustrating the quantum mechanical version of the Franck-Condon principle[168]. The most intense transition occurs from the v''=0 vibrational level of the electronic ground state to the v' = 3 vibrational level of the electronic excited state. The vibrational overlap integral is positive for this transition. Excitation leads to stretching of a bond.

2.3.5 Spin overlap integral and spin-orbit coupling

The multiplicity of a state of a molecule is equal to 2**S** + 1 where **S** is the sum of the spin

quantum numbers of the electrons in the molecule (**Fig. 2.5**). For a state in which all the electrons in the molecule are paired, **S** will equal zero and the multiplicity of the state will therefore be unity. Such a state is termed a "singlet state" and assigned the symbol S.

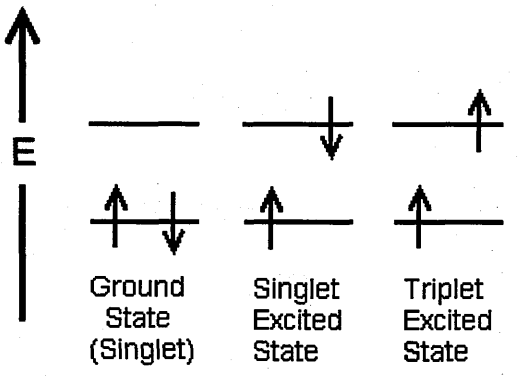

Fig. 2.5: Singlet (S) and triplet (T) states[155].

In the majority of organic molecules, the electrons are all paired in the ground state of the molecule and the ground state is symbolized as the S_0 state.

The effect of electron spin upon transition intensities is given by the factor $\int S_i S_f d\tau_s$ in the transition moment expression[155, 168]. There are three possible transitions:

a) Singlet-singlet transition for which the spin overlap integral is 1;

b) Triplet-triplet transition, where the spin overlap integral is 1;

c) Singlet-triplet transition; the promoted electron changes its spin and the spin overlap integral is 0; the transition is strongly forbidden.

Although singlet-triplet transitions are strongly forbidden, they can occur due to spin-orbit coupling, which is the interaction of the electron spin magnetic moment with the magnetic moment due to the orbital motion of the electron. The spin-orbit interaction is treated quantum mechanically by introducing a term for each electron designated $\hat{H}_{SO}$ (equation **2-16**) into the Hamiltonian operator:

$$\hat{H}_{SO} = \zeta\left(\hat{L}.\hat{S}\right) \qquad \textbf{2-16}$$

where:

$\hat{L}$ - the orbital angular momentum operator;

$\hat{S}$ - the spin angular momentum operator;

ζ - spin-orbit coupling constant.

Perturbation theory shows that if Ψ_S^o and Ψ_T^o are the wavefunctions of 'pure' singlet and triplet states respectively, then the triplet state produced under spin-orbit coupling can be written in the form of the following equation:

$$\Psi_T = \Psi_T^0 + \sum_k \frac{\langle \Psi_{Sk}^0 | H_{SO} | \Psi_T^0 \rangle}{(E_T - E_{Sk})} \cdot \Psi_{Sk}^0; \qquad \textbf{2-17}$$

Where S_k indicates the k-th singlet state, and E_T and E_{SK} are the energies of the triplet and the perturbing singlet states, respectively. The probability of the **S-T** transition therefore depends upon the energy gap between the states concerned as well as upon the spin-orbit coupling matrix element. The latter quantity increases very rapidly with increasing atomic number, giving rise to the *heavy atom effect* whereby the probability of a spin-forbidden transition is enhanced by the presence of an atom of high atomic number. Indeed, as $\hat{H}_{SO}$ depends on Z^4, the probability of an **S-T** transition shows dependence on the fourth power of the atomic number.

2.3.6 Orbital overlap and vibronic coupling

The overlap integral $\int \varphi_i \varphi_f d\tau_{e\text{-}orb}$ is a measure of the spatial overlap[168]. The pyridine molecule provides an example of the importance of orbital overlap. As the n and π orbitals occupy quite different regions of space in this molecule, a transition is forbidden due to a lack of overlap.

Beside transitions forbidden on the overlap ground, symmetry forbidden transitions can be also found[168]. They have small but finite intensities because the vibrational (nuclear) and electronic motions are not completely independent of each other but weakly coupled. This

coupling is known as vibronic coupling (vibrational-electronic). There are vibrations that distort the molecule's shape and reduce its symmetry so that the transition becomes weakly allowed.

2.3.7 Singlet - triplet splitting

The singlet-triplet splitting[168] is the energy difference between singlet and triplet states associated with differences in electron spatial distributions. Electrons with parallel spins avoid each other due to Pauli's exclusion principle. The spatial anti-symmetric wavefunction for a system of two electrons can be written as:

$$\Psi_A = \frac{1}{\sqrt{2}}[\varphi(r_1)\varphi'(r_2) - \varphi(r_2)\varphi'(r_1)] \qquad \textbf{2-18}$$

while the symmetric wavefunction is:

$$\Psi_S = \frac{1}{\sqrt{2}}[\varphi(r_1)\varphi'(r_2) + \varphi(r_2)\varphi'(r_1)] \qquad \textbf{2-19}$$

where:

φ, φ' - space orbitals;

r_1 and r_2 - coordinates of the electrons.

The probability of finding one electron at r_1 and the other at r_2 is given by Ψ_A^2. The electrons are further apart in systems described by Ψ_A (antisymmetric wavefunction) than in those described by Ψ_S (symmetric). The energies of the spatially antisymmetric states Ψ_A are always less than those of Ψ_S states. Triplet states have antisymmetric wavefunctions whereas singlets have symmetric wavefunctions.

2.4 Common transitions in organic molecules

The most common electronic transitions encountered in organic molecules are: $\pi \rightarrow \pi^*$, $n \rightarrow \pi^*$, $n \rightarrow \sigma^*$, and $\sigma \rightarrow \sigma^*$[155]. A given transition depends on the radiation wavelength and the electronic structure of the chemical compound. **Fig. 2.6** shows the approximate photon energy ranges in which these transitions occur. The energy of a photon does not always

match exactly the energy difference between the lowest vibrational levels of the ground and excited states; in many cases the state initially accessed is an upper vibrational/rotational state of the excited electronic state.

$n \rightarrow \pi^*$ - this transition occurs in unsaturated molecules which contain atoms such as oxygen, nitrogen and sulphur. Its intensity can be predicted by considering the symmetry properties of the ground and excited states.

$\sigma \rightarrow \sigma^*$ - occurs in compounds in which all the electrons are involved in single bonds, e.g. saturated hydrocarbons. The energy required for such transitions is large and the absorption bands lie in the vacuum ultraviolet.

$n \rightarrow \sigma^*$ - can occur in compounds containing atoms with lone-pair electrons.

$\pi \rightarrow \pi^*$ - can in principle occur in any molecule containing a π-electron system. Selection rules based on symmetry determine whether a transition to a particular π^* orbital is allowed or forbidden.

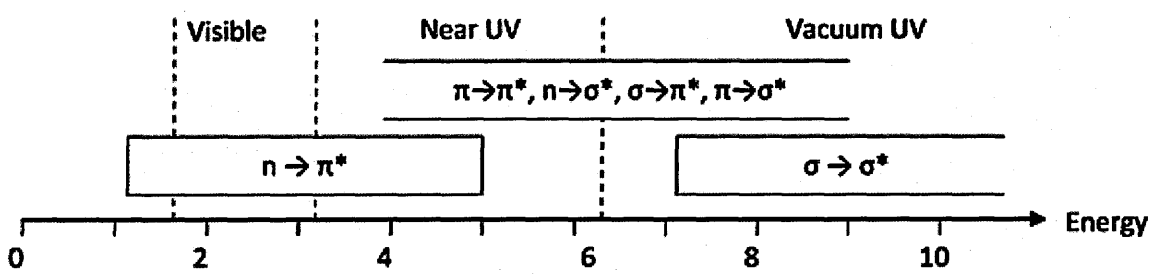

Fig. 2.6: Typical energy ranges [eV] of valence transitions[173].

2.5 Excited states of molecular complexes

2.5.1 Charge transfer transitions

Charge-transfer transitions[168] occur in molecular complexes containing a mixture of electron donors and electron acceptors and are typically characterised by broad and structureless spectroscopic features. The nature of the bonding in a donor-acceptor

complex was elucidated by Mulliken[174]. The ground state of a donor-acceptor complex is described by a wavefunction given in equation **2-6**.

The wavefunction for the excited states of the donor-acceptor complex is given by:

$$\Psi_{(S_1)} = a\Psi(D^+ - A^-) - b\Psi(:D,A) \qquad \textbf{2-20}$$

where Ψ(:D,A) corresponds to a 'non-bond' structure with the components held by weak intermolecular forces, and $\Psi(D^+ - A^-)$ corresponds to a structure in which an electron has been transferred from the donor to the acceptor. For the majority of donor-acceptor complexes b<<a, so $\Psi(S_0) \sim \Psi(:D,A)$, and $\Psi(S_1) \sim \Psi(D^+ - A^-)$. Hence the spectroscopic transition can de described in general terms as the light-induced transfer of an electron from the donor to the acceptor.

2.5.2 Excimers and exciplexes

Excimers (excited dimers) are dimeric species which are associated in an excited electronic state and dissociated in their ground electronic state[168, 175-177]. **Fig. 2.7** and **Fig. 2.8** show potential energy diagrams for excimer (A····A)* formation as tunnelling and vibrational effects, respectively. The wavefunction of an excimer combines both an electronic excitation resonance [AA*-A*A] and charge-transfer resonance:

$$\Psi_{excimer} = a\Psi_{AA^*} + b\Psi_{A^*A} + c\Psi_{A^-A^+} + d\Psi_{A^+A^-} \qquad \textbf{2-21}$$

Excimers commonly occur as the result of molecular rearrangement (**Fig. 2.8**), however they can be also formed by tunnelling (**Fig. 2.7**). For example the formation of a benzene excimer with a parallel stacked geometry from the T-shaped van der Waals dimer of benzene has been demonstrated to proceed by tunnelling between the respective potential wells[175].

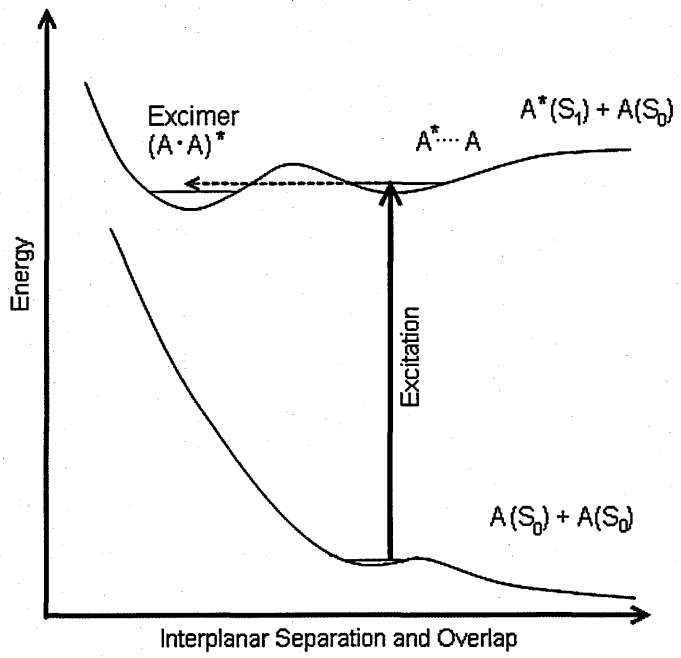

Fig. 2.7: Potential energy diagram for the formation of an excimer, (A·A)*, via local excitation of a ground state dimer A···A followed by a tunnelling process[175].

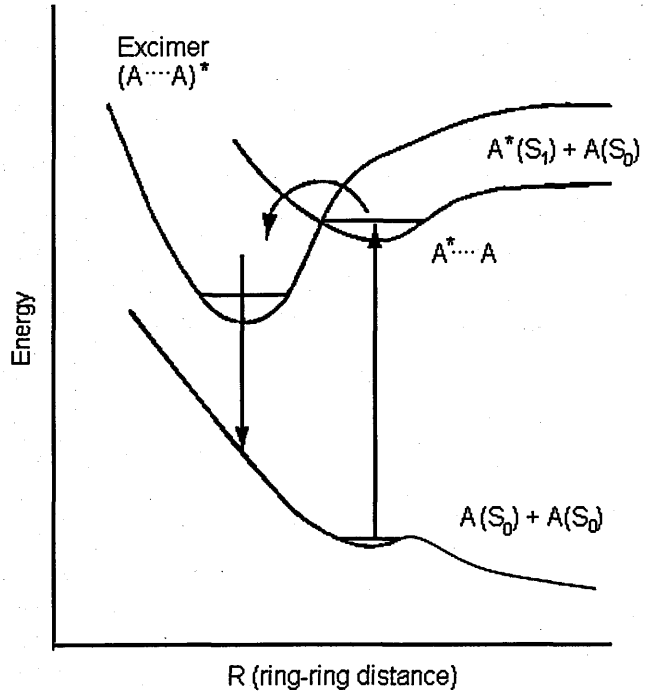

Fig. 2.8: Schematic energy level diagram for the aniline dimer excimer formation and relaxation process[176].

The term exciplex (excited complex) refers to the heterodimeric case. The wavefunction of an exciplex D····A * is given below (D – donor; A - acceptor):

$$\Psi_{exciplex} = a\Psi_{DA^*} + b\Psi_{D^*A} + c\Psi_{D^-A^+} + d\Psi_{D^+A^-} \qquad \textbf{2-22}$$

All terms are neglected except the fourth. The condition for the formation of exciplexes can be formulated in terms of the Gibbs free energy (ΔG) on the basis of the following charge transfer model:

$$\Delta G = I_D - E_A - E_{00} - \frac{e^2}{r} < 0 \qquad \textbf{2-23}$$

I_D - the ionization potential for the removal of an electron from the lowest-energy occupied bonding molecular orbital; E_A - electron affinity, a measure of the energy of the lowest-energy unoccupied anti-bonding molecular orbital. In the excited state, the energy of exciplex formation is lowered by the excitation energy (E_{00}) possessed by A*. Bringing the separated ions A^- and D^+ to their equilibrium distance r in the exciplex reduces ΔG by an electrostatic term $\frac{e^2}{r}$. Because a molecule in an excited state is both a better electron donor and a better electron acceptor than in its ground state, exciplex formation is expected to be a widespread phenomenon. Exciplexes and excimers, though difficult to detect directly, are implicated in many photochemical processes and their formation plays an important role in the photo-dynamics of clusters.

2.5.3 Bathochromic (red) and hypsochromic (blue) shifts in complexes

Polar solvents stabilize (ππ*) states and destabilize (nπ*) states with respect to the situation in non-polar solvents[155, 168]. The effects of hydrogen bonding with a solvent on electronic excited states can be investigated in small molecular complexes[178]. If molecular (ππ*) and (nπ*) states have comparable energies, changing the solvent may invert the energetic ordering of the levels with dramatic results (see **Fig. 2.9**).

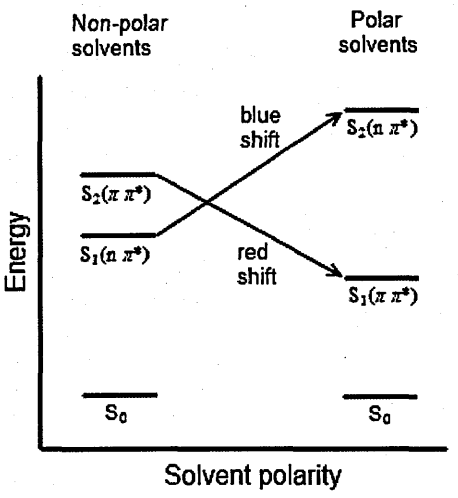

Fig. 2.9: The effect of solvent polarity on the ordering of (nπ*) and (ππ*) states[155].

The dipole moment of these nπ* state is usually smaller than that of the ground state since excitation involve moving charge from localized lone pair to a delocalized orbital. The general rule is that the larger dipole moment causes larger stabilization of a state when a molecule is surrounded by a polar solvent[171]. So, if the dipole moment of the ground state is larger than the excited state, the ground state will become more stable, and the final result will be an increased gap between states, i.e. blue shift[171].

2.6 Energy dissipation processes

Excited states formed as a result of the absorption of ultraviolet and visible radiation typically have lifetimes between femtoseconds and nanoseconds before returning to the ground state by loss of the excess energy. There are two major types of process by which molecules can dissipate the absorbed energy[168]. One type is termed a "radiative" process since the energy is lost by the emission of electromagnetic radiation, while the other is classified as a "non-radiative" process since no radiation is emitted during the relaxation from the excited state.

2.6.1 Radiative transitions

In a radiative transition[168], an excited species passes from a higher excited state to a lower one with the emission of a photon. The following processes can be distinguished:

1) Fluorescence - radiative transition between states of the same multiplicity. Fluorescence generally occurs on a timescale of 10^{-5}-10^{-8} s[179].
2) Phosphorescence - the transition occurs between states of different multiplicity, e.g. T_1-S_0. Phosphorescence results from the radiative transition from the lowest vibrational level of the first triplet state to the various vibrational levels of the ground state. Phosphorescence is a relatively slow process, typically occurring in a timeframe of 10^{-4}-10^{2} s[179].

2.6.2 Radiationless processes: internal conversion and intersystem crossing

When at least two potential energy surfaces approach each other and the coupling between them becomes important, a non-adiabatic process can occur[168, 171, 180, 181]. The rate of this process depends on the energy separating two potential energy surfaces. Non-adiabatic transitions can be quantified by the Landau-Zener formula, presented here[182, 183]:

$$P = exp\left(-\frac{\pi \Delta U^2}{h u \Delta s}\right) \qquad \textbf{2-24}$$

where:

P - probability of the nonadiabatic transition;

$\Delta U = |U_1(R_p) - U_2(R_p)|$ - the spacing between adiabatic potential curves U_1 and U_2 in the centre of the region of the non-adiabatic transition.

$u = \sqrt{\frac{2E_{kin}(R_p)}{\mu}}$ - velocity at the crossing point;

μ - the mass of the particle;

$E_{kin}(R_p)$ - local kinetic energy;

R_p - the centre of the region of the non-adiabatic transition;

Δs - difference of the slopes of the two diabatic surfaces at the crossing point.

The description by the Landau-Zener model of the non-adiabatic coupling at avoided crossing is limited by the condition that the kinetic energy of the nuclear motion within the interaction region should be considerably higher than the spacing between the potential energy surfaces in this region[183].

The fastest type of nonadiabatic transition can occur through conical intersection, i.e. when two potential energy surfaces intersect. Internal conversion (IC) is a radiationless transition between isoenergetic states of the same multiplicity, while intersystem crossing (ISC) is a radiationless transition between states of different multiplicity. A radiationless transition can be treated by time-dependent perturbation theory, with a perturbation H' inducing a time-dependent evolution of the system from an initial state (Ψ_1) into a final one (Ψ_2). For internal conversion H' arises from electrostatic interactions between the electrons and nuclei, while for intersystem crossing H' is the spin-orbit interaction.

The rate constant k_{nr} for the non-radiative transition from each populated level of state 1 is given by the Fermi Golden rule[168]:

$$k_{nr} = \frac{2\pi}{\hbar}\langle\Psi_1|H'|\Psi_2\rangle^2\rho \qquad \textbf{2-25}$$

where:

ρ - the state-density factor which describes the number of states in the quasi-continuum that is isoenergetic with the levels of state 1 from which the radiationless transition occurs;

$\langle\Psi_1|H'|\Psi_2\rangle$ - a matrix element giving the energy of the interaction between the initial and final states induced by the perturbation H'.

Invoking the Born-Oppenheimer approximation and factorizing the wavefunctions Ψ into electronic (ψ) and vibrational (θ) components, the approximate expression is obtained[168]:

$$k_{nr} \propto \langle\psi_1|H'|\psi_2\rangle^2 \sum_i \sum_j \langle\rho\,\theta_{1i}|\theta_{2j}\rangle^2 \qquad \textbf{2-26}$$

where:

$\langle \psi_1 | H' | \psi_2 \rangle$ - the electronic matrix element ($\int \psi_1 H' \psi_2 d\tau_e$), τ_e represents coordinates of all electrons;

$\langle \theta_{1i} | \theta_{2j} \rangle$ - the vibrational overlap integral (Franck-Condon factor) between the i-th vibrational level of the initial state and the j-th vibrational level of the final state. The double summation embraces all the populated levels of state 1 from which a radiationless transition can occur and the approximately isoenergetic levels of state 2 to which a transition can occur.

ρ in the equation **2-26** is also the state-density factor. The whole expression $\sum_i \sum_j \langle \rho\, \theta_{1i} | \theta_{2j} \rangle^2$ can be denoted as ρ_{FC} - so-called density of states weighted Franck-Condon factor. It shows that not only the number of ways the transition can happen matters (i.e. the density of possible final degenerate states characterized by ρ), but also the vibrational overlap integral for each of these transitions.

The electronic matrix element is the non-radiative counterpart of the electronic transition moment and will have very small values unless the initial and final orbitals overlap effectively. In general, only states of the same symmetry can internally convert. However internal conversion can also occur between electronic states of different symmetry due to vibronic coupling as high vibrational levels of one state can have the same symmetry as another despite the respective electronic states having different symmetries when vibrationally cold.

A molecule can be raised directly from the ground state S_0 to an excited singlet state by absorption of EM radiation of the appropriate wavelength but can only generally be raised to an excited triplet state by initial promotion to the corresponding singlet state followed by reversal of the spin orientation of the excited electron.

El Sayed's selection rules for intersystem crossing are[184]:

Allowed: $^1(n\pi^*) \leftrightarrow {}^3(\pi\pi^*)$; $^3(n\pi^*) \leftrightarrow {}^1(\pi\pi^*)$

Forbidden: $^1(n\pi^*) \leftrightarrow {}^3(n\pi^*)$; $^1(\pi\pi^*) \leftrightarrow {}^3(\pi\pi^*)$

Processes forbidden under these rules still occur due to the relaxation of symmetry restraints via vibronic spin-orbit coupling. However the rate constants 10^2 - 10^3 times are lower than those for allowed intersystem crossing.

There is an inverse correlation between the rates of non-radiative transitions involving the lowest states of similar molecular geometries and the difference in energy between the v=0 levels of the states involved: the smaller the energy gap, the bigger rate. The energy gap law can be rationalised by noting that as the gap increases the radiationless transition from a given level of state 1 will be to an increasingly high vibrational level of state 2, with reduced vibrational overlap and correspondingly reduced rate constant.

There is another effect which depends on Franck-Condon factors. With large and rigid molecules such as aromatics there is typically little change of geometry on electronic excitation, so the minimum in the S_1 surface is likely to be only slightly displaced with respect to that of S_0. In such cases internal conversion from the zero point level of S_1 to S_0 will be very small. This means that fluorescence can compete with radiationless depopulation of S_1, and hence the rule that rigid systems tend to fluorescence.

2.6.3 Vibrational relaxation

Excited species are often created with excess vibrational and rotational energy in addition to the electronic energy[168]. The rate constant for the emission of infrared photons is small and loss of vibrational energy (called vibrational relaxation or vibrational cascade) is largely dependent upon collisions, as a result of which vibrational energy is converted into kinetic energy distributed between the colliding species.

2.6.4 Vibrationally hot electronic ground state molecules

S_0^{**} designates the electronic ground state in a highly excited vibrational state[185], for example formed by rapid internal conversion from an electronic excited state. Intramolecular vibrational energy redistribution is complete within a period of time shorter than 1 ns. The molecule is populated in highly excited vibrational states with the

rovibrational energy equal to the incident photon energy plus the molecule's rovibrational energy in its electronic ground state prior to photo-absorption. This energy is distributed among all the vibrational modes (v_i) and the equivalent temperature of S_0** can reach more than a few thousand Kelvin for UV excitation. Depending on the relevant potential barriers, S_0** can isomerise and / or dissociate.

In some cases, a hot molecule produced by UV excitation can have enough internal energy to initiate reactions that would otherwise be much slower or energetically unfavourable. Such a hot molecule is in a microcanonical state with a narrow energy distribution, which means the reaction will give a specific rate constant and can be explained in terms of the RRKM (Rice-Ramsperger-Kassel-Marcus) statistical reactivity theory. The dissociation rate constant $k_{E,J}$ at an energy E and angular momentum quantum number J is given by the equation:

$$k_{E,J} = \frac{N_{E,J}}{h\,\rho_{E,J}} \qquad \textbf{2-27}$$

where:

$N_{E,J}$ - the number of quantum routes;

$\rho_{E,J}$ - the density of states of the parent molecule.

2.6.5 Photodissociation

The fragmentation of a molecule through absorption of one or more photons is called photodissociation[186]. The energy of the absorbed photon(s) is converted into internal energy of the molecule and if this exceeds the binding energy of the weakest bond, the molecule can irreversibly break apart. Dissociation energies vary from a few meV for van der Waals bound systems (e.g. certain types of molecular clusters) to several eV for covalently bound molecules. Different types of photodissociation can be distinguished[186]:

- direct photodissociation in the electronic excited state;

- multiphoton dissociation in the electronic ground state;

- electronic predissociation whereby fragmentation takes place in a different electronic state

than the one that was initially accessed by the photon absorption

- vibrational predissociation whereby fragmentation occurs in quasi-stable (so-called "resonance") states accessed by tunnelling through the barrier or by internal vibrational energy redistribution;

- photodissociation in a vibrationally hot electronic ground state

2.6.6 Photodimerization and photohydration

Photodimerization is a bimolecular photochemical process in which new chemical bonds are formed between initially distinct molecules through the vacation of electrons from carbon-carbon double bonds or carbon-oxygen double bonds. Cyclobutane pyrimidine dimers are typical products of this type of reaction occurring in DNA. The example of a photocycloaddition reaction is thymine photodimerization, represented below (**Fig. 2.10**) [168].

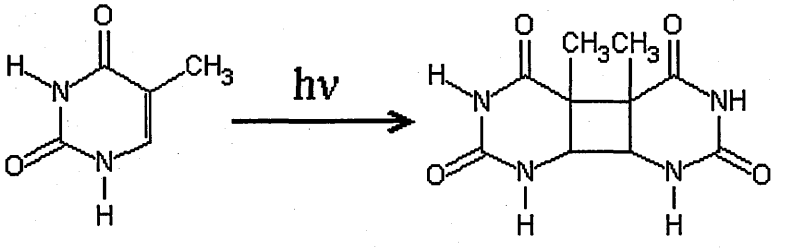

Fig. 2.10: Thymine photodimerization reaction[187].

The underlying molecular processes leading to the photodimerization of thymine remains unclear[188]. Photodimerization in the triplet excited state is one of the suggested mechanisms. Its efficiency is modulated by[187] the effectiveness of the triplet-triplet energy transfer process from a donor photosensitizer molecule, which relates to the relative position of the intermediate in the three acceptor systems, and of the intersystem crossing process to the ground state of the photoproduct. Indirect evidence for this reaction occurring in molecular beam conditions has been given by Kim[189, 190].

Photohydration is the term given to any photochemical reaction leading to the addition of

water across a double or triple bond or to a carbonyl group. An example of photohydration of uracil is the addition of a water molecule to 5-6 double bond during UV irradiation (**Fig. 2.11**). This reaction has been observed for uracil in a frozen solution[191].

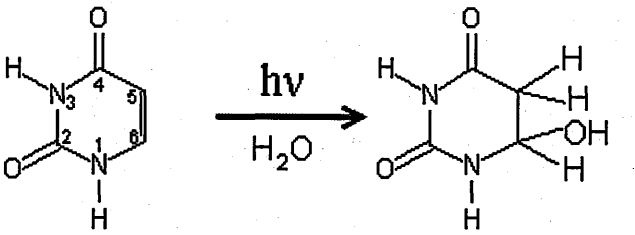

uracil 6-hydroxy-5-hydroxy uracil

Fig. 2.11: Uracil photohydration reaction[192].

2.7 Reactions in molecular clusters following photoionization

Intermolecular charge transfer and chemical reactions have been observed in various photoionization mass spectrometry experiments[193, 194]. The major types of these reactions are presented below:

1. Hydrogen-bonded systems can undergo an intermolecular **proton-transfer (PT) reaction** after ionization. For example, the ammonia dimer decays according to:

$$(NH_3)_2 + hv \rightarrow (NH_4)^+ + NH_2^* + e- \qquad \textbf{2-28}$$

at an energy of 50 meV above the ionization potential of the parent dimer ion[193]. The PT takes place from the primarily ionized molecule to its neutral partner via the H bond.

2. **Intra-cluster Penning Ionization.** If in mixed clusters a molecular subunit is electronically excited with energy larger than the ionization potential of one of its molecular partners, a charge transfer may take place by which the partner is ionized:

$$A^* B \rightarrow A B^+ + e^- \qquad \textbf{2-29}$$

The autoionization process is generally called Penning ionization and has been observed in molecular clusters[193].

3. **Electron transfer** in clusters. If a specific molecule in a cluster is ionized, it may be neutralized by electron transfer (ET) from a neighbouring solvent molecule. This redox

reaction is summarized by:

$$A^+ B_n \rightarrow (A B_n^+)^{\#} \rightarrow A + B_n^+ \qquad \textbf{2-30}$$

If the dissociation step does not take place, ET is not detectable by mass spectrometry. This reaction is called dissociative electron transfer[193].

4. In addition to charge-transfer processes, chemical reactions may also take place between an ion and its solvent shell. An example of this type of processes is the **nucleophilic substitution reaction** (S_N)[194].

3 Experimental setup

3.1 Overview

A new **REMPI-TOF** (**RE**sonant **M**ulti**P**hoton **I**onization - **T**ime **O**f **F**light mass spectrometry) apparatus has been developed to probe the ionization and fragmentation of biomolecules and clusters. This system is used to perform UV REMPI-TOF experiments on DNA/RNA bases in isolation and within hydrated clusters using 220-230 nm nanosecond laser pulses. Target beams of these molecules and clusters were formed by continuous supersonic expansion of argon seeded with sublimated DNA/RNA bases and sometimes water vapour. The experimental set-up is shown in **Fig. 3.1** (schematic) and in **Fig. 3.2** (labelled photograph). The individual components of the system are discussed in the following sections of this chapter: (**3.2**) the vacuum system, (**3.3**) the molecular beam source (**3.4**) the time-of-flight mass spectrometer, (**3.5**) the laser system, and (**3.6**) the computer control system. The multi-photon ionization technique used in this research is reviewed in section (**3.7**).

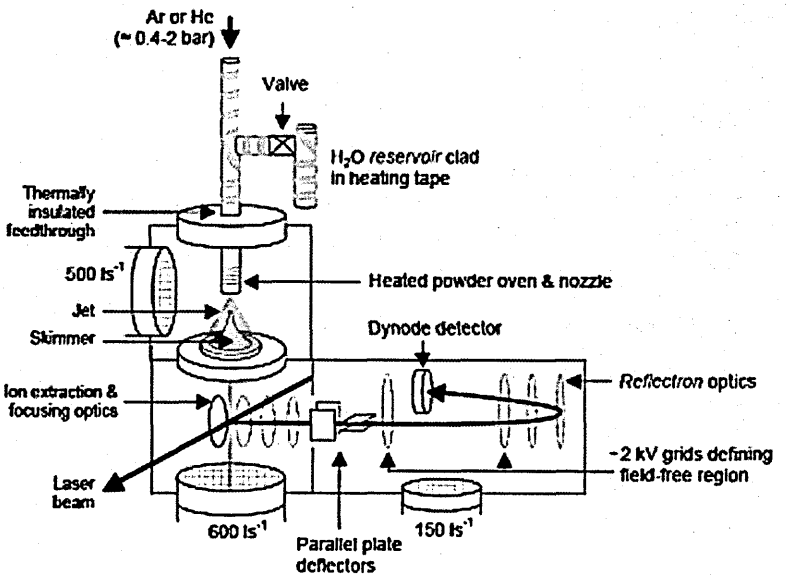

Fig. 3.1: Schematic diagram of the experimental apparatus.

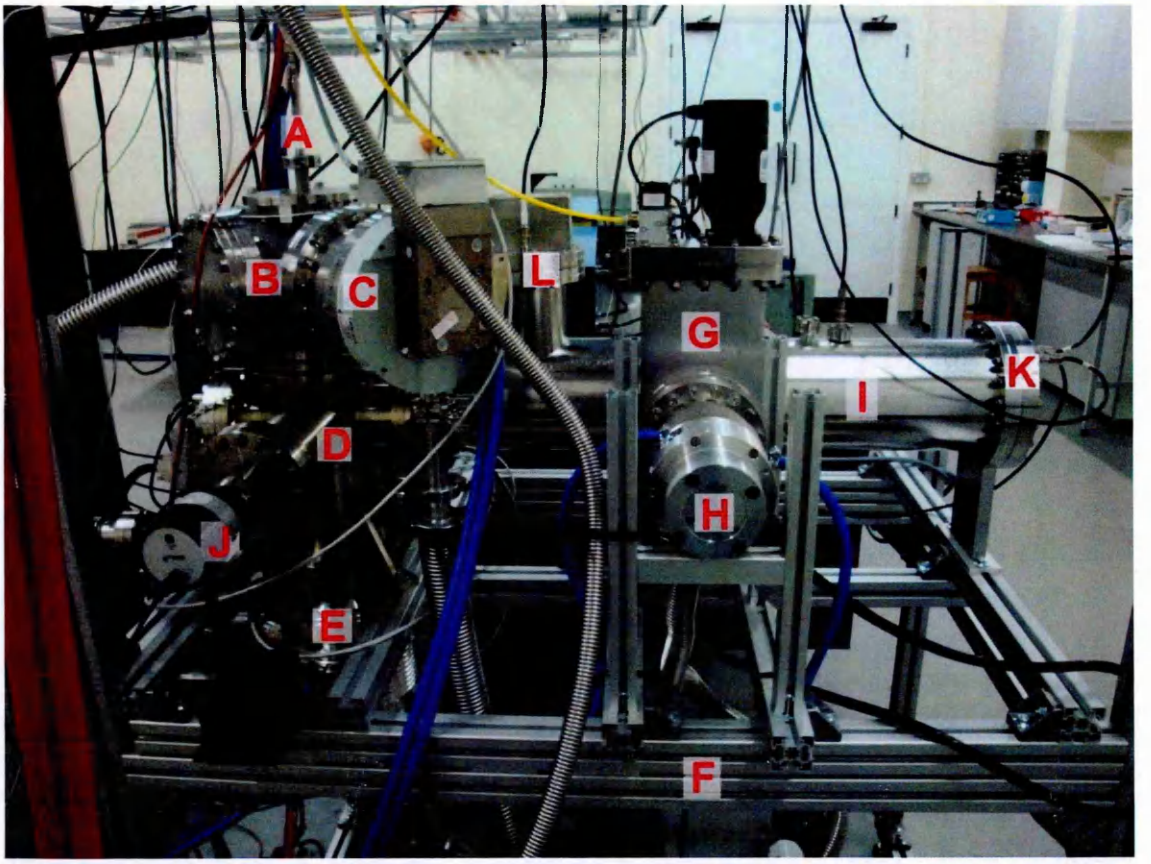

Fig. 3.2: Labelled photograph of the experimental set up. Argon seeded with DNA/RNA bases and sometimes water vapour expands from the high pressure tube (A) into the expansion chamber (B) through a 50 μm orifice. Part of this supersonic expansion passes through the 400 μm skimmer into the diagnostic chamber (D) where the molecular beam crosses the pulsed laser beam. Resultant ions are identified by reflectron TOF mass spectrometry. The other components of the system shown in the figure are: C - the turbomolecular pump (Pfeiffer Vacuum TMU 521) attached to the expansion chamber; E - the turbomolecular pump (Oerlikon Leybold MAG W 600) attached to the diagnostic chamber; F - the support frame; G - the gate valve; H - the turbomolecular pump (Oerlikon Leybold TURBOVAC 151) attached to the mass spectrometer flight tube; I - the mass spectrometer flight tube; J - the pyroelectric joulemeter; K - the reflectron mounting flange; L - the electron multiplier (dynode detector) mounting flange.

3.2 The vacuum system

3.2.1 Vacuum chambers, pumps, diagnostics, and their support system

The supersonic jet apparatus required to form the molecular clusters can be divided into three sections: the buffer gas line (high pressure zone), the expansion chamber, and the diagnostic chamber (both chambers custom-built by Caburn MDC). These sections are connected via a nozzle and a skimmer as shown in **Fig. 3.1** and **Fig. 3.2**. The pressure in the buffer gas line can be regulated above a minimum ~0.4 bar and measured within ±10 mbar using a transducer (Swagelok PTU series). The gas line is composed of 6 mm stainless steel tubing (see section **3.3.3** for more details), this section can be evacuated prior to experiments using a 5 m^3hr^{-1} rotary pump. The distance between the nozzle and the skimmer can be varied in order to optimize the intensity of the molecular beam. The present measurements were carried out with a separation of 10 mm.

The expansion chamber is evacuated using a turbomolecular pump: Pfeiffer Vacuum TMU 521 (pumping speed 500 l/s, connected to a 30 m^3hr^{-1}rotary backing pump). The diagnostic chamber is also evacuated using turbomolecular pump: Oerlikon Leybold MAG W 600 (pumping speed 600 l/s, connected to a 12 m^3hr^{-1}rotary backing pump). The mass spectrometer flight tube is additionally evacuated via a gate valve by a turbomolecular pump: Oerlikon Leybold TURBOVAC 151 (pumping speed 145 l/s connected to a 5 m^3hr^{-1} rotary backing pump). All backing pumps attached to turbomolecular pumps have Al_2O_3 traps to limit oil vapour back streaming.

Pressure was monitored throughout experiments and preparation using a thermovac TTR91 gauge (5×10^{-4} – 1000 mbar) connected to the expansion chamber and two Penningvac PTR 90 gauges (5×10^{-9} – 1000 mbar); one connected to the expansion chamber and one to diagnostic chamber. In addition, a Ceravac Transmitter CTR 90 (0.1 – 1000 Torr) was installed in the roughing line of the TURBOVAC 151 turbomolecular pump. The base pressures of the expansion and diagnostic chambers were typically 10^{-7} and 10^{-8} mbar, respectively. During measurements, the pressure in the mass spectrometer (connected directly to the diagnostic chamber) is kept below 10^{-6} to protect the electron

multiplier detector. With the present nozzle-skimmer arrangement and using argon buffer gas, the driving pressure was therefore limited to a maximum ~ 2 bar.

A support frame has been designed and assembled in order to accommodate the vacuum chambers and the other vacuum system components (expansion chamber, diagnostic chamber, mass spectrometer flight tube, gate valve) – see **Fig. 3.2**. Rexroth Bosch components (profiles, connectors, brackets, casters, levelling foods and sliders) have been used in the construction of the support frame.

3.2.2 Vacuum system testing

Stronger clustering conditions can be obtained with higher argon pressure above the expansion nozzle, however this also increases the pressure in the diagnostic chamber and hence the mass spectrometer. In order to define norms for safe operation of the electron multiplier, tests were carried out with the electron multiplier removed and a PTR 90 pressure gauge connected in its position. The second PTR90 gauge was installed at its standard position in the diagnostic chamber. Pressure was monitored at both positions as a function of air flow (controlled using a dosing valve) into the diagnostic chamber, approximating the effect of a molecular beam. **Fig. 3.3** shows the indications of these two pressure gauges recorded at two configurations of the gate valve attached to the mass spectrometer flight tube: open and closed.

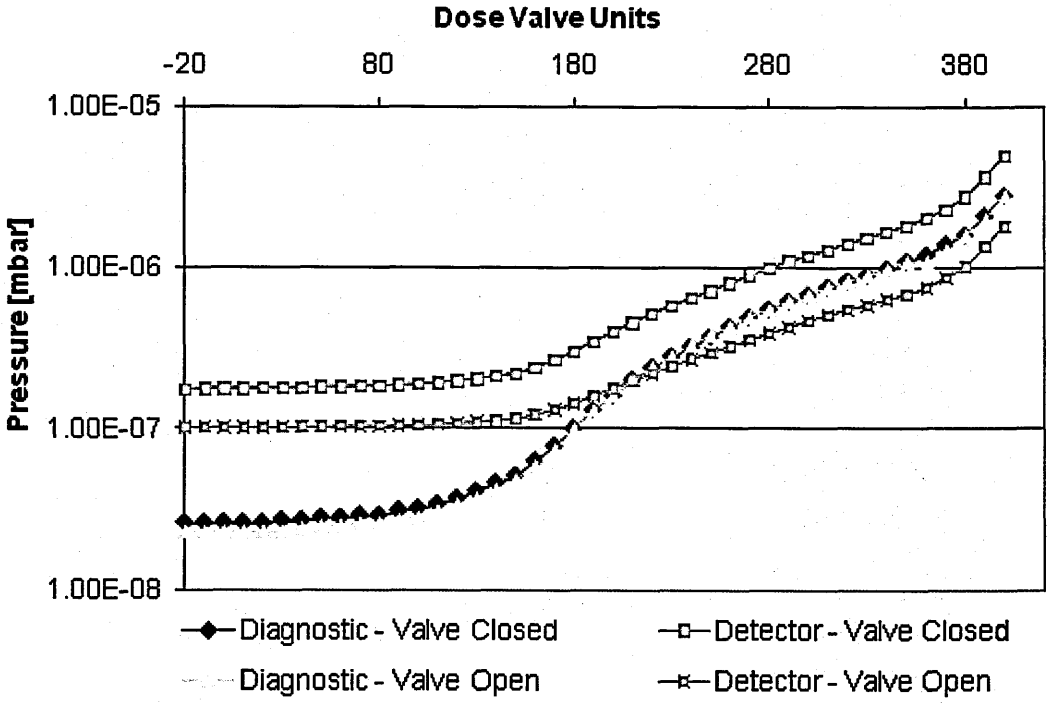

Fig. 3.3: Pressure measurements in the diagnostic chamber and the mass spectrometer flight tube (close to the detector position) with the gate valve open and closed.

The data presented above demonstrate the importance of the turbomolecular pump for the mass spectrometer. Pressure values in the mass spectrometer flight tube at the detector position are lower for operation with the additional turbomolecular pump. This allows higher argon pressure to be applied in the buffer gas line in order to enhance the creation of clusters in the molecular beam.

3.3 The molecular beam source

3.3.1 Gas dynamics in a supersonic beam source - choked flow model

A supersonic jet is produced by means of a continuous adiabatic expansion of argon seeded with vaporized molecules. This long-established method narrows the velocity and angular distribution of the atoms and molecules, reduces the internal energies of the molecules, and can enable aggregation to take place.

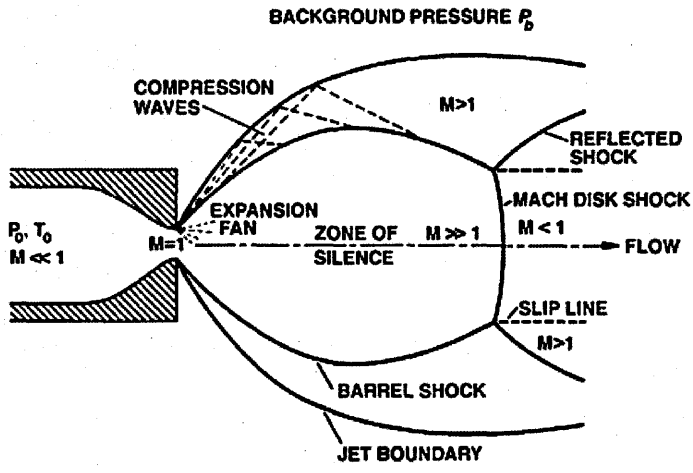

Fig. 3.4: Continuum free-jet expansion[195].

The central feature of a free-jet atomic and / or molecular beam is a supersonic gas expansion from a high pressure (P_0) gas source into a low pressure (P_b) background[195]. In the high pressure zone, the particle velocity is small compared to the speed of sound. The particle velocity increases during the gas expansion through an orifice up to the speed of sound, Mach number M = 1. The free-jet supersonic expansion then begins from the sonic (M = 1) surface. Many of the processes for which the free jet are used depend strongly on the flow field near the nozzle exit, where the supersonic flow begins[196]. **Fig. 3.4** shows the structure of a free expansion under continuum (steady state) conditions. While the diagram shows a short conical nozzle, expansions through other nozzle shapes can be defined using the same parameters. For the gas flow to be supersonic, the ratio P_0/P_b must exceed a critical value G[195, 197] given by:

$$G = \left(\frac{\gamma+1}{2}\right)^{\gamma/(\gamma-1)} \qquad \textbf{3-1}$$

The parameter γ is defined as $\gamma = c_p/c_v$, in terms of the specific heat capacities at constant pressure (c_p) and at constant volume (c_v) of the accelerating gas. G is lower than 2.05 for all gases.

Multiple molecular collisions taking place in a gas passing through the orifice transform the random thermal energy into directional kinetic energy. Consequently, the gas temperature is gradually reduced and the molecular velocity distribution becomes progressively

narrower (translational cooling)[198], however the beam temperature as the measure of random molecular motion is not a directly accessible quantity[199].

The velocity of the beam increases during the expansion and the beam parameters in the so-called collisionless 'zone of silence' (where no further cooling takes place) are independent of any boundary conditions (walls, P_b), which is caused by the fact that perturbation propagates at the speed of sound, whereas the gas moves faster than the speed of sound[197]. Therefore a skimmer placed inside this zone can extract a supersonic beam. If the background pressure P_b is small enough, a smooth transition to molecular flow occurs and the resultant beam is not affected by shock structures. The beam is only disrupted by scattering from the residual gas[197].

For ideal gases, the change of enthalpy (dh) is equal to $c_p\,dT$ where $c_p=(\gamma/(\gamma-1))\times(k_B/m)$. The maximum or terminal velocity (coinciding with $T<<T_0$)[197] is:

$$v_\infty = \sqrt{\frac{2k_B}{m}\left(\frac{\gamma}{\gamma-1}\right)T_0} \qquad \textbf{3-2}$$

where m is the particle mass m and k_B is the Boltzmann constant. For H_2 $\gamma=5/3$[197] at T_0=100 K, and v_∞ is 1436 m/s. T is the local temperature viewed from a reference frame travelling at the average velocity of the beam[200]. For isentropic expansion of an ideal gas, the temperature ratio is:

$$\frac{T}{T_0} = \left(1+\frac{\gamma-1}{2}M^2\right)^{-1}; \qquad \textbf{3-3}$$

with the assumption of constant c_p. $M=v/c$ is the Mach number where c the speed of sound, $c=\sqrt{\gamma k_B T/m}$ [195]. Furthermore, the mean beam velocity of the expanding gas as function of the Mach number is derived as:

$$v = M\sqrt{\frac{\gamma k_B T_0}{m}}\left(1+\frac{\gamma-1}{2}M^2\right)^{-1/2}. \qquad \textbf{3-4}$$

Hence at M=1, which is expected around the nozzle exit, v is equal to 718 m/s for H_2 with T_0=100 K[195]. Using M as calculated above for a free-jet axisymmetric expansion, the key

thermodynamic properties of temperature, particle density, collision frequency (between particles in the expansion, not background particles) and velocity vary with distance from the nozzle exit as shown **Fig. 3.5**.

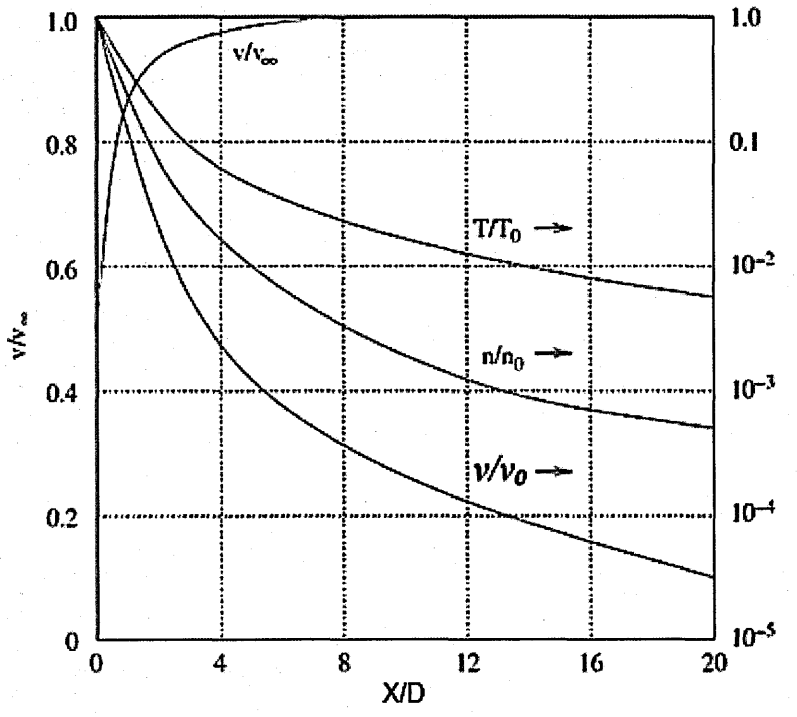

Fig. 3.5: Free jet on-axis properties versus distance from the source (X given in units of source diameter D) for a monoatomic gas (γ=5/3) with velocity v. The temperature T, the density n, and the binary hard-sphere collision frequency ν are normalized by the source-stagnation values T_0, n_0, and ν_0 (figure taken from Ref. [195]).

The relative density n/n_0 is expressed by the following equation[201]:

$$\frac{n}{n_0} = \left[1 + \frac{1}{2}(\gamma - 1)M^2\right]^{-1/(\gamma-1)} \qquad \textbf{3-5}$$

The so-called terminal Mach number, M_∞, for monoatomic gas is given by[201]:

$$M_\infty = 133(P_0 D)^{0.4}; \qquad \textbf{3-6}$$

where P_0 (stagnation pressure) and D (nozzle diameter) are expressed in bar and cm, respectively.

The terminal distance, X_∞, at which M_∞ occurs, is given by[202]:

$$X_\infty = D\left(\frac{M_\infty}{3.26}\right)^{1.5} \qquad \textbf{3-7}$$

This relatively simple picture of supersonic free-jet expansion is disrupted close to the shock waves in the expanding beam shown in **Fig. 3.4**. The central core of the expansion is surrounded concentrically by a shock boundary (Barrel shock). Particularly important is the shock front, called the Mach disc, perpendicular to the direction of the flow. The disc originates from molecules in the beam colliding with the surrounding gas. Therefore, the collisionless "zone of silence" defined above extends up to X_M, the distance at which the Mach disc occurs[201]:

$$X_M = 0.67D\sqrt{\frac{P_0}{P_b}} \qquad \textbf{3-8}$$

where P_b is the pressure in the expansion chamber.

Based on the analysis described above, the gas flow through the nozzle can be characterized according to the choked flow model. In particular, the mass flow [kg/s] is given by the equation[203]:

$$\dot{m} = \sqrt{\frac{\gamma}{R}\left(\frac{2}{\gamma+1}\right)^{(\gamma+1)/(\gamma-1)}} \cdot \frac{P_0}{\sqrt{T_0}} \cdot A^* \qquad \textbf{3-9}$$

A^* - the area of nozzle orifice;

R - gas constant.

It is important to note that although the gas velocity reaches a maximum and becomes choked, the mass flow rate is not choked. The mass flow rate can still be increased if the upstream source pressure is increased, (see[204] and references therein). Results of calculations performed in order to characterize the molecular beam source used in the present experiments are presented in the graphs below.

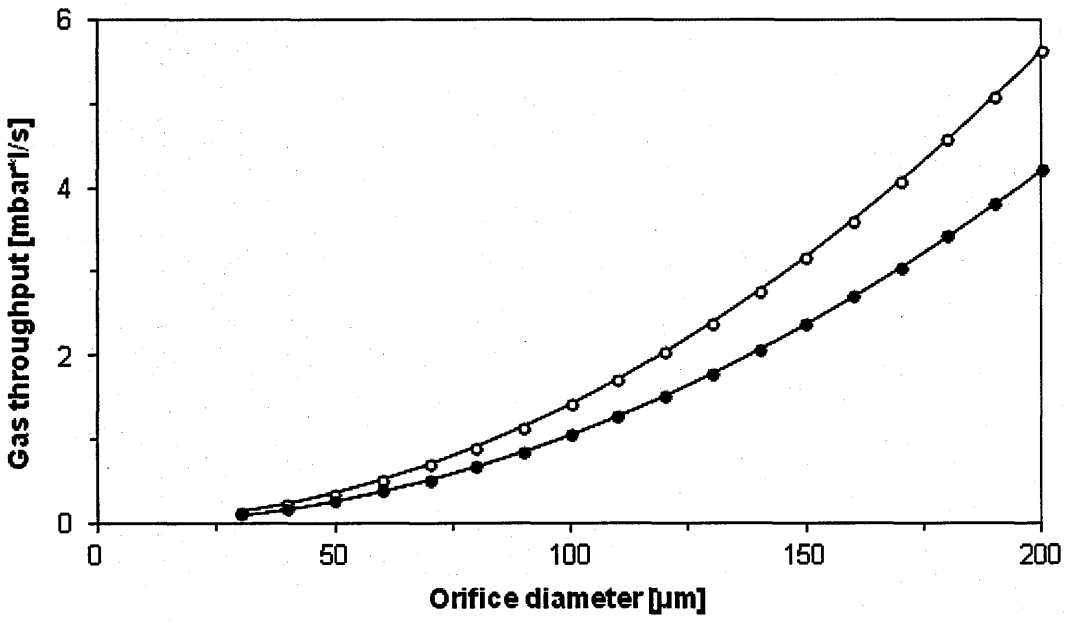

Fig. 3.6: Argon gas throughput through nozzles with different diameters at a stagnation pressure P_0=1 bar and temperature T_0=293 K - open circles and 523 K - closed circles.

For the nozzle used in the present experiments (50 µm diameter ± 10%) the value of argon flow equal to 0.33 mbar*l/s has been calculated using choked-flow model with 1 bar upstream (**Fig. 3.6**). The nucleobase vapour pressure at the temperatures used in the present experiments (typically 220-260 °C) can be approximated assuming 1mTorr (~0.0013 mbar) at 150 °C (Glavin et al.[205]) and average increase ~10 % per °C (Tabet et al.[206]), giving the result within the range of 1 - 50 mbar (≤ 12.5% of the Ar pressure). The flow characteristics in the *dry* measurements can therefore be approximated on the basis of argon's ratio of specific heats. This approximation does not hold, however, for the hydrated measurements (γ for water vapour = 1.32 compared with 1.67 for argon). Using that value of Q and the catalogue value for the pumping speed for the turbomolecular pump applied S = 500 l/s, the pressure in the expansion chamber can be calculated using the equation Q = S x P, the result of this calculation is presented on the **Fig. 3.7**.

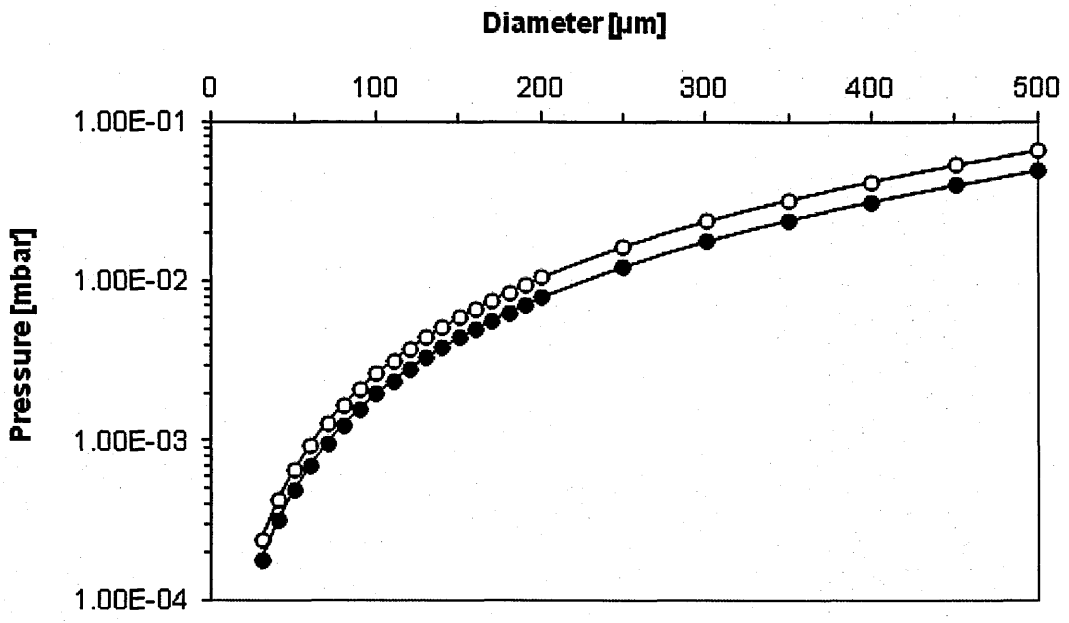

Fig. 3.7: Calculated pressure in the expansion chamber as a function of the nozzle diameter for pumping speed 500 l/s, temperature T_0=293 K - open circles and 523 K - closed circles, stagnation pressure P_0=1 bar.

Calculations indicate that for a nozzle diameter equal to 50 µm a pressure value below 10^{-3} mbar is expected, which is in agreement with the values measured experimentally, indeed in most cases the pressure in the diagnostic chamber during an experiment was within the range of 5 x 10^{-4} – 10^{-3} mbar. The most significant uncertainties are related to the flow through the nozzle, which can be limited notably by condensation or powder grains partially blocking the orifice when the nozzle is not at high temperature.

Calculations of the jet length (the distance at which the Mach disc occurs – X_M) have been made using equation **3-8** in order to establish the optimal nozzle – skimmer distance. The results are presented on the **Fig. 3.8**.

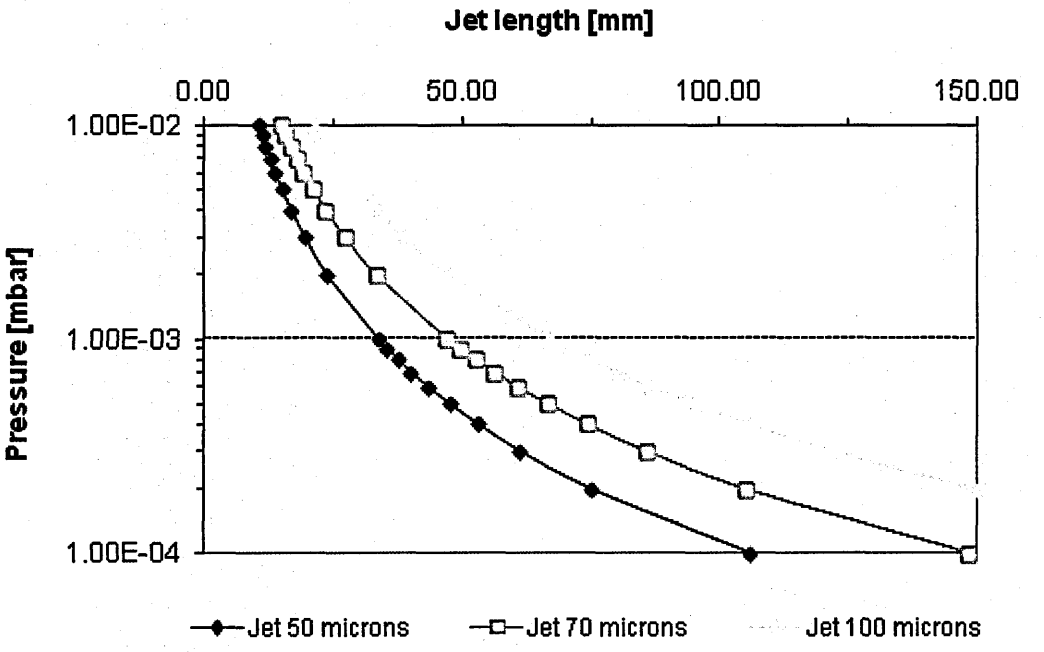

Fig. 3.8: Supersonic jet lengths for different nozzle diameters at driving argon pressure 1 bar and pressure in the expansion chamber given on the Y-axis.

It has been found that for expansion chamber pressures within the range of 5×10^{-4}-10^{-3} mbar a jet length from 47 to 33 mm is expected with 1 bar of argon in the molecular beam source. Measurements of the driving argon pressure and the diagnostic chamber pressure have been made (**Table 3.1**), and on the basis of these values the experimental jet lengths have been calculated and presented in **Fig. 3.9**. Most of the measurements indicate that the Mach disc position is between 30 and 40 mm downstream from the nozzle, which is roughly in agreement with theoretical predictions. Some of the higher indications (above 50 mm) are related to a drop of the diagnostic chamber pressure due to temporary clogging of the nozzle (measurements were carried out at room temperature, so powder or other contaminating particles could block the nozzle when gas was introduced or pumped out). Accordingly a nozzle – skimmer distance ~ 10 mm has been set in the experimental system such that the skimmer is within the supersonic expansion 'zone of silence'.

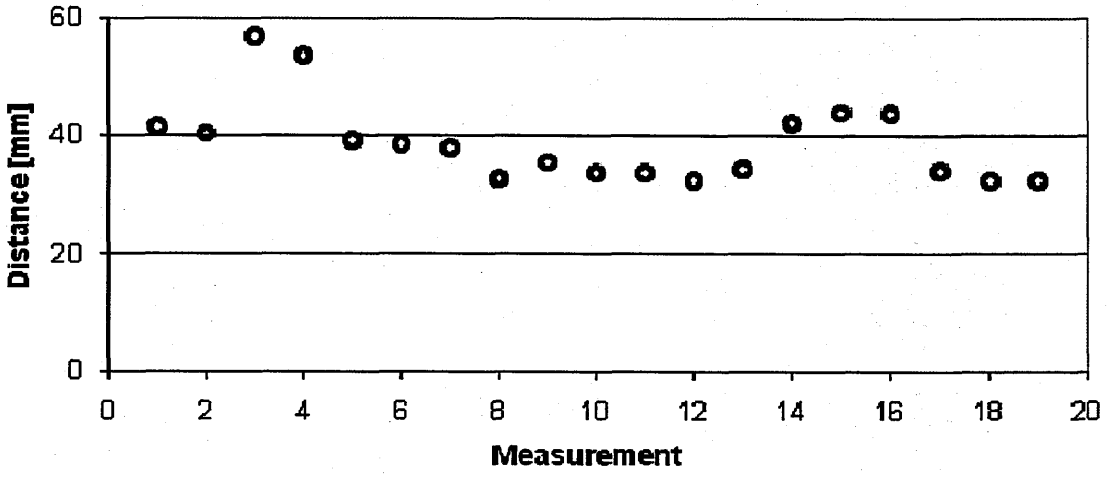

Fig. 3.9: Mach disc positions for 19 separate experimental measurements of argon stagnation P_0 pressure and expansion chamber pressures P_b calculated using equation **3-8**.

Table 3.1: Stagnation P_0 and expansion chamber pressure values P_b measured separately, i.e after each measurement the molecular beam source was pumped out and filled with argon again.

Measurement No	P_0 [bar]	P_b [mbar]
1	1.0	6.30E-04
2	0.6	4.40E-04
3	1.0	3.40E-04
4	1.0	3.80E-04
5	0.9	6.90E-04
6	0.9	7.10E-04
7	0.9	7.30E-04
8	0.9	1.00E-03
9	1.1	1.00E-03
10	1.0	1.00E-03
11	1.0	1.00E-03
12	1.0	1.10E-03
13	0.9	9.00E-04
14	1.1	7.00E-04
15	1.0	5.80E-04
16	1.0	5.90E-04
17	1.0	1.00E-03
18	1.0	1.10E-03
19	1.1	1.20E-03

The argon supersonic beam characteristic parameters (temperature, velocity and density) have been calculated for typical experimental conditions, i.e. stagnation pressure P_0 = 1

bar, orifice diameter D = 50 μm, temperature T = 523 K (250 °C), and the following values have been obtained: maximum terminal velocity v_∞ = 736 m/s (equation **3-2**); terminal Mach number M_∞ = 16 (equation **3-6**); the distance at which the terminal Mach number occurs X_∞ = 0.05423 cm (equation **3-7**); temperature T = 6 K (equation **3-3**) and the relative density $\frac{n}{n_0}$ = 0.0013 (equation **3-5**).

3.3.2 Clustering in a supersonic molecular beam

Due to the cooling process during the expansion, molecular beams are often used to produce condensates, notably atomic and molecular clusters. A large cluster binding energy enhances the formation of clusters and they release their condensation energy into the beam[207]. Conical nozzles can be used to achieve spatial confinement of the jet extending to long distances. The confined jet forms a narrow cone of high intensity and hence increases the probabilities of collisions and thence cluster formation[207]. Clustering also depends on the buffer gas properties and nozzle temperature. As an example, we can consider previous measurements of the production of large methane $(CH_4)_N$ (N up to 120) van der Waals clusters produced by the supersonic expansion of a gaseous mixture consisting of 90% H_2 and 10 % CH_4 at nozzle temperatures of -30 and 27 °C[208]. For identical stagnation pressures, the average methane cluster size produced by expansion at a nozzle temperature of -30 °C was larger than that produced at a nozzle temperature of 27 °C. In addition, methane cluster formation did not occur by supersonic expansion of pure methane gas at a nozzle temperature of 27 °C. These results reveal that the presence of H_2 permits the evacuation of the heat of condensation and thus promotes methane cluster nucleation[208]. Similarly, increased production of $(NH_3)_n$ clusters has been demonstrated at lower nozzle temperatures and higher stagnation pressures[209].

3.3.3 The molecular beam source design

In the present experiment a new molecular beam source has been designed, constructed and successfully commissioned. The molecular beam source installed in the expansion chamber is shown in **Fig. 3.10**.

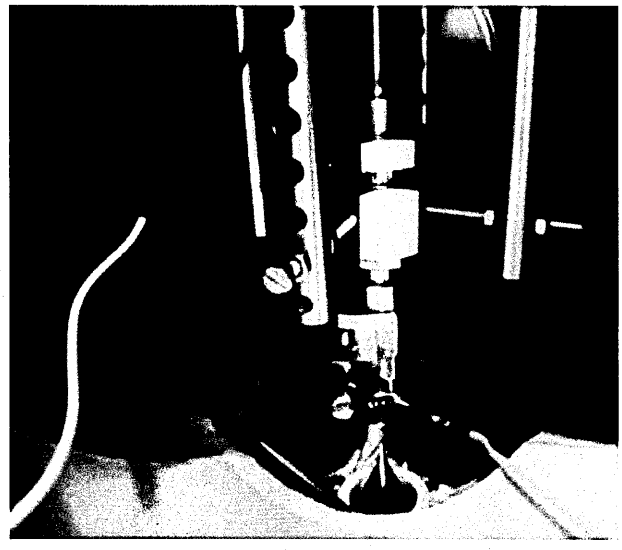

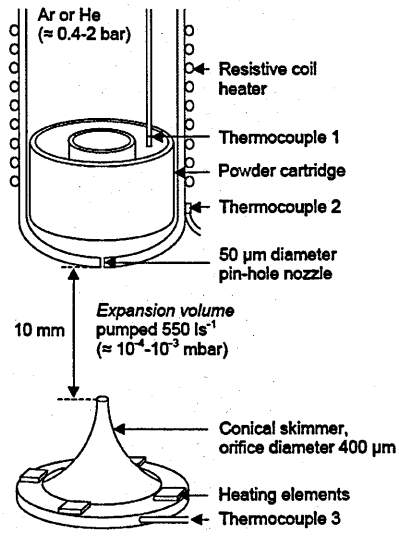

Fig. 3.10: The molecular beam source installed in the expansion chamber, shown during the aligning process (on the left), and the scheme of the molecular beam source (on the right).

The major component of the molecular beam source is the 50±5 µm diameter nozzle, which was laser-drilled into the closed end of the SS ½" tubing (Lennox Laser). This part can be interchanged in order to work with different nozzle diameters. The nozzle is presumed to be an approximate pin-hole but precise information on the shape and thickness is not available from the supplier. A detailed description of the welded and assembled tube fitting in the molecular beam source is given in the **Appendix 9.1**.

Two systems to introduce target molecules are available: a stainless steel powder cartridge positioned approximately 2 mm above the nozzle and a H_2O reservoir. The powder cartridge has a length of 10 mm, distinctly shorter than the heater (described below). Combined with the fact that the tube is only heated when there is a flow of buffer gas through the nozzle, this prevents any discernible condensation of the sublimated sample powder upstream from the cartridge. Alignment is carried out by shining a class 2 laser (Hero – PLP650AR – laser, 1 mW, adjustable focus) from a fixed point in the diagnostic chamber through the skimmer orifice and adjusting the nozzle position until the beam can be viewed though the central hole of the powder cartridge.

In order to achieve a stable vapour pressure of sublimated nucleobases, the source temperature was recorded using a thermocouple (type K, mineral insulated, 50 cm long from TC direct) inserted directly into the heated gas mixture. This temperature serves as the reference for a proportional–integral–derivative (PID) controller (Czaki R720) (**Fig. 3.11**) that supplies the coil heater for the nozzle. The outside of the nozzle is heated using the Tempco Hot runner coil heater (120 watts) with an axial clamp to achieve a good thermal contact. This serves the dual purpose of vaporizing the powder and preventing condensation in the nozzle.

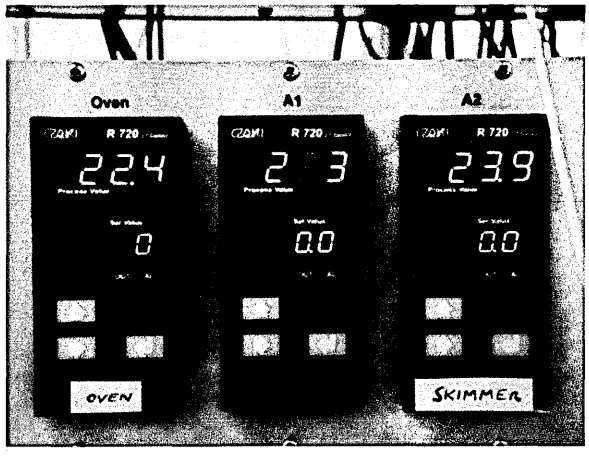

Fig. 3.11: Three temperature controllers Czaki R720.

The temperature of the gas mixture was thus controlled within ±1°C. **Fig. 3.12** shows the temperature variation of the gas above the nozzle during the acquisition of a typical mass spectrum. The second thermocouple (Type K Wire Sensor, fixed to an adjustable pipe fitting 11 mm wide; 12.7 mm diameter, 3M long PTFE/PTFE, 7 strand * 0.2 mm, with tails from Peak Sensors LTD) was installed on the outside of the nozzle, just below the coiled heater, as can be seen in **Fig. 3.10**. It is interesting to note that significant differences have been found between the readings of the internal and external thermocouples. They are presented on the **Fig. 3.13**.

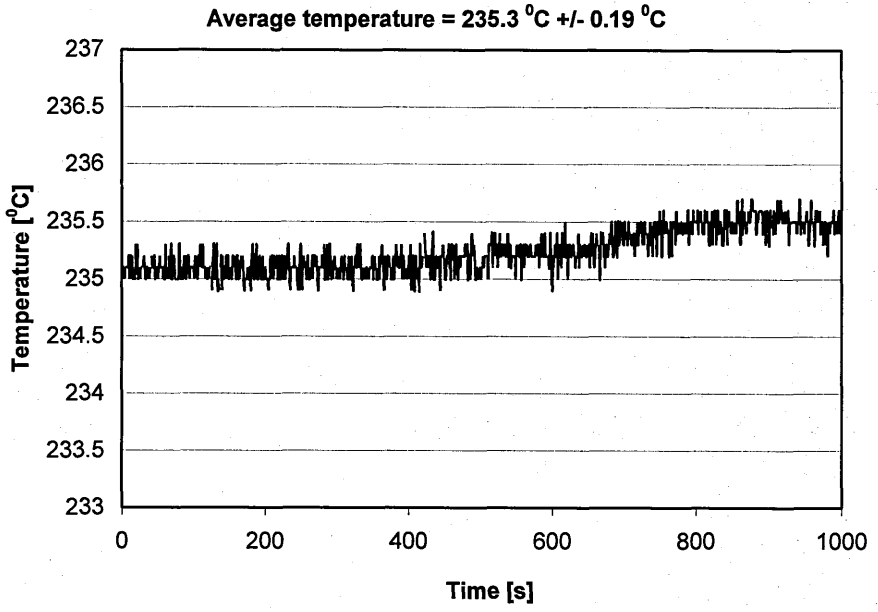

Fig. 3.12: Example of powder temperature variation of the gas mixture (in this case argon seeded with sublimated adenine) above the nozzle as a function of time during a typical mass spectrum acquisition with PID control based on the signal from the internal thermocouple. Note that the error given is the standard deviation.

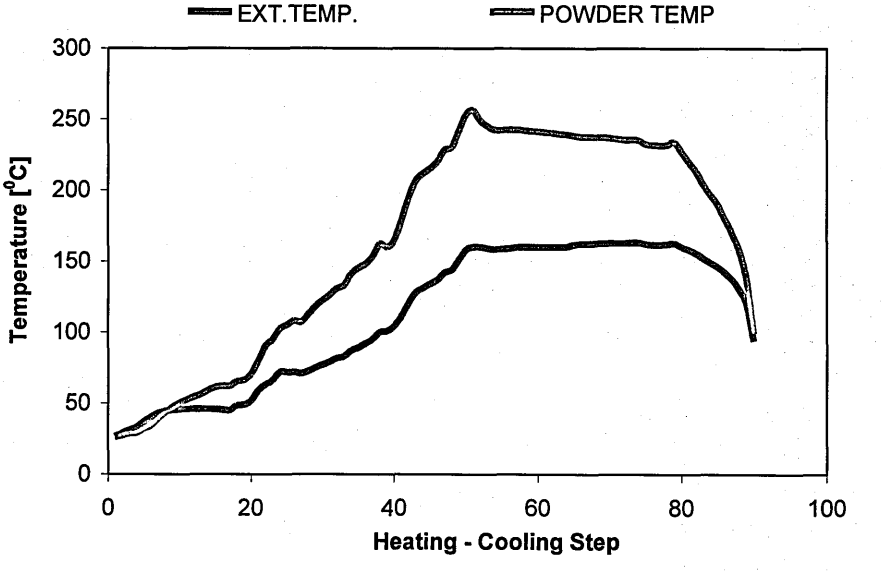

Fig. 3.13: Comparison of external (the outside of tube) and internal (powder) temperature measurements of the cluster source. The source heating was regulated with reference to the external thermocouple during this measurement. The plots show that the external measurement provides an underestimation of the powder temperature and that regulating using the external temperature does not equate to a steady powder temperature.

The stainless steel H_2O reservoir is connected to the buffer gas line via an on-off valve as shown in **Fig. 3.1**. The reservoir and the tubing between the valve and the nozzle are heated using resistive heating tape. The current in the heating tape is regulated using a PID controller (Eurotherm 808) with reference to the temperature recorded using a mineral insulated type K thermocouple (TC direct) in contact with the outside of the reservoir.

Argon was used as the buffer gas throughout the present measurements and the nucleobase powder samples were purchased from Sigma-Aldrich (minimum purity 99%). The pressure in the buffer gas line can be regulated above a minimum ~0.4 bar and measured using a pressure transducer (Swagelok PTU-S-AC9-12AC). The output signal from this pressure transducer is read by a myPCLab data logger connected to the PC via a USB port.

A copper skimmer was purchased from Beam Dynamics (model 2 conical shape). Its detailed dimensions are presented on the **Fig. 3.14**. The skimmer has been mounted in an aluminum clamping system with heat-resistant fluoro-elastomer O-rings. In order to prevent condensation on the skimmer, its brim is maintained at 126 °C using the Czaki PID controller supplying four resistive heating elements (1kΩ each), giving a total power of 14.4W at 240V mains. The skimmer temperature is measured using a mineral insulated type K thermocouple from TC direct inserted into a hole in the aluminium clamping system.

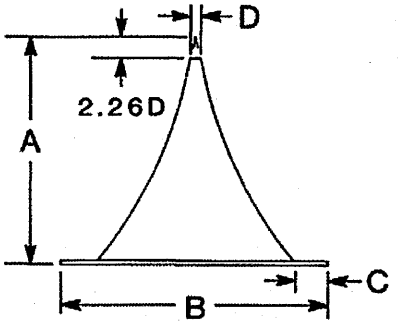

Fig. 3.14: Beam Dynamics Inc.[210] molecular beam skimmer, model no 2. Dimensions: A. Length to Apex - 25.4 mm; B. Base diameter - 27.9 mm; C. Width of flat part of brim (approx.) - 2.5 mm; D. Orifice diameter - 0.4 mm; Total Included Angle at orifice - 25° internal, 30° external; Total Included Angle at base 70°; Material - Copper; Orifice edge thickness - 10 μm max; Wall and brim thickness - 50 to 80 μm.

3.4 The mass spectrometer

3.4.1 Essential concepts

The time-of-flight (TOF) spectrometer has been assembled using components designed and constructed by KORE technology. The only part that was home-built was the divider system to control the voltages on the various electrodes, while the time-to-digital converter card was supplied by FastComtec. The mass spectrometer consists of an ion source, ion/electron deflectors (horizontal and vertical), a field-free drift tube casing, reflectron optics, and an electron multiplier (detector). The ions are formed in the ionization region (by laser MPI) of the ion source and then accelerated out of the source region by a series of constant electric fields. All product ions from the target are accelerated to approximately the same kinetic energy due to the small volume of the laser crossing with the supersonic beam. They pass through the deflector (compensating for the downward velocity distribution of molecules and clusters in the supersonic beam), through the field-free region and into the two-stage reflectron optics. The reflectron compensates for initial spread in the ion kinetic energies. In this stage of the mass spectrometer, ions are decelerated and then accelerated (reflected) back through the field-free region to strike the discrete dynode electron multiplier detector. The velocity of the ions in the free flight path is a function of the ratio of their mass, m, to their charge, q[211]. Therefore, when ions reach the detector they are temporally separated into bunches corresponding to m/q. Hence ions are often characterised using the unit Thomson (Th) in mass spectrometry, where 1 Th is one atomic mass unit (AMU) over one unit of elementary charge. If only singly charged ions are present, the lightest reach the detector first and are followed by groups of ions with successively heavier mass. Thus, each laser pulse results in a mass spectrum[211]. The individual parts of the instrument are described in the following sections.

3.4.2 The ion source

The ion source (**Fig. 3.15**) consists of a back plate, a pulse-out electrode, and two further electrodes to accelerate the ions up to the flight energy of the TOF analyser. The pulse-out electrode and electrode II are gridded but electrode I is gridless. The flight energy in this

TOF instrument is ~1.85 keV and the final element (Electrode II) of the TOF source is maintained at the same potential as the 'field-free region' (FFR). In order to minimize the distance to the pulsing electrode, the Kore pulser drive unit (described below) is attached to the feedthrough flange upon which the TOF source is mounted.

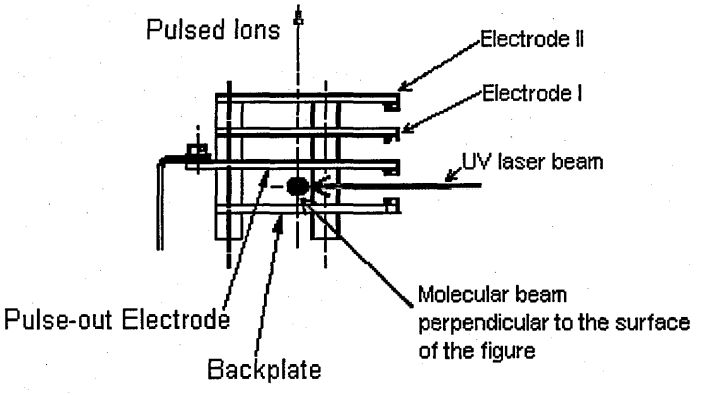

Fig. 3.15: TOF mass spectrometer ion source.

The TOF source high-frequency pulser electronics consists of a near-flange pulser drive unit, a separate pulser power supply board, and cabling to connect the two. The near-flange pulse drive unit provides high-speed pulses (amplitude -370 V, pulse width 3 µs, ns-order width of the leading edge) directly to the pulse-out electrode of the TOF source. The trigger signal is provided by a pulse generator (Quantum Composer 9520) at 10 Hz and 1 µs before the trigger pulse for the laser. The pulse drive unit contains FET (field-effect transistor) drivers to produce fast pulses between two DC rails. The main load on the system results from charging and discharging the load capacitance, which must be kept to a minimum. For this reason the extract pulse driver is designed to be close-coupled to the extract electrode, using a hard wired output cable with strain relief tag.

3.4.3 Deflectors

The purpose of the deflectors is to direct ions onto the detector, notably compensating for the initial velocity of the target neutrals in a direction perpendicular to the pulsed extraction voltage. Wang et al. have described a method of background reduction for MPI reflectron mass spectrometry of supersonic jets[212] in which ions generated from the jet and those from the background gas are distinguished on the basis of flight trajectories.

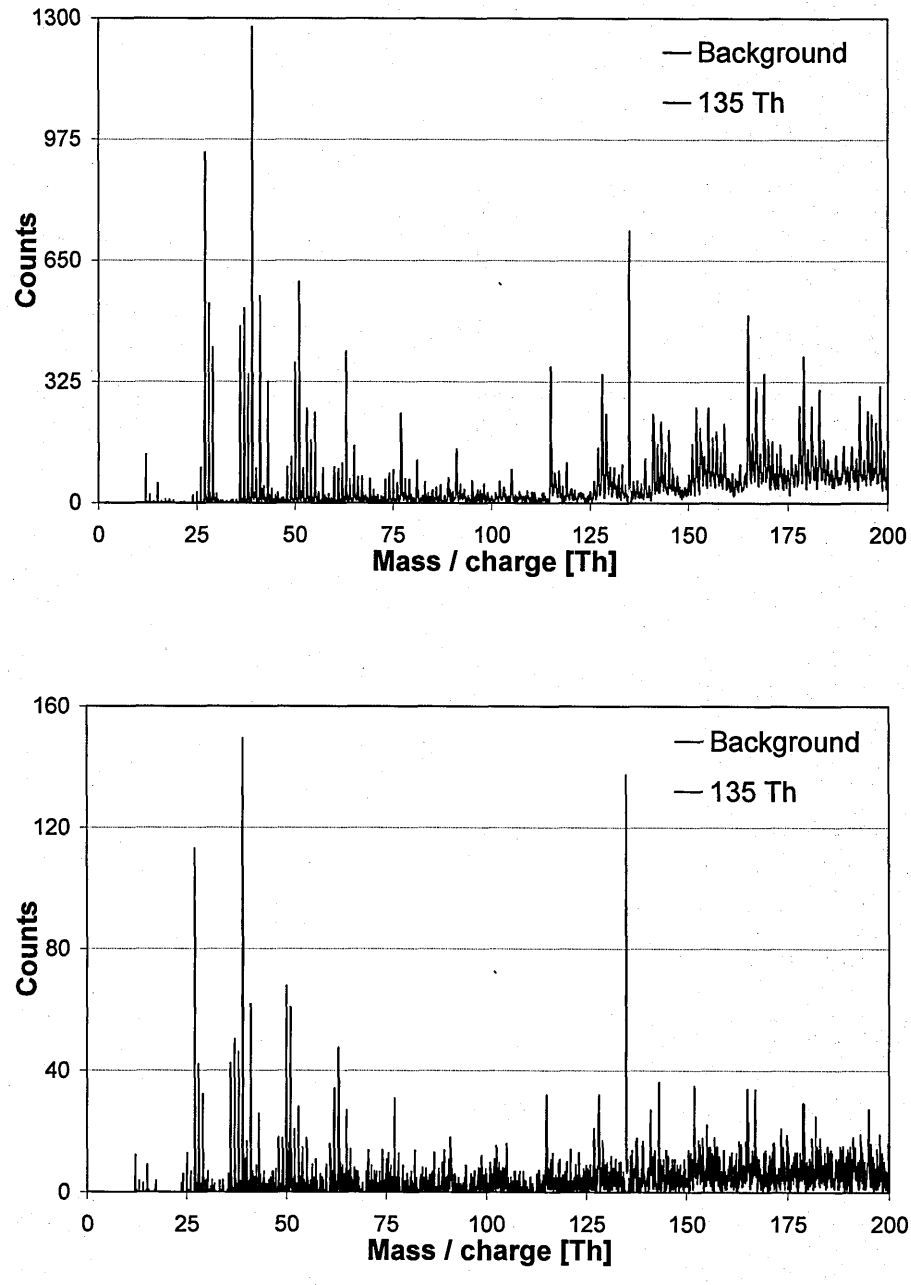

Fig. 3.16: Mass spectra of an adenine-argon supersonic beam with vertical deflector set at two vertical deflection voltages: - 2075 V (top) and - 2095 V (bottom), while the field free region was set to - 2 kV.

Jet-cooled sample molecules have much higher linear velocities in the jet expansion axis than the background molecules (with an isotropic velocity distribution)[212] and hence the deflector voltages can be set to selectively direct the sample ions onto the detector. The results of our preliminary tests using this technique (two different vertical deflection voltages) are presented in **Fig. 3.16**. Hence we were able to optimize the relative

contribution of the DNA base ion (and cluster ion) signal compared with the background ion signal (primarily from hydrocarbon molecules that diffused into the diagnostic chamber during the pump down stage).

3.4.4 The reflectron

The next stage along the ion flight path is the reflectron. The reflectron method was developed by Alikhanov[213, 214] (1957) and Mamyrin[215] (1973) to compensate for flight-time differences of ions with the same mass but different kinetic energy by stopping them in an electric deceleration field and reversing their flight direction before detecting them. Higher-energy ions penetrate deeper into the reflectron field and therefore spend more time in the reflectron field than lower-energy ions. If the retarding field of the reflectron is adjusted optimally then this effect compensates for the different flight times of the ions in the drift regions.

In the present instrument the reflectron consists of 18 rings (electrodes). 2 MΩ resistors are spot welded between the first six electrodes, and 1 MΩ resistors are welded between the next 12 electrodes, giving a total resistance, front to back, of 24MΩ. The field-free-region (FFR) voltage of - 2 kV is applied to the ion entrance electrode of the reflectron. In addition, adjustable voltages are applied to the retard electrode (the seventh, counting from FFR), and to the reflect electrode at the end of the reflectron. The ion entrance electrode and the retard electrode are gridded with woven stainless steel mesh. The electrodes are mounted on insulated rods spaced by precision ceramic spacers to form a rigid assembly. The whole assembly is mounted on a flange with 3 high voltage feedthroughs (for FFR, retard, and reflect).

3.4.5 Electron multiplier detector with conversion dynode

An electron multiplier has been used for the detection of molecular and cluster ions in the present time-of-flight experiments. The multiplier has a large active area (8 mm × 32 mm) to maximize signal intensity, 22 discrete dynodes, and an additional high-voltage conversion dynode. The complete assembly is mounted on a standard Conflat vacuum flange. A voltage of 2.175 kV is applied to the first dynode. The conversion dynode is held

at -10kV in order to accelerate ions (notably large clusters with relatively low momentum) in the last short section of their time-of-flight and thus increases their detection efficiency. A Glassman High Voltage Series FC (10 kV) unit supplies the conversion dynode voltage and a Stanford Research System Power Supply PS 325/2500 V – 25 W supplies the voltage on the first dynode. The dark noise of the electron multiplier is less than 3 counts/second

Since the signal produced by the detector is of low amplitude and an extra stage of amplification is required to boost the signal to a level that can be detected by suitable electronics, a digital pre-amplifier is mounted directly onto the detector flange. A FastComtec P7887 time-to-digital converter (TDC, see section 3.6.2) is applied for counting the output pulses from the detector. It requires negative edges with voltage levels that fall within the range +/- 1 V. The typical output pulse of the pre-amplifier has 10-15 ns width and -1 V of amplitude. A measure of protection is provided at the input of the amplifier by a very fast diode, primarily to speed up the recovery from excessively large input signals that can occur in a time-of-flight experiment, for example very strong buffer gas ion signals in certain experiments (this did not occur in the present laser ionization conditions).

3.4.6 OU voltage divider

Fig. 3.17: The Open University voltage divider coupled with the Glassman power supply.

The voltage divider (**Fig. 3.17**) was built by Open University technical support and coupled with a Glassman High Voltage Series FC Power Supply (2.5 kV output) to distribute voltages among the mass spectrometer electrodes. The variable pots of the voltage divider have resistance 500 kΩ and are connected across appropriate taps on the resistor chain.

The resistor chain consists of 50 x 15 kΩ resistors (3.333 mA), giving tapping points every 50 V from 0 V to -2500 V and each is decoupled with 1 μF in order to reduce jitter. On/off control and a switchable voltage monitor are also provided. The following values have been chosen during the process of mass spectrometer signal optimization: 0 V on the back plate of the TOF source, -1140 V on the intermediate electrode of the TOF source, -2.016 kV on the field-free region (including the field free tube, the final electrode of the TOF source, the front of the reflectron, and front of the detector), -2030 V on the Y (horizontal) deflector, -2125 V on the X (vertical) deflector, -1375 V on the retarding electrode in the reflectron, and -170 V on the reflect electrode of the reflectron.

3.4.7 Resolution and calibration

The electric fields in the mass spectrometer accelerate an ion with mass m and charge q into the field free region with a kinetic energy of qV, where q is the ion charge; and V is the difference between the FFR voltage and the voltage at the point in space where the ion is produced. As the laser beam and the molecular beam cross at a point approximately equidistant between the TOF source back plate and the pulsed extraction plate, ions are produced at an approximate voltage of -185 V (with variation due to the alignment and the laser spot size in a given measurement). The calibration equation is derived from the relationship of kinetic energy to mass and velocity:

$$\frac{1}{2}mv_i^2 = qV \Rightarrow v_i = \sqrt{\left(\frac{2qV}{m}\right)} \qquad \textbf{3-10}$$

Since the velocity of ions v_i is proportional to $\sqrt{\frac{q}{m}}$ for every voltage V applied in an idealized TOF mass spectrometer, their flight time t is proportional to $\sqrt{\frac{m}{q}}$, and calibration of the TOF mass spectrometer can be performed through experimental determination of the flight times of a pair of ions with different known masses and subsequent determination of the factors a and b in the equation below:

$$t = a\sqrt{\left(m/q\right)} + b \qquad \text{3-11}$$

The resolution R of the mass spectrometer can be calculated as:

$$R = \left(\frac{m}{\Delta m}\right) = \left(\frac{t}{2\Delta t}\right) \qquad \text{3-12}$$

where t is the total flight-time of an ion to the detector, and Δt is the temporal width of the (singly charged) ion cloud at the detector[214]. The FWHM (full width at half maximum) of an observed peak is used to determine Δt. Hence, the resolution R of a mass spectrometer configuration gives the maximum mass of a singly charged ion for which the peak is distinct from the peak for (m-1) to within the FWHM. In the present experimental conditions the maximum resolution of $\frac{m}{\Delta m}$ = 2000 has been achieved for tightly focused laser beam and $\frac{m}{\Delta m}$ = 250 for unfocused laser beam.

3.5 Laser system

3.5.1 Nd:YAG laser

The third harmonic output (355 nm) of a Nd:YAG laser system (Continuum Powerlite Precision II 8000) was used as the pump source for a dye laser (Sirah Cobra-Stretch) with a frequency doubling unit. Coumarin 450 dye gave access to the wavelength range 220-230 nm after frequency doubling. The parameters of the Continuum Powerlite Precision II 8000 laser (**Fig. 3.18**) are: 10 Hz repetition rate, 310 mJ maximum energy at 355 nm; 5-7 ns pulsewidth (FWHM), and 1 cm^{-1} linewidth (30 GHz, FWHM).

The active medium of solid-state lasers are cylindrical rods of glass or single crystals, which are doped with selected atoms, ions or molecules that can be optically pumped into excited states. The laser uses flashlamps as a pump source, which results in a pulsed laser output. In the case of an Nd:YAG laser the glass (present in an Nd-glass laser) is replaced by a crystal of yttrium-aluminium-garnet (YAG), which has a higher heat conductivity and thus enables more efficient cooling.

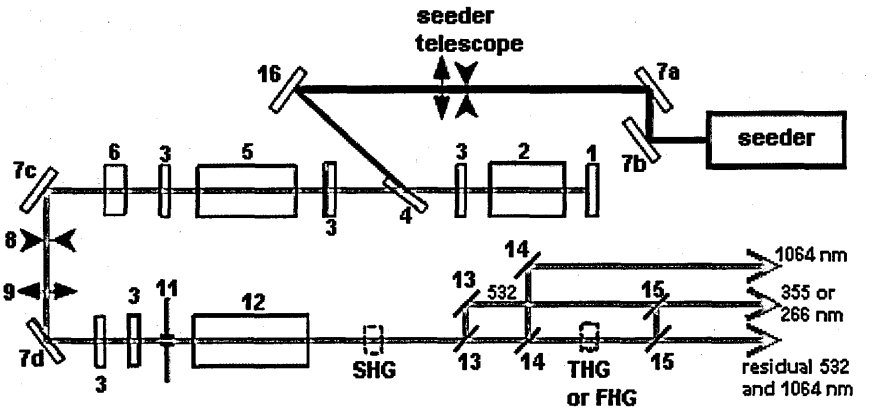

Fig. 3.18: Continuum Powerlite Precision II 8000 Nd:YAG optical layout[216].

3.5.2 Dye laser

The Nd:YAG laser presented above is used for pumping the Sirah Cobra-Stretch dye laser. The strongest Nd:YAG lasing line is at 1064 nm, which is unsuitable to pump dyes. Fortunately, its high peak power and near-diffraction-limited beam quality lend themselves to rather efficient frequency doubling, tripling and quadrupling. This provides suitable pump wavelengths of 532, 355 and 266nm[217].

Dye lasers are a class of liquid lasers, which can be operated in a pulsed mode[154]. The active media are large dye molecules dissolved in a liquid (methanol in the present system). These molecules have many vibration-rotation levels in the electronic ground state (singlet S_0) and in excited states (S_i or triplet states T_i). The strong interaction of the dye molecules with the liquid solvent results in a broadening of the transitions, which is larger than the average spacing between the different rotational-vibrational transitions. Hence, instead of many discrete lines, broad absorption and emission bands appear. The dye laser can oscillate on those transitions where the threshold is reached. From the broad emission line profile a specific wavelength can be selected by wavelength-selecting elements inside the laser resonator[154].

A grating with a groove density of 1800 l/mm is used to select wavelength in the present system with a resolution better than 10^{-3} nm. At the wavelength of the 2nd order of diffraction (called λ_{min}) the efficiency of the grating decreases significantly (Woods' anomaly – an effect whereby light that is incident on an optical grating is bent sideways 90 degrees

and transmits along the surface of the grating). In the worst case, loss in the cavity can quench lasing action. Using groove density 1800 l/mm, λ_{max} equals 1100 nm and λ_{min} equals 555 nm. Wood's anomaly not only affects the fundamental laser energy, but also the degree of polarisation of the dye laser beam, hence decreasing the non-linear conversion efficiency. The wavelength range between 575 nm and 900 nm is optimised for 1800 l/mm, however the system can also be optimised for operation between 400 nm to 500 nm.

The Sirah Frequency Conversion Unit (**Fig. 3.19**) is installed directly at the output of the Cobra Stretch dye laser. It is designed to double the frequency of a dye laser beam, by means of a non-linear HG – 220 crystal (BBO; Cut angle 57.4°, output 280 – 215 nm) followed by a compensator. The crystal's angle is tuned to maintain phase matching inside the crystal. An arrangement of 4 Pellin-Broca prisms (WS-4) separates the generated UV from the fundamental beam.

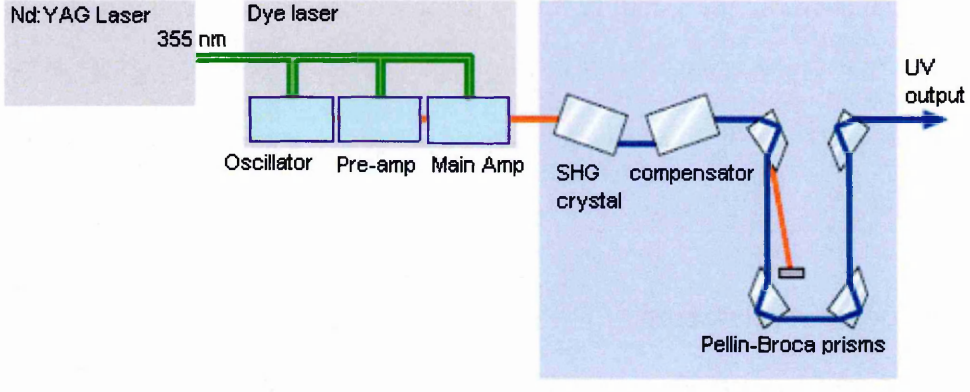

Fig. 3.19: The frequency conversion unit.

Wavelength separation is performed by the first prism: behind this prism, the fundamental beam is guided onto a ceramic dump, whereas the SHG (Second Harmonic Generation) beam passes close to the dump. The other three prisms are used to compensate the angle and the linear shift of the SHG beam, induced by each single prism. Finally, behind the fourth prism, the SHG beam is parallel to the SHG beam generated in the crystal.

The dye used in every experiment described in this thesis was Coumarin 2 (7-Amino-4-methylcoumarin) - $C_{13}H_{15}NO_2$. The dye is dissolved in methanol due to its excellent optical

transparency for UV-pumped dye lasers. Coumarin 2 is a crystalline solid slightly yellow in colour (peak: 450 nm; wavelength range: 435 – 467 nm or 217.5 – 233.5 after doubling; efficiency: 10%; concentration: 0.30 g/l; solvent: methanol[217, 218]. The photostability of the dye is reduced when pumping with UV light due to multiphoton excitation followed by dissociation or changes in molecular structure. This process is more probable during excitation with UV light than with visible light. The Coumarin 2 dye had to be changed every one or two days (depending on work load).

Without any additional optics between the laser output and the UV-grade entrance window of the diagnostic chamber, the laser spot area at the crossing point with the supersonic jet is 14 mm^2 (determined from burn paper profiles). However most measurements are carried out with a variable aperture and / or a converging lens (focal length 500 mm) positioned before the entrance window. The laser beam is typically focused to spot areas of 0.8 mm^2 or 0.04 mm^2 at the crossing point. This arrangement provides an effective means to vary the laser fluence, while the intrinsic high resolution of the mass spectrometer means that adequate resolution ($m/\Delta m \sim 250$) for many purposes can be achieved with the maximum spot area. The signal levels for low ionization efficiency measurements at low laser fluences are improved by the fact that larger spot areas sample a larger portion of the supersonic jet.

3.5.3 Pyroelectric detector

A SPJ-D-8 Pyroelectric Joulemeter (Spectrum Detector Inc.) has been installed behind the diagnostic chamber (**Fig. 3.20**) in order to record energy of each laser pulse intersecting the molecular beam. This joulemeter probe includes a pyroelectric detector element with a black absorbing coating; it is characterized by flat spectral response from 0.1 to 1000 µm, and operates for 50 nJ to 50 mJ pulses of fsec to µsec width. The joulemeter is powered through the USB port on the PC workstation. LabView software provides full instrument control and pulse energies can be recorded and saved independently on a pulse-by-pulse basis.

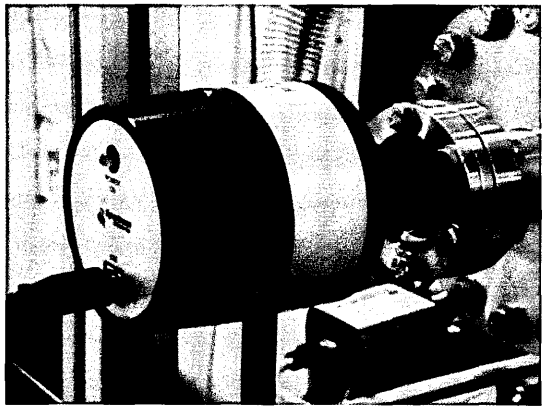

Fig. 3.20: The pyroelectric joulemeter.

3.6 Integrated experimental control and data acquisition

3.6.1 Hardware - PC workstation

The PC workstation has been configured from separate components and assembled in order to ensure the control over the experimental setup devices: pulse generator, dye laser, 3 temperature controllers, pressure transducer, TOF multiscaler (FastComtec), and pyroelectric detector. The PC workstation is housed in a Cooler Master chassis CM690 and features a 2200 MHz DualCore Intel Core 2 Duo processor. The pulse generator and the dye laser (including the FCU unit) are controlled through the RS232 interface of a 4 Port PCI Express Serial Card. A PCI Express RS-232 Multi-Port Communication Board supports 32 bytes hardware FIFO (First-in-First-out, described below). The temperature controllers (with RS232 interface) are connected to USB ports of the PC workstation using NEWlink USB to Serial cables. The multiscaler (acquisition card) occupies a PCI slot in the motherboard. Remaining free PCI and PCI-E slots can be used for further expansion of the computer control system. One of the crucial factors during configuration was to ensure efficient cooling for the time-of-flight multiscaler (FastComtec), which is a long board PCI card. In order to achieve this, additional fans (9) have been installed.

3.6.2 Multiple-event time digitizer P7887

The P7887 250 ps/ 4GHz Time-of-flight / Multiscaler has been sourced separately from the PC workstation and installed in the DG965WH motherboard PCI slot. The P7887 Multiscaler is a PCI Local Bus compliant device; it contains the configuration space register

organization as defined by the PCI Local Bus Specification. The multiscaler is installed in the PC workstation that is responsible for reading and writing to/from the PCI configuration registers to enable proper operation. In the present system, the P7887 PCI board has been applied as an ultra fast Multiscaler/TOF system for Time-of-Flight Mass-Spectrometry. The P7887 is capable of accepting one event (stop pulse) in every time bin. Burst/peak count rates of up to 4 GHz can be handled with no dead time between time bins (widths 250 ps).

The Stop-After-Sweep mode of operation has been used during TOF mass spectra acquisition. The P7887 measures the arrival time of STOP input events relative to a previous START signal. Hence, when the P7887 is armed it waits for a START input signal. The START signal triggers a sweep (hundreds of μs in the present measurements), during which the arrival times of the STOP input signals relative to the start are acquired. After a short (~200 ns) end-of-sweep dead time the P7887 is ready for a new start and begins a new sweep as soon as the next START signal arrives. The source of START signals in the experimental setup is the pulse generator (Quantum Composer) and STOP signals arrive from the electron multiplier (detector) pre-amp. The START (Trigger) and STOP (event) sockets are located on the mounting bracket. The input impedance is 50 Ω. The inputs are falling edge sensitive. The threshold level is software tuneable in a range of +/-1.0 V (-0.8 V is applied in the present configuration). The maximum resolution or minimum time bin width is 250 ps. In this work, usually 32 and 64 bin widths were applied, giving single channel width equal to 8 and 16 ns, respectively. The measured data is transferred into the PC.

A two step FIFO concept is used to get the ultra high burst count rate of up to 4 GHz while also providing a large average or sustained event rate. FIFO is an acronym for First In, First Out, an abstraction in ways of organizing and manipulating data relative to time and prioritization. This expression describes the principle of a queue processing technique or servicing conflicting demands by ordering process by first-come, first-served (FCFS) behaviour: what comes in first is handled first, what comes in next waits until the first is finished. The detected stop events are fed into a 127 words deep, 16 ns wide ultra fast multiple event First-In-First-Out memory. A sophisticated input logic allows buffer stop events to be buffered every 250 ps for at least 2.032 μs, which corresponds to a burst

count rate of 4 GHz for a whole 8k bin spectrum. In fact each of the 127 FIFO words contains a period of 16 ns regardless of the number of stop events. This data is then transferred to the second 16k words deep FIFO memory at over 12 MHz. The depth of this second FIFO assures that high speed DMA data transfer over the PCI bus is feasible without losing data by a filled up FIFO. The basic PCI protocol can transfer up to 132 Mbytes per second. The PCI specification permits a maximum clock rate of 33 MHz allowing one bus transfer to be performed every 30 nanoseconds The peak transfer rate is133 MB/s (133 megabytes per second) for 32-bit bus width (33.33 MHz × 32 bits at 8 bits/byte = 133 MB/s).

3.6.2.1 Pulse generator

The pulse generator (Quantum Composer shown in **Fig. 3.21**) is used to synchronize the experimental setup. First, it triggers the laser flashlamps (with 10 μs TTL/CMOS pulse); 299 μs later it triggers electric field of the pulse-out electrode of the ion source (1 μs TTL/CMOS) and provides the START pulse of the P7887 multiscaler (10 ns TTL/CMOS given through an attenuator); and finally 1 μs later, it triggers the laser Q-switch (10 μs TTL/CMOS), causing laser light emission. An attenuator (Mini-Circuits 15542, HAT-20+, 20 dB, 50 Ω, DC-2GHz) modifies the triggering pulse for the P7887 Multiscaler. The pulse generator has 250 ps timing resolution with <200 ps jitter; internal rate generator with 10 ns period resolution (frequency of 10 Hz is applied in experiments); complete channel and system setup stored in memory; and RS232 interface securing the connection to a PC.

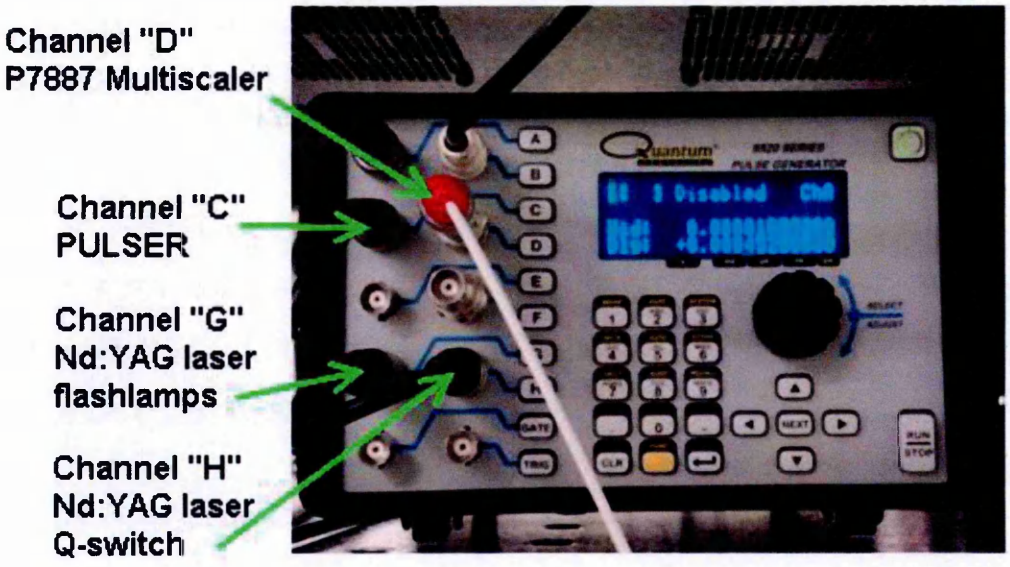

Fig. 3.21: The Quantum Composer 9520 Series Pulse Generator used to trigger Nd:YAG laser (channels "G" and "H"), the electric field on the pulse-out electrode (**Fig. 3.15**) of the mass spectrometer ion source (PULSER, channel "C") and to provide the START pulse of P7887 Multiscaler (channel "D").

3.6.3 Software

A data acquisition system was developed to record the temperatures of the heated components (the source, and the skimmer), read the pressure of the buffer gas, record the energy of every laser pulse, and to record the number of ions detected within a given range of flight times on a pulse-by-pulse basis. The interface of the system (the computer screen) is presented in the **Fig. 3.22**. The laser pulse energy and the number of ions which arrive at the detector within a given range of flight time are read by the LabView software from the computer memory simultaneously. In view of the variation in laser pulse energies (typically a standard deviation of the order ±15% during a mass spectrum acquisition), this provides an efficient and novel method for ion production within a defined *m/q* range to be analyzed as a function of pulse energy. The system can be operated in parallel with the FastComtec MCDWIN acquisition software (to record the entire mass spectrum) and is based on a LabView application interfacing with the P7887 multiscaler, the laser energy joulemeter, the temperature controllers, and the pressure transducer.

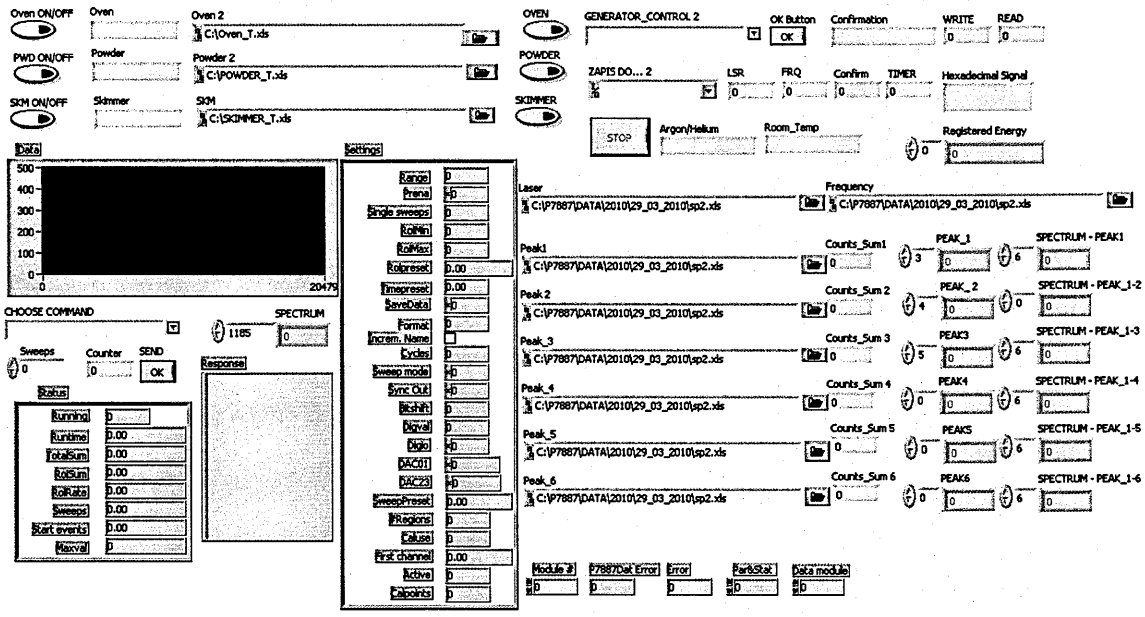

Fig. 3.22: The interface of the LabView computer control program.

The basic functions of the software components which have been developed in this work are: reading of the nozzle and the skimmer temperatures every second and saving them in an excel file, ON/OFF switch for the pulse generator and its particular channels, simultaneous recording of the laser pulse energy and number of ions produced by this pulse, and reading the pressure of argon buffer gas. The Labview structures and data access system used in the data acquisition program are summarized in the **Appendix 9.2**.

3.7 Molecular multiphoton spectroscopy with ionization detection

This section provides an overview of multiphoton ionization, the method to probe molecules and clusters in the present experiments.

3.7.1 Signal intensity in non-resonant and resonant multiphoton ionization

An atom or a molecule can be photoionized absorbing a single photon of energy equal to, or higher than the ionization energy E_J[219]. Single-photon absorption has a linear dependence on the radiation intensity. However, an atom or a molecule can be also ionized by photons with an energy $\hbar\omega$ much less than E_J, if the photon flux is strong enough. This can be achieved with laser radiation[220]. Multiphoton ionization of atoms and molecules is a

non-linear phenomenon which can occur whenever matter interacts with intense optical fields.

Non-resonant multiphoton ionization (NRMPI) from the ground state to the continuum takes place through laser-induced virtual states (**Fig. 3.23** (a)). In principle, this process does not require any intermediate electronic excited states. The lifetime of the virtual state is very short (~ 10^{-15} s) and multiphoton ionization depends on the absorption of successive photons through laser-induced virtual states occurring within that period of time. Due to their short lifetimes, virtual states do not play significant roles in the nano-second time-scale MPI pathways responsible for the ions observed in this work.

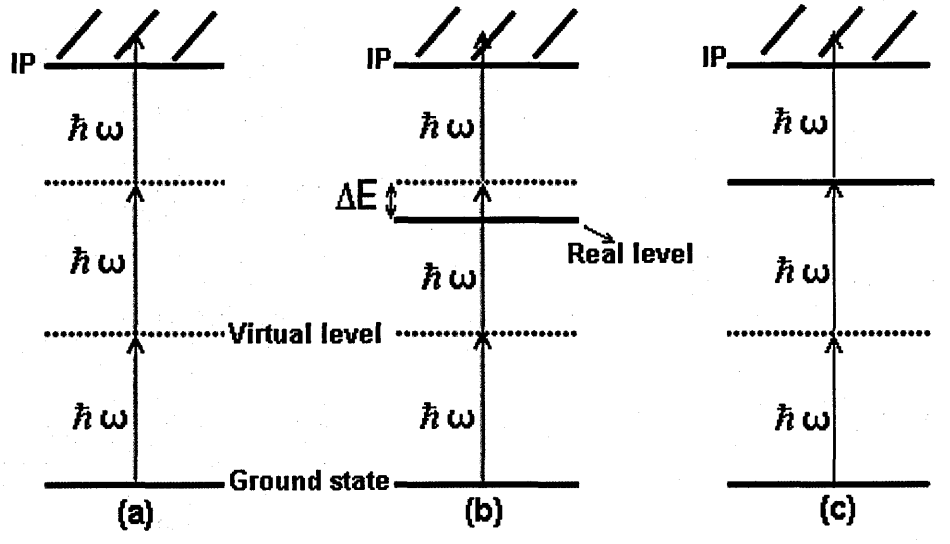

Fig. 3.23: Non-resonant (a) and resonant (b and c) three-photon ionization[219].

Non-resonant multiphoton processes are conveniently handled by time-dependent perturbation theory[221] or by employing Floquet methods[222]. In the non-resonant case, using theory developed from the evolution-operator formalism, the problem can be solved readily by considering the lowest-order non-vanishing term[221]. Hence the number of ions generated in the multiphoton ionization process N_i is given as:

$$N_i = \sigma_{k_0} I^{k_0} \qquad \textbf{3-13}$$

where σ_{k_0} is the generalized multiphoton ionization cross-section expressed in $cm^{2k_0} s^{k_0-1}$, I is the laser intensity expressed in photons/cm^2 and k_0 is the number of photons absorbed

in a non-resonant multiphoton ionization process. A log-log plot of N_i in such a process versus laser intensity I is a straight line with a slope giving the number of photons k_0 absorbed, which is equal to the effective order of non-linearity (photon order) defined as:

$$k_0 = \frac{\partial(\log N_i)}{\partial(\log I)}. \qquad \textbf{3-14}$$

In the resonant case, i.e., when the energy of one or several photons approaches that of a transition line as represented in **Fig. 3.23** (b) & (c), higher-order terms which had been neglected in the evolution-operator expansion are no longer negligible[221]. Whereas far from resonance the effective order of non-linearity is equal to the minimum number of photons required to reach the closest continuum from the initial energy level ($k = k_0$), this does not happen in the vicinity of a resonance. Indeed large variations of the effective order of non-linearity are obtained by studying the slope of the curve *log* N_i against *log* I[223]. Near a resonance, the ionisation probability depends strongly on the field frequency whereas the location of the resonance depends on the field intensity because of the AC Stark shift[224] (the shift of the molecular energy levels induced by a strong optical field). The result is that the effective order of non-linearity deviates strongly from k_0[225]. Consequently the order of non-linearity does not necessarily equal the number of photons absorbed in the resonant multiphoton process. This effect has been shown for atoms (5×10^7 – 10^9 W/cm^2)[221] and molecules (for the laser intensity of the order of a few GW/cm^2)[226]. It has been demonstrated for nitric oxide molecule that the order of non-linearity near a resonance broadened by Stark shifts can be much higher than the minimum number of photons required to ionize the molecule[226].

As it has been demonstrated above, the AC Stark effect can change the order of non-linearity (photon order) of the ionization signal near a sharp resonance. However it is expected that the spectra in which the resonance lines are already broad may be immune from the effects of AC Stark shift on the photon orders[224]. Therefore the values of photon orders measured in the present work are indeed interpreted as the numbers of photons required for ionization, since investigated molecules, i.e. adenine, thymine and uracil do not exhibit sharp resonances within the wavelength range applied (220 – 230 nm). This

methodological approach has been already applied in previous studies[227, 228] of adenine and its hydrated clusters, although it should be noted that the impact of AC Stark effect on broad resonance lines has never been systematically studied[224]. Another factor limiting the potential impact of the AC Stark effect in present experiments are low laser intensities starting at values of $10^5 - 10^6$ W/cm^2, which is at least one order of magnitude lower than in the experiments on dry and hydrated adenine mentioned above. It has been shown that at greatly reduced laser intensity (from max. 2-3 mJ focused ns laser pulse) the shape of resonance lines is not significantly disturbed due to the Stark effect[229].

Fragment molecular ions are often detected in multiphoton ionization experiments. Three basic processes for fragment ion production can be considered: (1) production of excited molecular ions $(AB^+)^*$ with sufficient internal energy for spontaneous dissociative ionization, (2) photolysis followed by photoionization of a neutral fragment, or (3) photodissociation of ions. **Fig. 3.24** illustrates possible 3-photon absorption pathways leading to fragment ion production.

Fragmentation reactions due to the absorption of photons by molecular ions become more probable with increasing laser intensity[230]. In the present experiments we observed no evidence for the production of fragment ions at the low laser fluence limit of around 10^5 W/cm^2, clear fragment ion signals at about 10^7 W/cm^2, and intense fragment ion production close to 10^8 W/cm^2.

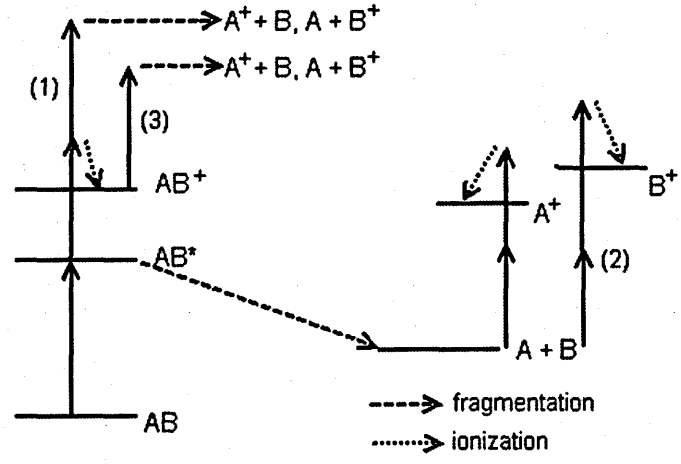

Fig. 3.24: Illustration of various possible pathways to produce fragment ions though REMPI of a prototypical molecule AB[231].

3.8 Summary

A new experimental system has been designed and built. The supersonic expansion parameters (pressure, temperature, direction), as well as the ionizing laser beam intensities have been optimized in order to produce measureable amounts of ionic molecular and cluster species in the mass spectrometer. The data acquisition system based on the PC computer and LabView software has been successfully integrated with the mass spectrometer, lasers, and the molecular beam source. The results presented in the experimental chapters (No 5-7) of the thesis will show how photon order measurements of clusters, molecules and their fragments, as well as detailed analysis of mass spectra (for example, evidence for specific fragment and cluster ions) can lead to the indirect characterization of the excited states dynamics of nucleic acid bases and related molecules. Supported by parallel theoretical investigations and ultrafast experiments, the present experimental system provides a valuable complementary tool in the research on UV chromophores.

4 Literature review: excited states and relaxation dynamics of isolated and solvated nucleic acid bases and related chromophores

This chapter reviews the existing experimental and theoretical literature describing ultrafast relaxation of UV-excited isolated adenine, thymine, uracil, and related chromophores. Recent progress in this subject provided impetus for the present ns MPI studies as well as an essential basis for our proposed interpretations. While time characteristics of excited states dynamics based on theoretical studies published elsewhere are presented in the interpretation of the nanosecond MPI ionization experiments in chapter 6, this chapter focuses on the accurate identification of these excited states. The assignment of particular excited states to the transients obtained in time-resolved experiments is a challenging task.

4.1 Adenine

The UV absorption spectrum of adenine is composed of two bands (**Fig. 4.1**). The photoactivation is followed by the relaxation processes, which are the subject of intensive studies. Over the past 10 years, a steadily growing number of theoretical studies have been carried out in order to elucidate the potential energy surfaces of adenine (e.g. see[232] and references therein). Conical intersections have been found to play important roles in the deactivation mechanisms of adenine excited states[233]. Indeed the short lifetime of the electronic excited states (due to existing conical intersections) of nucleic acid bases is understood to be the major factor of in their resistance to UV damage, although the complex DNA environment can modify the photo-dynamics[234, 235].

Following excitation into the strongly absorbing $^1\pi\pi^*$ state, the photophysics of adenine is dominated by ultrafast electronic relaxation to the electronic ground state[236]. In particular, coupling between $^1n\pi^*$ and $^1\pi\pi^*$ excited states caused by out-of-plane vibrational modes has been proposed to reduce the energy of the lower excited state towards the electronic ground state, leading to a crossing of the potential energy surfaces and efficient decay through internal conversion[237]. The observation of combination bands of the out-of-plane and in-plane vibrational modes in the dispersed fluorescence spectrum suggests that there is indeed strong vibronic coupling between the $^1n\pi^*$ and $^1\pi\pi^*$ excited states of adenine[238].

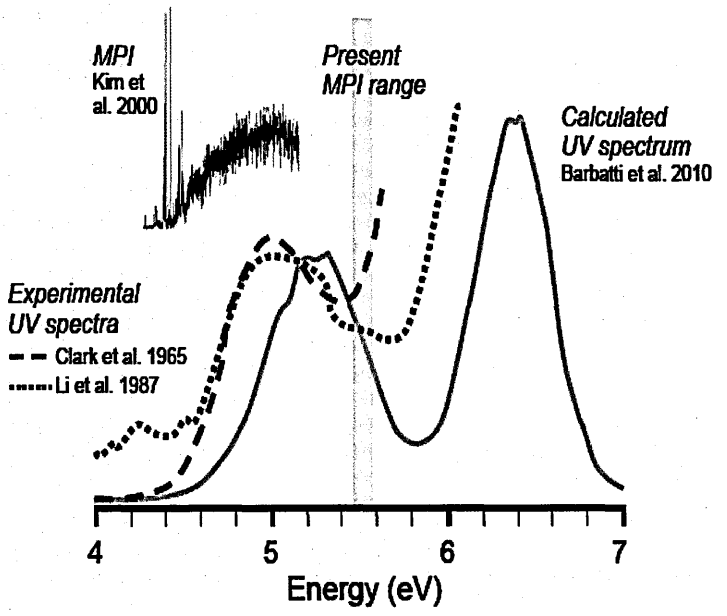

Fig. 4.1: The 1-colour MPI measurement of jet-cooled adenine that covers the widest spectral range in the literature (4.27-5.17 eV, 290-240 nm; ~4×10^{24} photons cm^{-2} s^{-1}) (Kim et al.)[239] compared with experimental and theoretical single-photon absorption spectra (Clark et al.[240], Li et al.[241], Barbatti et al.[242]). The photon energy range (5.46-5.56 eV, 227-223 nm) probed in the present experiments is shaded.

The possible role of the $^1\pi\sigma^*$ electronic excited state in the relaxation pathway of adenine has been extensively studied[236]. Complete active space self-consistent field (CASSCF) and density functional theory (DFT) methods employed for the 9-H adenine tautomer show that the potential energy function of the lowest $^1\pi\sigma^*$ state is dissociative with respect to the NH bond of the azine group[243]. The $^1\pi\sigma^*$ potential energy function intersects the $^1\pi\pi^*$ and $^1n\pi^*$ excited states, as well as the electronic ground state (S_0). It is argued[55, 243-245] that predissociation of the $^1\pi\pi^*$ and $^1n\pi^*$ states via the $^1\pi\sigma^*$ state and conical intersection of the $^1\pi\sigma^*$ state with the S_0 state provide the mechanisms for the ultrafast radiationless deactivation of the excited singlet states of adenine[243]. However the precise role of $^1\pi\sigma^*$ potential energy surface in the relaxation of photo-excited adenine is not completely resolved.

Mechanisms for the internal conversion of adenine have been investigated by femtosecond pump-probe transient ionization time-of-flight mass spectrometry[246]. Kim and co-workers'

results provide evidence that the $^1n\pi^*$ state, rather than the $^1\pi\sigma^*$ state, plays the role of a doorway state for internal conversion via a conical intersection to the ground state[246, 247]. Conversely, comparisons between the femtosecond time-resolved photoelectron spectroscopy of adenine and 9-methyladenine at 267 nm (4.64 eV) indicate that relaxation through the $^1\pi\sigma^*$ state plays a major role[248]. Time-resolved photoelectron spectroscopy experiments on adenine monomers have revealed strong $^1n\pi^*$ state signals[249]. It has been suggested that these signals are reduced in the adenine dimer and vanish in adenine-water clusters due to competing relaxation via the $^1\pi\sigma^*$ states.

Coupled-cluster calculations at three different levels of accuracy for adenine and its derivatives indicate that the ultrafast internal conversion of the optically excited $^1\pi\pi^*$ state occurs through a state switch to a biradical state (i.e. with two independent radical centres), which intersects the ground state at a lower energy[250]. A dynamics simulation shows that the $^1\pi\pi^*$ excited state of 9H-adenine decays to the electronic ground state through two different radiationless pathways[251]. Following 5.0 eV excitation, the dominant decay channel involves the out-of-plane vibration of the amino group, whereas decay following 4.8 eV excitation is strongly associated with the deformation of the pyrimidine ring in adenine at the C2 atom. The lifetime of the $^1n\pi^*$ state determined in the simulation study is 630 fs for the 5.0 eV excitation and 1120 fs for the 4.8 eV excitation[251]. Previous theoretical studies[245, 252] using CASSCF/CASPT2 methods identified the following mechanisms for radiationless deactivation of the excited singlet states of 9H-adenine: 1) out-of-plane deformation of the six-membered ring; 2) hydrogen abstraction from the amino and azine groups; 3) opening of the five-membered ring. These excited state photochemical reaction paths lead to low-lying conical intersections.

Recent theoretical investigations have attributed the experimentally-observed biexponential decay with 0.1 and 1 ps lifetimes solely to the ^1L_a ($\pi\pi^*$) state[232], i.e. the initially excited bright singlet state. In-plane vibrational relaxation plus ring puckering deformation are responsible for faster decay (0.1 ps), whereas the slower decay (1 ps) is associated with out-of plane N2-H bending. Both pathways lead to conical intersection with S_0. The same study[232] shows that N_9-H and N_{10}-H photocleavages are possible (albeit with a very low

quantum yield) at the respective excitation energies ≥5.0 eV and ≥5.5 eV. The results presented by Barbatti et al.[253] showed adenine relaxation dynamics as a two-step decay with an ultrashort S3 → S2 → S1 [$^1(\pi\pi^* L_a) \rightarrow {}^1(\pi\pi^* L_b) \rightarrow {}^1n\pi$] 22 fs first step, and the second step $^1n\pi \rightarrow S_0$ taking about 0.5 ps.

Platt's nomenclature used above enables us to distinguish between the two low-lying $^1\pi\pi^*$ states: $^1(\pi\pi^* L_a)$ describes mainly the highest occupied molecular orbital (HOMO) → lowest unoccupied molecular orbital (LUMO) one-electron promotion, whereas $^1(\pi\pi^* L_b)$ describes the asymmetric combinations of HOMO→LUMO+1 and HOMO-1→LUMO[254]. At higher energy, $^1(\pi\pi^* B_a)$ is essentially composed of the HOMO-1→LUMO+1 configuration and $^1(\pi\pi^* B_b)$ by the symmetric combination of HOMO→LUMO+1 and HOMO-1→LUMO[255]. Depending on the system and its symmetry, ^1L_b and ^1B_b states may interact strongly leading to weak and intense transitions, respectively.

Gonzalez-Luque et al.[256] have recently demonstrated that the necessary potential energy hypersurface intersections and significant values of spin orbit coupling matrix elements for ISC are also fulfilled for adenine. Indeed the population of the triplet state $^3\pi\pi^*$ through Intersystem crossing from $^1n\pi$ state has been proposed in the theoretical study[232].

4.2 Thymine

Experimental UV absorption spectra for thymine are only available in solution within neutral water[54, 242, 257]. Theoretical simulation[242] shows a two-band structure similar to the experimental spectra in water. The first band is centred at about 5.23 eV and the second and more intense band is centred at about 6.58 eV. The simulated gas phase spectrum[242] is blue shifted by 0.53 eV and 0.62 eV in comparison to the solvated experimental results[54, 257].

The photophysical relaxation of thymine starts with a fast (< 100 fs) planar relaxation from the $S_2(\pi\pi^*)$ state into the $\pi_O\pi^*$ minimum of the S_2 state (Szymczak et al.[258]). The deactivation to the S_1 state through S_2/S_1 intersections occurs in an average time of 2.6 ps at the lowest energy region of the crossing seam. After that, thymine relaxes to the minimum of the S_1 ($n\pi^*$) state, where it remains until transfer to the ground state takes

place. The dynamics simulations show that not only $\pi_O\pi^*$ S_2 trapping but also trapping in the $^1n\pi^*$ S_1 minimum contribute to the elongation of the excited-state lifetime of thymine[258]. From the $^1n\pi^*$ minimum, thymine may deactivate through the $^1n\pi^*$/cs (closed shell) conical intersection or cross the barrier with the $^1\pi\pi^*$ state to deactivate at $^1\pi\pi^*$/cs conical intersection[259].

There are different kinds of conical intersections in thymine[260]:

- ring puckered formation;
- bond elongations;
- out-of-plane distortions of the carbonyl oxygen and methyl group.

It has been shown that there exist two kinds of reaction deactivation paths, involving $^1n\pi^*/S_0$ or $^1\pi\pi^*/S_0$ crossings[260]. The shape of PES in the vicinity of the intersections indicate a much longer lifetime of $^1\pi\pi^*$ excited thymine than of other DNA bases.

Quantum chemistry and quantum molecular dynamics methods show that a true minimum on the bright S_2 electronic state of thymine is responsible for the first step that occurs on a femtosecond time scale and the observed femtosecond decay does not correspond to surface crossing[261]. It has also been suggested that subsequent barrier crossing to the minimal energy S_2/S_1 conical intersection is responsible for the picoseconds-order decay[261].

The sloped-to-peaked S_2/S_1 seam of intersection between the lowest $^1\pi\pi^*$ and $^1n\pi^*$ excited states of thymine has been explored with electronic structure and direct quantum dynamics calculations (ab initio CASSCF calculations and direct dynamics variational multiconfiguration Gaussian (DD-vMCG) quantum dynamics on the full-dimensional CASSCF surface, with 39 degrees of freedom). The authors suggested that a sloped-to-peaked topography can be used to control photochemical reactivity, by driving the wave packet to different regions of the seam where a different outcome of the propagation can be expected[262].

The picture presented above has been confirmed by a quantum mechanical study (Picconi

et al.[263]) indicating that within the region of the $^1\pi\pi^*$ surface, connecting the Franck-Condon point with the $^1\pi\pi^*$ plateau, $^1\pi\pi^*$ and $^1n\pi^*$ are almost isoenergetic and that a $^1\pi\pi^* \rightarrow {}^1n\pi^*$ population transfer occurs. The complementary quantum dynamical approaches predicted a very fast and effective $^1\pi\pi^* \rightarrow {}^1n\pi^*$ population transfer, i.e. the $^1n\pi^*$ state is significantly populated (20-40%) after 50 fs, and this population persists or even increases on a longer time scale.

A different picture of ultrafast decay in gas-phase thymine has been ascribed to the barrierless character of the pathway along the low-lying $^1\pi\pi^*$ hypersurface connecting the Franck-Condon region with the ground state via conical intersection by Merchan et al.[264]. Longer lifetime decays and low quantum yield emission are related to the presence of a $^1\pi\pi^*$ state planar minimum on the S_1 surface and the barriers to access other conical intersections[264]. According to these calculations using high-level CASPT2//CASSCF quantum chemical methods and ANO-type basis sets, close-lying excited states of $^1n\pi^*$ type are not expected to participate in the key photochemical event taking place along the main decay pathway toward ethane-like CI[264].

The mechanisms for the population of the triplet manifold in thymine have been studied at the multiconfigurational CASSCF/CASPT2 level[256]. Computational calculations at the B3LYP/DZP++ level of theory indicated that the singlet-triplet gap in gas phase thymine is 2.74 eV, while the addition of one and two water molecules to thymine causes a negligible increase in the vertical excitation energies and singlet-triplet gap[265].

4.2.1 Photophysical properties of a thymine analogue

The infrared and electronic absorption spectra and the excited-state nonradiative processes of supersonic jet-cooled 5-methyl-2-hydroxypyrimidine (5M2HP) have been investigated using two-colour resonant two-photon ionization (R2PI) and infrared-UV depletion spectroscopies (Lobsiger et al.[266]). Unlike uracil and thymine[267], which exhibit no fine structure in the UV absorption spectra, the spectrum of 5M2HP is structured with narrow vibronic bands. The S_1-S_0 electronic transition is of $^1n\pi^*$ character, with vibronic bands becoming steadily broader at increasing energy, signalling a coupling to a lower-

lying electronic state. Delayed ionization measurements show that the coupled electronic state has lifetime > 5 μs, while no fluorescence has been observed from the $^1n\pi^*$ state. The structureless region of the REMPI spectrum has been rationalized by ultrafast relaxation of the optically excited $^1n\pi^*$ state to a long-lived state, and it has been concluded that ultrafast relaxation occurs to a triplet state[266], indicating that relaxation back to S_0 would not lead to a long-lived ion signal.

4.3 Uracil

The electronic absorption spectrum of uracil vapour at 211°C exhibits a broad and structureless first band, which is assigned to the S($\pi\pi^*$) state[268]. The absorption maximum of this band is at 244 nm (5.08 eV)[240], while the second absorption band of uracil with larger intensity is centred at about 6.63 eV. Experimental and theoretical absorption spectra of uracil are presented in **Fig. 4.2**.

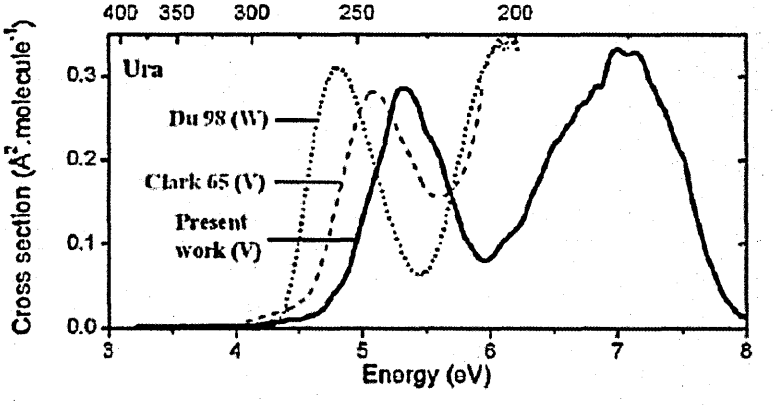

Fig. 4.2: Simulated and experimental absorption spectra for uracil[240, 242, 257]. The bottom axis gives the transition energy in eV, while the top axis gives the wavelength (nm). Clark et al.'s cross sections[240] for uracil was normalized to the theoretical result.

The uracil absorption spectrum recorded in a water solution has a similar two band structure[242]. The characteristic feature for that spectrum is the red-shift by 0.29 eV in comparison to the vapour spectrum. Theoretical calculations of uracil vertical excitation energies showed these values to be close to the maximum of the gas-phase absorption spectrum[269].

The following energies have been theoretically obtained using the complete active space CAS SCF method combined with multiconfigurational second-order perturbation theory for uracil $\pi \rightarrow \pi^*$ vertical transitions: 5.0, 5.8, 6.5, and 7.0 eV. The corresponding data for the four lowest $n \rightarrow \pi^*$ vertical transitions are: 4.5, 6.0, 6.4, and 7.0 eV (Lorentzon et al.[270]). Vertical excitation energies and oscillator strengths of uracil have been presented at the ground state minimum structure indicating theoretical absorption band maxima at 5.36 eV and 6.96 eV on the basis of semi-classical simulations at the resolution-of-identity coupled cluster to the second-order (RI-CC2) level[242]. Both in the gas phase and water, deviations between experimental and theoretical spectra have been rationalized by electronic structure methods, which tend to blue-shift the theoretical results[242].

The absorption threshold has been indicated as the next important parameter for the photostability of heteroatomic systems. In uracil the existence of barrierless reaction paths towards low-lying S_0-S_1 conical intersections is supported by a high vertical excitation energy of the lowest $^1\pi\pi^*$ state[269].

The fluorescence excitation spectra of the jet-cooled uracil revealed[268] two band systems with 0-0 transition wavenumbers of 35288 cm^{-1} (4.38 eV, system I) and 30917 cm^{-1} (3.83 eV, system II), assigned to $^1n \rightarrow \pi^*$ transitions in the diketo and keto-enol tautomer, respectively. However these results have been contested on the basis of the production of an impurity formed from uracil in the oven[267]. The REMPI spectrum of uracil (4.51 – 4.58 eV) in a supersonic jet has been found to be weak and structureless[267], rationalized by a strong mixing of electronic states or by a large geometry change between the ground state and the destination $^1\pi\pi^*$ excited electronic state[267].

Several possible mechanisms have been proposed for the nonradiative relaxation of uracil. The existence of a conical intersection between the optically active $^1\pi\pi^*$ state and the ground state has often been used to suggest that the nonradiative relaxation proceeds through a direct $^1\pi\pi^*$ - S_0 decay[269]. Another mechanism which has been proposed is a two-step relaxation, involving a $^1\pi\pi^*$ - $^1n\pi^*$ - S_0 path, which can be relevant for systems where the $^1\pi\pi^*$ state is higher in energy than the $^1n\pi^*$ state in the Franck-Condon region[271].

There are several unresolved issues concerning uracil relaxation dynamics in the gas phase[272]:

- relevance of the $^1n\pi^*/ ^1\pi\pi^*$ crossing in the excited state dynamics;
- existence of a minimum on $^1\pi\pi^*$ (and on its eventual geometry and stability with respect to $^1n\pi^*$),
- role played by the $^1\pi\pi^*$ minimum in the dynamics, and in the possible participation of an additional bright state (involving the carbonyl double bond) in the excited-state decay.

Theoretical and experimental studies showing different aspects and interpretations of uracil excited state relaxation dynamics are presented below. An ab initio study using the CASSCF, CASPT2, and CC2 methods[269] shows that the radiationless deactivation of uracil is governed by a barrierless reaction path in the $^1\pi\pi^*$ state leading to a low-lying S_0-S_1 conical intersection (CI). The reaction coordinate for out-of-plane deformation of the $^1\pi\pi^*$ state is primarily the twisting of the C=C double bond. The low-lying conical intersection between the S_0 and S_1 states for uracil has been established, which is accessible from the Franck-Condon region of the $^1\pi\pi^*$ state through out-of-plane deformations related to C=C torsions of the heterocyclic ring. The $^1n\pi^*$ state in uracil increases in energy upon C=C torsion, this leads to a state crossing in uracil. **Fig. 4.3** shows that the relaxed scan for the twisting of the C=C bond in the $^1\pi\pi^*$ state of uracil also leads, in a completely barrierless manner, to an S_0-S_1 conical intersection.

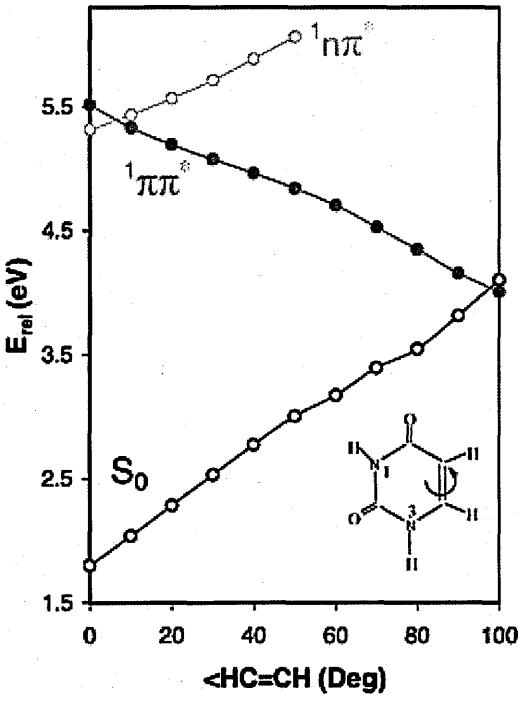

Fig. 4.3: Potential-energy profiles for C=C twist out-of-plane deformation of uracil. Geometry optimizations were carried out for the $^1\pi\pi^*$ state (filled circles). The $^1n\pi^*$ and S_0 energies (open circles) were calculated at the same geometry. The relative energies are referenced to the energy of the ground-state equilibrium geometry[269].

Nachtigallova et al.[273] presented the mechanism of uracil deactivation characterized relaxation into the S_2 minimum of $^1\pi\pi^*$ character followed by the relaxation to the S_1 minimum of $^1n\pi^*$ character which contributes to the slower relaxation with a decay constant larger than 1.5 ps. A minor fraction of trajectories decays to the ground state with a time constant of about 0.7 ps. These trajectories follow the $^1\pi\pi^*$ channel and hops to the ground state via an ethylenic conical intersection, however some contribution of the relaxation proceeding via a ring-opening conical intersection was also observed.

Direct simulation of the uracil excited-state dynamics using the ab initio multiple spawning method (AIMS) indicate that a true minimum on the bright electronic state may be responsible for the first step of excited-state uracil relaxation that occurs on a femtosecond timescale[261]. This indicates that the observed femtosecond decay does not correspond to surface crossing, hence the authors suggested that subsequent barrier crossing to the lowest energy S_2/S_1 conical intersection is responsible for the picosecond decay[261].

Earlier calculations[274] have indicated that the radiationless deactivation of uracil is governed by a barrierless reaction path in the S_2 ($^1\pi\pi^*$) state leading to a low-lying S_0-S_1 conical intersection. A dark state, S_1 ($^1n\pi^*$) involving excitation from the lone pair on oxygen to a π^* orbital, is localized below S_2. Conical intersections have been located between the S_2 and S_1 states 0.9 eV below the vertical excitation to S_2 and between S_1 and the ground state, approximately 1.8 eV below the vertical excitation energy to S_2[274]. The CASPT2//CASSCF protocol indicates that dark states do not play a key role in the nonradiative decay mechanism of uracil[264], which strongly supports uracil nonradiative decay studies using non-adiabatic ab initio molecular dynamics[275].

Three mechanisms of uracil relaxation have been characterized using nonadiabatic trajectories dynamics simulations method[259]. The characteristic feature of the first mechanism is trapping in the minimum of the second excited state ($^1\pi\pi^*$) followed by relaxation to the $^1n\pi^*$ minimum. In the second mechanism, uracil trajectories follow the $^1\pi\pi^*$ reaction pathway. The third mechanism leads to deactivation at a N_3-C_4 ring opening conical intersection[259]. Singlet-triplet transitions are relatively slow and cannot compete with sub-picosecond processes, while dynamical studies can investigate regions of phase space where the singlet state remains for a longer period of time and triplet state formation through a doorway state can occur. Triplet states are suspected to play a role in photodimerization reactions[259].

Photochemistry and photodissociation dynamics of uracil have been also investigated experimentally by two-colour photofragment Doppler spectroscopy and by two-colour slice imaging at excitation wavelengths 235-268 nm[56]. The translational energy distribution confirmed dissociation in the vibrationally hot electronic ground state. Experiments on uracil-1,3-D_2 show that there is no site selectivity in the dissociation process. No evidence was found for the direct dissociation via a $\sigma\pi^*$ excited state, whereas some studies have reported an equivalent pathway to be relevant in the photochemistry of adenine[56].

4.3.1 Photophysical properties of uracil analogues

Interesting features of uracil excited state relaxation pathway can be characterized on the basis of comparison with aza-analogues of uracil, for example 6-Azauracil shown below.

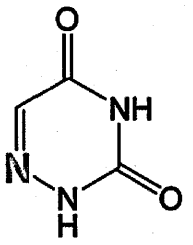

6-Azauracil
(6AU)

Fig. 4.4: Molecular structure of the aza-analogue of uracil[276].

The dominant relaxation process in uracil is ultrafast internal conversion. The excited state dynamics of 6-azauracil (6AU), which has an N atom inserted into the C6 (**Fig. 4.**) space of uracil is different, and ISC is the dominant relaxation process[277]. It has been suggested that the dark $^1n\pi^*$ state below the first allowed $^1\pi\pi^*$ state plays an important role in the ISC process of aza-analogues of nucleic acid bases[276].

A strong effect of fluorination on the excited state lifetime has been observed in uracil[278]: stabilization of the $^1\pi\pi^*$ state explains the dramatically longer excited state lifetime of 5-fluorouracil relative to uracil[278]. The authors proposed the relaxation model in which internal conversion of uracil occurs through a barrierless state switch from the initially excited $^1\pi\pi^*$ state to the out-of-plane deformed excited state of biradical character, which intersects the ground state at a lower energy. An energy barrier before conical intersection with the biradical state is introduced by replacing the C5 hydrogen atom by a fluorine atom. It has been indicated that the replacement of the C5 hydrogen by fluorine plays important role in 5-fluorouracil relaxation dynamics[279, 280]. Differences in excited state dynamics are expected to influence the results of the present nanosecond MPI experiments.

A combined experimental and theoretical study on the excited state behaviour of the uracil analogues, 5-OH-Ura and 5-NH_2-Ura was reported by Nachtigallova et al.[281]. Two-photon ionization and IR/UV double-resonant spectra show that there is only one tautomer present

for each with an excited state lifetime of 1.8 ns for 5-hydroxyuracil (5-OH-Ura) and 12.0 ns for 5-aminouracil (5-NH_2-Ura). The authors used relatively long pump wavelengths: 290.3 nm for 5-OH-Ura and 312 nm for 5-NH_2-Ura (where the probe laser was 266 nm) limiting the number of energetically accessible conical intersections to one. The path towards this conical intersection is barrierless in the case of natural bases, while for amino- and hydroxyl-substituted species there is a sizeable barrier. The barrier height determines the energy above which the conical intersection becomes accessible: at wavelengths that excite the molecule below the barrier the excited state can be long-lived whereas at photon energies above the barrier the excited state can become very short lived. These experimental findings have been supported by multireference ab initio methods. Calculations of vertical excitation energies, excited state minima, minima on the crossing seam and reaction paths indicated sizeable barriers on these paths which provide an explanation for the lifetimes of several nanosecond observed in the experiment[281]. The energy ordering of the states in the Franck-Condon region of 5-NH2-Ura and 5-OH-Ura is reversed compared to the natural bases uracil and thymine, and this inversion plays an important role in the dynamics of the uracil analogues. The experimentally measured excitation energies at the band origin are 3.96 (~313.1 nm) and 4.27 eV (~290.4 nm) for 5-NH2-Ura and 5-OH-Ura, respectively.

4.4 Solvent effects on uracil, thymine and related chromophores

As it has been mentioned in the section **2.5.3** polar solvents (for example water) stabilize ππ* states and destabilize nπ* states with respect to the situation in non-polar solvents[155, 168]. The theoretical studies of this effect for DNA/RNA bases are reported in the literature presented below.

Vertical excitation energies in uracil in the gas phase and in water solution were investigated by the equation-of-motion coupled cluster and multireference configuration interaction methods[282]. The authors' best estimations for the vertical excitation energies for the lowest singlet ^{1}nπ* and ^{1}ππ* are 5.0±0.1 eV and 5.3±0.1 eV, respectively. The solvent effects for these states are estimated to be +0.5 eV and ±0.1 eV, respectively.

On the basis of the experiment[283], it has been suggested that the $^1\pi\pi^*$ population created by UV excitation of pyrimidine bases (uracil, thymine, and cytosine) in room temperature aqueous solution decays via two very different nonradiative decay channels: ultrafast IC to S_0 and decay to a dark state[283]. The latter state, which has a ~100-fold-longer lifetime than the $^1\pi\pi^*$ state, has been assigned to the $^1n\pi^*$ state and proposed to be a gateway state to the triplet state. The calculations predict that in aqueous solution the lowest energy transition corresponds to the $^1\pi\pi^*$ transition, contrary to what was found in the gas phase[284].

The effects of hydrogen bonding with a protic solvent on uracil have been considered in the presence of two, four or six water molecules[178]. The calculations confirm that the first absorption band arises from the $^1\pi\pi^*$ excitation. The attachment of water molecules produces a significant blue shift of $^1n\pi^*$ excitations while leaving $^1\pi\pi^*$ excitations nearly uninfluenced.

Theoretical studies on adenine photophysics in aqueous solution with the sequential Monte Carlo/CASPT2 approach have been performed by Ludwig et al.[285]. It has been found that conical intersections connecting the $^1\pi\pi^*$ and $^1n\pi^*$ states with the ground state are present in solution, however the authors suggested that the large destabilization of the $^1n\pi^*$ state in aqueous solution prevents its involvement in the relaxation process. In the gas phase the lowest lying electronic states follow the order: $^1n\pi^*$, $^1(\pi\pi^*\ L_b)$, and $^1(\pi\pi^*\ L_a)$, however in aqueous solution the situation changes. The lowest-lying $^1n\pi^*$ state is blue-shifted by 0.58 eV, while the $^1\pi\pi^*$ states are red shifted by 0.17 and 0.34 eV, for the L_b and L_a states, respectively. Therefore the new order is obtained: $^1(\pi\pi^*\ L_b)$, $^1(\pi\pi^*\ L_a)$, and $^1n\pi^*$. These studies indicated also, that the barriers along the relaxation pathways are significantly smaller in solvated conditions.

Further studies have been carried out in acetonitrile (polar aprotic solvent). The excited state properties of uracil, thymine and four uracil analogue compounds have been studied in acetonitrile by steady-state and time-resolved spectroscopy[286]. The excited state lifetimes of uracil and its 1- and 3-methyl substituted derivatives in acetonitrile are well described by one ultrafast (≤ 100 fs) component. The fluorescence decays are faster in

acetonitrile than in aqueous solution showing that the excited state deactivation mechanism, which involves out-of-plane motion of the 5-substituent, is sensitive to the solvent[286].

4.4.1 Solvent effects on ionization energies

It is also worth considering changes in ionization potentials of natural and rare nucleic acid base tautomers. Close et al.[287] calculated the influence of microhydration on the ionization energy thresholds of uracil and thymine. In the case of uracil, one added water decreases the IET (ionization energy threshold) of about 0.15 eV, the second and third water molecules cause a further decrease by about 0.07 eV each. For thymine, the first water molecule decrease the IET by about 0.1 eV, while the second and third water molecules cause a further decrease of less than 0.1 eV each. Further calculations by Close et al.[288] indicate that the IETs of thymine keto-enol tautomers are lower than the IET of the diketo tautomer. The addition of water molecules to enol-keto tautomers also lowers IET. In the separate theoretical study, Close et al.[34] indicated that the IET of 9-H adenine is barely influenced by hydration with 1-3 water molecules, while the experimental data of Belau et al.[33] indicate the following values of IE for adenine (A) and adenine-water clusters (AW): A (8.30 ± 0.05), AW (8.20 ± 0.05), and AW_2 (8.1 ± 0.1); T (8.90 ± 0.05); and thymine - TW (8.75 ± 0.05), TW_2 (8.6 ± 0.1), TW_3 (8.6 ± 0.1) in single photon ionization experiments. Kim et al. noted slightly different values in electron impact ionization: A (8.45); AW (7.95) AW2 (7.8) AW3 (7.7). T(9.15); TW (8.85) TW2 (8.65) TW3 (8.5).

All studies mentioned above indicate that hydration does not change or lowers the values of ionization energies for hydrated clusters in relation to non-hydrated monomers.

4.5 Chemical relaxation pathways

Electronic excitation of DNA/RNA bases may result in the formation of photoproducts (photodimers, photohydrates). Literature review of processes leading to photochemically changed nucleic acid bases is presented in this section.

It has been suggested that the photodimer (**Fig. 4.5**) formation arises from the reaction of

one molecule in a triplet state with a second in its ground state[289, 290], on the basis of combined femtosecond broadband time-resolved fluorescence spectroscopy and transient absorption spectroscopy experiments in which a triplet state has been identified as a major precursor for cyclobutane pyrimidine dimer (CPD) damage[188].

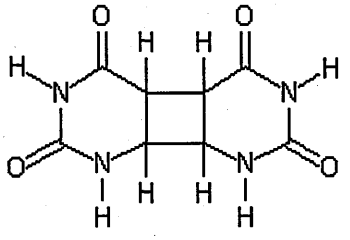

Fig. 4.5: Uracil cyclobutane photodimer.

However the kinetics of CPD formation is still under debate. In principle the CPD lesion in DNA can be formed via excited singlet or triplet states[291]; femtosecond IR experiments are consistent with CPD formation in DNA via a singlet channel and rule out a significant contribution of a triplet pathway[292].

Multiphoton ionization of thymine and uracil clusters (Kim et al.[189, 190]) revealed a remarkable alternation of mass spectral intensities between even- and odd-numbered clusters in one-colour R2PI spectra using a 6 ns laser pulse at 274 nm at a fluence of 1.6×10^{6} W/cm^{2}.

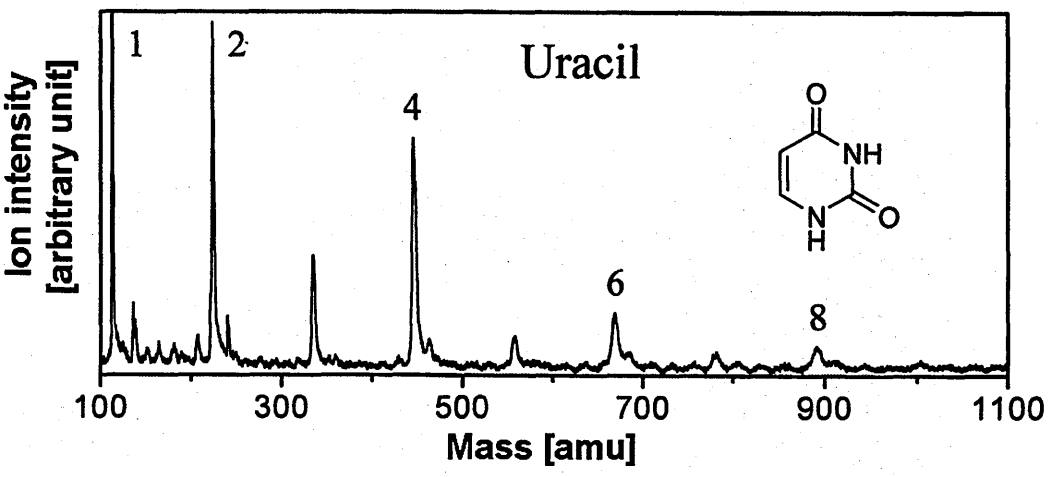

Fig. 4.6: Cluster ion mass spectra of uracil showing alternation of mass spectral intensity in MPI experiment with a nanosecond laser pulse[189]. The numbers (1, 2, 4, 6, 8) above peaks indicate a number of uracil molecules in detected cluster ions.

It should be noted from the bulk studies that the photodimerization yield is much higher in an ordered medium such as frozen solution or bacteria than in a disordered, labile environment such as aqueous solution[293]. A quantum yield as high as ~100% has been reported in frozen solution, in contrast to a typical value of a few percent in a more labile medium[294]. In addition the photodimerization rate in frozen solution was estimated to be faster than the singlet excimer fluorescence lifetime[295]. It has been suggested that certain crystal structures of thymine in ice favour photodimerization and the jet-cooled clusters in the present study may provide an efficient medium for photodimerization[189].

Clusters of thymine were found to undergo facile and extensive photodimeriztion upon strong UV irradiation[189]. Multiphoton excitation/ionization yields cluster ions with excess energy, which undergo thermal fragmentation during flight in a TOF mass spectrometer. A cluster ion that consists of an even number of molecules tends to lose two molecules, while one that consists of an odd number of molecules tends to lose one molecule. The two-molecule loss was found to be a single fission process of a dimeric unit, which was in accord with a model of the cluster ion that consists of mostly dimeric units[190].

The major product obtained by irradiation of uracil in ice is a cyclobutane dimer[296]. Ultraviolet irradiation of ^{14}C-uracil in aqueous solution results in the formation of hydrate

and dimer photoproducts. The rate of dimerization increases with increasing uracil concentration. Uracil-uracil dimerization occurs by a reaction involving the triplet state of uracil, but uracil-water complexing occurs from the excited singlet state[297]. The quantum yield for intersystem crossing (ISC) to the triplet depends on the irradiation wavelength, increasing from 0.0014 at 280 nm to 0.016 at 230 nm. The increase in ISC with photon energy suggests that ISC is favoured from excited vibrational levels[297].

Fragmentation of the uracil cyclobutane dimer leads to sizeable amounts of protonated uracil monomers[298]. In laser desorption Fourier transform mass spectrometry experiments on pyrimidine cyclobutane dimers, deprotonated negative ions of the 5,6-uracil dimer and the deprotonated uracil monomer (m/z=111 Th) have been generated[299]. Even-odd alternation of uracil clusters has been recorded in the mass spectrum presented in **Fig. 4.6**[189] and rationalized as an intracluster photodimerization, i.e. the creation of uracil cyclobutane photodimers (**Fig. 4.5**) within a cluster. However, mass spectrometry cannot provide direct evidence for the formation of photodimers and photohydrates.

UV induced photohydration reactions are also possible. It has been proposed that pyrimidine photohydrates are formed from both the ground state and first singlet excited states[300]. If photohydration of pyrimidine bases occurs mainly from a vibrationally excited S_0 then the uracil photohydrate should be formed much more readily than the cytosine photohydrate[300]. Competing photoreactions, such as hydration, dimerization or adduct formation, diminish the selectivity of the photoionization[301], since all photoproducts (photohydrates, dimers, (6-4) photoproducts) have low absorbance at 260 nm[301].

The mechanism of photohydrate formation of pyrimidines and the influence of substitution by methyl groups in uracil on hydrate formation have been discussed by Gorner[192]: all attempts to generate photohydrates via the triplet state of pyrimidines have failed and a direct singlet route is generally accepted[192]. The chromophore lost during continuous 254 nm irradiation is essentially ascribed to photohydration when the recovery (by heating) of an aerated pyrimidine solution is complete after UV irradiation[192]. It has been reported that the rate of photohydration of uracil is a function of the pH in the range 1.5 to 8. This can be understood in terms of a mechanism which includes protonation of singlet excited uracil

molecules and in which the main product-forming reaction is between an excited $^1(UH)^*$ and a neutral water molecule[302]. Other possible pathways of uracil photohydration mechanism have been also analyzed in[192].

The photohydration reaction of 6-azauracil has been investigated and the involvement of the triplet state has been reported[303]. It has been concluded that the photochemically active state of 6-azauracil leading to hydration differs from that of uracil where the hydrate forming reaction occurs via the excited singlet state[303].

UV-radiation induced formation of purine (adenine and guanine) photohydrates like 4,6-Diamino-5-formamidopyrimidine (FapyAde) and hydration of pyrimidines with the hydroxyl group located at C(5) in DNA had been reported by Doetsch et al.[304]. It has been concluded that the formation of FapyAde by UV radiation does not involve participation of hydroxyl radicals[304]. Although these results have been contested[305, 306], such monomeric base damage products could be biologically important components of the photoproducts that are responsible for the deleterious effects of UV radiation. There are two stages where such a photochemical reaction within hydrated adenine clusters could potentially occur: 1) in the electronically excited state; 2) in the vibrationally hot electronic ground state. The imidazole ring opening structures in adenine are shown in **Fig. 4.7**.

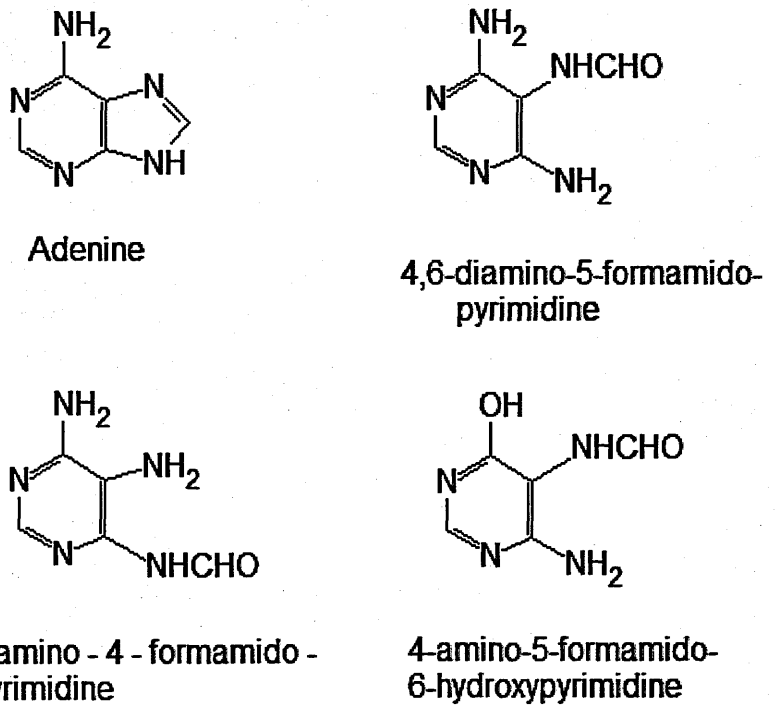

Fig. 4.7: Adenine and some products of imidazole ring cleavage[307].

4.6 Summary

Due to their biological importance, relaxation mechanisms in DNA bases after initial single photon absorption have been studied extensively by means of theoretical and experimental methods. The results of these studies showed that nucleobases have efficient deactivation processes that enable dissipation of the absorbed energy before photochemical reactions occur[308]. Detailed mechanisms characterized in single photon studies can help to interpret data obtained in the present project, which is focused on challenging multi-photon phenomena induced by laser radiation in isolated molecules and their hydrated complexes. The particular complexity of the current research problem, and indeed our interest, relates to intermolecular interactions modifying the photophysical properties of molecules embedded in clusters, as well as the complicated dynamics induced by sequential absorption of UV photons. The aim of the present experiments using the new system is to contribute towards solving these issues. The results of this work are presented in chapters 5, 6 and 7.

5 Adenine, thymine and uracil molecular ions detected in MPI experiments under dry conditions

5.1 Introduction

The results presented in this chapter focus on multi-photon processes leading to the non-dissociative multi-photon ionization of isolated biomolecules. One-colour multiphoton ionization experiments have been carried out on the DNA/RNA bases: adenine, thymine, and uracil. In each case, molecular ions with masses equivalent to the neutral molecules have been detected. The multiphoton ionization mechanisms leading to the creation of these molecular ions are discussed, notably with respect to the character of intermediate excited states lifetimes. Molecular ion production is presented as a function of laser fluence, and the applicability of power dependence for determining the total number of photons required to access ionic states is discussed.

Laser wavelengths in the range 223-227 nm (5.56-5.46 eV) and approximate fluence 1.5 x 10^5 - 2 x 10^8 W/cm^2 [of the order 10^{23} - 10^{26} photons cm^{-2} s^{-1}] have been applied in these experiments. Assuming photoabsorption cross sections for nucleic acid bases monomers ~10^{-17} cm^2[242] and an approximately square temporal distribution of laser pulses, this fluence range corresponds to average times between subsequent photon absorption ranging from hundreds of picoseconds to hundreds of nanoseconds.

5.2 Adenine

5.2.1 Literature review

Relatively long-lived intermediate excited states (timescales of hundreds of ps or ns) are necessary for effective multi-photon ionization using nanosecond lasers. However, experimental femtosecond time-resolved studies of adenine have shown ultrafast relaxation of electronic excited states[309]. Excitation with 200 and 238 nm photons (6.20 and 5.21 eV) indicate two components of relaxation to the ground state with lifetimes ~800-831 fs and <100 fs[309]. The longer-lived channel has been assigned to the $S_2(\pi\pi^*)\rightarrow S_1(n\pi^*)\rightarrow S_0$ pathway; the faster channel to $S_2(\pi\pi^*)\rightarrow S_3(\pi\sigma^*)\rightarrow S_0$. The contribution of the latter channel increases with photon energy (from ~10 % at 5.21 eV to ~100 % at 6.20 eV)[309]. Similar

time-resolved photoelectron spectroscopy (TRPES) measurements have shown that the initially excited $S_2(\pi\pi^*)$ state decays quickly (excited state lifetime, τ_1=71 ± 16 fs) to populate the intermediate state interpreted as $S_1(n\pi^*)$, followed by a slower decay to the S_0 state (τ_2=950 ± 50 fs)[310]. Semiclassical dynamics simulations[251] have determined the lifetime of the $^1n\pi^*$ state to be 630 and 1120 fs for excitation at 5.0 and 4.8 eV, respectively. Time-resolved experiments with femtosecond lasers have shown excited state lifetimes of isolated adenine to be ~1ps for a pump wavelength of 267 nm (4.65 eV)[21, 237] and a probe wavelength of 800 nm (1.55 eV). A lifetime of 9 ps has been observed for excitation at 277 nm (4.48 eV)[139], bringing the molecule to the minimum of the $^1\pi\pi^*$ state. Considering the relative inaccessibility of conical intersections to $^1n\pi^*$ or $^1\pi\sigma^*$ states[236] in this case, relaxation is suggested to proceed through intersystem crossing to a triplet state[248]. This interpretation is consistent with the increased lifetime and with an asymptotic offset observed in the experimental data[248]. Ullrich et al. observed a relaxation component in the time-resolved photoelectron spectrum of adenine with a lifetime of several ns following 267 nm (4.64 eV) excitation[311, 312]. This component has been characterized as a minor signal with decreasing yields at higher excitation energies, and has been tentatively assigned to a $^3\pi\pi^*$ triplet state populated via the $S_1(n\pi^*)$ state.

All the above results have been achieved using femtosecond laser systems. An earlier experiment applying nanosecond excimer laser pulses to determine the lifetime of a long-lived excited state of nucleobases[313] at 193 nm (6.42 eV) showed a different picture. The authors reported excited state lifetimes ≥5 μs for nucleobases and suggested that coupling with an unspecified triplet state may play a significant role in these slow relaxation pathways. It is worth mentioning that isomeric transitions can take place in MPI experiments, as been suggested in supersonic beam experiments (pump-probe delayed ionization) on phenylacetylene (PA)[314]. A characteristic feature of the experiments revealing long-living components of adenine excited states is the relatively high energy of ionizing photons: 200 nm (6.20 eV)[311] and 193 nm (6.42 eV)[313]. This may significantly increase the likelihood of ionization from a low-lying triplet state[315], compared with the previous measurements that showed no long-lived relaxation components, for example (1+3) ionization measurements using 267 nm (4.64) pump and 800 nm (1.55 eV) probe fs

pulses[21, 237]. A similar phenomenon has been reported for highly chlorinated dioxins / dibenzofurans: single-colour MPI via triplet states using 4 ps laser pulses was more efficient at 213 nm than at 266 nm[315].

Many examples can be given where short-lived excited states have a negative influence on detection efficiency in MPI experiments using nanosecond lasers. In particular, UV-UV hole burning experiments on caffeine revealed spectral bands of vibronic states that undergo ultrafast relaxation[316], preventing effective detection using nanosecond REMPI methods. Various other species defy analysis or are detected with very low efficiency by conventional nanosecond MPI[317] including certain metalorganics[318], halogenated benzenes and phenols[319], nitroaromatics[320], bioorganic compounds[321] and products of the thermal decomposition of polystyrene[322]. Furthermore, in the case of complexes the absence of specific guanine-cytosine base pair conformers in ns REMPI spectra has been attributed to sub-picosecond excited state lifetimes[20, 323, 324].

Three previous UV MPI studies are particularly closely related to the present experiments. Mass spectra and ionization efficiencies of thermally evaporated adenine in a supersonic molecular beam have been measured with 15 ns and 500 fs focused laser pulses at equal wavelength (248 nm, 5.00 eV) and pulse energy 0.02-1 mJ[325]. 135 Th ions have been clearly observed in both spectra, however the signal increased 10-fold when the femtosecond laser was used[325]. Hahn et al. observed 135 Th ions by 266 nm multiphoton ionization of adenine molecules desorbed from a surface using 10.6 µm CO_2 laser pulses 70-90 µs before ionizing Nd:YAG laser pulses[326]. Tembreull and Lubman[327] entrained laser-desobed adenine in a supersonic jet expansion prior to MPI-TOF measurements using 222 nm laser pulses with fluence ~10^6 W/cm^2. 135 Th ions were detected as well as 28 Th ions (attributed to the molecular fragment ion $HCNH^+$ of adenine). All of these experiments have been interpreted as 1+1 resonant ionization processes of adenine. Similarly, one-colour nanosecond MPI spectra of nitrogen-containing aliphatic and aromatic compounds (pyridine, pyrazine, indole, quinoline, carbazole) recorded over a wide wavelength range 220-340 nm (5.64-3.54 eV) have been attributed to 1+1 resonance

ionization processes[328]. These interpretations were purely based on comparing photon energies with the ionization energies of these molecules.

5.2.2 Adenine MPI - experimental data

Whereas ns-timescale MPI of adenine may be expected to be inefficient due to the short electronic excited state lifetimes[20, 316-324], **Fig. 5.1** shows a clear signal for the molecular ion 135 Th (1 Th is one atomic mass unit (AMU) over one unit of elementary charge). This is consistent with previous ns MPI studies[325-327].

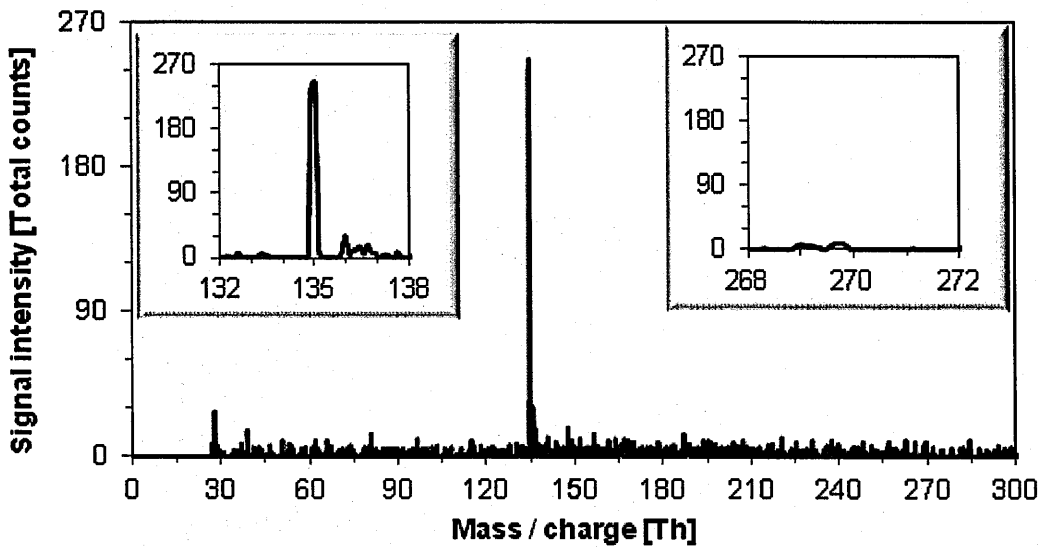

Fig. 5.1: One-color (226 nm, ~ 2.2×10^7 W/cm^2, 2117 laser shots) MPI mass spectrum of dry adenine (208°C, 0.5 bar argon).

It is important to consider the possible presence of adenine clusters in the irradiated supersonic jet, even in the case where no cluster ions are directly detected. The **Fig. 5.1** mass spectrum was recorded with the powder temperature of 208°C and an argon driving pressure of 0.5 bar. Even at the highest argon pressure possible (~2 bar) with the present nozzle and pumping system, no A_2^+ (270 Th) ions were detected at adenine temperatures below 240°C. However the absence of any detected adenine cluster ions does not discount the possible presence of clusters in the neutral beam[228].

The insert in **Fig. 5.1** shows the 136 and 135 Th peaks in detail. A weak tail feature can be noticed at 136 Th. **Fig. 5.2** shows a mass spectrum with better statistics (46217 laser

shots) with a similar tail toward higher masses at 136 Th. This feature indicates cluster fragmentation in the initial ~ 255 ns flight time in the extraction zone of the mass spectrometer, i.e. between the backplate and pulse-out electrodes of the ion source (see **Fig. 3.15**). Indeed, a theoretically derived TOF difference for A^+ and A_2^+ ions in that part of the MS is ~ 300 ns.

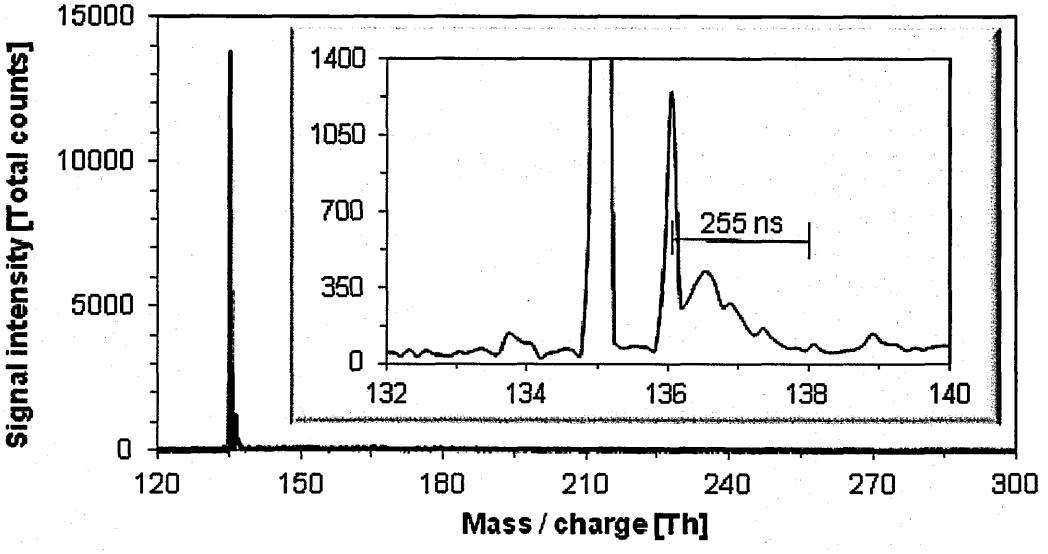

Fig. 5.2: Long tail of 136 Th peak in one-color (226 nm, approximate fluence range: 5.4×10^5 - 8.2×10^7 W/cm^2, 46217 laser shots) MPI mass spectrum of dry adenine (224°C, 0.5 bar).

The ratio of the integrated peak intensities AH^+/A^+ is equal to 21.6±0.4 % and exceeds the value of 8 % expected due to adenine isotopomers calculated according to Hu et al.[329]. Hence **Fig. 5.2** provides evidence for production of protonated adenine ions associated with proton or hydrogen transfer in clusters. Kim et al.'s[17] 266 nm ns MPI data showed a major increase in the 136 / 135 Th ratio due to the formation of pure adenine clusters.

The adenine signal at 135 Th has been registered for various wavelengths in the range 220 – 230 nm (i.e. 220, 221, 222, 223, 223.8, 224, 225, 226, 227, 229, 230 nm). For each of these measurements a clear signal attributed to A^+ has been identified. Although detailed studies on the wavelength dependence have not been carried out, a structureless adenine REMPI spectrum in the present wavelength range is expected. Kim et al.[239] reported the MPI spectrum of adenine monomers in the range 290-240 nm: a progression of sharp vibronic lines between 282 and 273 nm is followed by an unstructured absorption band

extending to shorter wavelengths. The diffuse shape of the band indicates rapid excited state relaxation, while its absence in the LIF spectrum shows that non-radiative decay dominates.

135 Th ion intensity was analyzed as a function of laser pulse energy; three mass spectra recorded for different average laser pulse energies are shown in **Fig. 5.3**. According to the perturbation theory expression for non-resonant multiphoton ionization (details are presented in section **3.7**), the number of photons absorbed (photon order, α) can be determined as the slope of the curve log C (count rate) versus log I (laser pulse energy), in the low fluence limit (i.e. where saturation is negligible with respect to pumping the molecules in the laser field to electronic excited states or ionic states). This expression is applied in this thesis for the determination of the total number of photons absorbed (α) in resonant MPI[227, 228], although caution is required in these interpretations notably in view of potential AC Stark effects discussed by Otis et al.[226] (see section **3.7.1**). Also the assumption needs to be fulfilled that the effective crossing volume of laser and molecular beams remains unchanged throughout the measurement.

In order to minimize the possibility of saturation, the measurements shown in **Fig. 5.3** were recorded close to the minimum fluence at which we could observe a practical signal for analysis. This was achieved by using maximum spot area (no lens, ~14 mm^2) and laser pulse energy of 200 - 300 μJ, providing an approximate fluence of 2.0 - 3.0 $\times 10^5$ W/cm^2. The data were recorded with low driving pressure (0.4 bar argon), however clustering in the neutral beam cannot be ruled out. Cluster mediated MPI of adenine is discussed in section **6.8**.

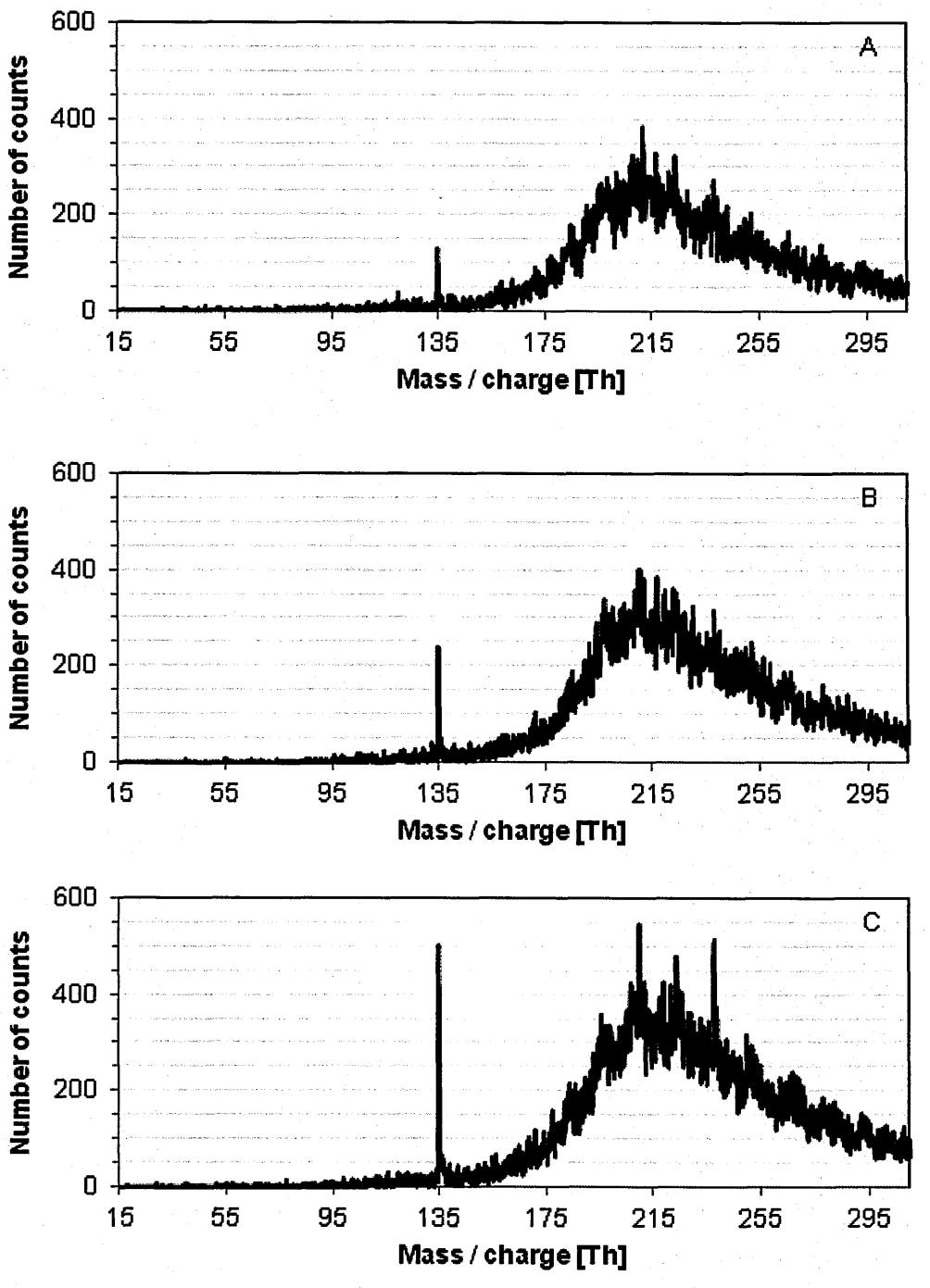

Fig. 5.3: One-color (223.8 nm) MPI mass spectra of dry adenine (235°C, 0.4 bar argon) recorded with no lens and at three different average pulse energies: (A) 195.2 ± 49.3 µJ, (B) 244.0 ± 22.1 µJ, and (C) and 297.1 ± 25.0 µJ; corresponding to approximate fluences: (A) 2×10^5 W/cm^2, (B) 2.5×10^5 W/cm^2, (C) 3×10^5 W/cm^2.

Beside the 135 Th peak, the mass spectra in **Fig. 5.3** show a large background gas signal (a broad bump at m/z > 135 Th). The broad background signal originates from the ionization of vacuum pump oil molecules. These ions were not resolved by the mass spectrometer due to the large volume intersected by the unfocused laser beam. The

unresolved background presence is relatively weak in **Fig. 5.1** due to the smaller volume of the focused laser beam as well as the strong signal of resolved ions produced at the crossing point of the focused laser and the supersonic beam.

The resultant log-log plot of the adenine ion signal intensity as a function of average laser pulse energy is presented in **Fig. 5.4**. A correction has been applied to account for small differences in the adenine temperature between the three measurements shown in **Fig. 5.3** (233.6, 234.2, and 234.8°C). Details of the corrections for temperature variations are given in **Appendix 9.3**.

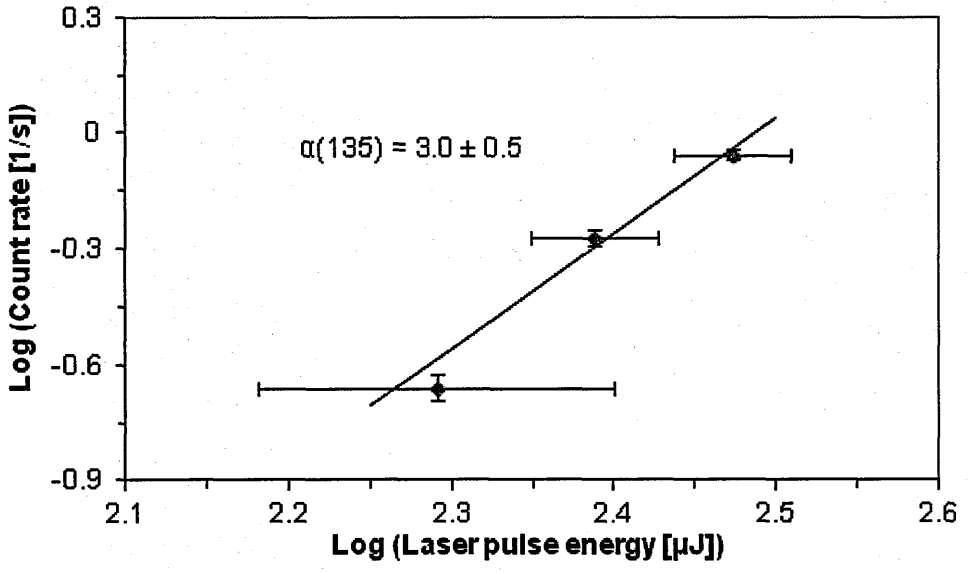

Fig. 5.4: Adenine signal intensity as a function of average laser pulse energy for adenine at low fluence. The characteristics of the laser (223.8 nm) and the supersonic jet are noted in the **Fig. 5.3** caption.

The error bars shown on the average laser pulse energy values correspond to the standard deviations for each measurement. The error bars on the average counts per second are standard deviations of single Gaussian peak area fitted to **Fig. 5.3** peaks, calculated by the commercial MCDWIN software (see **3.6.2** and **3.6.3**). A weighted linear fit[330] based on the errors on Log C and Log I has been applied to determine the exponent of 3.0±0.5, interpreted as the number of photons (α) absorbed in the MPI process.

The same data set has been analysed by the pulse-by-pulse method in which simultaneous recording of the laser pulse energy and number of ions produced by this pulse is

performed. The results are presented in **Fig. 5.5**. In this analysis the values on Y axis are reduced compared to the Y axis values in **Fig. 5.4**. Counts per pulse in **Fig. 5.5** represent only the number of laser pulses producing a detector signal, i.e. a laser pulse causing multiple ions arriving to the detector is counted as a single count. This treatment excludes false counts due to detector ringing, but also excludes true multiple ions arriving in a packet. The data from the three measurements shown in **Fig. 5.3** and **Fig. 5.4** was combined in order to construct a histogram based on pre-selected pulse energy bin sizes. **Fig. 5.5** was constructed with 20 μJ bin widths and the pulse energy points shown are the average energies of the pulses in each bin (error bars correspond to the standard deviation). The errors on the average counts per pulse are based on Poisson statistics. As the background is low at 135 Th in **Fig. 5.3** it does not have a significant effect on the analysis of adenine ion production as a function of laser intensity. A weighted linear fit gave the slope of $\beta(135) = 3.1 \pm 0.3$.

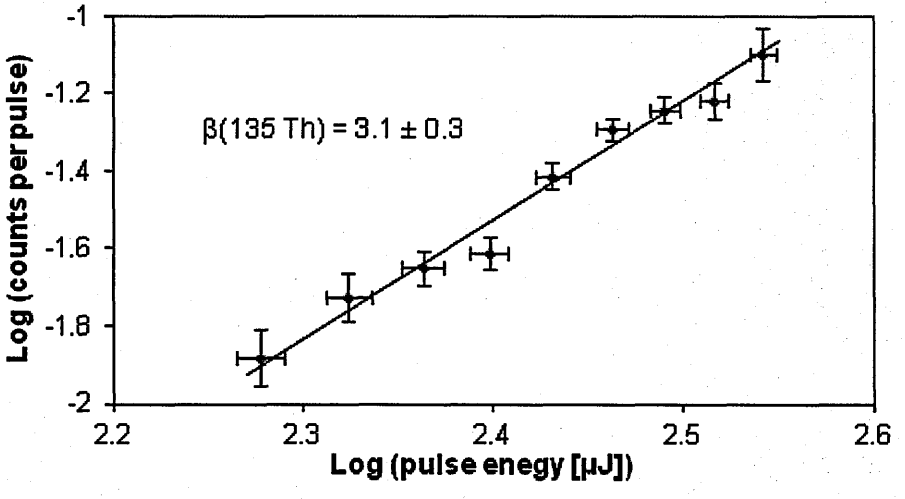

Fig. 5.5: Pulse energy dependence for the 135 Th peak in one-color (223.8 nm, ~ 2.3×10^5 W/cm^2) MPI mass spectrum of dry adenine (235°C, 0.4 bar argon).

Fig. 5.4 and **Fig. 5.5** show that the two analytical methods give similar results; both indicate the cubic dependence between the signal intensity (total or reduced) and laser pulse energy. This suggests that adenine MPI is a 3-photon process (or >3 photons if some level of saturation occurs) in the present experimental conditions. Interpretations of possible 3-photon ionization pathway(s) of isolated adenine molecules are mentioned in section **5.5**.

The major uncertainty of this result is related to the effective crossing volume of laser and molecular beams and can be only assessed qualitatively. The unfocused laser beam diameter is larger than the diameter of the molecular beam, therefore possible systematic spatial fluctuations of laser pulse energy can influence the signal intensity dependence (photon order). Since changes of the laser beam spatial profile as a function of laser pulse energy have not been assessed in the present experiment, their possible impact on the obtained results remains unknown. Further experimental effort, i.e. determination of the laser beam profile as a function of laser pulse intensity is required to solve this issue.

Whereas no previous photon order measurements are available in the present wavelength range (223-227 nm), some previous attempts to determine the number of photons required for UV MPI of isolated adenine have been reported at longer wavelengths[227, 228]. It should be noted that the fluence (~ 2×10^5 W/cm^2) in the measurements shown in **Fig. 5.4** and **Fig. 5.5** is at least an order of magnitude lower than any previous experiments. Using 266 nm pulses in the fluence range 2×10^6 - 3×10^7 W/cm^2 (assuming 6 ns pulses, as standard for their Nd:YAG laser model) Nam et al.[228] observed a photon order (order of non-linearity) of α=1.6 for adenine ionization in non-hydrated conditions, suggesting 2-photon ionization. Also at 266 nm, Wells et al.[227] reported α=1.1 and 0.9 for adenine$^+$ production using focused laser beams with respective pulse widths and energies of 4–5 ns, 1-15 mJ and ~120 fs, 1-30 μJ. At 248 nm (5.00 eV), Lin et al.[325] measured adenine$^+$ signal intensities as a function of pulse energy in the range 0.02 to 1.0 mJ using focused 15 ns and 500 fs laser beams. While the authors did not derive photon orders, their linear-scale plot indicates approximate photon orders ≤1. The results of Wells[227] and Lin[325] indicate strong signal saturation; indeed they used focused laser beams in their experiments.

5.3 Thymine

5.3.1 Literature review

A review of the previous experimental studies on gas-phase thymine indicates that multi-photon ionization occurs via excited states with nanosecond-order lifetimes. Kang et al.[237] used femtosecond pump-probe ionization to investigate the excited state dynamics of

thymine after photoexcitation at 267 nm. The excited state signals decayed with exponential components of 6.4 ps and ≥ 100 ps, as well as a long-lived component assigned to a triplet state[237]. Time-resolved photoelectron spectroscopy with 250 nm excitation also revealed three components with lifetimes <50 fs, ~1 ps and an unspecified nanosecond-order lifetime[311]. Similar results were found in a study[331] of thymine monomers, where lifetimes of ~50 fs, 6-9 ps and ≥ ns were reported. Finally Gonzalez-Vazquez et al.'s[332] 267 nm pump and 400-800 nm probe experiments on gas phase thymine revealed three transient species with lifetimes of <100 fs, 7 ps and > 1 ns. At the same pump-probe wavelengths, only Canuel et al.[333] negated the existence of an additional long-lived transient measuring 105 fs and 5.12 ps transients.

The REMPI spectrum of thymine is broad and diffuse[267], similar to that of uracil. The ionization scheme used in Brady et al.'s[267] REMPI study (270-285.7 nm pump, 193 nm probe) favours ionization from a low-lying triplet state (single pump photon and single probe photon).

Schneider et al.[334] ionized thymine at 260 nm (4.769 eV) using unfocused (~ 2-3 mm beam diameter at 0.1-1 mJ) ns laser pulses. The authors suggested that nanosecond multiphoton ionization is possible due to the existence of a lower lying dark state with a nanosecond lifetime populated by a deactivation of the initially excited $^1\pi\pi^*$ state. Shorter wavelengths are required to ionize this state efficiently (according to He et al.'s model of the decay mechanism of the pyrimidine bases[335]), which was explained by a poor Franck-Condon overlap of the dark state with low-lying vibrational levels of the ionic ground state[336]. It has been assumed that absorption of a second photon in the range 240-270 nm is not enough for ionization; instead it promotes thymine into a highly excited neutral state[334].

In general, relaxation pathways of thymine comprising long (ns) transients have been reported in the literature more often than for adenine and have usually been assigned to long-lived triplet states. This makes nanosecond 2-photon ionization likely to occur as long as the energy of the second photon is sufficient to overcome the ionization potential of thymine from a triplet state. However it can be also noticed that particular transients also depend on the laser ionization scheme applied. Most of the studies presented above were

carried out using thermally generated thymine vapour in supersonic beams, the method which has been applied in the present work.

5.3.2 Thymine MPI - experimental data

In this work thymine has been multi-photon ionized at three different wavelengths: 222, 226, and 229 nm. The peak at 126 Th attributed to thymine has been identified in each of these measurements. Wavelength dependence in this narrow range has not been found. No sharp vibronic bands are expected, since it has been demonstrated that the REMPI spectrum of thymine is broad and diffuse[267]. The mass spectrum recorded using a focused laser beam at 226 nm is presented in **Fig. 5.6**.

Fig. 5.6 does not show any evidence for the production of T_2^+ ions (252 Th). However, the absence of cluster ions in the MPI mass spectrum does not discount the possibility of clusters in the neutral beam. In order to minimize the possibility of clustering, the data presented in this section were recorded with thymine temperatures (~220°C) and argon driving pressures (~0.5 bar) close to the minima required to produce a practical thymine$^+$ signal. The integrated peak intensities (TH^+/T^+) ratio of 26 ± 2 % in **Fig. 5.6** is distinctly higher than the ratio of 6.8 % due to thymine isotopomers[329], and indicates the presence of neutral thymine clusters in the targeted supersonic jet. Therefore there is a distinct possibility that the 126 Th peaks analyzed below contain contributions from ionized and dissociated clusters as well as from ionized monomers.

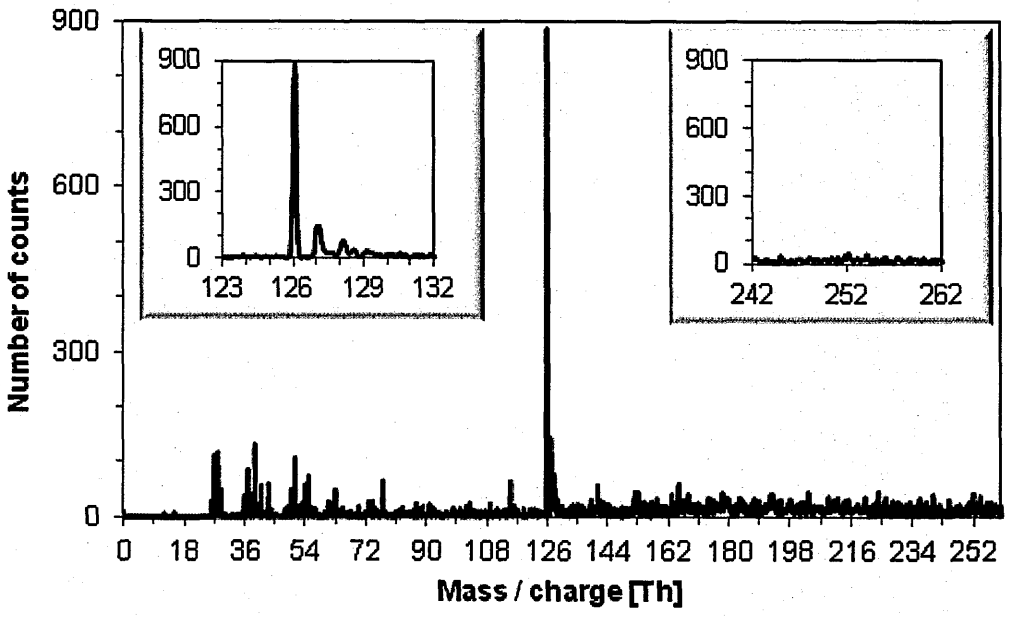

Fig. 5.6: One-colour (226nm, ~ 2.2×10^7 W/cm^2) MPI mass spectrum of non-hydrated thymine (217°C, 0.5 bar argon).

Tembreull and Lubman's[327] experiments at 222 nm produced no signal for thymine ions with laser fluence ~ 10^6 W/cm^2, whereas their equivalent experiments on laser-desorbed adenine produced a clear signal for the monomer ion. The lowest fluence used in the present thymine experiments was ~ 4.8×10^6 W/cm^2, close to the limit at which an analytically useful signal (~0.01 counts per pulse) could be measured.

Fig. 5.7 shows the dependence of total thymine ion production on laser pulse energy from 8 different measurements recorded with a focused laser beam. The data covers a wide range of pulse energies between 4.8×10^6 and 2.2×10^8 W/cm^2. The curve slope's clearly decreases towards higher fluence, which is attributable to partial saturation. The insert in **Fig. 5.7** shows the low fluence part of range. A weighted linear fit of this low fluence part gives a photon order of 1.4±0.1. **Fig. 5.8** shows that the alternative pulse-by-pulse analysis (reduced signal intensity equivalent with the method used to generate **Fig. 5.5** for adenine) gives $\beta(126) = 1.9 \pm 0.2$. The difference between β and α in the case of thymine is caused by different fluence ranges used to plot characteristics in the **Fig. 5.7** insert and in **Fig. 5.8** (narrowed fluence range in the latter). The present data supports 2-photon ionization of thymine under the present laser conditions. Interpretations of the most likely 2-photon ionization pathway(s) are discussed in section **5.5**.

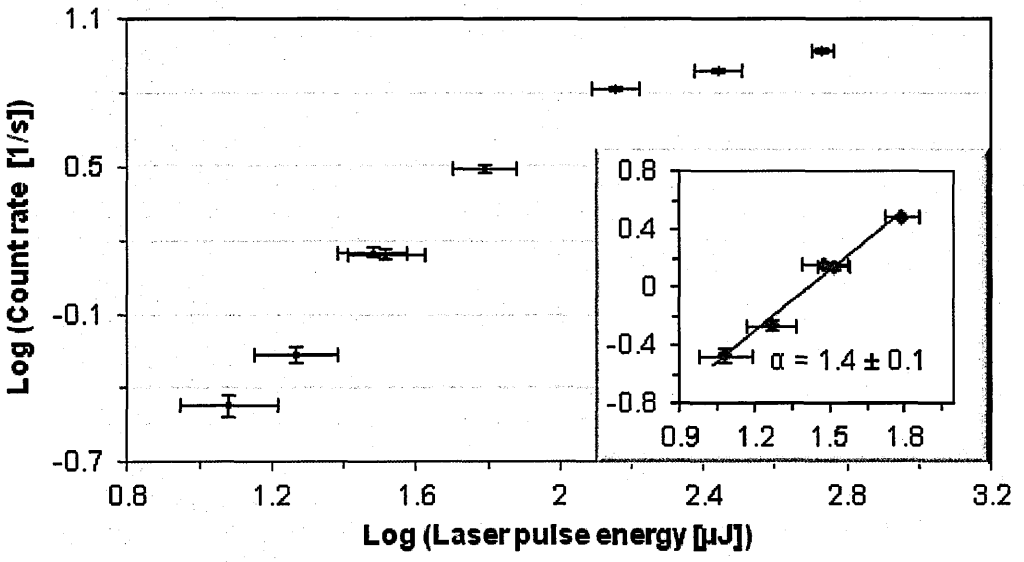

Fig. 5.7: Thymine$^+$ count rate as a function of pulse energy without pulse-by-pulse analysis. Thymine temperature 217°C, argon pressure 0.5 bar, wavelength 226 nm, approximate fluence range 3.2×10^6 - 1.4×10^8 W/cm^2.

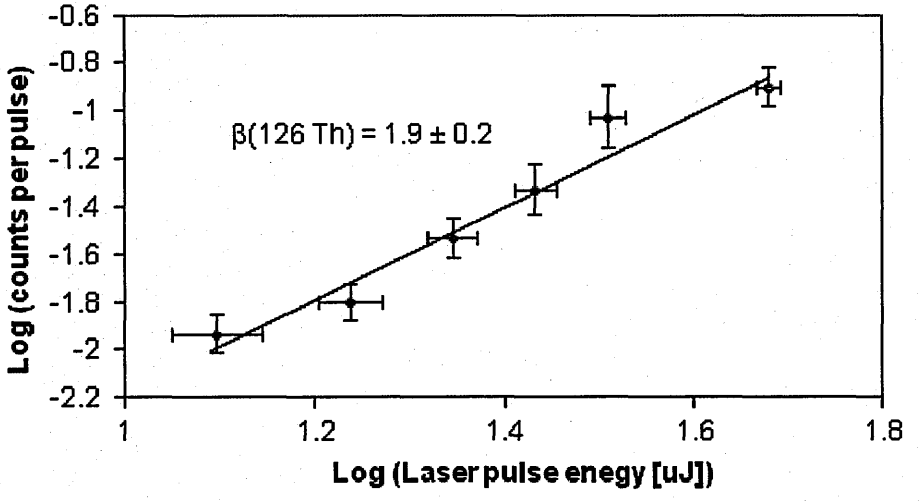

Fig. 5.8: Pulse-by-pulse analysis of 126 Th ion (T^+) production as a function of pulse energy for one-colour (226 nm, approximate fluence range: 3.2×10^6 - 1.3×10^7 W/cm^2) MPI mass spectrum of non-hydrated thymine (217°C, 0.5 bar argon).

5.4 Uracil

5.4.1 Literature review

Femtosecond MPI experiments show short lifetimes of uracil excited states. In experiments with 267 nm pump and 2 x 400 nm probe pulses, bi-exponential fits of transients of uracil UV excited states revealed decay times of 130 fs and 1.05 ps[333] (relative uncertainty 10%). A separate study (excited state prepared at 267 nm and dynamics followed with 3 x 800 nm ionization)[237] identified a decay time component of 2.4 ps. In addition, an excited state lifetime of 750 fs has been reported in experiments with 250 nm pump and 200 nm probe pulses[312], Ullrich et al.'s lifetime value was shorter than the previous pump-probe measurements due to the inclusion of a weak long time-scale channel (arbitrarily fixed to 1 ns) for excitation at 250 nm and ionization promoted by a fs 200 nm pulse[312].

The ultrafast relaxation of uracil discussed above leads to very weak signals in one-colour nanosecond multi-photon ionization experiments. Attempts to ionize uracil at 222 nm (~ 10^6 W/cm^2)[327] and at 248 nm had no success[325]. Similarly, no peak for the uracil cation (112^+) has been obtained using a nanosecond laser beam (spot diameter 2-3 mm in diameter, pulse energy 0.2-1 mJ) in the wavelength range 235-268 nm[56]. By contrast, a strong signal (sufficient to record a REMPI spectrum) has been observed using a 270-285.7 nm pump and 193 nm probe ns time-scale photoionization scheme[267].

Due to the challenge of obtaining strong signals in ns MPI experiments on uracil, methylated species have been used in several previous studies as models for this RNA base. Nanosecond time-resolved studies on 1,3-dimethylated uracil (1,3-DMU) in the gas phase (pump 251 nm, probe 220 nm) show the exponential decay equal to 56 ns[336]. The theoretical dependence between the number and position of methyl groups, and the properties of excited states has been studied by Etinski et al.[337, 338].

5.4.2 Uracil MPI - experimental data

The uracil mass spectrum recorded at 223.8 nm is presented in **Fig. 5.9**. The 112^+ cation has been detected, although with quite low intensity compared with the background.

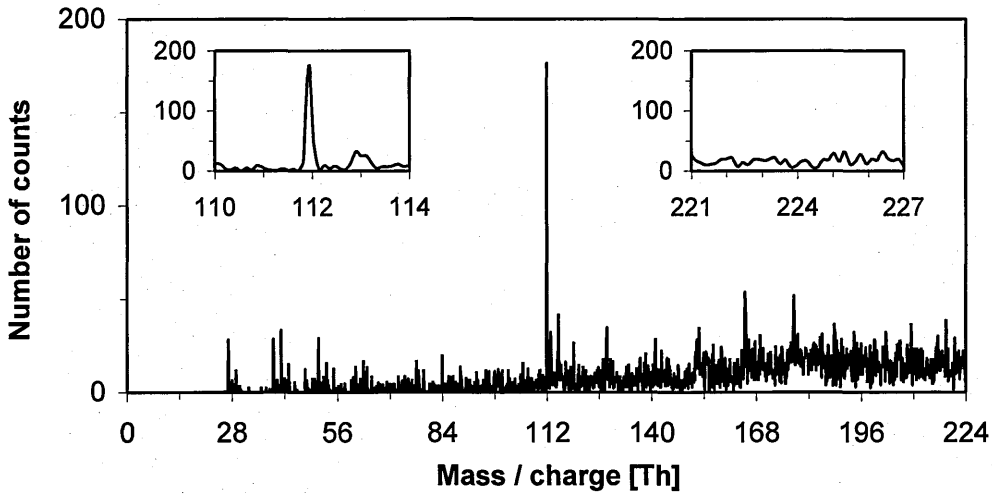

Fig. 5.9: One-colour (223.8 nm, ~ 3.4×10^6 W/cm^2) MPI mass spectrum of non-hydrated uracil (250°C, 0.6 bar argon).

No evidence was observed for the production of uracil dimer ions (224 Th) in the data analyzed in this section. In order to minimize uracil clustering in the neutral beam, the present results were recorded with powder temperatures close to the minimum required to observe a practical signal and at low driving pressures compared with previous measurements focusing on uracil monomers in supersonic beams (e.g. 4-21 bar helium in Brady et al.'s experiments[267]). Nonetheless, the UH^+/U^+ ratio (33 ± 6 % in **Fig. 5.9**) was distinctly higher than the isotopomer ratio of 5.3 % calculated using the equation of Hu et al.[329]. This indicates the production of protonated uracil (UH^+) from the ionization and dissociation of uracil clusters. Therefore it is also possible that the uracil$^+$ signals analyzed in this section contained contributions from ionized and dissociated clusters.

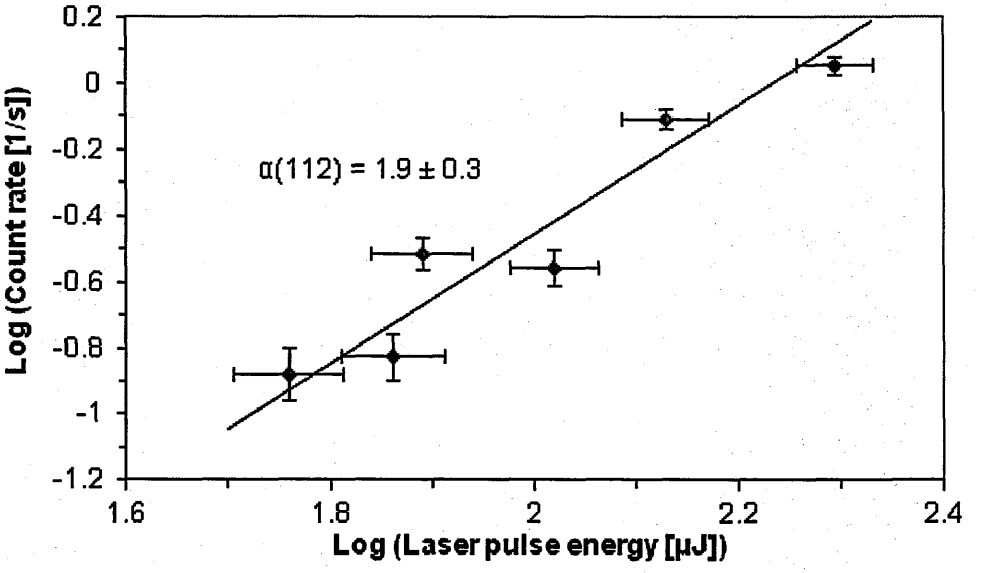

Fig. 5.10: 112 U (uracil$^+$) count rate as a function of pulse energy without pulse-by-pulse analysis. Uracil temperature 250°C, wavelength 223.8 nm, argon pressure 0.60 bar, approximate fluence range 1.3×10^6 - 5.1×10^6 W/cm^2.

No previous experiments have been carried out to assess the photon order of ns-timescale MPI of uracil. **Fig. 5.10** shows the U^+ signal intensity as a function of laser fluence on a log-log scale (based on an equivalent analysis to **Fig. 5.4** and **Fig. 5.7** for adenine and thymine) registered with a focused laser beam. To minimize the possibility of saturation, this dependence was recorded close to the lowest fluence that produced a clear U^+ signal (1.4×10^6 - 9.4×10^6 W/cm^2). The weighted linear plot in **Fig. 5.10** gives a photon order of 1.9±0.3. The pulse-by-pulse analysis of the data enables the fluence range to be narrowed to 1.3×10^6 - 3.2×10^6 W/cm^2, giving a photon order of 2.0±0.3 (**Fig. 5.11**). Both analytical methods indicate that uracil photoionization is a two-photon process in the present conditions.

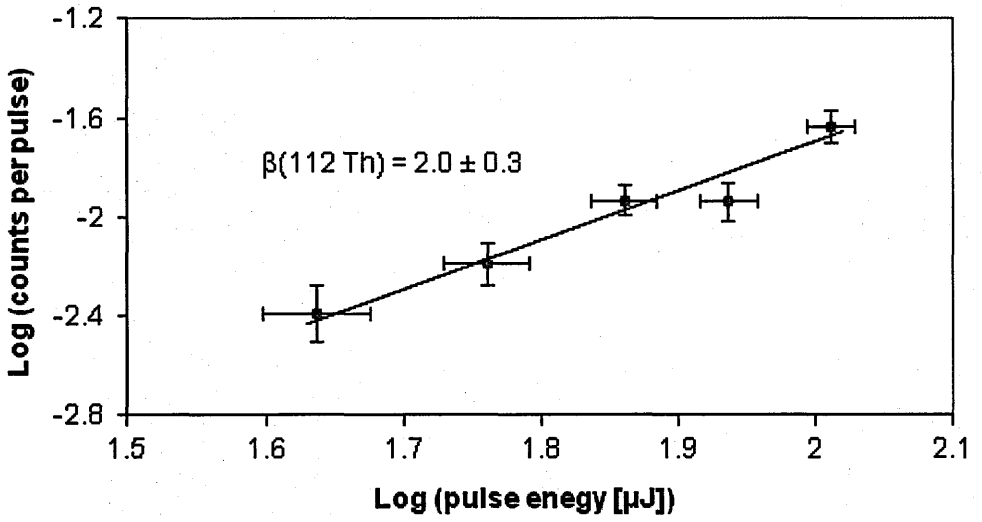

Fig. 5.11: Pulse-by-pulse analysis of 112 Th ion (U^+) production as a function of pulse energy for one-colour (223.8 nm, approximate fluence range 1.0×10^6 - 2.8×10^6 W/cm^2) MPI mass spectrum of non-hydrated uracil (250 °C, 0.60 bar argon).

5.5 Interpretation of the MPI pathways

Uracil, thymine and adenine molecules seeded in argon jets were successfully photoionized using a UV nanosecond dye laser in the wavelength range 223 – 227 nm with approximate minimum laser fluences 1.3×10^6 W/cm^2 (uracil), 3.2×10^6 W/cm^2 (thymine), and 2×10^5 W/cm^2 (adenine). Photon order measurements for the pyrimidine bases thymine (226 nm) and uracil (223.8 nm) reveal evidence for 2-photon ionization, while a photon order equal to 3.0±0.5 was observed for adenine. The adenine (a purine base) measurements were carried out at lower fluence than any previous experiments (~ 2 - 3×10^5 W/cm^2), and lower than for the pyrimidine bases in the present project. This minimizes the possibilities of saturation. No previous photon order measurements are available in the literature for thymine and uracil. Theoretical studies presented in chapter 4 show that at the present wavelengths, all three molecules are excited to high vibronic levels of short-lived bright $^1\pi\pi^*$ states. First stages in a number of possible 2- and 3-photoionization pathways for measured photon order characteristics are presented in **Fig. 5.12**. This provides a framework for the forthcoming discussion.

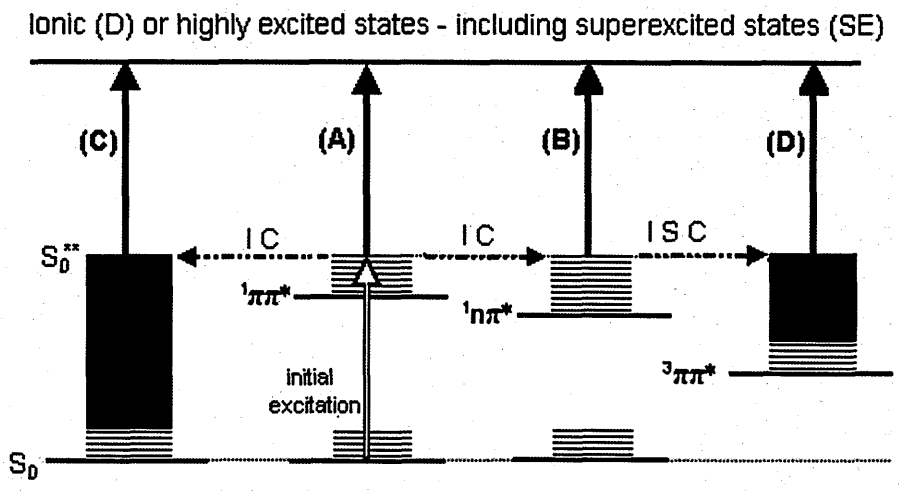

Fig. 5.12: Schematic representation of a selection of possible 2-photon processes. Absorption of a second photon can occur in various singlet and triplet electronic states and does not always lead to ionization. Transitions between electronic states occur through Internal Conversion (IC) and Intersystem Crossing (ISC) processes. SE (superexcited) states can auto-ionize, fragment into neutrals or - if they live long enough - absorb a third photon leading to ionization.

(A) In this pathway absorption of a second photon occurs in the initially excited bright $^1\pi\pi^*$ state, which is unlikely under the present nanosecond laser fluence conditions since this state undergoes ultrafast relaxation on the femtosecond time scale for adenine (sections **4.1** and **5.2.1**), up to 10 ps for thymine (sections **4.2** and **5.3.1**), and single ps for uracil (sections **4.3** and **5.4.1**).

(B) Absorption of a second photon occurs after internal conversion to the $^1n\pi^*$ state. The role of these states is unclear, it is often a challenging task to disentangle their dynamics from the dynamics of $^1\pi\pi^*$ states. However the $^1n\pi^*$ states are considered as an intermediate states in the molecular relaxation process, especially their role in mediation in transition of initially excited bright $^1\pi\pi^*$ states into long-lived $^3\pi\pi^*$ triplet states. Their proposed lifetimes (before internal conversion to electronic ground state) do not exceed 10 ps in the case of adenine, thymine, and

uracil (see appropriate sections mentioned in **(A)**); which is very low in terms of ionization effectiveness in the present nanosecond regime[319].

(C) The next pathway which has to be considered, leads to the vibrationally hot electronic ground states (S_0**) populated on the picosecond time scale through rapid internal conversion from $^1\pi\pi^*$, $^1\pi\sigma^*$ or $^1n\pi^*$ states. Detailed analysis of unimolecular reactions in the vibrationally hot electronic ground state is possible on the basis of the Rice-Ramsperger-Kassel-Marcus (RRKM) statistical model[185, 339, 340], however it has not been performed in the framework of this work. Further absorption of photons by ground state reactants (tautomers, or isomers) could contribute to a detected signal. However experimental evidence shows that absorption of successive photons will cause neutral dissociation limiting the effectiveness of photoionization through vibrationally excited electronic ground state[341]. Hofstein et al.[314] excluded internal conversion into highly excited vibrational levels of the molecular ground state, as a possible intermediate step in 2-photon ionization process.

(D) The present results for adenine, thymine and uracil can be rationalized by ISC (Intersystem Crossing) followed by the absorption in long-lived triplet state. It is possible that the present α = 3.0±0.5 result for adenine indicates the following 3-photon ionization pathway: (1) $^1\pi\pi^*$ excitation and rapid internal conversion to the $^1n\pi^*$ state followed by ISC to nanosecond lifetime triplet state; (2) triplet-triplet transition accessing high-lying triplet superexcited (SE) state; (3) absorption of a third photon leading to ionization. Ionization from initially populated vibrationally hot low-lying triplet states would provide a straight-forward interpretation for the 2-photon ionization of thymine and uracil. However these measurements were carried out at higher laser fluences than for adenine, so signal saturation at the excitation or ionization steps cannot be excluded, especially for thymine where the photon order characteristic has been measured at the highest average laser fluence.

Since nanosecond and sub-nanosecond time intervals are expected to characterize multi-photon absorption in the present laser fluence range, longer-lived excited states (triplet) excited states are considered in detail. It is natural to ask the question why absorption of

the second photon in a triplet state would not lead to ionization, but to neutral excitation of adenine, while the total 2 photon energy absorbed 11.18 eV is distinctly higher than ionization thresholds of the molecules studied? Montero et al.[342] has recently demonstrated such neutral super-excited states (with energies exceeding ionization potentials) for naphthalene (IP=8.14 eV) pumped by two photons of: 2×304 nm = 8.17 eV and 2×267 nm = 9.30 eV; as well as for aminonaphthalene (IP = 7.48 eV) pumped by two-photons of 2×333 nm = 7.45 eV, 2×300 nm = 8.28 eV, and 2×267 nm = 9.30 eV. These excitation schemes promoted molecules to excited states nearby or significantly above the ionization potential via excited S_1/S_2 states. It has been shown that such an excitation efficiently competes with direct ionization. Moreover, Pinnaduwage and Zhu[343] showed experimentally that molecules (benzene, deuterated benzene and triethylamine) excited by 248 and 193 nm nanosecond excimer laser to energies within several eV (0.75 - 5.3 eV) above their lowest ionization thresholds can survive for several microseconds in the neutral form. The latter results correlate very well with the excited states (possibly triplet states) lifetimes measured for nucleic acid bases by Nir et al.[313] using 193 nm nanosecond laser pulses.

The detailed scheme of adenine excited states is presented in **Fig. 5.13**. The energy levels and the appearance energy of adenine cation in single photon ionization experiment are taken from the literature (Gonzalez-Luque et al[256], Petke et al.[344], Jochims et al.[146]).

Higher vibrational levels of the initially excited state bright $^1\pi\pi^*$ state (vertical excitation energy 5.35 eV calculated by Gonzalez-Luque et al.[256]) undergo internal conversion or intersystem crossing in the region of potential energy surfaces crossing at around 5.2 eV, the second step of IC and ISC processes leaves a molecule trapped in the $^3\pi\pi^*$ triplet state. Following triplet-triplet absorption of the second photon may lead to a triplet superexcited (SE) or ionic state. Triplet states on the left and right sides of the figure are in fact the same state, which can absorb photons causing ionization, however different pathways lead to this state. The levels of triplet T_n states on the far left side of the figure are presented on the basis of Petke's et al.[344] calculations.

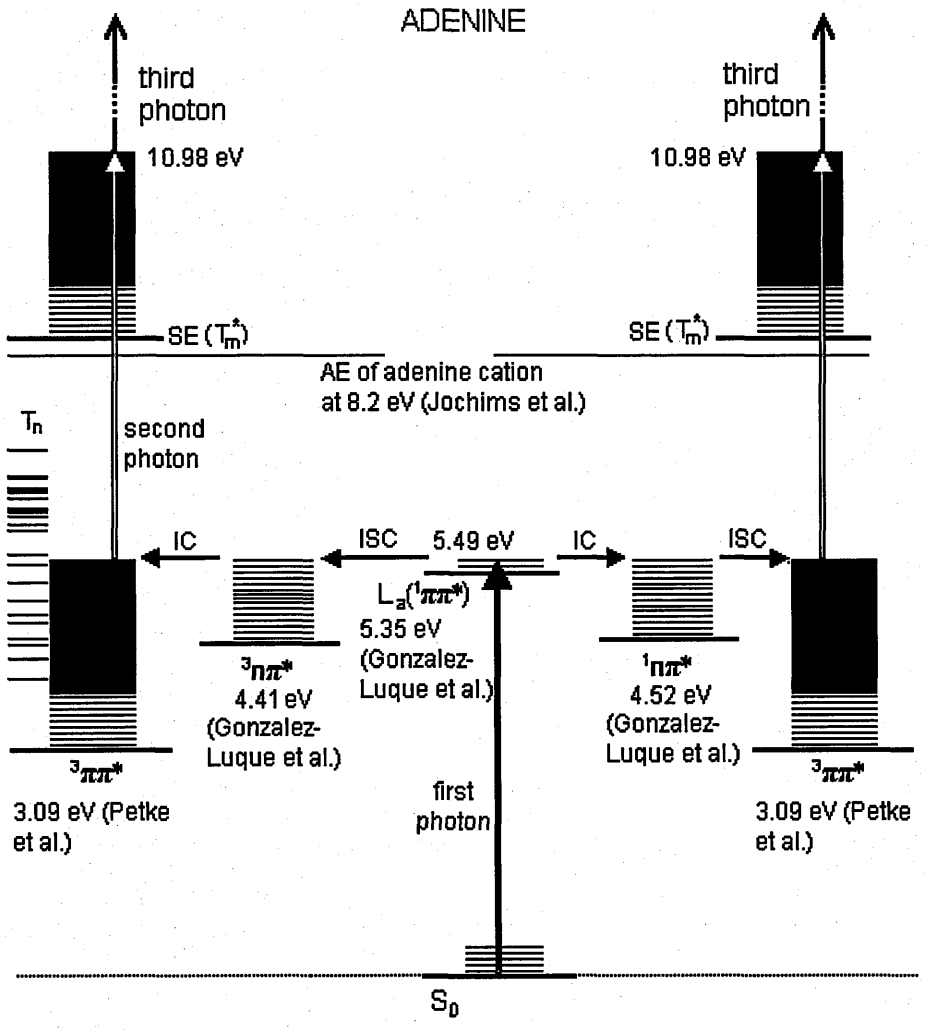

Fig. 5.13: Excited states of adenine. The arrows show possible excitation/ionization pathways. Two-photon absorption may lead to a neutral super-excited (SE) or an ionic state. See the paragraph below for a description.

Petke et al.[344] calculated the electronic absorption spectra of adenine with ab initio methods. MRCI (multi reference configuration interaction) method calculations of triplet states T_n showed that the lowest triplet state, T_1, in adenine lies approximately 24930 cm^{-1} (3.09 eV) above the ground state, which is consistent with the experimentally derived maximum phosphorescence of adenine in solution systems found at 3.05 eV. Theoretical methods used by Gonzalez-Luque et al.[256] indicated the lowest triplet state band origin at 3.36 eV. This triplet state can be populated in adenine through a high-lying crossing region at 5.2 eV related to the presence of low-lying singlet and triplet npi* states[256]. This high-lying region is accessible with the present laser pulses of energy 5.5 – 5.6 eV. The highest triplet state calculated by Petke et al.[344] lies at 55930 cm^{-1} (6.94 eV), however it is possible

that higher lying states of that type including states of Rydberg character, lie above this level, and even above the IP of adenine. States characterized in this way are candidates for superexcited states.

The lowest triplet state in the present experiment would be produced with vibrational energy excess of ~ 2.4 eV (for excitation at 226 nm, i.e. 5.49 eV). Absorption of a subsequent photon can lead to $T_1 \rightarrow T_m^*$ transition, where T_m^* is vibrationally excited high-lying triplet state. Due to Franck-Condon factors the most intense transitions from vibrationally excited T_1 state will lead to vibrationally excited T_m^*, with the energy excess equal to the initial amount of T_1 vibrational excitation. Such a super-excited triplet state T_m^* is accessible with the second photon. The total energy of 2 absorbed photons equal to 10.98 eV (with maximum at ~8.5 eV of electronic energy) may lead to direct ionization (adenine IP 8.2 eV[146]). However a plausible scenario is that superexcitation successfully competes with direct ionization. Indeed, the adiabatic ionization potential of adenine triplet state may lie above the lowest adiabatic ionization potential correlating with the lowest ionic singlet state. Indeed an analogous effect has been demonstrated theoretically by Betterton et al.[345] for simpler molecules - phosphorus compounds cyanophosphinogen (HPCN) and its nitrogen-centered isomer HNCP. The adiabatic ionization energies calculated for HPCN and HNCP were 10.16 eV and 8.3 eV, respectively. However the singlet state of HPCN+ (at 10.16 eV) has been found approximately 1.3 eV below the lowest energy triplet state of HPCN+ (at 11.48 eV). In contrast to HPCN+, the triplet state of HNCP+ (8.30 eV) is lower in energy than that of the singlet state (9.26 eV) by approximately 1 eV. A similar effect could support superexcitation over adenine ionization after absorption of the second photon in the triplet state. It is also worth noticing that ionization potentials may change upon relaxation; in recent theoretical studies Barbatti and Ullrich[346] show adenine ionization energy variations up to 4.5 eV between the Franck-Condon region and conical intersections. The ionization energy of adenine in the lowest triplet state and the energy interval between the electronic energy of the SE state accessed and the lowest ionic state remain unknown. Excited states lying close to ionization potential are prone to auto-ionization, field ionization or neutral dissociation[65, 342, 347]. The data obtained in this thesis for adenine may indicate that the molecule excited by two photons to a SE state can

survive on a nanosecond timescale and be ionized afterwards by the third photon, with auto-ionization and neutral fragmentation taking place over relatively long timescales.

Similar processes may take place in thymine and uracil. As discussed earlier initial photoabsorption in thymine to the bright $^1\pi\pi^*$ state is followed by its deactivation to the ground state on the picoseconds scale, however a transition to a triplet state is also possible. Excitation spectra of uracil and thymine computed by Etinski[337] show singlet and triplet states levels within the ranges presented in **Fig. 5.14**.

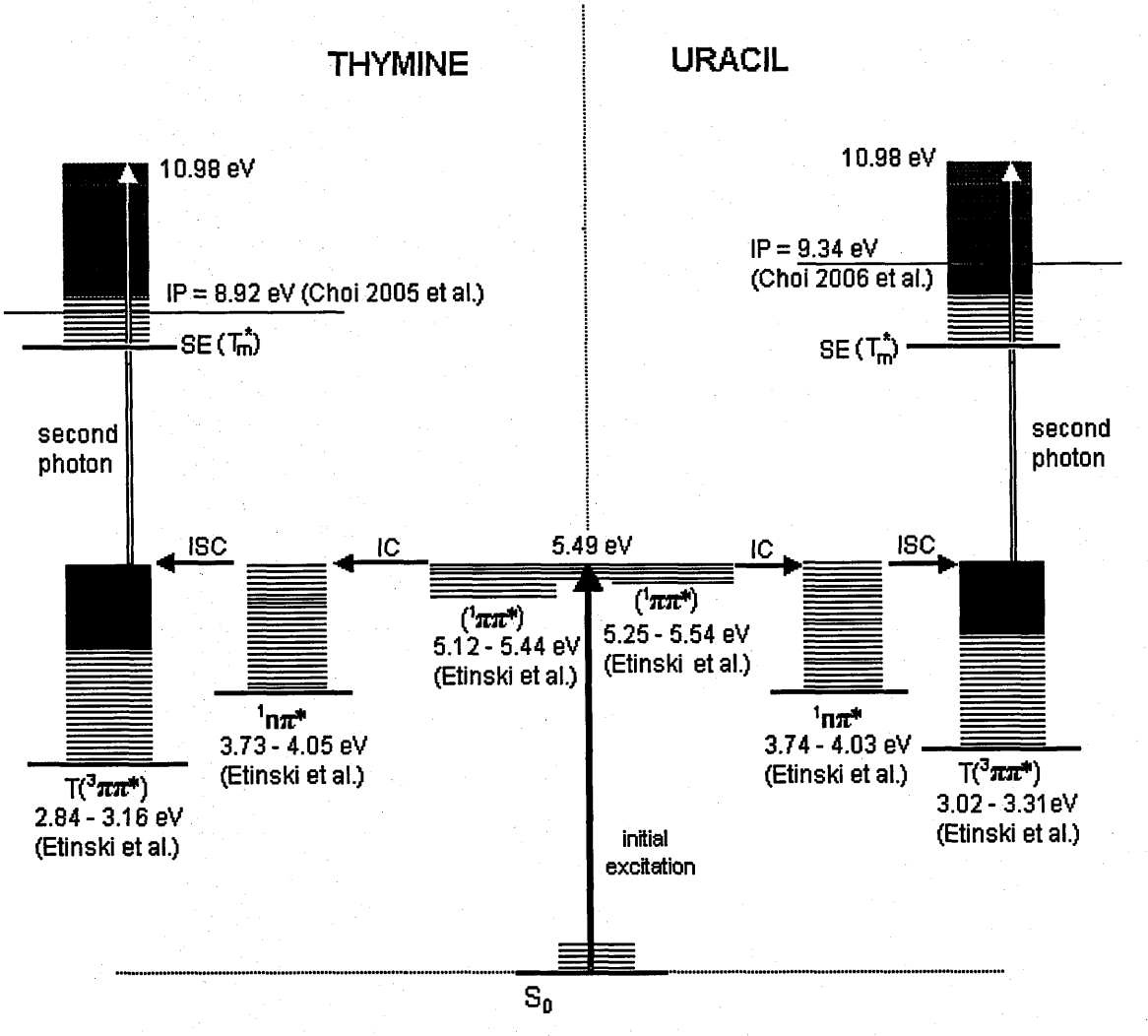

Fig. 5.14: Two-photon excitation pathways of thymine and uracil. The ranges of $^1\pi\pi^*$ vertical excitation energies, band origins of $^1n\pi^*$ states and triplet $^3\pi\pi^*$ states are taken from Etinski et al.[337]. Adiabatic ionization energies of thymine and uracil have been measured by Choi et al.[149, 150]. Absorption of the second photon may induce superexcitation which can be followed by vibrational auto-ionization.

A broad phosphorescence band with maximum at 450 nm (2.76 eV) was observed by Becker and Kogan[348] at 77 K for uracil in a polar aprotic solvent (2-MTHF – 2-methyl-tetrahydrofuran). This phosphorescence has been assigned to occur from the $^3(\pi\pi^*)$ state following $S_0 - S_2$ ($\pi\pi^*$) absorption and ISC. Calculated phosphorescence lifetimes support the assumption that it stems from the T_1 ($\pi\pi^*$) state[178]. Etinski et al.[337] theoretically characterized the lowest lying singlet and triplet states of uracil and thymine, and performed calculations indicating that the T_1 ($\pi\pi^*$) state is populated from the intermediate $S_1(n\pi^*)$ state on a subnanosecond time scale (as shown in **Fig. 5.14**).

Taking into account the maximum calculated values (3.31 eV and 3.16 eV) for T_1 ($\pi\pi^*$) states at band origin for uracil and thymine and adding one 5.54 eV photon, maximum electronic excitations at 8.85 eV and 8.7 are obtained for uracil and thymine, respectively. Both are lower than the respective adiabatic IPs of uracil (9.1 eV) and thymine (8.9 eV). Therefore a molecule with total energy ~ 11 eV may remain in a highly excited state, in which case the present data (photon orders ≤2 for T^+ and U^+ production) would be due to vibrational auto-ionization. Indeed, the appearance of an ion due to vibrational auto-ionization of a highly excited state could be also possible; significant vibrational energy excess acquired due to earlier IC and ISC can play a role in this process. High levels of signal obtained by Pinnaduwage and Zhu[343] applying field ionization (90 V/cm) for molecules excited by two photons to different levels of total energy above IP indicate field ionization as an efficient process for highly excited states.

5.6 Summary

Possible two- and three-photon ionization pathways of adenine, uracil and thymine are presented. Photon orders of 1.4±0.1 and 1.9±0.3 obtained for thymine and uracil in the present experiments indicate that their MPI is at least two-photon process. The value of 1.4±0.1 for thymine suggests partial saturation at the excitation or ionization step. Since the laser beam was focused in the experiments on thymine and uracil, possible systematic fluctuations of the laser beam profile are less likely to have an impact as in the case of adenine, where photon order of 3.0±0.5 was found for an unfocused laser beam crossing the molecular beam only partially. Therefore some uncertainty related to experimental

conditions exists with regards to whether $\alpha(135) = 3.0 \pm 0.5$ reflects a true 3-photon ionization process.

6 Cluster ions of nucleic acid bases and water

6.1 Introduction

The photophysical and photochemical properties of a molecule embedded within a hydrogen bonded complex can be significantly different from those of isolated molecules. Environmental effects on excited state dynamics and ionization potentials can be probed experimentally in supersonic expansion conditions where condensing molecules are grouped into weakly bonded complexes. In this chapter, mass distributions of dry and hydrated nucleic acid (NA) bases cluster ions have been characterized (sections **6.3** and **6.4**). Further experimental effort has been focused on photon order measurements in clustering conditions and their comparison with those of isolated molecules (**6.6**). Potential multiphoton ionization pathways of molecular complexes are discussed on the basis of the present results and of theoretical and experimental investigations in the literature (**6.7**).

In addition to nucleic acid bases, two related chromophores have been studied in the present project: 5-fluorouracil and hypoxanthine. 5-halogenated uracils (5-XU, where X = chlorine, bromine, or iodine) can substitute thymine in DNA. They might be expected to display hydrogen-bonding properties closely related to those of uracil (U) and thymine. Studying clusters of 5-fluorouracil is also interesting due to its wide use for the treatment of solid tumors, notably in combination drug regimens for cancer chemotherapy[349]. Transformation of uracil into 5-X uracil (X=halogen) significantly changes its chemical and spectroscopic properties, as well as its in vivo activity[350].

Hypoxanthine has potential applications in diverse techniques including polymerase chain reaction (PCR) hybridization probes and gene therapies, where the exact sequence of nucleobases in the target DNA strand must be known in order to construct a complementary strand (a primer) that will selectively bind to the desired region (see[351] and references therein). Hypoxanthine can play the role of a "universal" nucleobase that binds without discrimination to any of the natural bases and results in duplexes of similar stability as the corresponding duplexes composed entirely of natural nucleobases. A negative activation barrier for hypoxanthine production in the closing system of four water molecules

around adenine has been predicted theoretically[352, 353].Therefore experimental studies on hypoxanthine pairing with DNA bases and water are important.

Section **6.2** summarizes the basic thermodynamics of nucleobase complex formation. Multi-photon ionization experiments on neat adenine molecular beams, as well as adenine-thymine and adenine-uracil mixed systems are presented in section **6.3**. Homogeneous and heterogeneous base pair ions have been detected in these experiments, however with very low intensity despite applying quite high oven temperatures (above 250°C). Different pathways leading to the formation of protonated monomers in mass spectra are discussed in section **6.4**. Larger numbers of clusters have been observed after the addition of water vapour to the expanding gaseous mixture; the results of MPI process in hydrated clusters are presented in section **6.4**. Photon order measurements in hydrated clustering conditions (**6.6**) are followed by the results discussion (**6.7** and **6.8**), where MPI pathways are proposed that are distinct from those of isolated molecules. The chapter is summarized in section **6.9**.

6.2 Background: nucleic acid bases clustering

The complexity of the clustering process in supersonic expansion conditions has been characterized[354] as the interplay between kinetic and thermodynamic factors, with competition between continually evaporating and condensing molecules. "Pseudo association constants" for the formation of the dimers of free DNA nucleobases and nucleosides in the gas phase have been calculated from experimental results[355]. The following order of "pseudo association constants" has been reported: GC>GG>CC>TA>AA, TT, AG > AC, TC, GT (formation of the other three conceivable base pairs was not observed, while uracil was not studied). This experimental order is consistent with the stabilization energies calculated by Sponer et al.[356], as far as the three most stable base pairs are concerned, but there are differences for the remaining base pairs.

The process leading to the formation of a generic base pair $X\cdots Y$ from the isolated bases X and Y can be demonstrated as[357]:

$$X + Y \leftrightarrow X\cdots Y \qquad \textbf{6-1}$$

The stabilization of noncovalent complexes formed in vacuum depends on the energy of a complex being lower than the sum of the energies of its separated subsystems[358]. In an environment, the equilibrium of any noncovalent (as well as covalent) process is determined not by the change in energy (enthalpy) but by the change in the Gibbs energy[358]. The equilibrium constant (K_T) of the process at temperature (T) is related to the standard change in the Gibbs energy (ΔG_T^0) and the molar gas constant (R) by the following equation:

$$\Delta G_T^0 = -RT\,ln(K_T) \qquad \textbf{6-2}$$

The ΔG_T^0 term can be determined from knowledge of the enthalpy and entropy of the base pair formation, ΔH_T^0 and ΔS_T^0, using the equation:

$$\Delta G_T^0 = \Delta H_T^0 - T\Delta S_T^0 \qquad \textbf{6-3}$$

The entropy term in the case of complex formation is always repulsive and compensates the attractive enthalpy contribution[357]. The interpretation of experimental data for noncovalent systems is not straightforward because absolute temperature determination in molecular beam experiments is difficult. For low temperatures after expansion the information obtained from the PES (potential energy surface) could be used[358], however for temperature above 0 K the system will pass from the PES to the Gibbs free energy surface (FES).

6.3 Dry clusters

6.3.1 Adenine and 5-fluorouracil in dry molecular beams

The mass spectra of adenine and 5-fluorouracil seeded in two separate molecular beams presented in this section (**Fig. 6.1** and **Fig. 6.2**) are the only ones among monomolecular beams studied in the present project which show production of dimer ions in dry conditions. Expansion conditions leading to the appearance of cluster ions, as well as differences in the mass spectra are characterized.

No adenine cluster ions were detected in dry conditions with adenine temperatures <240°C (see section **5.2.2**). Indeed, the only mass spectra showing the production of adenine dimer ions (270 Th) in dry conditions were recorded at higher temperatures. **Fig. 6.1** shows our dry measurement with the maximum A_2^+ signal, achieved with an oven temperature of 262°C. It is worth noting that the ratio of the 136 Th / 135 Th integrated signal intensities is 38±3 % in **Fig. 6.1**. A percentage of 8 % is expected due to adenine isotopomers (consistent with Gador et al.'s[21] estimation, and Hu et al.'s[329] equation). In addition, the 136 Th peak is wider than the 135 Th peak: FWHM(135) = 11.3 ns; FWHM(136) = 23.9 ns. Therefore, **Fig. 6.1** provides evidence for significant production of protonated adenine ions associated with hydrogen or proton transfers. Kim et al.'s[17] 266 nm (4.66 eV) ns MPI data shows a major increase in the 136 Th / 135 Th ratio with the formation of pure adenine clusters. Therefore the high 136 Th / 135 Th ratio in **Fig. 6.1** is consistent with extensive laser-induced fragmentation of clusters in the supersonic jet.

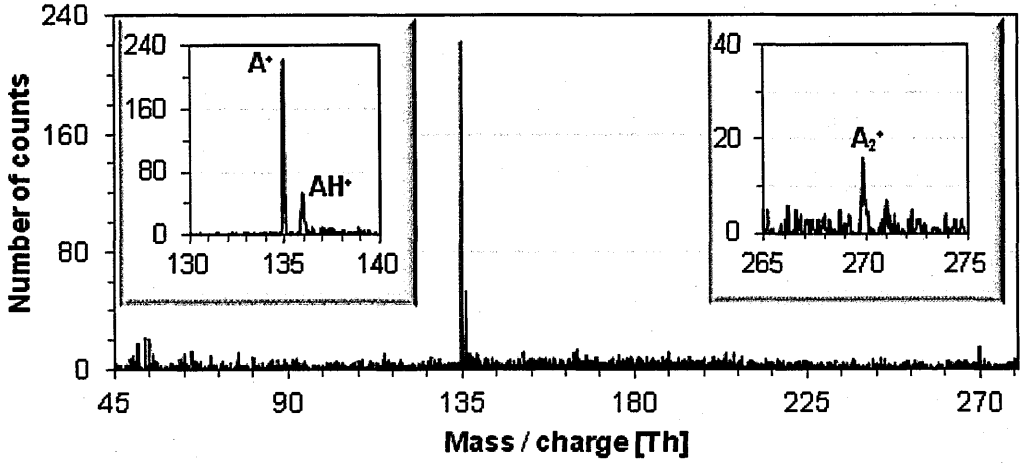

Fig. 6.1: One-colour (222 nm, ~ 4×10^6 W/cm^2) MPI mass spectrum of dry adenine (262°C, 2 bar argon).

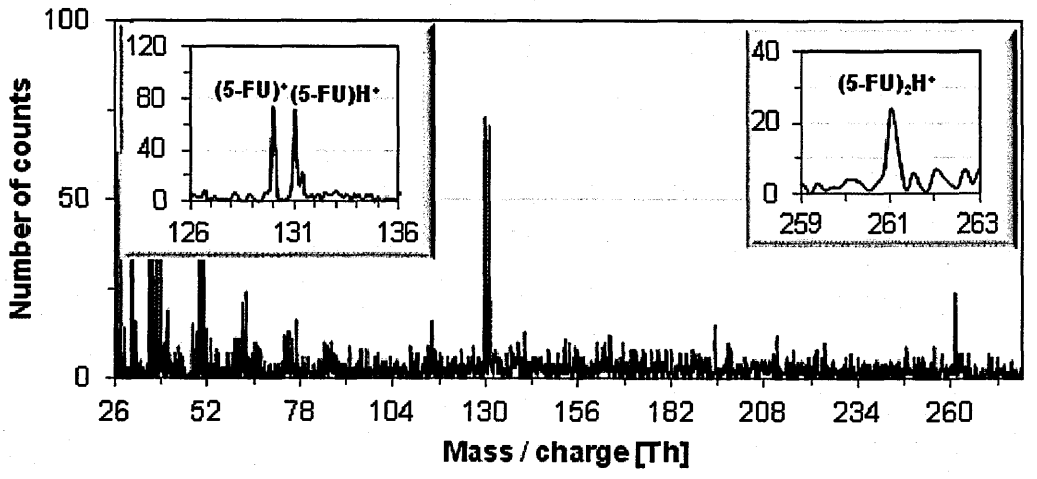

Fig. 6.2: One-colour (223.8 nm, ~ 6.7×10^7 W/cm^2) MPI mass spectrum of non-hydrated argon beam (0.5 bar) seeded with 5-fluorouracil at 250°C.

Fig. 6.2 shows the mass spectrum of 5-fluorouracil recorded at 223.8 nm. Differences in relative signal intensities between molecular ions (A^+, 5-FU^+) and cluster ion fragments (AH+, 5-FU-H+) in **Fig. 6.1** and **Fig. 6.2** can be noticed. In general, the intensities of detected ions and their fragments depend on the initial abundance of their neutral precursors in the molecular beam, as well as on their photophysical properties. In particular, excited states lifetimes have crucial impact on the ionization efficiency. The differences in mass spectra presented in these two figures are due to one or more of the following possible factors: (1) an intrinsic tendency for increased clustering of 5-FU than adenine in supersonic expansion conditions, (2) longer excited state lifetimes of 5-FU clusters in relation to the average length of time between successive photon absorption, and (3) more efficient hydrogen/proton transfer processes for molecular clusters of 5-FU. The possibility of processes described above is indicated by the observation that relative to monomer ion production, much higher levels of protonated monomer ions (clusters fragments) have been observed in the case of 5-FU despite lower pressure and temperature in the nozzle. In addition, the mass spectrum in **Fig. 6.2** has been recorded for significantly stronger laser pulse fluence than the mass spectrum in **Fig. 6.1**, tending to enhance photofragmentation of cluster ions, as well as molecular ions. **Fig. 6.2** shows clear protonated dimer $(5\text{-FU})_2H^+$ and protonated monomer $(5\text{-FU})H^+$ signals at 261 and 131 Th, respectively, indicating the creation of larger clusters with strong fragmentation

accompanied by proton or hydrogen transfers. No evidence for a signal at 260 Th (non-protonated 5-FU dimer ions) above the background level was observed. 5-FU exhibited the strongest signal for protonated monomer and dimer ions in relation to non-protonated monomers in dry conditions among all molecules investigated in this project. The integrated signal intensities percentage $(5\text{-FUH}^+)/(5\text{-FU}^+)$ is 92±13 %.

6.3.2 Adenine-thymine base pair ions

Fig. 6.3 and **Fig. 6.4** show mass spectra for argon beams seeded both with sublimated adenine and thymine (achieved by using a powder sample mixed by volume). The results show clear signals for cluster ions and their fragments. Protonated monomers of adenine and thymine are readily observable in the mass spectra, especially in the higher temperature (**Fig. 6.4**) measurement (with more clustering expected due to higher density of adenine and thymine molecules). Thymine monomers and protonated monomers (126 and 127 Th) have lower intensities than equivalent adenine peaks (135 and 136 Th). However relatively small signals of A_2^+ and AH^+ (270, 271 Th) are observed compared with T_2^+, T_2H^+, AT^+, and ATH^+ (252, 253, 261, 262 Th) – see **Fig. 6.3** and **Fig. 6.4**.

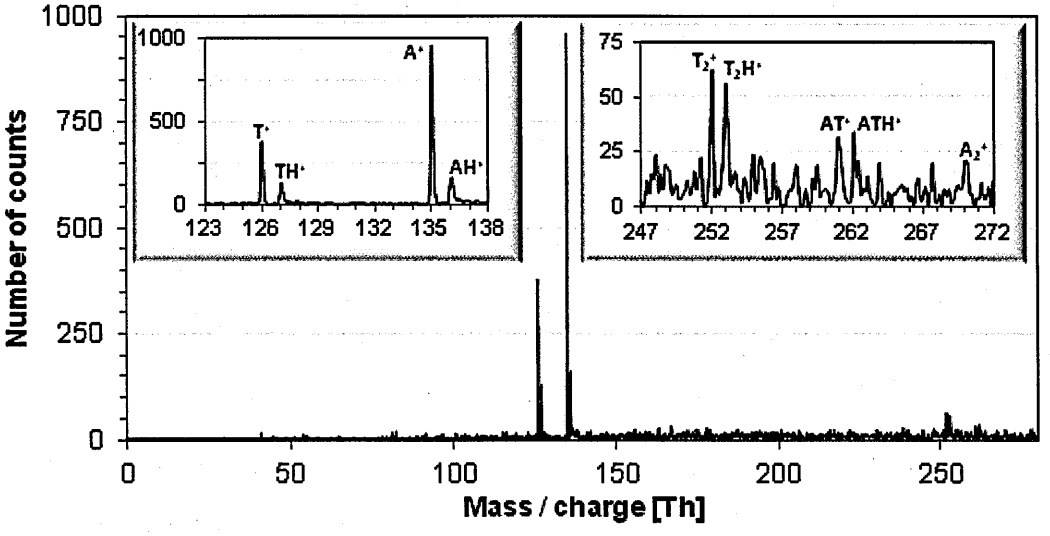

Fig. 6.3: One-colour (225nm, ~ 2.5×10^6 W/cm^2) MPI mass spectrum of non-hydrated adenine-thymine system (250°C, 1.2 bar argon).

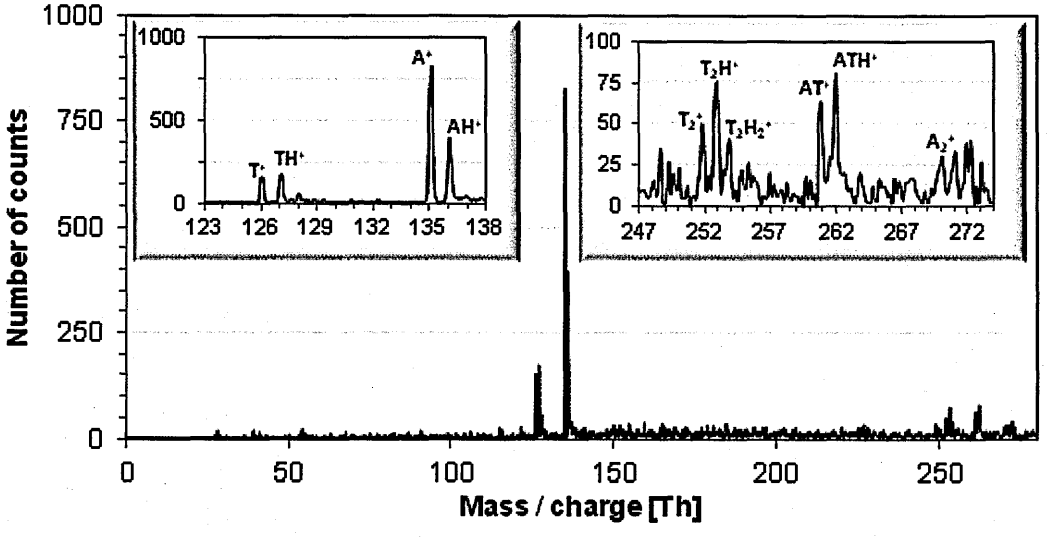

Fig. 6.4: One-colour (225nm, ~ 5×10^6 W/cm^2) MPI mass spectrum of non-hydrated adenine-thymine system (265°C, 1.2 bar argon).

In general, the production of cluster ions is lower than that of monomer ions, however the abundance of cluster fragments (protonated monomers) is significant; i.e. $TH^+/T^+ = 88 \pm 7$ %, $AH^+/A^+ = 51 \pm 2$ % in **Fig. 6.3** and $TH^+/T^+ = 50 \pm 4$ %, $AH^+/A^+ = 26 \pm 2$ % in **Fig. 6.4**.

The experimental data shown in **Fig. 6.3** and **Fig. 6.4** indicate the presence of protonated dimers T_2H^+, ATH^+. These are fragments of larger clusters of potentially long-lived excited states. The weakness of adenine dimer ion signals compared with the T_2^+ and mixed AT^+ signals can be caused by generally longer excited states lifetimes expected for clusters containing the thymine chromophore leading to their more efficient MPI in the nanosecond regime. Indeed in the present range of expansion (pressures and temperatures) and laser conditions, only extremely weak signals for adenine dimers and larger cluster ions in non-hydrated adenine-argon molecular beams have been observed (maximum in **Fig. 6.1**).

Adenine-thymine base pairs have been detected previously in nanosecond MPI experiments. One-colour resonant two-photon ionization (R2PI) spectroscopy measurements were carried out by Plutzer et al.[359] on free jets of thermally evaporated adenine and thymine under favourable conditions for the formation of small clusters in the reddest band (35064 cm^{-1}, 4.35 eV), below the $^1\pi\pi^*$ origin of gas-phase 9-H adenine (36105 cm^{-1}, 4.48 eV). Whereas Plutzer et al.'s[359] laser wavelength conditions created electronically excited base pairs with minimum excess of vibrational energy, the present

measurements at 225 nm (5.51 eV) accessed higher vibronic states. Furthermore, the red shift of at least 0.13 eV of the adenine bright $^1\pi\pi^*$ origin due to base pair formation increases the amount of vibrational excitation, assuming that adenine is the radiation chromophore. Indeed, excitation to high vibrational levels of the lowest bright $^1\pi\pi^*$ state is expected to lead to significant fragmentation of clusters.

Samoylova et al. studied ultrafast relaxation following 267 nm photoexcition of adenine–thymine pairs[331] with femtosecond laser pulses. An identical pump wavelength of 267 nm, but different probe wavelengths of 800 nm or 400 nm were used. These measurements with different laser ionization schemes showed different excited states dynamics in terms of the relative strength of signal contributions with different time constants τ_1, τ_2, τ_3, and τ_4, whereas the short-time constants $\tau_1^{(AH+,\ TH+)}$=0.1 ps and $\tau_2^{(AH+)}$ = 1 ps and $\tau_2^{(TH+)}$ = 7 ps were more pronounced at 800 nm, significantly larger contributions with $\tau_3^{(TH+)}$= 37 and $\tau_3^{(AH+)}$ = 50 ps and $\tau_4^{(TH+)}$ > 1ns were observed for the probe wavelength of 400 nm[331]. It has been concluded that the relative strength of signal contributions with different time constants depends on the probe wavelength. Long time constants (>1 ns) have been observed for the fragments of clusters: A^+, T^+, AH^+ and TH^+, which proves that excited states lifetimes in adenine-thymine clusters may support efficient nanosecond multiphoton ionization. Intramolecular processes dominate on the short fs-ps time scale, whereas further signal contributions with large time constants (> 1 ns) have been assigned to long-lived states in the thymine chromophore or to residuals stemming from larger cluster fragmentation.

6.3.3 Adenine-uracil base pair ions

Non-hydrated and hydrated mixed adenine-uracil clusters have also been observed in the present experiments. No previous reports on these particular mixed cluster ions detected in multiphoton ionization experiments are found in the literature. The adenine-uracil system in non-hydrated conditions is presented in **Fig. 6.5**. It is demonstrated that for adenine and uracil powders mixed in the oven, 135 Th ions are detected with significantly higher intensity than 112 Th ions. Adenine ions are detected at the highest rate among molecules studied in the present experiments. Comparing integrated signal intensities in **Fig. 6.3** and

Fig. 6.5 (T^+/A^+ = 39±2 % and U^+/A^+ = 3.2±0.3 %), indicates that thymine and uracil are the next in order, respectively.

A_2^+ and UA^+ dimer ions are present in the mass spectrum; however U_2^+ ions have not been detected. Similar effects have been observed in hydrated conditions (**Fig. 6.26**), where U_2^+ and its hydrates have been detected with very low intensity in relation to clusters containing adenine molecules. In contrast to mixed adenine-thymine base pairs where $A_2^+ < AT^+$ (or T_2^+), A_2^+ is detected with higher intensity than the mixed $(A\text{-}U)^+$ base pair.

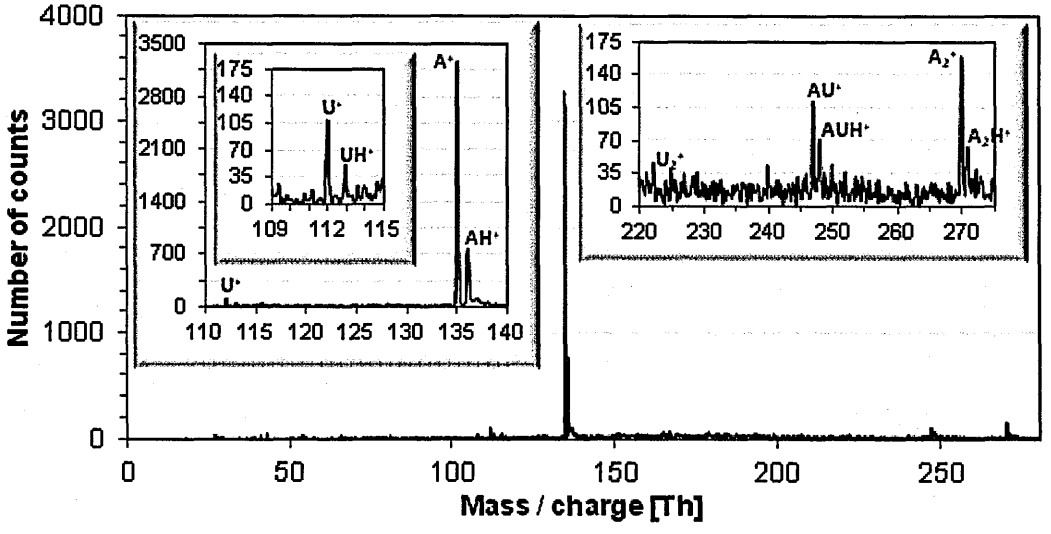

Fig. 6.5: One-colour (224 nm, ~ 3.0×10^6 W/cm^2) MPI mass spectrum of non-hydrated uracil-adenine system (290°C, 1.0 bar argon).

High temperatures were required in order to produce a non-negligible amount of cluster ions, however it also enhances a danger of thermally driven decomposition in the nozzle.

It is interesting to note that in **Fig. 6.5** the monomer ion U^+ and the dimer ion AU^+ have been detected at similar levels where AU^+/U^+ ratio is equal to 1.3±0.2 compared to A_2^+/A^+ signal ratio equal to 0.08±0.01. These data indicate that a significant contribution in the total uracil signal (clustered and isolated) comes from adenine-uracil clusters and can be rationalized by much more efficient MPI attributed to the presence of adenine, which leads to the production of $(A_nU_m)^+$ cluster ions. The U^+ signal in **Fig. 6.5** is 31±3 times lower than A^+, while the AU^+/A_2^+ ratio is 0.6±0.1. U_n^+ (n>1) signals are indistinguishable from the background signal. A potential impact of uracil vapour pressure discriminating the U^+/A^+ signal ratio seems to be unlikely since higher values of vapour pressures are reported in

the literature for uracil[206, 360]. Another factor is possible preferential clustering with adenine removing neutral U_n contributions from a molecular beam.

It is interesting to compare these results with those of Lubman and Tembreull showing no signal for uracil and thymine, but clear signals for adenine in their MPI experiments at 222 nm. Lubman and Tembreull[327] applied a different method to bring adenine, thymine and uracil molecules into the gas phase, i.e. laser desorption, and did not manage to get measurable signal levels for uracil and thymine at 222 nm. In the present MPI experiments on mixed systems thymine (T^+) and uracil (U^+) signals are lower than adenine (A^+).

6.3.4 Dry clusters - results discussion

Low signal levels of dimer and larger cluster ions (compared to monomer ions), were observed in the present dry experimental conditions. The production of cluster ions depends on sublimated nucleobases partial pressures, which are a function of temperature. Indeed, increased temperatures (≥ 250 °C) were used in order to observe non-negligible cluster ion peaks in mass spectra. This observation agrees with the tendency reported for cytosine dimers by Kostko et al.[361] in single photon ionization experiments. Desorption temperatures of around 310 °C (cytosine vapour pressure is lower than that of adenine, thymine and uracil) was applied in their experiment in order to produce sufficient vapour pressure of cytosine to induce clustering in the molecular beam. Only 3 % cluster contribution (dimer + protonated monomer) was observed around 550 K (277 °C), compared with 41% at 640 K (367 °C). In order to avoid the products of thermal fragmentation significantly contaminating the molecular beam source, temperatures applied in this work were kept below 300°C.

Cluster formation can be also enhanced by conical nozzle shapes[33]. However the shape of the nozzle applied in the present research has not been adapted for the production of large molecular clusters. Further enhancements of cluster abundance in molecular beams can be obtained due to increased argon buffer gas pressure.

MPI measurements of mixed clusters (adenine-thymine and adenine-uracil) presented in this section show differences in monomer and cluster ions intensities. The order of

monomer ions intensities is $A^+ > T^+ > U^+$. In principle these differences could be attributed to vapour pressures, gas transport in the nozzle, and/or the efficiency of multiphoton ionization process. The lowest signal levels have been observed for uracil (U^+), despite the literature[206, 360] indicating that uracil has the lowest sublimation enthalpy. This suggests a much higher MPI efficiency of adenine (A^+). Comparison with thymine (T^+) is not so straightforward and conclusive, since the literature[206, 360] is not consistent about relative differences in adenine and thymine sublimation enthalpies. Moreover, differences in signal intensities for adenine and thymine are not as significant as in the case of adenine-uracil system.

MPI measurements of mixed clusters can be a tool for comparative studies on relative photoionization efficiency. These comparisons give direct information on the efficiency of the MPI process and open an indirect window to interpretations based on theoretical simulations of excited states dynamics, as long as potential signal differences related to vapour pressures and the effectiveness of gas transport in the nozzle are taken into account. Application of a second ionization method, like femtosecond MPI or EI (electron impact) ionization could verify the present results. Independent measurements of the total mass flow through the nozzle for different molecules in identical conditions of temperature and pressure would verify factors related to vapour pressures and gas transport.

The MPI efficiency can be a crucial factor in shaping mass spectra. It should be noted that the absence (or weakness) of any signal for dry adenine cluster ions in our measurements does not necessarily indicate that the production of dry neutral adenine clusters is not significant in the supersonic jets probed. In a series of 193 nm (6.42 eV) nanosecond MPI mass spectrometry experiments on pyrrole clusters with various size distributions, only monomer ions have been observed[362]. Poterya et al.[362] reported that ionization by two or more successively absorbed photons (193 nm, 25 ns, 10^9 W/cm^2) leads to a higher degree of dissociative ionization than electron impact ionization (even with 70 eV energy) for pyrrole, imidazole and pyrazole hydrogen-bonded molecular clusters[362]. This indicates the difficulty in assessing the presence of complexes in a supersonic jet by nanosecond MPI mass spectrometry alone. Indeed the mass spectrum is often dominated by the

fragmentation of larger complexes. In the present experimental conditions clustering has been deduced on the basis of protonated species intensity: cluster fragments in the form of protonated monomers are readily observed in the mass spectra. However it was not possible to assess the effects of neutral dissociation in the excited state.

The measurements carried out on fluorinated uracil (5-FU) indicated non-negligibly level of clustering in dry conditions at relatively low argon backing pressure. 5-FU appears to be a good candidate for cluster studies in dry conditions, since it exhibits high, stable cluster signal at relatively low temperature.

6.4 Hydrated clusters

6.4.1 Hydrated adenine

Water vapour has been added to the gaseous mixture of sublimated nucleic acid bases and argon in order to produce hydrated clusters in the supersonic expansion. Significant production of adenine dimer ions (A_2^+, 270 Th) can be obtained in hydrated conditions (**Fig. 6.6**). In addition, protonated monomers (AH^+) and dimers (A_2H^+) were detected. The presence of A_2H^+ in the mass spectrum indicates that larger (A_n^+, n>2) neutral clusters of adenine are produced in the expansion. The signal percentage A_2H^+/ A_2^+ is 27±4 %, while 17.4 % is expected due to isotopomers. The negligible signal of adenine-water clusters is the characteristic feature of that molecular beam, determined by the expansion conditions (temperature and partial pressures) of the gaseous mixture. It shows that the addition of water vapour does not always lead to the production of hydrated cluster ions.

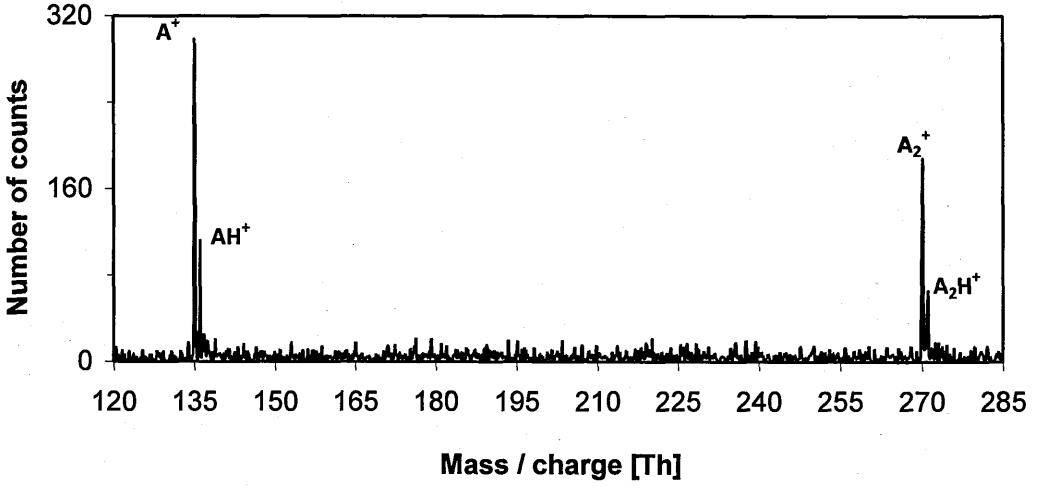

Fig. 6.6: One-colour (224 nm, ~ 2.5×10^6 W/cm^2) MPI mass spectrum of hydrated adenine (252°C, 0.8 bar argon, water reservoir at 70°C).

Fig. 6.7 shows more extensive production of hydrated cluster ions in modified expansion conditions (increased adenine temperature and argon pressure), while it should also be noted that the laser fluence is slightly lower than in **Fig. 6.6**.

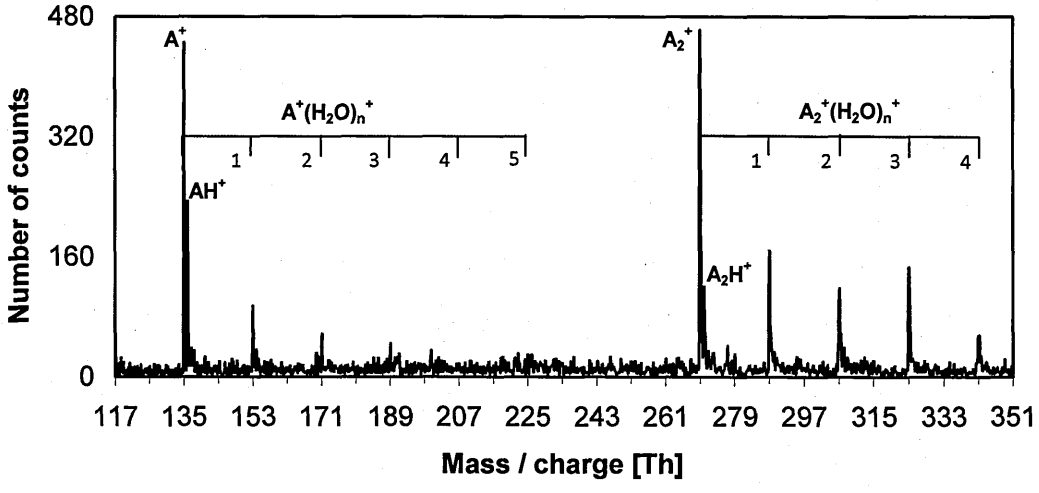

Fig. 6.7: One-colour (224 nm, ~ 1.5×10^6 W/cm^2) MPI mass spectrum of hydrated adenine (260°C, 1 bar argon, water 70°C).

Unlike **Fig. 6.7**, Kim et al.[363] and Nam et al.[228] reported ns MPI mass spectra at 220 and 230 nm showing $A(H_2O)_n^+$ production to be generally similar to the $A_2(H_2O)_n^+$ intensity. It has been found that the relative intensity of $A(H_2O)_n^+$ and $A_2(H_2O)_n^+$ ions varied according to the supersonic jet and laser fluence conditions.

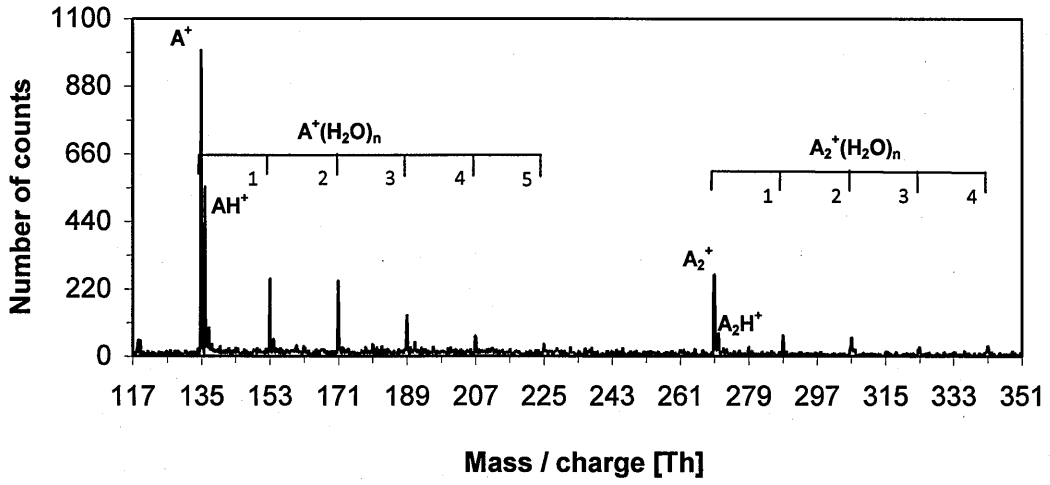

Fig. 6.8: One-colour (224 nm, ~ 2×10^7 W/cm^2) MPI mass spectrum of hydrated adenine (adenine 220-240°C, 1.4 bar argon, water up to 120°C).

Previously, the characteristic adenine-water cluster size distribution with $A_2(H_2O)_n^+$ production greater than $A_1(H_2O)_1^+$ observed for longer wavelengths (λ > 260 nm) was discussed in terms of MPI deficiency caused by dissociation of hydrated adenine monomers in the excited state. Kang et al.[19] have suggested that the adenine-water hydrogen bond is dissociated on the repulsive part of the potential energy surface for the $^1n\pi^*$ state of adenine. A similar phenomenon has been proposed for caffeine[316]. The following mechanism has been given as an explanation: the highly allowed $^1\pi\pi^*$ transition initially populates the $^1\pi\pi^*$ state but a fast internal conversion from the $^1\pi\pi^*$ state to the $^1n\pi^*$ state leads to subsequent fragmentation[363]. The failure of molecular beam experiments to observe pyrazine-water complexes has also been explained in terms of short-lived clusters[364].

However, it has been found that the $A_2(H_2O)_1^+ > A_1(H_2O)_1^+$ effect does not occur for shorter wavelengths. Similar ion intensities of $A_1^+(H_2O)_n$ and $A_2^+(H_2O)_n$ have been found in the range 210-230 nm (5.90-5.39 eV)[363], while for higher excitation energy (7eV) the intensity of $A_1^+(H_2O)_n$ ions became even larger than the intensity of $A_2^+(H_2O)_n$[363]. It is demonstrated in the present studies that $A_2(H_2O)_1^+ > A_1(H_2O)_1^+$ can be obtained for the excitation wavelength of 224 nm (**Fig. 6.7**) by the optimization of expansion conditions favouring the production of large hydrated adenine clusters and applying lower laser fluences than in other mass spectra presented in this chapter (**Fig. 6.8 - Fig. 6.10**).

The present data set for hydrated monomer ions consistently shows strong $A(H_2O)_n^+$ peaks at n = 1 and 2 followed by weaker peaks at n = 3 and 4, while signals for ions with n>4 are either absent or extremely weak (**Fig. 6.8**, **Fig. 6.9**, **Fig. 6.10**). This may be interpreted as being broadly consistent with a closed shell structure at n = 4, as proposed by Kim et al.[17].

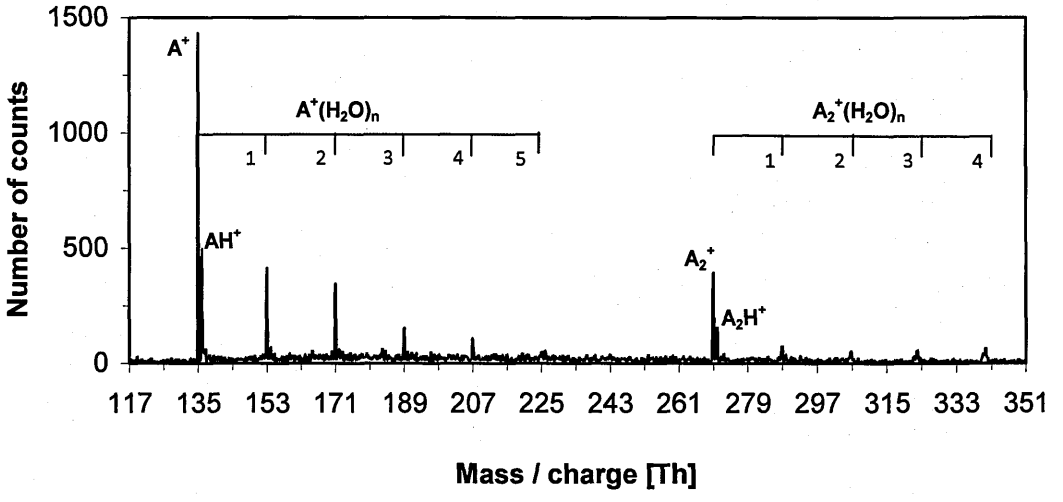

Fig. 6.9: One-colour (223.8 nm, ~ 4.3×10^7 W/cm^2) MPI mass spectrum of hydrated adenine (adenine 250°C, 1.3 bar argon, water 110°C).

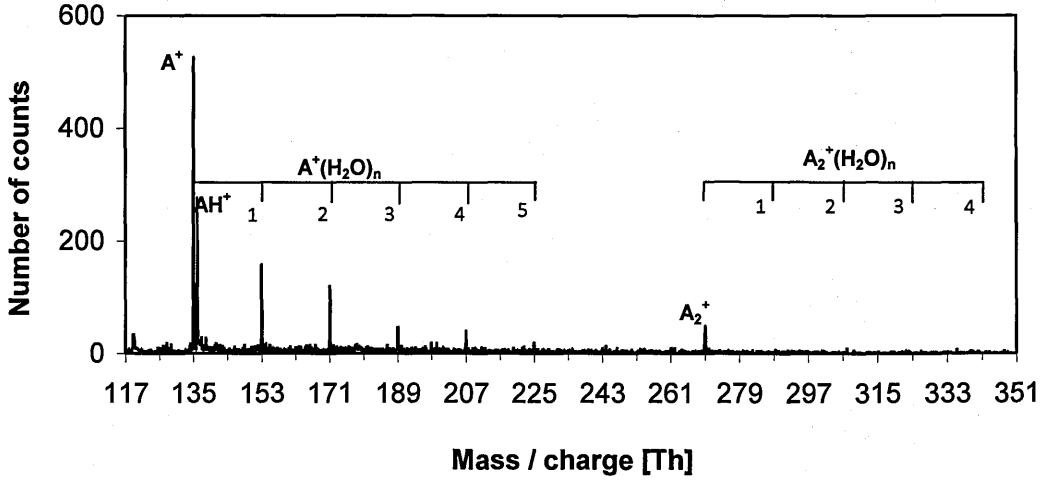

Fig. 6.10: One-colour (224 nm, ~ 4.4×10^6 W/cm^2) MPI mass spectrum of hydrated adenine (235°C, 1.0 bar argon, water up to 90°C).

Kim et al.[17] carried out resonant 2-photon ionization (R2PI at 266 and 277 nm) experiments on pure and hydrated adenine clusters. By monitoring the tendency of $A_1(H_2O)_n^+$ ($n\leq7$) to give up a single solvent molecule in metastable decay, a clear gradual increase in H_2O loss / n was observed at $n\geq5$. The authors interpreted this result as suggesting a closed shell of 4 water molecules around A^+, in contrast to the tendency of

H_2O to accumulate in a *globule* at one site on neutral adenine[104, 365]. Further interpretation can be based on favourable hydration sites of adenine calculated by Kim et al.[104]. They performed ab initio calculations for exploring hydration patterns of adenine using density functional theory – see **6.4.1.1**.

The largest clusters of adenine in hydrated conditions are presented in **Fig. 6.11**. Cluster ions with the maximum number of water molecules attached to adenine dimers equal to 7 have been detected. Weak adenine trimer ions at m/z = 405 Th have been also observed. A suppression of adenine signal upon addition of water vapour to the cluster source has been observed and presented in **Fig. 6.12**.

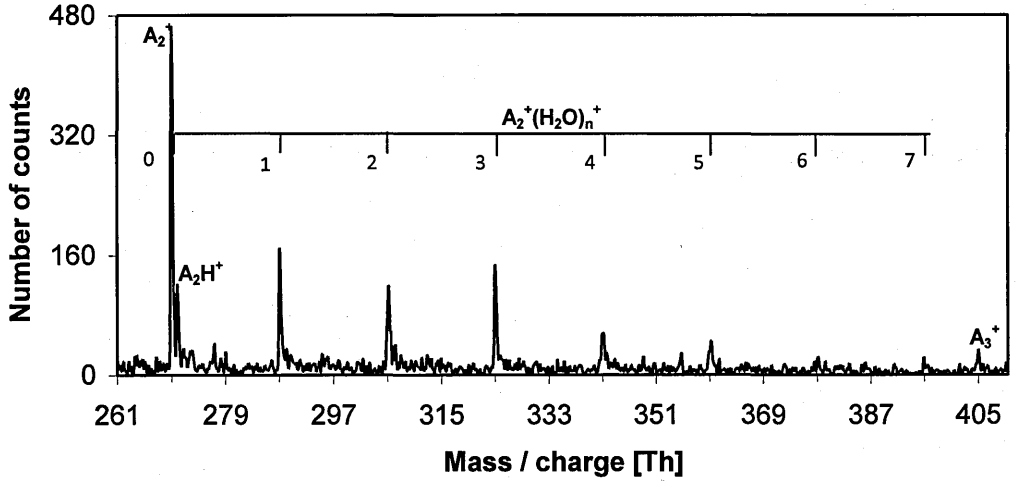

Fig. 6.11: One-colour (224 nm, ~ 1.5×10^6 W/cm^2) MPI mass spectrum of hydrated adenine (adenine 260°C, 1.0 bar argon, water 70°C).

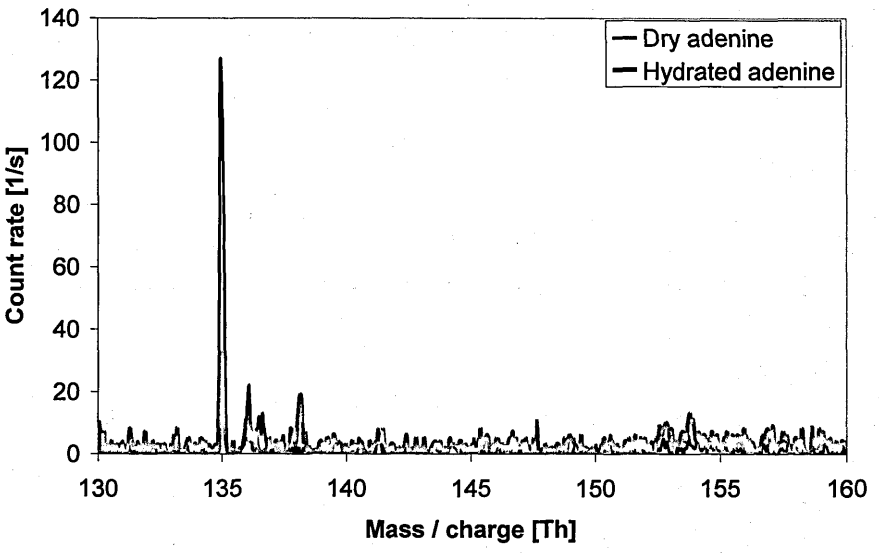

Fig. 6.12: Suppression of adenine signal upon hydration at 238±1°C; 1.5 bar; laser pulse energies: dry - 139 µJ, hydrated - 130 µJ, water temperature 100°C for the hydrated mass spectrum (red line).

6.4.1.1 Adenine-water neutral cluster configurations

Kim et al.[104] performed ab inito calculations of adenine hydration patterns. His results presented in this subsection provide a structural description of the most energetically stable adenine-water clusters.

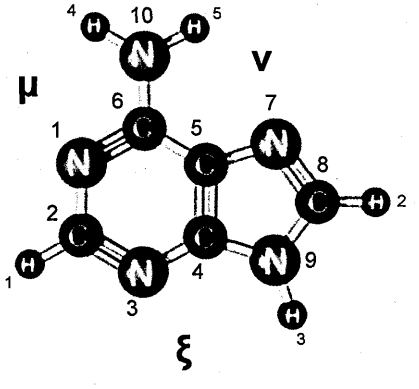

Fig. 6.13: Ground-state geometry of the planar amine tautomer $A_{am}N(9)H$, the most stable form of gas-phase adenine[136]. Following Park et al.'s[163] scheme, the three major sites for hydrogen bonding are labeled µ, v, and ξ.

It can be expected that these clusters are also produced in the present experiments, however direct structural information cannot be obtained from the present results.

The DFT optimization of cluster geometries revealed that the $A(H_2O)_{1-2}$ clusters have planar geometries, while structures of $A(H_2O)_{3-4}$ complexes are mixed with planar and non-planar geometries. These calculations showed that the ξ site is the most energetically favorable binding site in the single water hydration step of adenine, however the stabilization energy of adenine-$(H_2O)_1$ at the μ site is almost the same as the stabilization energy of ξ site, the difference in stabilization energies is equal to 0.2 kcal/mol (~ 0.009 eV). The most stable complex of adenine and two water molecules is that with the single cooperative ξ binding site A-$(H_2O)_2$- ξ2, the complex with separate binding sites A-$(H_2O)_2$- ξμ is less stable. The planar geometry is broken when adenine binds three water molecules at a single hydration site. For water accumulation at a single cooperative binding site, the complex of adenine with three water molecules at the ξ site is the most stable A-$(H_2O)_3$ configuration. However the complex with separated binding sites A-(H_2O)- ξ2μ1 is more stable; this complex also maintains the planar geometry. In the case of adenine and four water molecules, the most stable complex is $A(H_2O)_4$- ξ3μ1 with separate binding sites, however the stabilization energy differences between that complex and ξ2v1μ1 or ξ4 square-shaped structure are negligible.

These structural calculations imply that $A_1(H_2O)_1^+$ and $A_1(H_2O)_2^+$ detected in the present experiments are those with one or two water molecules attached to ξ binding site, while for $A_1(H_2O)_3^+$ and $A_1(H_2O)_4^+$ multiple binding sites are populated with at least two water molecules attached to the most favourable ξ site. However it is very important to note that the cluster size distribution obtained in the mass spectrum does not match the original cluster size distribution of neutral molecular clusters, indeed significant fragmentation can be expected in the ns-timescale MPI process. Also structural shape of ionic complexes may not necessary be ideally correlated with the most stable neutral structures. The results of Kim[104] are important in the discussion of the MPI pathway of adenine-water clusters – see section **6.7.1**.

6.4.2 Hydrated thymine

Fig. 6.14 shows an MPI mass spectrum of thymine in a quite weakly hydrated argon beam. The mass spectrum is similar to adenine in **Fig. 6.6**. Thymine cluster ions are observed

(dimer ions and protonated dimer ions at 252 and 253 Th, respectively) as well as the protonated monomer at 127 Th, whereas hydrated thymine ($T(H_2O)_1^+$) at m/z = 144 Th and further peaks in the hydrated cluster series (162, 180, 198, 216, 234 Th) have not been registered. **Fig. 6.15** and **Fig. 6.16** show MPI mass spectra for hydrated thymine with extensive clustering. Unfortunately, as the mass of seven water molecules is identical to that of thymine, $T_m(H_2O)_n^+$ cannot be distinguish from $T_{m+1}(H_2O)_{n-7}$ ($n \geq 7$). Hence the maximum size of $T(H_2O)_n^+$ cannot be determined. Notwithstanding this inherent ambiguity, the strong signal at 252 Th compared to the peak on its left (234 Th assigned to $T(H_2O)_6^+$) in **Fig. 6.15** and **Fig. 6.16** suggests a significant contribution of T_2^+ ions. This is consistent with Kim et al.[17] measurements using D_2O as a solvent in order to clearly distinguish $T_m(D_2O)_n^+$ from $T_{m+1}(D_2O)_{n-7}$ ($n \geq 7$).

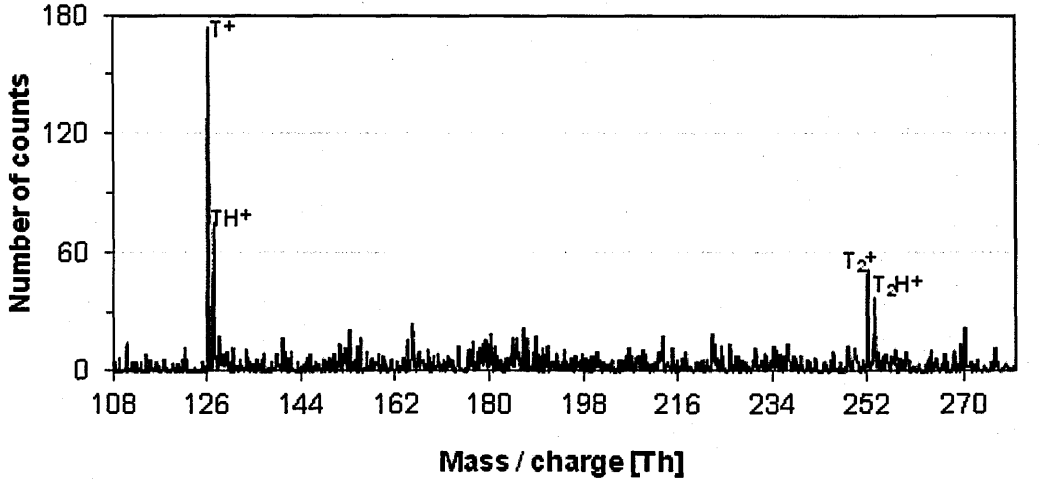

Fig. 6.14: One-colour (226 nm, ~ 7.4×10^5 W/cm^2) MPI mass spectrum of hydrated thymine (high temp > 220°C, 0.8 bar argon, water 20°C).

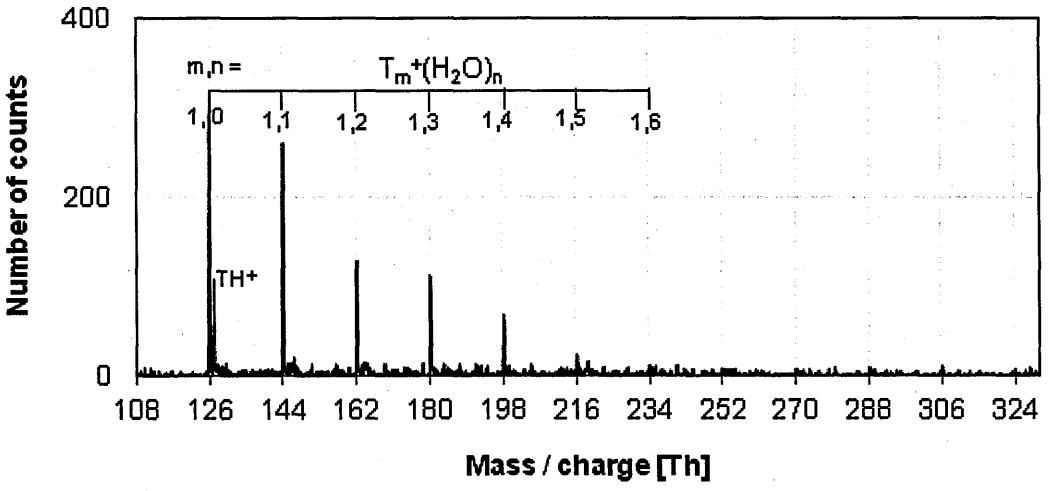

Fig. 6.15: One-colour (226 nm, ~ 9.1×10^6 W/cm^2) MPI mass spectrum of hydrated thymine (230°C, 1.8 bar argon, water 90°C).

In the strongest clustering conditions (**Fig. 6.16**), the cluster ions of $T^+(H_2O)_3$ and $T^+(H_2O)_4$ dominate among other hydrates. The stability of these cluster ions has been confirmed later for mixed adenine-thymine hydrated system (see section **6.4.4**).

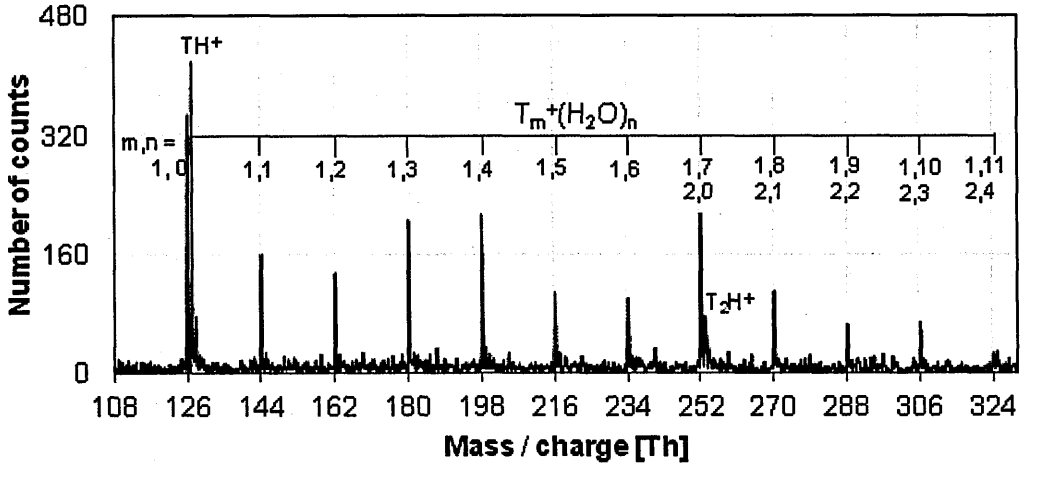

Fig. 6.16: One-colour (225 nm, ~ 1.9×10^7 W/cm^2) MPI mass spectrum of hydrated thymine (222°C, 1.7 bar argon, water 70°C).

Hydrated thymine clusters size distributions obtained in the present project can be compared with the results of Busker et al.[366] for hydrated clusters of 1-methylthymine and 1-methyluracil with ns laser pulse excitation at 273.2 nm, ionization at 193 nm, and 40 ns delay between the excitation and ionization. Busker et al.[366] observed the cluster ion intensities decreasing smoothly with increasing cluster size, which was rationalized by a

higher number of collisions being required to form larger clusters (i.e. the cluster ion distribution reflecting the neutral cluster distribution with no evidence for particularly stable configurations). By contrast, a sharp drop of the ion-signal intensities for clusters with more than four water molecules has been observed by He et al.[336] in one-colour ns REMPI mass spectra of hydrated thymine clusters obtained at the excitation wavelengths of 229 nm. In addition to the sharp drop of the ion-signal intensities for clusters with more than four water molecules He at al.[336] showed intensities in the following order (from the highest to the lowest): $T(H_2O)_2^+$, $T(H_2O)_3^+$, $T(H_2O)_1^+$, $T(H_2O)_4^+$. The present results in **Fig. 6.16** resemble He et al.'s results, while the results in **Fig. 6.15** resemble Busker et al's. This can be due to the fact that in strongly clustering collisions caused by higher concentration of water vapour, cluster formation is not so significantly limited by the available number of collisions (due to the excessive availability of water molecules), and energetic preferences start to play a more important role. In addition He et al.[336] observed dramatic loss of thymine-water cluster ions signal for absorption at 268 nm and attributed this phenomenon to signal loss during excitation or ionization, without proposing specific pathways. Kim et al.[17] have carried out 266 nm ns MPI experiments in which the mass spectra of hydrated thymine cluster ions is characterized by relatively weak $T(H_2O)_n^+$ signals in relation to the monomer T^+ signal. This is a likely consequence of MPI processes in hydrated DNA bases, the detailed pathways for hydrated monomers irradiated by 220 - 230 nm laser pulses are proposed and discussed in section **6.7**.

6.4.2.1 Thymine-water neutral cluster configurations

Kim et al.[367] calculated hydration patterns of thymine using B3LYP density functional. In the most stable structure of the thymine monohydrate, the water molecule forms a cyclic hydrogen bond (i.e., involving two hydrogen bonds) with thymine via the H1 and O2 atoms (see **Fig. 6.17**). In the most stable thymine dihydrate, two water molecules form a cyclic hydrogen bond via H1 and O2. The intermolecular hydrogen bonds between thymine and water molecules are stronger for that structure than for thymine monohydrate mentioned above. The formation of a cyclic hydrogen bond involving two water molecules is energetically more favourable than the formation of two cyclic hydrogen bonds involving one water molecule.

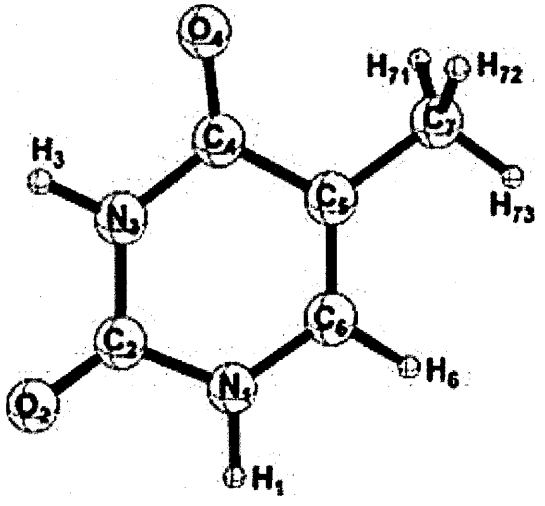

Fig. 6.17: Numbering scheme for the canonical structure of thymine[367].

Considering the relative energies of the monohydrates, the most favourable binding site is the space between the H1 and O2 atoms, after this site is occupied with up to two water molecules, further hydration is expected at the next favourable site, which is between H3 and O4. So the most stable tri- and tetrahydrates correspond to structures in which one and two water molecules bind to the most stable dihydrate at the H3O4 site. In the most stable thymine pentahydrate, the fifth water molecule is attached between the H3 and O2 atoms[367]. For larger systems the hydration shell formation of thymine and uracil in complexes comprising 11 water molecules was studied theoretically at the B3LYP/6-31G(d), B3LYP/6-31+G(d) and MP2/6-31G(d)[368] levels. Structures showing a clustering of the water molecules were found to be preferred over structures with water distributed around thymine/uracil due to increased attractive interaction between the water molecules in the clustered complexes.

The results of the structural analysis presented above indicate that in the most stable hydrated clusters, water molecules attached to thymine create bridges between its respective H1 and O2, as well as between H3 and O4 atoms. This is a crucial condition for the excited state tautomerization, i.e. hydrogen atom transfer from N1 to O2 or from N3 to O4 via the water chain connecting respective atoms. This mechanism is proposed as playing a dominant role in MPI of hydrated thymine monomers in section **6.7**.

6.4.3 Hydrated uracil

Whereas previous one-colour nanosecond MPI experiments on dry uracil produced negligible signals (summarized in section **5.4.1**), monomer ions have been observed successfully in the present project. Moreover, the present experiments provide the first MPI mass spectra of uracil-water clusters. Various theoretical studies have been carried out on uracil-water clusters[368-374], however experimental studies are scarce. Methylated molecule (uracil) has been used[335, 366] as the model system to study photoionization dynamics of that RNA base without a clear motivation being given. Rare examples of studies on uracil and uracil-water complexes in supersonic beams can be mentioned, i.e. large non-hydrated uracil cluster ions produced in MPI experiment[189] (see also **Fig. 4.6** in section **4.5**), and uracil-water clusters in electron impact ionization experiments[18].

Fig. 6.18 and **Fig. 6.19** show MPI mass spectra for hydrated uracil complexes produced in different supersonic beam conditions. The cluster ion size distribution depends strongly on the density of water and uracil vapour flowing through the nozzle. Hydrated uracil monomers $U^+(H_2O)_n$ and cluster fragments UH^+, UH_2^+ dominate in both mass spectra. $U^+(H_2O)_n$ cluster ion intensities decreasing smoothly with increasing cluster size can be observed in **Fig. 6.18**, while $U^+(H_2O)_2$ and $U^+(H_2O)_3$ dominate in **Fig. 6.19**. Similar effects related to cluster size distribution have been observed in the present work for thymine hydrates (**6.4.2**).

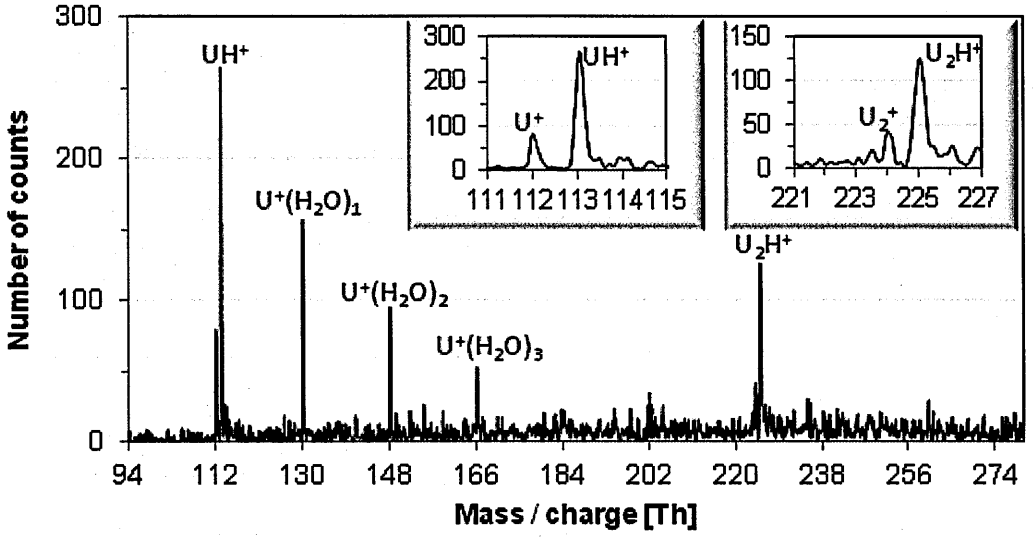

Fig. 6.18: One-colour (224 nm, ~1.3×10^6 W/cm^2) MPI mass spectrum of hydrated uracil (260°C, 1.0 bar argon, water 90°C).

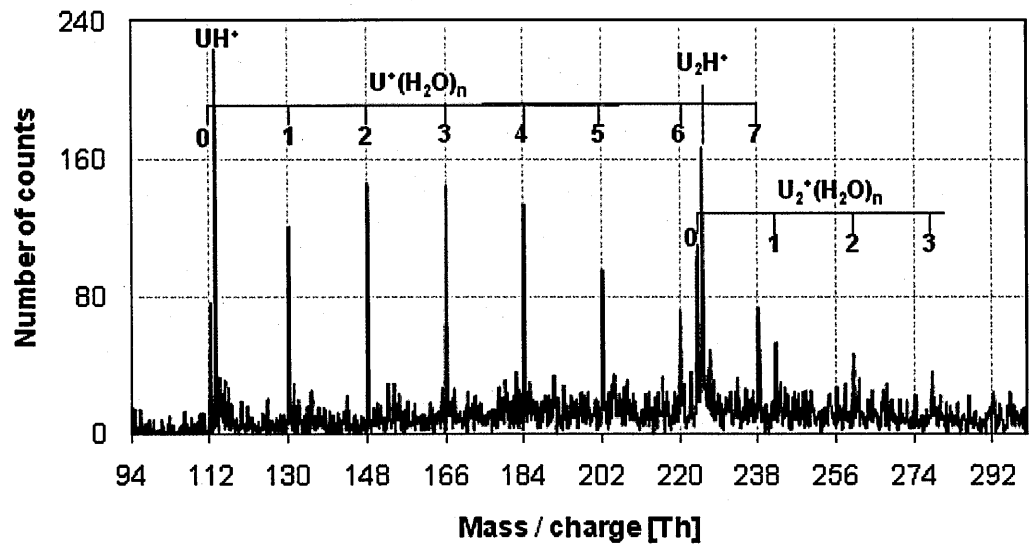

Fig. 6.19: One-colour (222 nm, ~ 2.0×10^6 W/cm^2) MPI mass spectrum of hydrated uracil (250°C, 1.1 bar argon, water 90°C).

The present results confirm strong nucleation in the argon supersonic expansion seeded with uracil and water vapour. The uracil monomer ion signal at 112 Th is relatively weak; moreover it is likely that U^+ ions are fragments of larger complexes. Relatively strong signals for protonated monomers (113 Th) and protonated dimers (225 Th) indicate extensive fragmentation of larger cluster ions (**Fig. 6.18**). The results presented in **Fig.**

6.19 show significant production of $U^+(H_2O)_7$ (238 Th) but no clear evidence for larger uracil monomer hydrates.

It is interesting to consider the present experiments in the context of IR cavity ringdown laser absorption spectroscopy (CRDS) results[105], where uracil and water clusters have been produced using a pulsed slit molecular beam source heated to 210-220 °C with an He carrier gas backing pressure of 50-60 psi (3-4 bar). Large red shifts in uracil OH bond stretching were observed for uracil-water clusters, providing evidence supporting the strong hydrogen bonds formed between these molecules predicted in ab initio calculations[105]. Spectra in the NH stretching region indicated the presence of several doubly H-bonded isomers of uracil, but no singly H-bonded species were observed[105].

6.4.3.1 Uracil-water neutral cluster configurations

Structures of neutral hydrated uracil clusters have been calculated by Bachrach et al.[375]. There are four regions where uracil can attach a water molecule. Region A is located between the N1-H as a proton acceptor and oxygen on C2 (O2) as proton acceptor, regions B and C offer the N3-H as a proton donor and either O2 (region B) or the oxygen on C4 (O4) as proton acceptor.

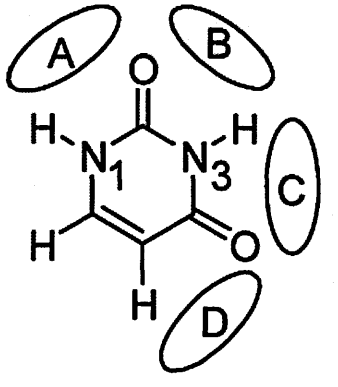

Fig. 6.20: Water binding regions of uracil[375].

Region D is likely to be the least favourable location for a water molecule to bind; while O4 is a suitable proton acceptor, the C5-H is a much weaker proton donor than an N-H group. All the computational studies indicate that the arrangement of uracil monohydrate is a water molecule placed in region A hydrogen bonded to N1-H and O2 atom[375]. The two lowest energy configurations of the uracil dihydrate are with two water molecules attached to

region A (similar to thymine) – they form a two-water chain that bridges, via hydrogen bonds, the N1 hydrogen and O2. For one- and two-water clusters of uracil, water preferentially locate in the region A; the next best region is C. Most of the 22 optimized clusters formed from uracil and three water molecules have water molecules in regions A-C. It has been found that a cluster formed of a three-water chain that bridges the N1 hydrogen and O2 within region A is the lowest energy cluster, second is the cluster that has a two-water bridge in region A and the third water in region C. The lowest energy uracil tetrahydrates have a two-water bridge in regions A and C. The lowest energy uracil pentahydrate has a three-water chain in region A and a two-water chain in region C, hexahydrate has a three-water chain in regions A and C. Although the authors of this study have not presented a detailed configuration of $U^+(H_2O)_7$, it can be speculated, that the seventh water molecule is attached between H3 and O2 atoms (region B), creating neutral precursor of $U^+(H_2O)_7$ cluster ion, and possibly suggesting a closed-shell configuration at n=7. This may be interpreted as being consistent with the maximum $U^+(H2O)_7$ size observed in the present measurements (**Fig. 6.19**).

The structural analysis above shows similarities with thymine, i.e water molecules bridging H1 with O2, and H3 with O4 (see **Fig. 6.21**). These structures favour excited tautomerization, which can be the important step in the MPI process of hydrated uracil clusters. Moreover, analysis of the interaction energies of $(H_2O)_n$ and $U(H_2O)_n$ clusters predicts that the first hydration shell of uracil contains "around 6" water molecules, and water-water interactions are dominant for clusters with 12 or more water molecules [Gadre et al. [369]].

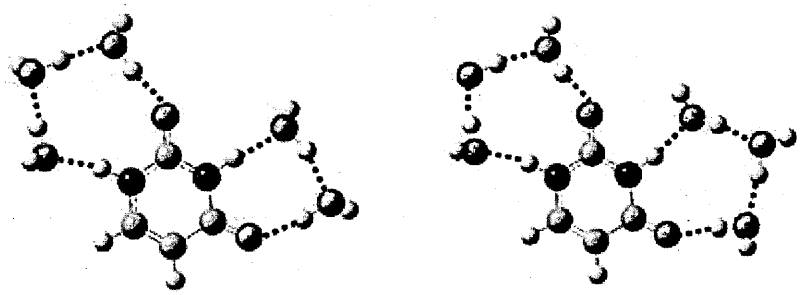

Fig. 6.21: Optimized structures of the lowest energy configurations with five (left) and six (right) waters of uracil[375].

6.4.4 Hydrated adenine-thymine system

More complex hetrogenuous systems have been also investigated in the present project. Hydrated adenine-thymine clusters are presented in this section. **Fig. 6.22** shows very strong clustering obtained for that mixture, with the largest cluster ion found at 432 Th, attributable to $AAT^+(H_2O)_2$ or $TTT^+(H_2O)_3$. This mass spectrum is among the measurements that show the most extensive series of cluster ions registered in the present project. Indeed, hydrated ions comprising 3 nucleobases have not been observed in any of the present measurements using dry nucleobase powders.

For better observation and analysis, the part of the mass spectrum corresponding to hydrated monomer ions is shown in detail in **Fig. 6.23**. The following monomer and cluster ions of thymine were observed: $T^+(H_2O)_n$ (n=0-6 i.e. 126, 144, 162, 180, 198, 216, and 234 Th) and TH^+ (127). Larger thymine monomer hydrates (n ≥ 7) were not possible to distinguish from dimer ions and their hydrates. For adenine, the following monomer ions and hydrates were observed: $A^+(H_2O)_n$ (n=0-4 i.e. 135, 153, 171, 189, and 207 Th) and AH^+ (136). As well as the $A^+(H_2O)_n$ cluster ions forming a shorter series than $T^+(H_2O)_n$, the $A^+(H_2O)_n$ peaks were detected with much lower intensity for n≥1. Conversely the A^+ and AH^+ peaks were stronger than the thymine equivalents. Again the high abundance of protonated monomers indicates the fragmentation of larger clusters. The maximum $A^+(H_2O)_n$ size was n=4. This is similar to the hydrated adenine mass spectra without any thymine, where the n=1-4 peaks were much stronger than n>4. So this indicates that thymine had little effect on the formation of these cluster ions.

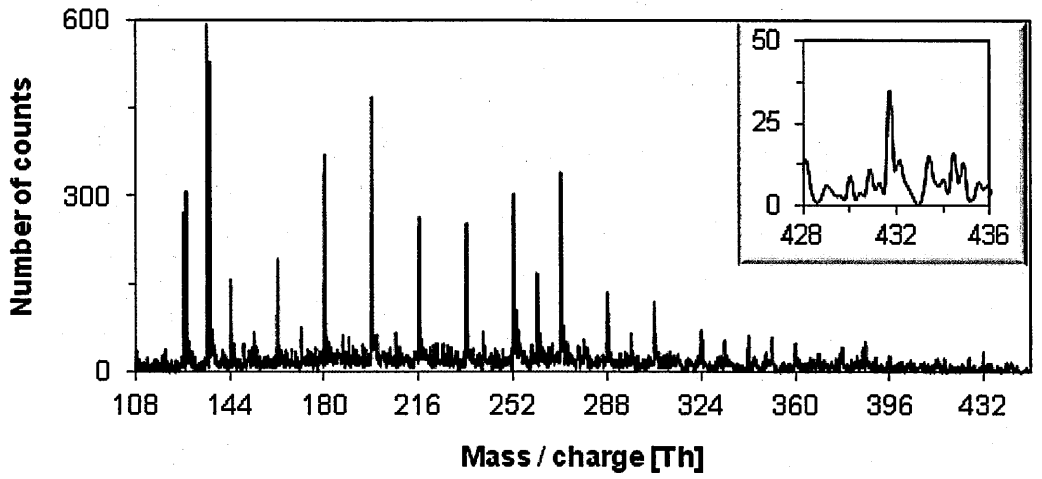

Fig. 6.22: One-colour (223.8 nm, ~ 3.4×10^6 W/cm^2) MPI mass spectra of hydrated adenine-thymine (powder 235°C, 1.0 bar argon, water 86°C).

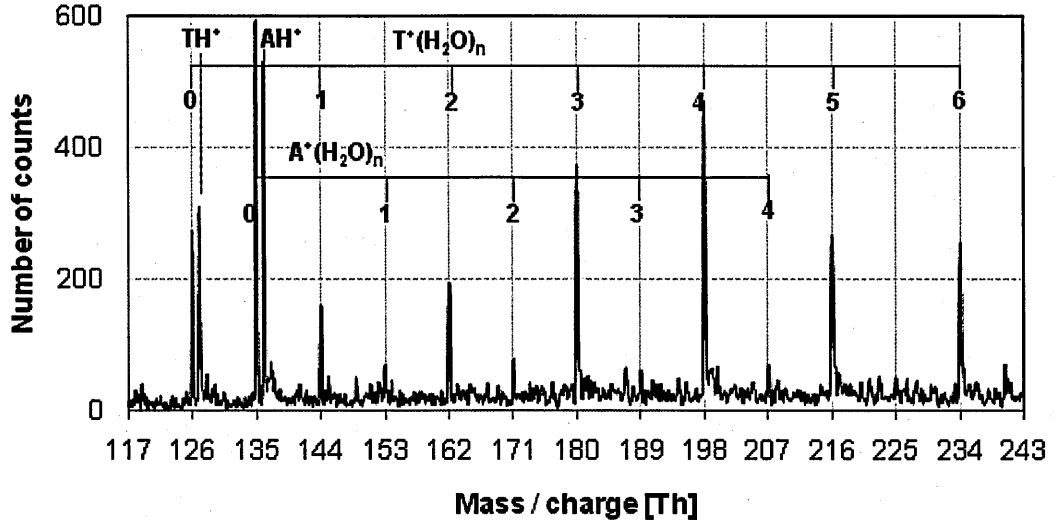

Fig. 6.23: Detail from **Fig. 6.22** showing hydrated monomer ions produced by one-colour (223.8 nm, ~ 3.4×10^6 W/cm^2) MPI of hydrated adenine-thymine (powder 235°C, 1.0 bar argon, water 86°C).

The second part of the mass spectrum from **Fig. 6.22** is presented in **Fig. 6.24**. As mentioned above, $T^+(H_2O)_n$ for n≥7 cannot be distinguished from $T_2^+(H_2O)_n$, and $A_2^+(H_2O)_n$ for n≥1. These clusters create one row of clear peaks at 252, 270, 288, 306, 324, 342, and 360 Th. Hydrated adenine-thymine base pairs $AT^+(H_2O)_n$ create the series of peaks for n=0-6 at 261 , 279 , 297, 315, 333, 351, 369 Th. The intensities of $AT^+(H_2O)_n$ cluster ions observed in **Fig. 6.24** are lower than that of the overlapping series of hydrated thymine

monomers, hydrated adenine dimers and hydrated thymine dimers.

Regarding trimers, T_2A^+ (387 Th) is clearly identifiable in **Fig. 6.24**. Weak peaks at 378 and 396 Th may be attributed to T_3^+ and A_2T^+, respectively, although it is not possible to confirm these assignments as the m/q ratios coincide with $T_2^+(H_2O)_7$ and $T_2^+(H_2O)_8$. No evidence is observed for A_3^+ at 405 Th.

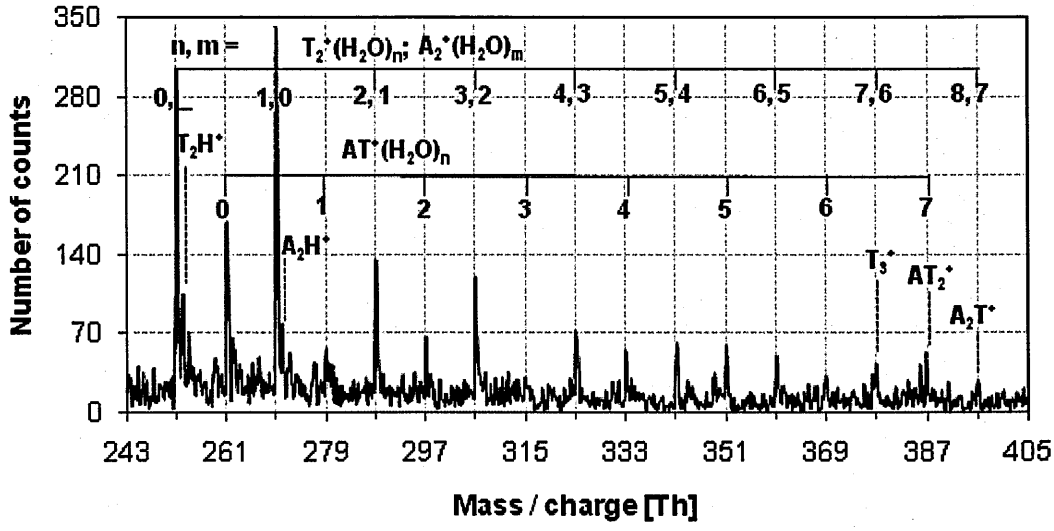

Fig. 6.24: Detail from **Fig. 6.22** showing hydrated dimer ions produced by one-colour (223.8 nm, ~ 3.4×10^6 W/cm^2) MPI of hydrated adenine-thymine (235°C, 1.0 bar argon, water 86°C).

The present measurements for adenine-thymine water mixed systems were made at relatively low powder temperature (235-233 °C) and adenine dimer ions could be observed. No dimer ions have been observed for dry adenine below 240°C, including in measurements with distinctly higher driving pressures (up to 1.5 bar).

Water molecules can affect hydrogen bonded structures of nucleic acid bases. The structural changes in hydrated adenine-thymine base pairs are presented in **Fig. 6.25**. The presence of one water molecule does not affect the structure of any H-bonded base pair, but a higher number of water molecules (notably two) does[376]. For dihydrated adenine-adenine H-bonded and stacked structures the interaction energies are -38.98 kcal/mol and -36.12 kcal/mol, respectively. For H-bonded T-T dihydrate the interaction energy is -33.72 kcal/mol and for the stacked one the interaction energy is -36.14 kcal/mol[376]. This shows

that the H-bonded form of dihydrated adenine is preferred over the stacked structure, but the stacked structure is preferred in the case of the thymine dihydrate and the adenine-thymine dihydrate (see **Fig. 6.25**).

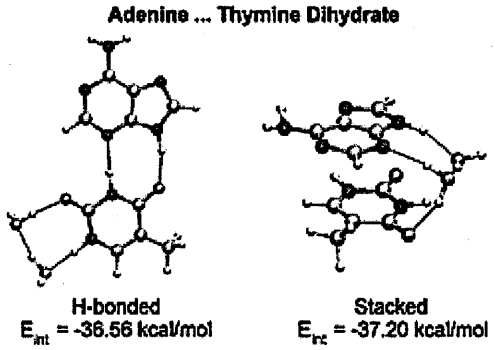

Fig. 6.25: Interaction energies of H-bonded and stacked structures of the A-T dihydrate (Kabelac and Hobza[376]).

The presence of stacked structures in the supersonic expansion can influence the effectiveness of the MPI process, since excitation of a stacked base pair can lead to creation of a long-lived excimer excited state. This has been proposed as an interpretation of the ns-order decay time constant in time-resolved experiments on hydrated adenine-adenine base pairs[377]. Indeed, strong signals of adenine-thymine, thymine-thymine and adenine-adenine base pairs have been observed in the present experiments (**Fig. 6.24**).

6.4.5 Hydrated adenine-uracil system

The mass spectrum of hydrated adenine-uracil is presented in **Fig. 6.26**, **Fig. 6.27**, and **Fig. 6.28**. Similarly to non-hydrated conditions (**Fig. 6.3** and **Fig. 6.4**), the uracil signal intensity is low compared to adenine. It is worth noticing that the series of hydrated uracil monomers $U^+(H_2O)_n$ is significantly lower in intensity than the $AU^+(H_2O)_n$ series, while no $U_m^+(H_2O)_n$ (m>1, n>0) signals have been observed above the background. The relatively low signal levels for $U^+(H_2O)_n$, $U_2^+(H_2O)_n$ and $U_3^+(H_2O)_n$ cluster ions can be attributed to a combination of relatively inefficient MPI processes for uracil and preferable clustering with adenine in hydrated conditions.

Fig. 6.27 shows uracil and its water clusters $U^+(H_2O)_n$ n=0-3 at 112, 130, 148 and 166 Th. Their signal intensities are not only lower than that of the adenine monomer; they are also

lower than the $A^+(H_2O)_1$ and $A^+(H_2O)_2$ peaks (153 and 171 Th). $UA^+(H_2O)_n$ peaks in **Fig. 6.28** are observed with n=0-7 at 247, 265, 283, 301, 319, 337, and 373 Th. This appears to be consistent with recent calculations of the structure of hydrated adenine-uracil base pair showing a closed hydration shell configuration with 7 water molecules by Zhanpeisov et al.[378]. The solvent effect was modelled by explicit inclusion of seven water molecules which create the first coordination sphere around the adenine-uracil base pair[378]. It has been found that the standard Hoogsten adenine-uracil base pair solvated by 7 waters and stabilized by two hydrogen bonds involving the amino group and the N7 site of adenine, as well as the O4 site and N3-H group of uracil is the global minimum for PES. Experimental evidence for this closed shell configuration has not been reported before.

Evidence for mixed trimer ions (A_2U^+, AU_2^+ and $AU_2^+(H_2O)$) can be found in **Fig. 6.26** and **Fig. 6.28**, however no evidence for pure trimer ions have been found. U_2H^+ is stronger than U_2^+, however for AU^+ and A_2^+ there is no evidence for strong protonated peaks.

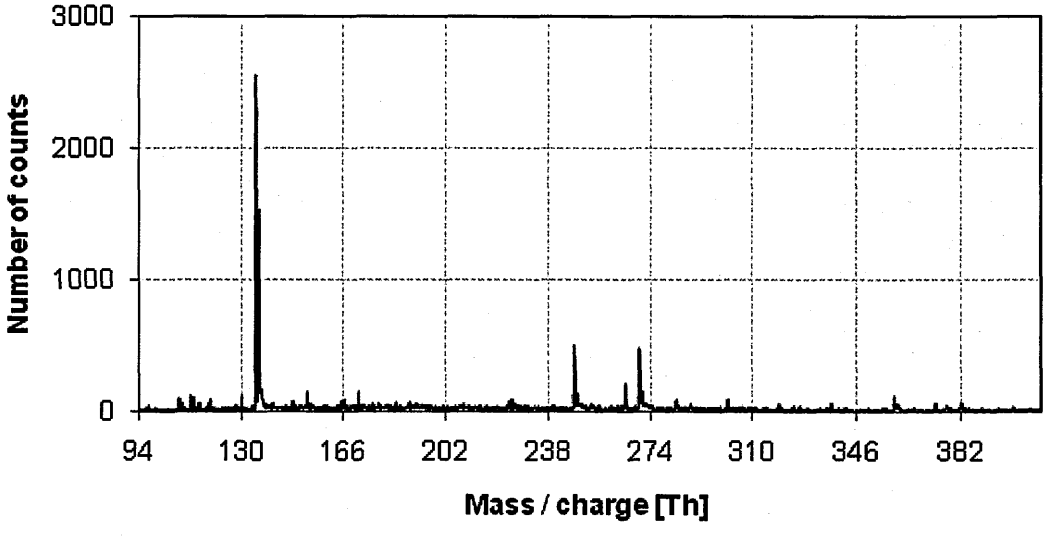

Fig. 6.26: One-colour (223.8 nm, ~ 4.7×10^6 W/cm^2) MPI mass spectrum of hydrated uracil-adenine (powder 240°C, 1.2 bar argon, water 90°C).

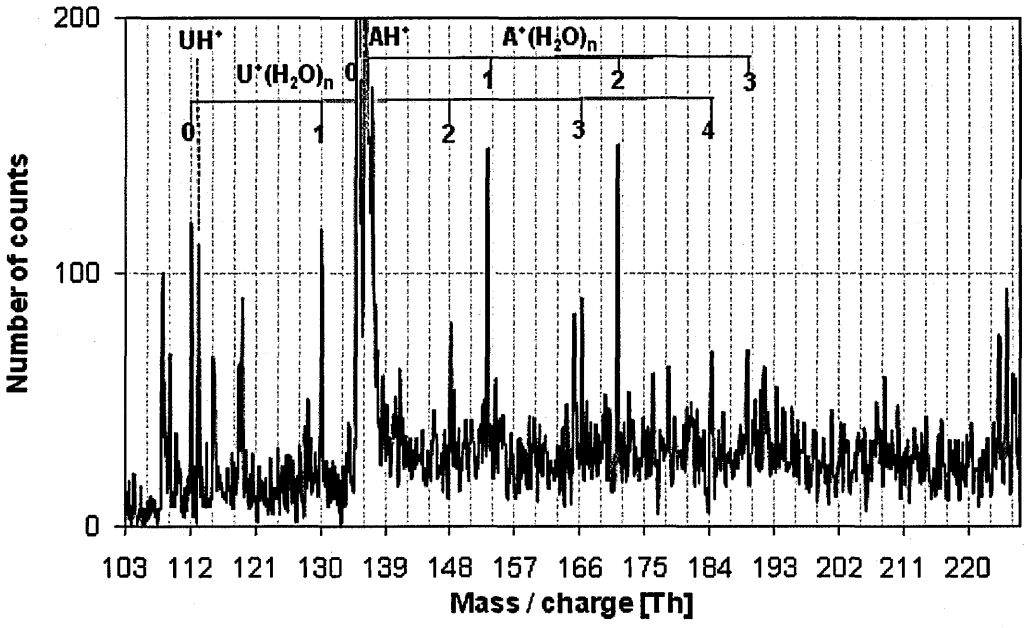

Fig. 6.27: Detail of **Fig. 6.26** showing monomer hydrates in the MPI (223.8 nm, ~ 4.7×10^6 W/cm^2) mass spectrum of hydrated uracil-adenine system (powder 240°C, 1.2 bar argon, water 90°C).

A common feature in the hydrated adenine-thymine and hydrated adenine-uracil measurements is that the abundance of the thymine and uracil hydrated cluster ions is high compared with their non-hydrated monomers, while for adenine this ratio is reversed. Dry measurements revealed that the uracil signal was much weaker than the adenine signal. The thymine signal was also weaker than the adenine signal, but to lesser extent. Similar signal intensities for $A^+(H_2O)_n$ and $U^+(H_2O)_n$ have been found, but the $T^+(H_2O)_n$ intensity is much higher than the intensity of $A^+(H_2O)_n$.

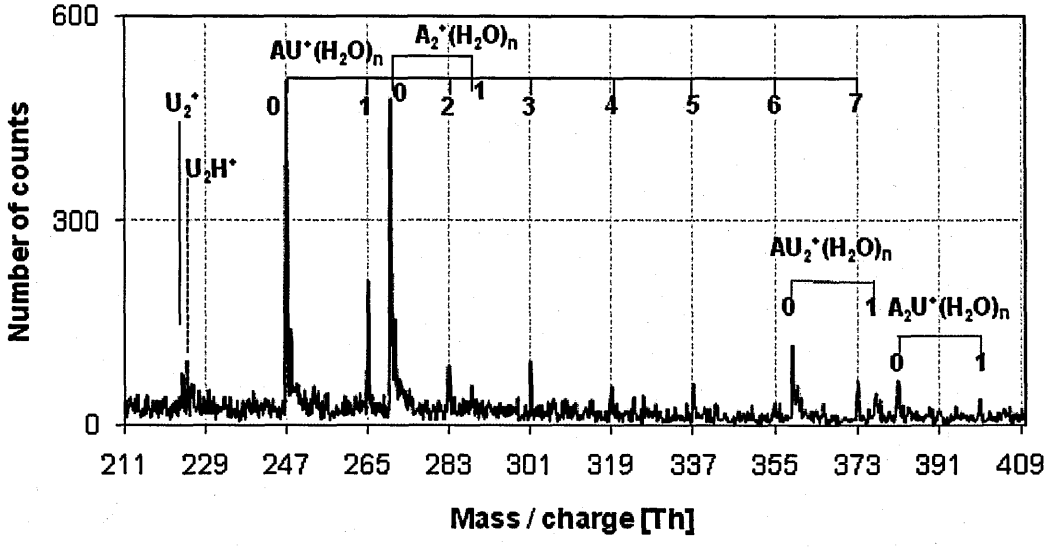

Fig. 6.28: Detail of **Fig. 6.26** showing dimer hydrates in the MPI (223.8 nm, ~ 4.7×10^6 W/cm^2) mass spectrum of hydrated uracil-adenine (powder 240°C, 1.2 bar argon, water 90°C).

6.5 Intracluster proton and hydrogen transfer

The appearance of protonated adenine monomers (AH^+) in the present mass spectra is explained by proton or hydrogen transfer in larger complexes followed by dissociation. **Fig. 6.29** shows MPI mass spectra for adenine and water vapor seeded in argon at three different driving pressures (0.4, 0.8, and 1.0 bar). The pressure-dependent effects are attributed to stronger clustering. The absence of any peaks in **Fig. 6.29** for hydrated adenine cluster ions indicates efficient cluster dissociation upon excitation and / or ionization.

The intensity of the 136 Th peak in **Fig. 6.29** increases significantly as a function of argon pressure. At 0.4 bar, the ratio of 136 / 135 Th counts is 7±1 %, consistent with the isotopomer ratio of adenine[21] and suggesting minimal clustering in the neutral beam. At 0.8 and 1 bar, the respective 136 / 135 Th ratios are 35±2 % and 154±8 %. As discussed below, the production of 136 Th ions with intensities greater than the adenine isotopomer ratio is attributed to intermolecular proton or hydrogen transfer.

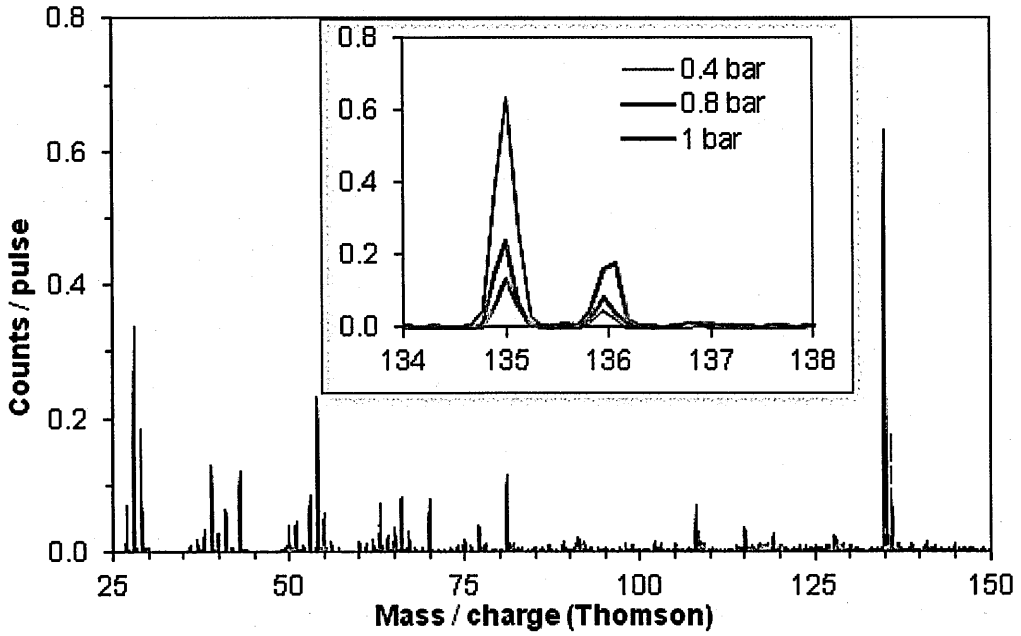

Fig. 6.29: One-color (226 nm, ~ 6×10^6 W/cm^2) MPI mass spectra of adenine in hydrated conditions (adenine 240°C, water 80°C) as a function of argon pressure (0.4 - 1 bar).

Proton transfer in the ionic state of an adenine cluster, for example an adenine dimer, can be interpreted on the base of thermochemistry. The proton affinity of neutral adenine has been reported as 225 kcal/mol[379], and the acidity of the adenine radical cation is 221 kcal/mol[380]. Thus proton transfer from A^+ to A in a dimer cation is exothermic by 4 kcal/mol (0.17 eV) and cluster fragmentation is expected to produce a protonated adenine ion and a neutral deprotonated adenine radical. Similarly, the proton affinity of neutral thymine is equal to 211 kcal/mol (Liu et al.[381]) and the acidity of the thymine radical cation has been calculated at the Becke3LYP/6-311+G(2d,p)//Becke3LYP/6-31G(d) + ZPVE level of theory for the most acidic site (allylic) site as 199 kcal/mol[382]. Therefore proton transfer from T^+ to T in a thymine dimer cation is also exothermic. On the basis of the proton affinities and acidities presented above, proton transfer will occur from T^+ to A in a $(A\text{-}T)^+$ dimer cation, however it will not occur from A^+ to T. The proton affinity of uracil has been experimentally derived as 209 kcal/mol for the most basic site by Kurinovich et al.[383] and the acidity of the most acidic site of the uracil cation is 198 kcal/mol (Turecek et al.[384]), supporting proton transfer from U^+ to U in uracil cation dimer, but not from A^+ to U in adenine-uracil cation dimer.

The phenomenon of intracluster proton and hydrogen transfer has been investigated theoretically and experimentally. Hünig et al.'s[385] time-dependent pump-probe experiments demonstrated that AH^+ fragment ions were produced by proton transfer in the adenine dimer ion. Park et al.'s[163] DFT studies showed that proton transfer in hydrated adenine dimer cations can occur with negligible barriers. Kim et al.[363] discussed the possibility that proton transfer from water to adenine in the $^1n\pi^*$ excited state could explain the strong AH^+ production (as well as weak $A^+(H_2O)_n$ production) in their 266 nm MPI experiments, however they concluded that this reaction was highly unlikely due to its large endothermicity (estimated at 3 eV) in hydrated adenine.

The mechanisms leading to the creation of protonated peaks in the present mass spectra can be also based on hydrogen transfer in the excited or ionic state. One of the possible pathways[385] for the production of AH^+ (136 Th) assumes dissociation of the adenine dimer after initial photoexcitation resulting in the appearance of an $AH^\bullet$ radical and its subsequent ionization. Theoretical calculations indicate the vertical ionization potential for the $AH^\bullet$ radical to be 5.32 eV[386] (233.5 nm), so single photon ionization in our experiments could be possible. Hydrogen transfer in the excited state of adenine cluster may depend on the laser wavelength used for excitation; it has been reported for 285 nm (4.35 eV)[385], but ruled out at 266 nm (4.66 eV)[21]. Similarly, pump-probe photoelectron spectroscopy experiments on the aminopyridine dimer (a model base pair) have demonstrated significant changes in excited-state hydrogen transfer dynamics as a function of pump laser wavelength[387, 388]. In particular, excited state hydrogen atom transfer has been identified as the pathway connecting the locally excited $^1\pi\pi^*$ charge-transfer state (strongly stabilized by the transfer of a proton) and the electronic ground state in 2-aminopyridine clusters via a conical intersection[388]. Described as an intermolecular electron-density transfer upon electronic excitation followed by a slower transfer of the proton, this mechanism has also been suggested as a possibility in adenine clusters for excitation at 285 nm (4.35 eV) with a nanosecond laser[385].

It is possible that different pathways lead to the creation of protonated peaks in the present studies, the dynamics in the neutral and ionic states, hence proton and hydrogen transfers

cannot be easily distinguished on the basis of cluster ions mass spectra. Experimental evidence presented in section **6.6** supports the interpretation that protonated monomers result from photodissociation induced by photon absorption in cluster ions.

6.6 Photon orders - hydrated adenine and uracil

6.6.1 Adenine

Photon orders based on the total signal intensity (α) and pulse-by-pulse analysis (β) were determined by analyzing the production of specific ions and cluster ions as a function of laser fluence in hydrated conditions.

The photon order for adenine$^+$ production β(135 Th) by 223.8 nm ns MPI of adenine in isolation and in clusters (**Fig. 6.30**, **Fig. 6.31**) have been compared. Due to the low signal levels in hydrated conditions, a higher level of fluence was used for these measurements (~ 2×10^6 W/cm^2) compared to dry adenine measurements presented in section **5.2.2**. In dry conditions, **Fig. 6.30** demonstrates partial saturation (β = 1.0±0.1) for the production of 135 Th ions. Photon order based on the total signal intensity (α = 0.4±0.1) has been derived for higher fluences (7.2×10^6 W/cm^2 - 5.8×10^7 W/cm^2), its lower value compared to β = 1.0±0.1 at ~ 2×10^6 W/cm^2 is consistent with an increased saturation effect - see **Fig. 7.2**.

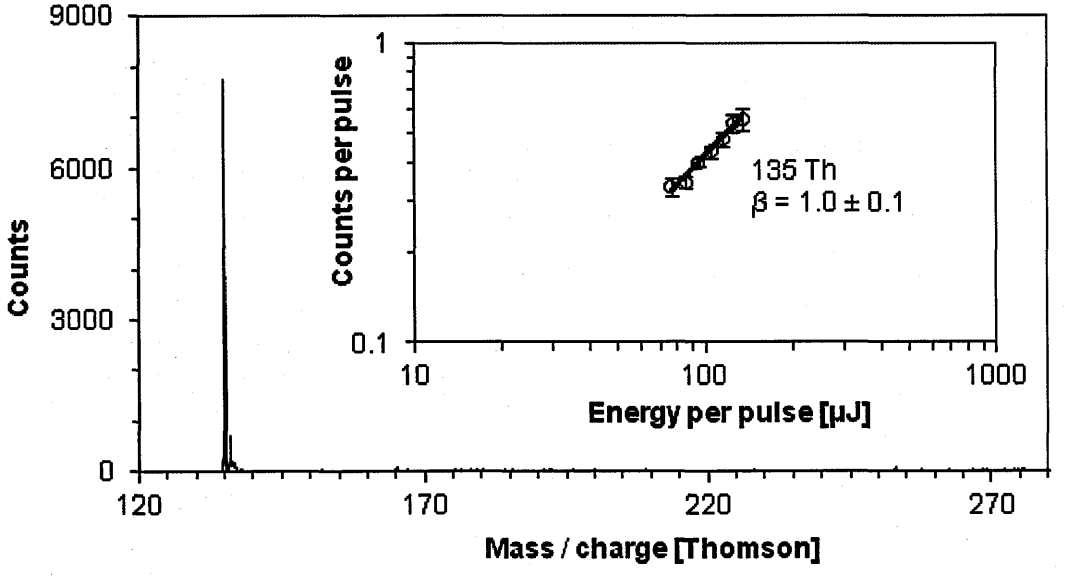

Fig. 6.30: One-color (223.8 nm, ~ 2×10^6 W/cm^2) MPI mass spectrum of adenine (234°C, no water, argon 0.5 bar).

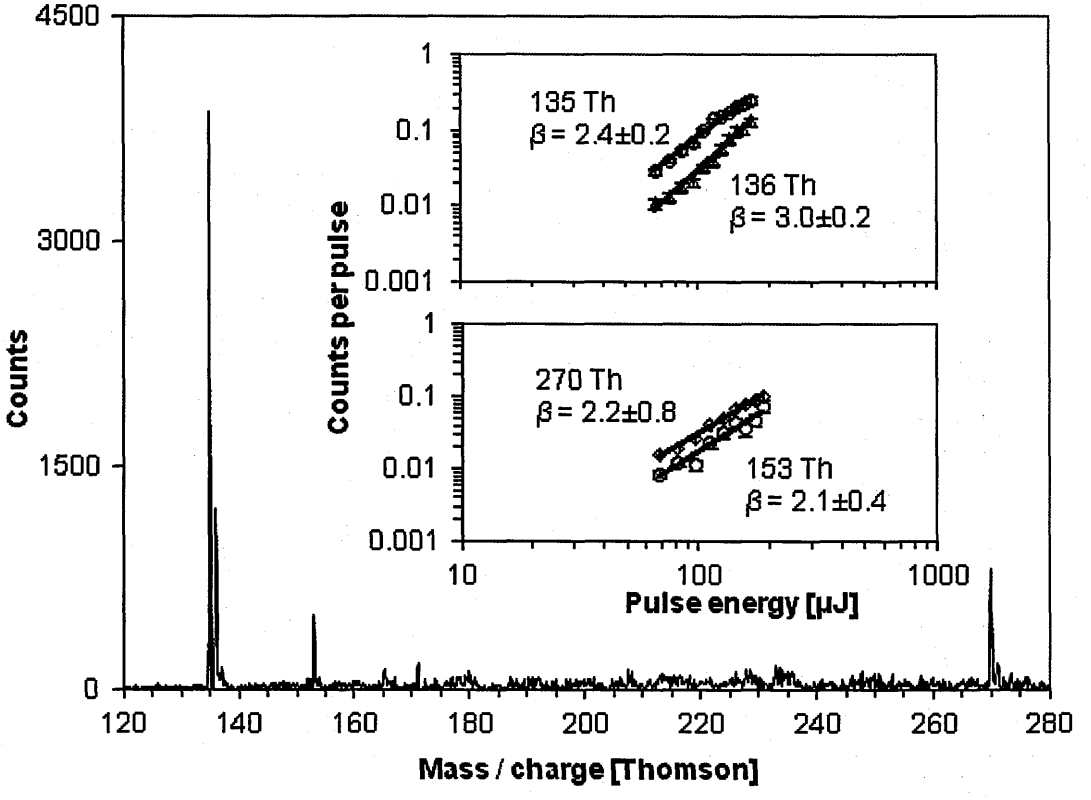

Fig. 6.31: One-color (223.8 nm, ~2×10^6 W/cm^2) MPI mass spectra adenine (249°C, water 100°C, argon 0.9 bar).

As in Nam et al.'s[228] 266 nm measurements, **Fig. 6.31** show that the measured photon order significantly increased due to clustering. With clear signals for AH^+, $A^+(H_2O)$, $A^+(H_2O)_2$, and A_2^+, β(135 Th) = 2.5±0.1. At a broadly similar fluence (2×10^6 - 3×10^7 Wcm^{-2}), Nam et al.[228] observed α(135 Th) = 1.6 and 2.5 in dry and hydrated conditions, respectively.

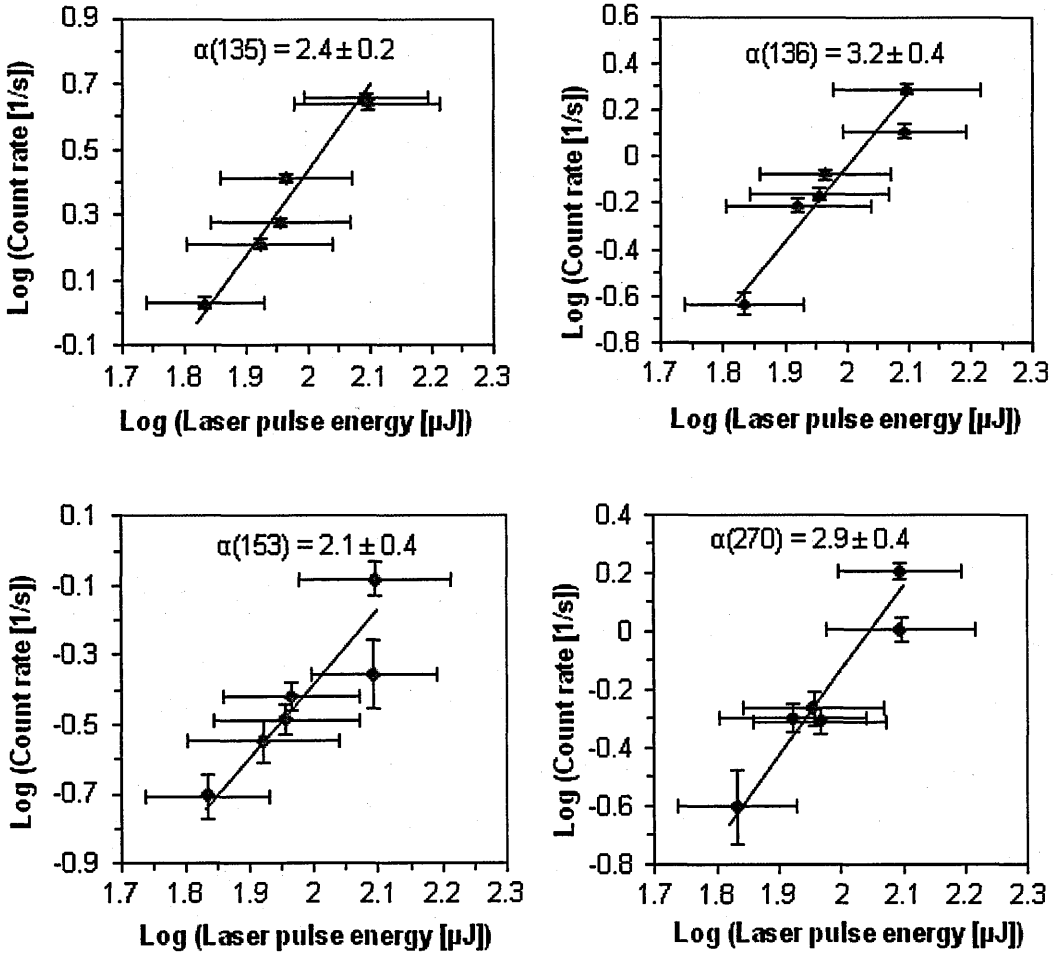

Fig. 6.32: A^+ photon orders in hydrated conditions; approximate laser fluence range: 1.2×10^6 - 1.9×10^6 W/cm^2; wavelength 223.8 nm; Ar pressure 0.9 bar; powder temperature from the weakest signal to the strongest: 250, 249.7, 249.8, 249.9, 249.1, 249.9°C; water 100°C.

Photon orders based on total signal intensity (α in **Fig. 6.32**) are in agreement with those derived from pulse-by-pulse measurements (β in **Fig. 6.31**):

$$\alpha(135) = 2.4\pm0.2\ ,\ \beta(135) = 2.4\pm0.2\ ;$$

$$\alpha(136) = 3.2\pm0.4\ ,\ \beta(136) = 3.0\pm0.2\ ;$$

$$\alpha(153) = 2.1\pm0.4\ ,\ \beta(153) = 2.1\pm0.4\ ;$$

$$\alpha(270) = 2.9\pm0.4\ ,\ \beta(270) = 2.2\pm0.8.$$

β(135 Th) = 3.2±0.5 in stronger clustering conditions is shown in **Fig. 6.33**. Increased photon order in these conditions compared to **Fig. 6.31** can be attributed to the effect of A^+

creation via AH^+ dissociation. The large uncertainties on β(270 Th) are due to a relatively low signal / background ratio. The difference of 2 between the photon order for A^+ in dry and hydrated conditions shows that the A^+ signal saturation in the latter conditions occurs for higher laser pulse powers, which means that MPI leading to A^+ is less efficient in hydrated conditions.

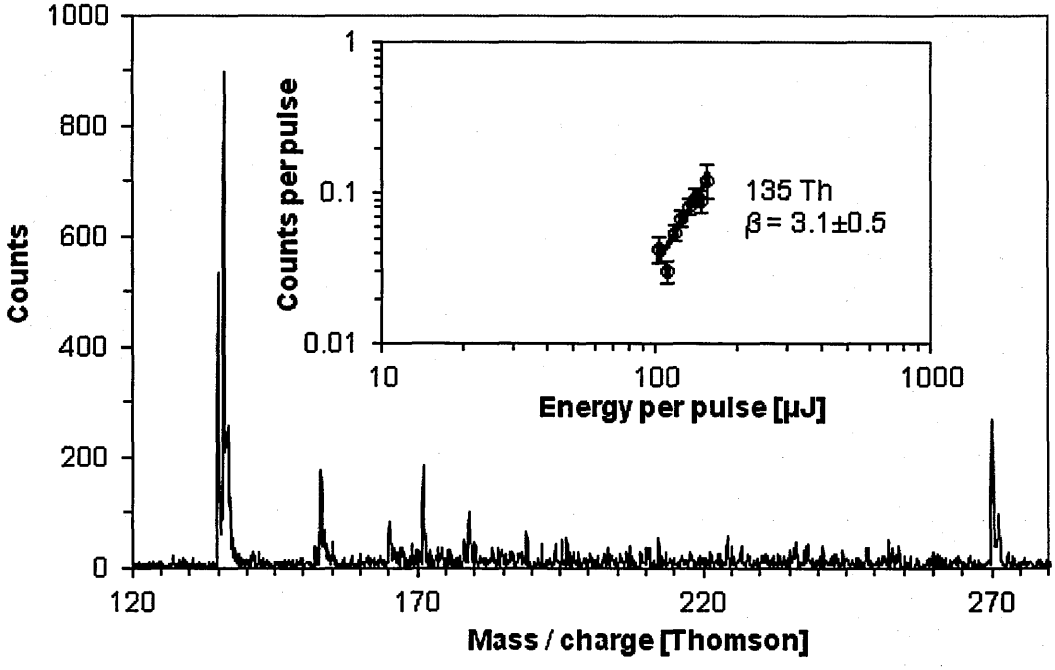

Fig. 6.33: One-color (223.8 nm, ~ 2×10^6 W/cm^2) MPI mass spectra of adenine: 260°C, water 95°C, argon 1.1 bar. The insert shows pulse energy dependence A^+.

Protonated adenine production (β = 3.0±0.2) is assigned to photo-dissociation of adenine dimer ions (or larger hydrated cluster ions). The peak at 136 is assigned to the protonated adenine monomer; it arises from fragmentation of larger clusters following proton transfer across adenine-adenine bonds. In this case, protonated species could only be produced by the loss of at least one adenine molecule from the complex. As water molecules are generally less strongly bonded[389], complete water loss is expected to precede any adenine loss.

In broad agreement with the present work (notwithstanding the wavelength difference), Nam et al.[228] observed equal photon orders (2.5) for 135 and 136 Th ions at 266 nm in hydrated conditions. Conversely, the distinctly lower β(153 Th) in **Fig. 6.33** indicates a fundamental difference in the ionization pathway producing $A^+(H_2O)$.

No previous photon order measurements have been carried out on adenine-water cluster ions. The photon order of 2.1±0.4 for $A^+(H_2O)$ production suggests excitation to long-lived electronic excited states in certain hydrated clusters, enabling the absorption of a second photon prior to internal conversion. Smith et al.[377] reported 266 nm (4.66 eV) access to ns-lifetime excimer states of π-stacked hydrated dimers in addition to the short-lived $^1\pi\pi^*$ states. Similarly, Crespo-Hernandez et al.[390] observed lifetimes for singlet excited states of adenine homopolymers ranging from fs to ns at 267 nm and proposed that the long-lived components may be associated with photodimerization. However, even if such long-lived excimer states are accessible at 223.8 nm, $A^+(H_2O)$ is an unlikely MPI product of $A_m(H_2O)_n$ ($m \geq 2$) ns MPI. This is because complete loss of water molecules is expected to precede adenine cleavage due to the generally high adenine-adenine binding energy (e.g. 1.34 eV in $A_2^+(H_2O)$) compared with adenine-water (e.g. 0.49 eV in $A_2^+(H_2O)$)[389].

Detailed multiphoton ionization pathways leading to the production of molecular cluster ions and their fragments are proposed in this work, and presented in section **6.7**.

6.6.2 Uracil

Photon orders based on the total signal intensity (α) have been also derived for uracil in hydrated conditions. The summed mass spectrum used to determine photon order characteristics is shown in **Fig. 6.34**. Photon orders of uracil monomer U^+ (112 Th), protonated uracil monomer UH^+ (113 Th), hydrated uracil cluster ions $U^+(H_2O)_n$ (n=1-4: 130, 148, 166, 184 Th), uracil dimer U_2^+ (224 Th), and protonated uracil dimer U_2H^+ (225 Th) are presented in **Fig. 6.35**.

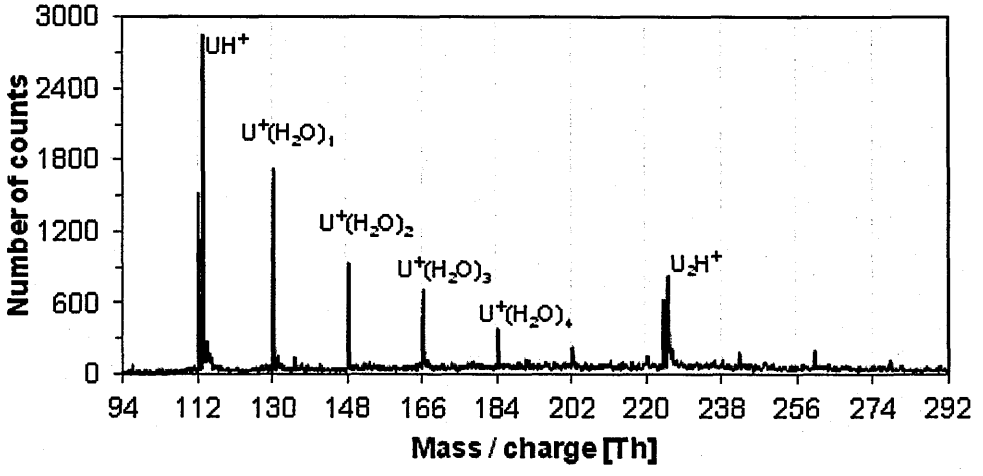

Fig. 6.34: One-colour mass spectrum of hydrated uracil (224 nm, approximate fluence range: 1×10^6 - 4×10^6 W/cm^2; Ar pressure 1.1 - 1.2 bar; powder temperature 250°C; water 80 - 100°C).

The results presented in **Fig. 6.35** for uracil in hydrated conditions are similar to adenine characteristics in **Fig. 6.32**. As with adenine, the photon order of U^+ recorded in hydrated conditions indicates significant contribution from cluster dissociation. Agreement has been also obtained for protonated monomers (AH^+ and UH^+); photon orders of 3.2±0.4 and 3.0±0.1 were measured for adenine and uracil, respectively. Both values indicate photofragmentation of larger cluster ions after absorption of a third photon. The possible explanation which has been presented for adenine assumes that proton transfer occurs between two bases in a cluster ion. Hydrated adenine and uracil monomer ions show photon orders indicating that a two-photon ionization process is responsible for $U^+(H_2O)_n$ and $A^+(H_2O)_n$ production. The larger uncertainties obtained for cluster ions compared to monomer ions reflect unstable conditions of the hydrated expansion in the nozzle (fluctuations of water vapour flow) and larger background contributions in the case of monohydrated adenine and adenine dimer. Unstable clustering conditions are especially evident in the U_2^+ (224 Th) and U_2H^+ (225 Th) photon order measurements (**Fig. 6.35**), where a large spread of signal intensities can be observed.

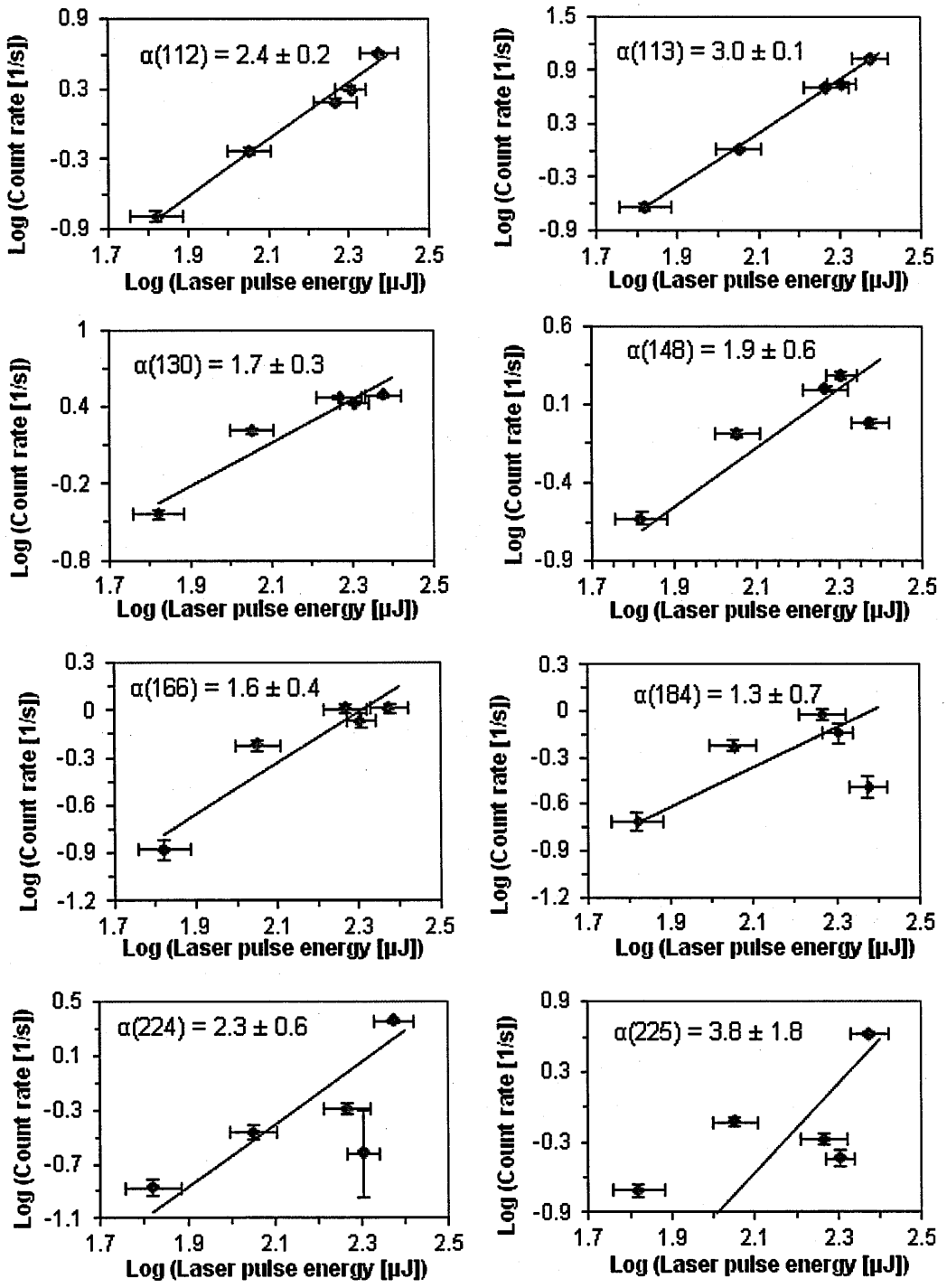

Fig. 6.35: Hydrated uracil cluster ions photon orders (224 nm, approximate fluence range: 1×10^6 - 4×10^6 W/cm^2; Ar pressure 1.1 - 1.2 bar; powder temperature 250°C; water 80 - 100°C).

6.7 Multiphoton ionization pathways of hydrated clusters - results discussion

6.7.1 Adenine-water clusters

Hydrated adenine monomer and dimer ions were detected in the present one-colour MPI experiments with 223.8 and 224 nm nanosecond laser pulses. The photon order measurements carried out in the same fluence range ~ 2×10^6 W/cm^2 indicate that these cluster ions (A^+ at 135 Th, and $A^+(H_2O)_1$ at 153 Th) are produced by different ionization pathways than adenine monomer ion in non-hydrated conditions, since the values of $\beta(135) = 1.0\pm0.2$ and $\beta(153) = 2.1\pm0.4$ have been obtained. Data presented in this chapter indicate two-photon ionization mechanism for hydrated adenine monomers $A_1^+(H_2O)_m$. A relatively long-lived intermediate excited state could support this process and its identification is the subject of the following discussion.

Nam et al.[228] presented the intensities of the hydrated adenine monomer ions $A_1^+(H_2O)_m$ much lower than those of the hydrated adenine dimer ions, $A_2^+(H_2O)_m$, when the fourth harmonic of Nd:YAG laser (266 nm, 4.66 eV) is employed. However they have also recorded the wavelength dependence of hydrated adenine ion $A^+(H_2O)_n$ intensities in the range of 216-280 nm, and observed that as the wavelength becomes shorter, the relative intensities of $A_1^+(H_2O)_m$ increase. A similar effect has been presented by Kim et al.[363]. Nam et al.[228] interpreted the wavelength dependence in terms of competing branching ratios to the $^1n\pi^*$ and the $^1\pi\sigma^*$ states leading to the ground state through conical intersections, assuming that the overall lifetime becomes longer at higher excitation energy due to the enhanced contribution of the relatively slow component ($^1n\pi^*$ state). A longer lifetime in the high excitation energy means that the possibility of direct ionization (two photon process) increases with the decrease of the deactivation rate to the ground state. Indeed, they have concluded the increase in the intensity of $A_1^+(H_2O)_m$ is due to the increase in lifetime of the intermediate $^1n\pi^*$ state and thus the ionization efficiency.

Nam's interpretation[228] of hydrated adenine results presented above can be discussed together with femtosecond photoelectron time-resolved experiments on isolated adenine carried out by Evans and Ullrich[309] in a molecular beam at multiple excitation energies

between 4.7-6.2 eV. They interpreted the data adopting the mechanism in which the initially excited $S_2(\pi\pi^*)$ state is populated by all excitation wavelengths and decays quickly within 100 fs. For excitation below ~5.2 eV, the pathway leading through $S_1(n\pi^*)$, i.e. $S_2(\pi\pi^*)\rightarrow S_1(n\pi^*)\rightarrow S_0$ dominates the deactivation process, with the $S_1(n\pi^*)\rightarrow S_0$ lifetime (1032-700 fs) displaying a trend toward shorter time constants with increasing excitation energy. An additional channel has been observed after photoexcitation above 5.2 eV with lifetime less than 100 fs, and it has been assigned to the $S_2(\pi\pi^*)\rightarrow S_3(\pi\sigma^*)\rightarrow S_0$ pathway.

Hence Nam's[228] interpretation of increased relative intensities of $A^+(H_2O)_n$ clusters for shorter wavelengths attributed to the contribution of $^1n\pi^*$ state is not consistent with the results of femtosecond MPI experiments, although strict comparisons cannot be drawn since experimental conditions in both cases were different (hydrated and dry conditions). However further experimental data obtained in hydrated conditions indicate that the monohydrated adenine complex lives only ~100 fs after absorption of a 250-266 nm photon[249]. This ultrafast decay has been assigned to the relaxation via the $^1\pi\sigma^*$ state. It is unlikely that excited states with such a short lifetimes are efficiently ionized by nanosecond laser pulses in the present experiments.

Further experimental evidence supports ultrafast decay of hydrated adenine complexes. Two isomers of $A(H_2O)_1$ have been identified by quantum chemical vibrational analysis with the water molecule hydrogen bonded to the amino group or to the N9-H group[391]. It has been found that the relaxation pathway of the monohydrated adenine $^1\pi\pi^*$ excited state depends on the position where the water molecule is hydrogen-bonded with adenine[391]. In particular, for the N9-H bound hydrate, excited state dissociation is suggested to be more efficient than internal conversion (IC), whereas for the amino-bound species, IC is dominant. Both pathways can significantly limit the availability of excited states involved in nanosecond multiphoton ionization of clusters. Nosenko et al.[391] concluded that adenine hydrates are extremely short-lived in their excited states and fast state relaxation of an isolated complex must lead to dissociation. Depending on the nature of the electronically excited states involved the hydrate may dissociate either directly or after vibronic

relaxation. So the question remains: what is the pathway leading to 2-photon MPI of hydrated adenine monomers on a nanosecond time scale?

Taking into account the very short excited states lifetimes of the hydrated adenine 9-H tautomer reported in the literature, it is proposed in this thesis that ns MPI of hydrated adenine monomers occurs via one of the following competitive pathways: tautomeric transition in the excited state, induced effectively by photons of higher energy (shorter wavelengths); or ultrafast intersystem crossing to a triplet state. The efficient detection of hydrated adenine monomer ions in the present project can be also related to the presence of clusters larger than monohydrated monomers, for which ultrafast relaxation pathways have been identified in previous time-resolved experiments[249, 391]. It is conceivable that hydration with more than one water molecule extends the lifetimes of the initially excited $^1\pi\pi^*$ state or the dark $^1n\pi^*$, $^1\pi\sigma^*$ states sufficiently (i.e. from fs – ps to 100s of ps – ns) to act as intermediate excited states in efficient ns MPI. In this thesis $A(H_2O)_n$ ns MPI mechanisms via successor states of the initially-populated short-lived states are proposed and discussed. IC to the vibrationally ground state is expected to cause complete loss of water on a fast timescale and hence it is not expected to contribute towards ns MPI production of hydrated cluster ions. Since ISC to a triplet state has been carefully analyzed in the case of isolated adenine (chapter 5), the excited state tautomerization is discussed below.

Chaban and Salter[392] presented the energetic order of the adenine tautomers in the ground state: 9H < 7H < 3H < 1H (structures can be found in **Fig. 1.4**). They have found that 3H and 1H tautomers, which are higher in energy on the ground state potential surface, become lower in energy than 9H and 7H tautomers in the excited state, i.e. the energetic order in the excited state is different: 3H < 1H < 9H < 7H. The 0-0 excitation energies for the 9H, 7H, 3H and 1H tautomers have been also calculated as 4.4, 4.2, 3.6, and 3.4 eV, respectively. The authors[392] recognized that excitation energies of the 3H and 1H tautomers are significantly lower than those of the 9H and 7H, and suggested that 9→3 tautomerization on the excited potential energy surface could result in accumulation of the 3H tautomer after the exposure of adenine to UV radiation. However, the energy of the

transition state for the hydrogen transfer reaction in the ground state is 63 kcal/mol[392] (relative to the lower energy tautomer), while the energy of the transition structure for 9→3 tautomerization on the excited-state surface is lower: 43 kcal/mol[392] (relative to the higher energy tautomer 9-H). These energy barriers make this process highly unlikely for adenine excited in isolated conditions.

The situation changes in hydrated clusters. Interactions with the water molecules are found to lower the barrier of this tautomeric transition. Kim et al.[393] calculated that the binding of a water molecule dramatically lowers the 9→3 barrier from 63 to 16 kcal/mol (water molecule acts as a catalyst); moreover binding two water molecules lowers the barrier even more to 9.7 kcal/mol (0.42 eV). The mechanism of this reaction is presented below.

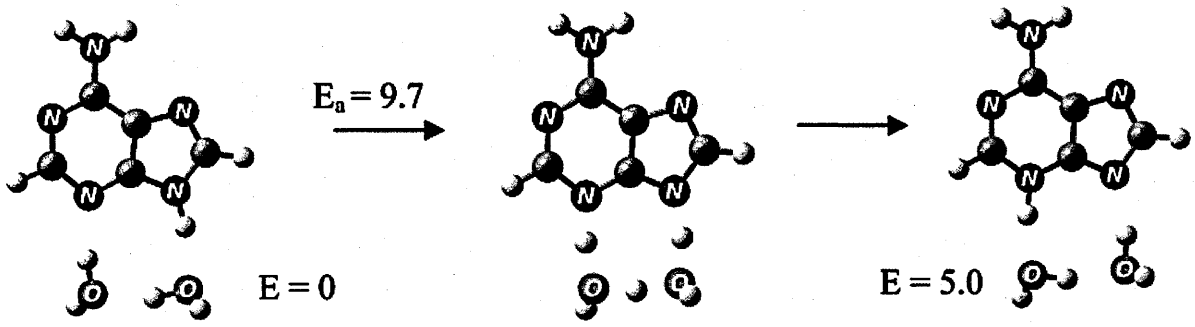

Fig. 6.36: Excited state 9→3 tautomerization processes in adenine facilitated by water (energies given in kcal/mol.)[393]

It is worth noting that the hydration site between N3 and H at N9 atoms is the most energetically stable among adenine dihydrates, which has been discussed in detail in sub-section **6.4.1.1**. Mishra et al.[394] calculated electronic spectra of adenine in the gas phase and aqueous solutions, and concluded that the calculated molecular electrostatic potential (MEP) maps strongly support the possibility that the N9-H form of hydrated adenine may be phototautomerized consequent to $^1\pi\pi^*$ singlet excitation to the N3-H form.

Although the relaxation dynamics of the rare N3-H adenine tautomer have not been studied directly, the present results showing efficient 2-photon nanosecond MPI production of $A^+(H_2O)$, as well as the strong signals in the experiments mentioned above[228], suggest that if this excited tautomer is indeed produced it does not undergo ultrafast relaxation to

the vibrationally hot ground state. Further evidence that this state is a strong candidate for an intermediate state in 2-photon MPI of hydrated adenine monomers comes from the wavelength dependence discussed earlier[228, 363], i.e. the relative signal of $A^+(H_2O)$ is stronger for shorter wavelengths. This can be related to the energy barrier for 9→3 tautomeric transition of 9.7 kcal/mol (~0.4 eV); applying shorter wavelengths enables this barrier to be successfully exceeded. Taking into account the adenine band origin at 4.47 eV, the condition 4.47 + 0.4 = 4.87 eV (254 nm) is fulfilled for the wavelengths used in the present project, supporting more efficient tautomeric transition, and subsequent ionization due to an elongated excited state lifetime. The proposed excited state tautomerization is presented in **Fig. 6.37**.

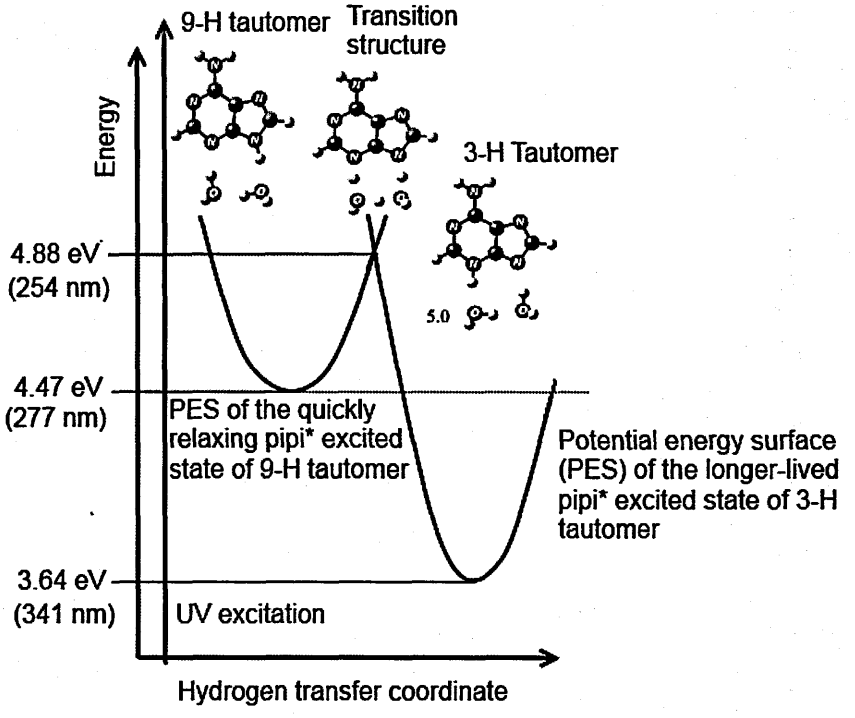

Fig. 6.37: Adenine 9→3 excited state tautomerization. Structures of adenine tautomers and energy levels presented in the Figure are taken from Kim, H.-S. et al.[393]; Salter and Chaban[392]; Kim, N.J.[239].

In the case of lower energies (below ~ 4.9 eV) tautomeric transition is hindered by the energy barrier, hence ultrafast relaxation of 9-H tautomer leads to vibrationally hot electronic ground state and is followed by drastic loss of water molecules. In the present

experiments a major drop of the total adenine signal in hydrated conditions has been observed, which may be related to closing the very efficient (triplet?) route in non-hydrated conditions (discussed in chapter 5) and opening a completely independent, but less efficient tautomeric channel in hydrated conditions. Indeed, the photon order measurements within the same fluence range for adenine monomer ion at m/z = 135 are 1.0±0.2 (partially saturated) and 3.1±0.5 in isolated and hydrated conditions, respectively. This strongly supports independent MPI channels for isolated adenine and its hydrated form. A significant amount of A^+ ions are produced as cluster fragments (otherwise photon order would be unaffected). Photodissociation of hydrated cluster ions is the most likely source of A^+ ($\beta(135)=3.2\pm0.5$) in strongly hydrated conditions.

The apparently strong production of adenine dimer ions (**Fig. 6.7**) is likely to be due to MPI via ns-lifetime states. For all $A_2(H_2O)_n$ (n=1-5) clusters, excited state lifetimes >1ns have been observed in femtosecond time-resolved experiment with 266 nm excitation and 400 or 800 nm ionization[377]. It has been suggested that the long-lived state may correspond to the excimer state described for solvated, single-stranded poly(dA) strands[395]. The type of base pair structure favouring the excimer formation has been shown in **Fig. 6.25** (section **6.4.4**). This long-lived state also appeared in the A_2^+ peak in hydrated conditions, and it has been interpreted as the result of considerable cluster fragmentation[377]. Further time-resolved experiments in the nanosecond time regime are required in order to describe the dynamics of that potential excimer excited state more accurately. The present photon order measurement of $\beta(270) = 2.2\pm0.8$ and $\alpha(270) = 2.9\pm0.4$ suggests two or three photon phenomenon leading to the creation of A_2^+ cluster ion, respectively. The large uncertainty in the photon order results is due to the background contribution at 270 Th in these particular measurements.

The present α(136 Th) = 2.9±0.2 result (**Fig. 6.31**) can be interpreted in terms of a third photon being required to dissociate an $A_m^+(H_2O)_n$ ($m \geq 2$) cluster ion and thus produce AH^+ as it has been already discussed in the section **6.6.1**.

6.7.2 Hydrated thymine and uracil

Strong evidence can be presented that tautomerism can play an important role in ns MPI of hydrated uracil and thymine in the present project. Shukla and Leszczynski[396] performed a detailed study of the molecular geometry and electronic spectra of uracil tautomers, anions and their hydrated complexes. Keto-enol tautomerism of uracil has been investigated in the ground and excited states. These calculations showed that the relative ground state stability of uracil tautomers in the gas phase follows the order: U-keto>U-O2H1>U-enol>U-O4H3>U-O2H3. The nomenclature used here and tautomeric structures have been explained in the introduction – section **1.3.1**. The calculations[396] indicate that under hydration, the lowest singlet vertical $^1\pi\pi^*$ excited state of the U-O2H1 and U-O4H3 tautomers lies close to the corresponding state of diketo-uracil, i.e. uracil (keto) – 4.85 eV, enol – 4.77 eV, U-O2H1 – 4.61 eV, U-O4H3 – 4.65 eV, U-O2H3 – 4.95 eV. Therefore there will be strong interaction among the lowest vertical singlet $^1\pi\pi^*$ states of the keto, U-O2H1 and U-O4H3 tautomers of uracil. Under electronic excitation of uracil, an energy transfer from the lowest singlet $^1\pi\pi^*$ state of uracil to the corresponding state of U-O2H1 and U-O4H3 may take place. There is strong probability that uracil will phototautomerize to the U-O2H1 and U-O4H3 enol tautomers through energy transfer and necessary structural modifications. It has been concluded that the U-O2H1 and U-O4H3 enol forms of uracil would be formed via excited state phototautomerization of the keto uracil. These tautomers will yield red-shifted fluorescence. However no data allowing for a direct comparison of relaxed $^1\pi\pi^*$ states of different uracil tautomers are available.

Excited state uracil tautomerization in the $^1\pi\pi^*$ state can be supported by its elongated lifetime through the relaxation phenomenon suggested by Mercier et al.[397] whereby the energy gap between $^1n\pi^*$ minimum and $^1\pi\pi^*/^1n\pi^*$ conical intersection is rather small, depending on the adopted basis set 1-4 kcal/mol (1 kcal/mol ≈ 0.04 eV) in hydrogen bonding solvents. Therefore after thermalization in the $^1n\pi^*$ minimum, the system can recross the $^1\pi\pi^*/^1n\pi^*$ conical intersection and then quickly proceed towards the $^1\pi\pi^*$/ground state conical intersection. The key step in this mechanism is the second (back) transition through the $^1\pi\pi^*/^1n\pi^*$ conical intersection to the $^1\pi\pi^*$ state, associated with the longer component of the excited state lifetime. Theoretical studies on ultrafast

molecular dynamics reviewed in chapter 4 (section **4.3**) showed that the role of the $^1n\pi^*$ state in isolated uracil has not been completely solved. As shown in **Fig. 4.3**, direct relaxation of $^1\pi\pi^*$ via conical intersection with the ground state is possible through the C=C bond twisting. Assuming that the most efficient ISC to a triplet state occurs via $^1n\pi^*$ (see discussion in **5.5**, as well as azauracil in section **4.3.1**), the data presented in this thesis, i.e. the low signal intensity for uracil in dry conditions (compared with adenine and thymine) suggest that the ionization pathway via triplet state populated from $^1n\pi^*$ is weak, and the major relaxation channel of $^1\pi\pi^*$ excited uracil may not proceed through the $^1n\pi^*$ state. Conversely, the longer time spent in the $^1\pi\pi^*$ state favours a tautomeric transition in hydrated uracil. This is supported by large ratios of $U^+(H_2O)_n$ / U^+ signals in the present hydrated experiments indicating low effectiveness of MPI for uracil as an isolated molecule or as a dissociated neutral cluster fragment. Time-resolved experiments (see section **5.4.1**) showed 1.05 ps[333] and 2.4 ps[237] relaxation components of uracil's initially excited bright $^1\pi\pi^*$ state.

Shukla and Leszczynski[396] related their investigation of uracil phototautomerizm to experimental data obtained for thymine, since electronic spectral properties of uracil and thymine are generally similar. Separate calculations have not been performed for thymine, however experimental data suggest excited state tautomerism in the case of thymine. Morsy et al.[398] studied fluorescence of thymine tautomers at room temperature in an aqueous solution. Fluorescence decay with an average lifetime of 3.84 ns has been identified and assigned to the keto-enol tautomer (T-O2H1) for pH=7 solutions. These results have been contested by Rejnek et al.[135], however an analogy with hydrated thymine experiments (He et al.[336]) can be drawn. With the pump wavelength set at 267 nm and the ionization wavelength at 220 nm, the lifetimes of the dark state of thymine and the $T(H_2O)_1$ cluster were measured to be 22 and 12 ns, respectively[336]. These nanosecond-order lifetimes correlate well with thymine fluorescence measured in aqueous solution. Moreover, He and co-workers[336] noticed that heavier clusters disappear faster than lighter ones for the increased delay time between the pump and probe laser pulses. Such a decreasing excited state lifetime can be related to the shorter fluorescence emission in bulk water mentioned above. However, in cluster studies this lifetime has been

assigned to $^1n\pi^*$ state relaxation by the authors.

In a separate study Busker et al.[366] performed time-resolved experiments on 1-methylthymine (1MT)[366]. As the ionized molecule survives hydration, the photostability of 1MT cannot be attributed solely to hydration[366], while a decay time of 363+/-30 ns has been registered for 273.2 nm excitation and 193 nm ionization in hydrated conditions for $1MT^+$ monomer ion channel[366]. On this basis, the authors suggested that after initial excitation by a nanosecond laser, the excited molecules failed to return to the ground state but rather were trapped in a dark state for tens to hundreds of nanoseconds.

Photodynamics studies in thymine clusters have also been carried out recently by Nosenko et al.[399] The authors recorded the vibrational spectrum and recognized that the T12-W structure (water bridging O2 and H at N1) provides the best agreement of the calculated vibrational frequencies with the observed spectrum.

Gonzalez-Vazquez et al.[332] analysed the time-dependent ion signal of thymine and thymine-water clusters: the isolated molecule exhibited a nanosecond-timescale component whereas thymine hydrates did not. Time components of 100 fs and 7 ps for $T(H_2O)_1$ and only 100 fs for $T_1(H_2O)_2$ excited with 266 nm and ionized with 800 nm have been measured. Similarly, the nanosecond signal is very weak following 267 nm excitation in He's et al.'s[336] experiments, whereas a strong signal of hydrated thymine ions has been recorded in one-colour MPI at 229 nm. Gonzalez-Vazquez et al.[332] interpreted the long component in isolated thymine as a crossing to the triplet manifold or the observation of transient signals from local minima on the potential energy surface. This interpretation is in agreement with the MPI ionization pathway of isolated thymine presented in this thesis (chapter 5). However, for thymine-water clusters MPI at 223-227 nm a pathway via tautomeric transition in the excited states is proposed. This pathway correlates very well with decreased excited state lifetime upon hydration reported by He et al.[336], as well as with the results of the fluorescence experiments in water solutions mentioned earlier. This can be also related to the wavelength dependence presented in the literature: the hydrated thymine signal disappears or is very weak for excitation with longer wavelengths (> 260 nm), suggesting that additional energy above the $^1\pi\pi^*$ state origin induces excited state

tautomeric transition in hydrated thymine to potentially longer-lived states in O2H1 or O4H3 tautomers.

Moreover, it should be noted that after relaxation into the triplet state the molecule will be rather vibrationally "hot", since the energy excess of ~ 1.3 eV after 266 nm excitation, given a triplet state energy of 3.3 eV, will be deposited into vibrations. This energy corresponds to a vibrational temperature of 800 K, as derived experimentally by Kunitski et al.[400]. In the present experimental conditions the vibrational temperature is even higher, since 220 – 230 nm photons are used for excitation instead 266 nm. This potentially leads to extensive neutral fragmentation of thymine-water clusters in the triplet excited state. Unlike $A^+(H_2O)_n$ which showed short series (very weak peaks for n>4), the extended series of $T^+(H_2O)_n$ clusters presented in this thesis do not indicate that this process takes place.

Kunitski et al.[400] have investigated the relaxation dynamics of jet-cooled T upon excitation to the $^1\pi\pi^*$ state (S2): the time constants of 80 fs, 4.8 ps and 280 ns have been obtained in 267 nm (pump) - 400 nm (probe) MPI measurments. The assignment of the long-lived state to the triplet state has been made. It clearly does not correlate with the 12 and 22 ns lifetimes measured in hydrated conditions[336]. The long-lived component is about ten times larger than that reported by He at al.[336] and this difference has been attributed to the significant water content in He's et al.[336] experiment. However, a detailed explanation for the significant differences in excited states lifetimes for thymine in hydrated and isolated conditions has not been given.

It is therefore proposed in this thesis that tautomeric excited states of hydrated thymine monomers play a role in the MPI process.

Studies in aqueous solutions show that the involvement of the $^1n\pi^*$ state in the relaxation dynamics of thymine, uracil and 9 other uracil derivatives should be ruled out (Gustavsson et al.[284]). Excited-state geometry optimization in aqueous solution showed the existence of an energy minimum for the $^1\pi\pi^*$ state, strongly suggesting that the existence of a minimum on the $^1\pi\pi^*$ surface is due to solvent effect that significantly stabilizes the $^1\pi\pi^*$ over the $^1n\pi^*$ state. The authors summarized that in all of the above compounds a low-lying $^1n\pi^*$ dark state can be involved in the excited state dynamics, leading to long-lived

excited states. However, this is more relevant in the gas phase or in a polar solvent, due to the general destabilization of $n\pi^*$ states and stabilization of $\pi\pi^*$ states in polar solutions.

6.7.3 Significant barrier height values for excited state tautomerism in hydrated hypoxanthine

In contrast with adenine, very few experimental studies of the photophysical properties of hypoxanthine ($C_5H_4N_4O$, 136 a.m.u. in **Fig. 6.38**) have been reported in the literature. However from the theoretical standpoint, electronic spectra, excited state geometries and molecular electrostatic potentials have been investigated[401], both in isolated and hydrated conditions. Combined computational and experimental studies of hydrogen bonding between hypoxanthine and xanthine have been performed[402]. Because of the interest in hypoxanthine as a potential universal nucleobase[351], hydrogen bonding and stacking interactions with other DNA bases (adenine, guanine, cytosine and thymine) were calculated[351]. Gas phase acidity and proton affinity of hypoxanthine have been examined using quantum mechanical calculations and gas-phase mass spectrometric experimental methods[403].

In the present work, MPI experiments on argon seeded with dry and hydrated hypoxanthine were carried out using similar jet and laser conditions as the adenine-water measurements (225 nm, source temperature ≤240°C, water temperature ≤80°C, argon pressure up to 0.83 bar). The results were indistinguishable from background measurements recorded for unseeded argon jets. Tembreull and Lubman[327] were also unable to ionize hypoxanthine at 222 nm (~10^6 Wm^{-2}). Shukla et al. reported that hypoxanthine is not ionized effectively in 10 nanosecond laser pulses[404] but has been ionized using 100 femtosecond pulse laser[404], although details about the wavelengths used have not been given.

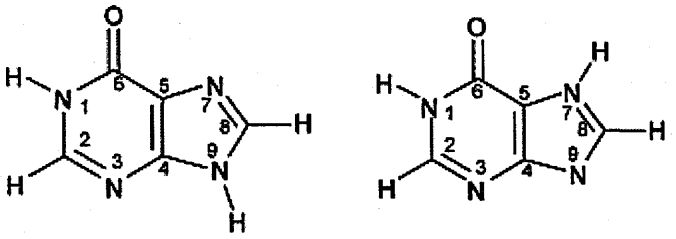

Fig. 6.38: The hypoxanthine molecule. Molecular structure for keto-N1H/N9H (HX/N9H) and keto-N1H/N7H (HX/N7H) tautomers of hypoxanthine – two major forms in the gas phase; HX/N9H is the dominant one[143].

Barrier heights for hypoxanthine keto-enol tautomerization in the ground state and the lowest singlet $^1\pi\pi^*$ excited state have been calculated in the gas phase and in aqueous solution[405]. Despite the inclusion of a water molecule bridging the N1-H site and the nearby O atom, the keto-enol tautomerization barrier for the two dominant tautomeric forms of hypoxanthine has been shown to increase in the lowest singlet $^1\pi\pi^*$ excited state both in the gas phase and in the aqueous medium. The obtained barrier height values increased from 17.05 kcal/mol (in the ground state) to 26.09 kcal/mol (in the excited state) and from 18.22 kcal/mol to 33.79 kcal/mol for gas phase HX-N9H-H2O and HX-N7H-H2O complexes, respectively[405] (1 kcal/mol ≈ 0.04 eV). These values are higher than barriers for water assisted 9→3 tautomerizm in adenine[393], i.e. 9.7 kcal/mol and 16 kcal/mol for tautomerizm in the excited state mediated by two and one water molecule, respectively. Further theoretical and experimental work is required in order to elucidate the excited states dynamics of HX-N9H and HX-N7H keto tautomers and the influence of the closed excited state tautomerization pathway on the nanosecond MPI efficiency of hypoxanthine-water complexes, however it is possible that the absence of any hypoxanthine signal may be due to the large barriers for tautomeric transitions restricting that range of potential available MPI pathways.

A negative activation barrier for hypoxanthine production in the closing system of four water molecules around adenine has been predicted theoretically[352, 353]. Hence it is possible that deamination reactions resulting in hypoxanthine production may contribute to adenine signal suppression in hydrated conditions. Hydrolytic deamination of cytosine resulting in

uracil production in the supersonic expansion of sublimated cytosine and water vapour has been proposed by Kim et al.[18].

6.8 Cluster mediated MPI.

As discussed in section **6.3.4** the absence (or weakness) of any signal for dry adenine cluster ions in the present measurements does not necessarily indicate that the production of non-hydrated neutral adenine clusters is not significant in the supersonic jets produced in these experiments. Since the most stable geometry of the adenine dimer ion is formed by proton transfer[389], electron impact ionization should indicate the presence of clusters in a molecular beam, at least by producing their protonated fragments. The intermediate excitation step is avoided in electron impact ionization, while in MPI experiments the excitation step can lead to neutral cluster dissociation. Potential products of that dissociation can absorb further photons and contribute to the non-protonated monomer ion signal. Preliminary electron impact (EI) ionization experiments have been carried out for thymine in dry conditions; the results are presented in **Appendix 9.4**. These measurements showed the signal level of protonated thymine (TH^+) much higher than in any MPI experiments. Further EI and MPI measurements are required under similar pressure and temperature conditions.

6.8.1 Discussion on possible tautomeric transitions in dry adenine-adenine base pairs

The MPI pathway through neutral clusters dissociation assumes the presence of complexes in the molecular beam, however they remain undetected due to dissociation in the excited state. In the case of adenine the most stable dimers have the structure in which two ξ sites of two adenine monomers create double hydrogen bond (**Fig. 6.39**).

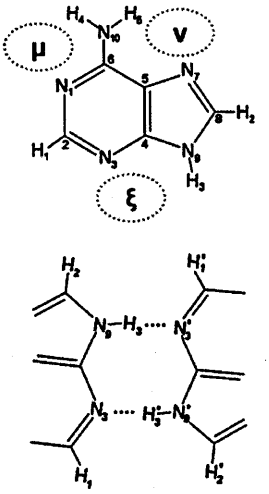

Fig. 6.39: The most stable structure of adenine dimer[163].

Samoylova et al.[331] investigated excited state dynamics of adenine dimers, and obtained 0.7 and 0.9 ps time constants in 250 or 263 +400 nm and 272+800 nm pump probe experiments, respectively. It is unlikely that adenine dimers decaying on such a time scale can be detected in the present nanosecond experiments. Similarities with other compounds can be drawn. Nanosecond and femtosecond MPI ionization of metal organic compounds have been studied using 8 ns and 500 fs laser pulses[406]. The compounds containing only carbon monoxide as ligands to metal atom, for example $Fe(CO)_5$, $Cr(CO)_6$, $Mo(CO)_6$, $W(CO)_6$ exhibit dissociative lifetimes in the region of 1 ps after excitation into the first excited singlet state[318]. As a result, the only observable peak in the nanosecond MPI mass spectrum is that of the bare metal ion, i.e Fe+ (m/z 56), Cr+ (m/z 52), Mo (m/z 96), and W^+ (m/z 184). By applying 500 fs laser pulses for ionization, mass spectra were produced, showing fragments characteristic of the compound under investigation.

Moreover the picosecond time constants obtained by Samoylova et al.[331] correlate well with the timescale of ESPDT (excited state double-proton transfer) in 7-azaindole dimer – studied as the model DNA base pair. This shows that a similar phenomenon could possibly occur in adenine dimer. Double proton transfer was initially interpreted as a one-step process on the order of 1.1 to 1.4 ps in the condensed phase studies[407-409], while gas-phase studies reported a two-step ESDPT process in the 7-Aza dimer, yielding times of 650 fs and 3.3 ps for the first and second proton transfers, respectively, for excitations near the 0-0 transition (Zewail and co-workers[410]). The structure of the 7-azaindole dimer

resembles that of the most stable adenine dimer, while the mechanisms of ESDPT proposed by Sakota et al.[411] are presented in **Fig. 6.40**.

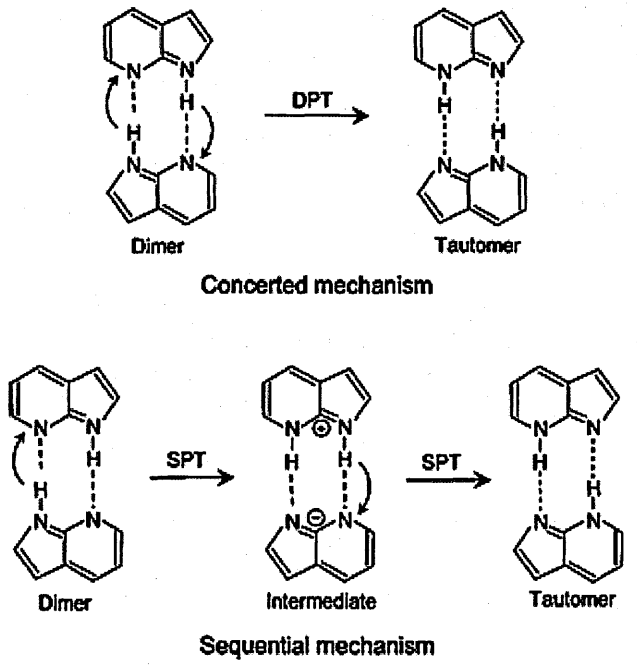

Fig. 6.40: Concerted and sequential mechanisms of ESDPT in 7-azaindole, model DNA base pair[411].

A similar mechanism in adenine followed by neutral dissociation, would lead to the transformation of two 9-H tautomers into two 3-H tautomers, which could be ionized by further absorption of one or two photons. It can be speculated that addition of water to the dimer may hamper or enhance ESDPT rates, or change the dynamics of ESDPT toward one-way excited state hydrogen transfer.

Similar processes may occur in other, double-bonded base pairs. The most stable structure of uracil and thymine dimers is a H-bonded dimer with two N1-H···O2 H-bonds[412, 413]. In the case of the AT dimer, the most stable configuration involves hydrogen bonding at the N3 atom and N9-H site in adenine, as well as the N1-H site and O2 atom in thymine[413]. Zhanpeisov et al.[378] showed that the standard Hoogsteen adenine–uracil base pair can be stabilized through the formation of two parallel H-bonds: one involves the amino group and the N7 site of adenine while the second involves the O4 site and N3–H group of uracil. The structural analysis of these hydrogen-bonded base pairs shows that there are possibilities

of excited state tautomeric transitions. Single hydrogen transfer can be a competing de-excitation route.

Samoylova et al.[331] restricted the discussion of time resolved experiments on adenine and thymine clusters to the dynamical processes involving the $^1\pi\pi^*$, $^1n\pi^*$, and $^1\pi\sigma^*$ states in the corresponding monomers. However other possible relaxation pathways which are specific to the clusters have also been mentioned, i.e. pathways involving charge transfers in the excited state, and a double proton transfer demonstrated for the model chromophore azaindole dimer. The former pathway can result in the formation of protonated monomers, while the latter leads to non-protonated rare tautomeric forms of nucleic acid bases. The absorption of further photons by these species can lead to the formation of monomer ions; this process will be more efficient for tautomers exhibiting longer excited state lifetimes. This pathway is competitive with the monomolecular pathways discussed in chapter 5. Its relevance can be examined in parallel electron impact ionization experiments.

6.9 Summary

The experimental system developed in this work has been used to produce dry and hydrated cluster ions of nucleic acid bases and related chromophores. Under dry conditions a higher nozzle temperature ≥250 °C and backing argon gas pressures of 1 – 2 bar were used in order to obtain A_2^+, T_2^+, A-T^+, A-U^+ dimer ions in mass spectra of adenine-thymine and adenine-uracil mixed systems. In the case of dry adenine seeded in argon molecular beams a very weak A_2^+ signal was only found at a nozzle temperature of 262 °C and 2 bar Ar pressure. Experiments with thymine (0.5 bar and 217 °C) and uracil (0.6 bar and 250 °C) molecular beams did not result in the production of U_2^+ and T_2^+ dimer ions, although their fragments (UH^+ and TH^+) were identified. 5-FU appears to be an exception, fragments of larger cluster ions (protonated dimers) have been found in the mass spectrum at relatively low driving pressure (0.5 bar) and temperature 250 °C without the addition of water vapour.

Adenine dimer and hydrated monomer ions have been observed under hydrated conditions for the temperature range of 240 – 260 °C and 0.8 – 1.4 bar Ar gas pressure, which are lower than for the only A_2^+ signal found for 262 °C and 2 bar in dry conditions. Indeed, even

for temperatures above 300°C and pressure 1.6 bar no evidence for adenine dimer ions and their fragments (AH+) was found under dry adenine molecular beam conditions, while the dimers and their fragments appear for lower temperatures and pressures in the dry mixed adenine-thymine and adenine-uracil molecular beams. High levels of water vapour concentration in the nozzle induced by additional heating of the water reservoir are required in order to observe hydrated complexes in a mass spectrum. Hydrated cluster ions of thymine have been registered for temperatures and Ar pressure ranges of 220-230 °C and 1.7 – 1.8, respectively; while hydrated clusters of uracil required 250 – 260 °C and 1 – 1.1 bar.

The MPI pathways of such clusters have been discussed. Tautomeric transition in the excited state is a likely intermediate step leading to efficient detection of hydrated cluster ions in the present ns MPI experiments. ISC to triplet states through $^1n\pi^*$ states is likely to be limited due to destabilization of $^1n\pi^*$ states caused by hydration. Two competitive alternative processes - the triplet pathway and the excited state tautomerism followed by dissociation - are suggested to play an important role in the production of monomer ions (A^+, T^+, U^+) under non-hydrated conditions.

Photon orders indicating two- and three-photon processes leading to the production of hydrated cluster ions and their fragments (protonated and non-protonated monomers), have been measured in hydrated conditions. In particularly, hydrated adenine and uracil monomer ions show photon orders indicating that a two-photon ionization process is responsible for $U^+(H_2O)_n$ and $A^+(H_2O)_n$ production. Photon orders of 3.2±0.4 and 3.0±0.1 indicating photofragmentation of larger cluster ions after absorption of a third photon were measured for adenine and uracil protonated monomers (AH^+ and UH^+), respectively.

Adenine cluster ions with up to 4 water molecules attached to a single base have been observed. $A^+(H_2O)_n$ signals were relatively strong for n=1-4 and negligible for n>4. It has been found that the relative intensity of $A(H_2O)_n^+$ and $A_2(H_2O)_n^+$ ions varied according to the supersonic jet and laser fluence conditions. Cluster ions with the maximum number of water molecules attached to adenine dimers equal to 7 have been detected, the same number of water molecules attached has been found for the largest hydrated adenine-uracil

base pair ion $AU^+(H_2O)_7$. Uracil cluster ions $U^+(H_2O)_n$ have been observed up to a maximum of n=7, while the largest hydrated thymine cluster ion $T^+(H_2O)_n$ could not be identified since it is not possible to distinguish $T_m(H_2O)_n^+$ from $T_{m+1}(H_2O)_{n-7}$ ($n \geq 7$, $m \geq 1$). $T^+(H_2O)_6$ is the largest which could be unambiguously assigned.

7 Multiphoton fragmentation studies of adenine, thymine, uracil and 5-fluorouracil

7.1 Introduction

In this chapter multiphoton fragmentation leading to ionic fragments with m/z less than m/z of a parent molecular ion is presented for adenine, thymine, uracil and 5-fluorouracil under dry and hydrated conditions. The present results have been compared with dissociative ionization carried out using electron and single photon ionization. MPI data obtained in this work are presented in the form of mass spectra, while the most intense fragments registered in electron impact and single photon ionization experiments reported in the literature are usually summarized in tables. Earlier fragmentation studies of nucleic acid bases in the gas phase reflect the interest in ionization induced processes in cancer radiotherapies (notably using beams of X-rays, electrons, protons, or carbon ions)[414, 415], as well as in astrobiology and exobiology, where the goal is to elucidate the possible formation of these molecules in the interstellar medium or on cometary grains[416]. Fragmentation studies are also important in the field of biotechnological applications, such as sensors and molecular electronics[417]. Furthermore, laser-induced multi-photon dissociative ionization studies of isolated molecules and clusters in the gas phase can enhance our understanding of processes in biological material subjected to intense laser pulses[61-63].

In this work fragmentation of isolated nucleic acid bases and their clusters has been investigated using tightly focused UV (223 – 227 nm) laser pulses of energy up to 500 – 600 μJ. A number of ions with mass/charge less than the parent molecular ion have been observed. These *low-mass* ions include fragments of the target molecules and products from impurities in the diagnostic chamber and / or the supersonic jet. The signal/background ratio depends on the quality of the laser beam – molecular beam alignment and the effectiveness of the fragmentation processes. In some cases the background level is significant and the signal is presented together with the background recorded at a much lower oven/nozzle temperature.

7.2 Adenine fragment ions

7.2.1 Fragmentation of adenine monomers

Fig. 7.1 shows the multi-photon ionization mass spectrum of adenine fragment ions. The fragment ion signals are much lower than the adenine monomer ion signal at the laser fluences applied in these measurements.

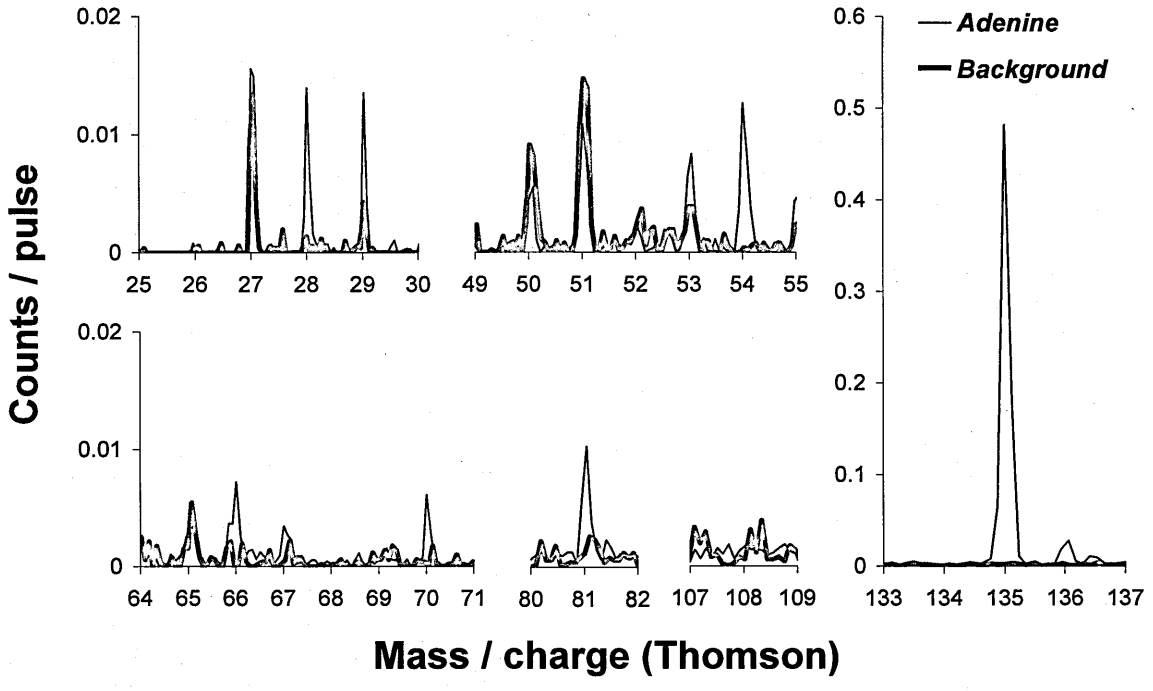

Fig. 7.1: Comparison of MPI (226 nm) mass spectra of argon jets (0.4 bar) seeded with adenine at 229.7 ± 0.4 °C (labeled *Adenine* ~ 4.6×10^6 W/cm^2) and at 110°C (*Background* ~ 4.7×10^6 W/cm^2). The selected ranges show details of the clearest fragment ion peaks traceable to adenine (28, 54, 66, 70, and 81Th) and of the *absent peak* at 108 Th.

Peaks with higher intensity than the background at mass/charge <135 Th can be attributed to adenine fragment ions. One of the most significant adenine fragments observed in the mass spectrum shown in **Fig. 7.1** is the 28 Th fragment ion. Previous REMPI-TOF measurements at 222 nm (5.58 eV)[327] have shown 28 Th products from laser-desorbed adenine in a supersonic jet; but no other fragments have been detected. Lin et al.[325] reported significant photodissociation of adenine in their 248 nm ns MPI experiments but did not specify the fragment ions. The 28 Th ion has an appearance energy (AE) of 13.1±0.1 eV in single photon ionization (SPI) experiment and is assigned to H_2CN^+[146]. It

has been suggested that this species is produced by dissociation of the parent adenine ion into H_2CN^+ and $C_4H_3N_4$, however other pathways for H_2CN^+ formation are also possible[146].

The mass spectrum presented in **Fig. 7.1** also indicates the presence of 29 Th fragment ions from adenine, although there is also a background contribution at this m/q ratio. Jochims et al.[146] attributed this fragment ion to NH_2CH^+ and reported an appearance energy of 14.0 eV[146].

The principal pathway of adenine parent ion dissociative ionization has been reported to involve the successive loss of neutral HCN (m = 27 a.m.u.) groups, leading to the creation of 108, 81, 54, 27 Th[146]. The initial HCN loss requires at least two bond ruptures, and accordingly has a greater activation energy than the succeeding HCN losses[146]. The 81 and 54 Th ions can be clearly distinguished in **Fig. 7.1**. The 108 Th fragment ion is absent in both MPI mass spectra presented in this section, however it has been observed in electron and single photon ionization experiments[146] on adenine summarized briefly in **Table 7.1**. Although the present results and the literature data have been recorded using different sources of radiation and different adenine source conditions (effusive beams for Knudsen-type oven sources), similar fragments of adenine are observed.

The 54 Th fragment ion produces a strong peak in the single-photon (20 eV) and electron impact (70 eV) mass spectra (see **Table 7.1**)[146]. The 54 Th ion (AE = 13.7±0.1 eV) has been assigned to $C_2H_2N_2^+$ formed by sequential HCN loss from adenine parent ion with significant nuclear rearrangements[146].

Table 7.1: The ten strongest fragment ions in 70 eV electron impact[418] and 20 eV single photon[146] ionization mass spectra of adenine. The intensity is given as a percentage of the parent adenine molecular ion. Fragment ions which can be clearly traced to adenine (as opposed to background) in the present MPI experiments (**Fig. 7.1** and **Fig. 7.4**) are highlighted in red bold text.

70 eV electron impact[418]		20 eV photon absorption[146]	
Fragment ion	Intensity / A^+ signal	Fragment ion	Intensity / A^+ signal
28^+	78 %	**28^+**	110 %
$108^{+\dagger}$	34 %	**29^+**	60 %
54^+	31 %	**$108^{+\dagger}$**	57 %
53^+	24 %	**54^+**	55 %
81^+	19 %	**81^+**	50 %
66^+	15 %	**66^+**	41 %
43^+	12 %	43^+	34 %
29^+	12 %	**53^+**	28 %
27^+	12 %	**70^+**	17 %
38^+	10 %	42^+	16 %

† In the present measurements, the peak at 108 Th was only observed under hydrated conditions.

Jochims et al.[146] presented a number of other pathways leading to the creation of other adenine fragment ions. The fragmentation pathway starting from the $C_4H_4N_4^+$ fragment ion (108 Th) may lead to the creation of $C_3H_2N_2^+$ (66 Th) through the loss of NH_2CN, while a further loss of HCN leads to C_2N^+ (39 Th). Another formation pathway for the 66 Th ion may be rupture of the C5-C6 bond and the C4-N3 bond in the adenine parent ion (see **Fig. 1.4**). Another possible pathway to form the C_2HN^+ (39 Th) is NH_2CN loss from 81 Th. Various other peaks observed in the previous single-photon and electron impact ionization data cannot be distinguished unambiguously in the present data due to strong background signals (e.g. 27 Th, 39 Th and 43 Th). It is worth noting that the 51 Th signal in the present adenine and background data has never previously been observed as an adenine fragment; therefore the 51 Th fragment ion may be a good indicator of the background level.

Direct loss of NH_2CN from the parent ion would give a 93 Th fragment ion formed by the rupture of three bonds requiring a high internal energy in the parent ion[146]. No evidence for 93 Th ions have been found in **Fig. 7.1** or indeed in the previous electron impact or single photon ionization data[146]. The loss of C_3HN_2 (65 a.m.u) from the parent ion results in $C_2H_4N_3^+$ (70 Th); a further loss of HCN leads to $C_3HN_2^+$ (43 Th). A peak at 70 Th can be identified in the mass spectrum (**Fig. 7.1**), but a strong background signal is present at 43 Th. There can be also a pathway to 70 Th ion production via 108 Th, where the neutral loss from the 108 Th precursor is C_2N (38 a.m.u.)[146].

The signal intensity of the adenine parent ion (135 Th) and its 28 (Th) fragment as a function of laser fluence is shown in **Fig. 7.2**. Both dependencies have been recorded simultaneously and the plot was constructed on the basis of four separate measurements taken under identical supersonic jet conditions and laser focusing / alignments. The resultant photon order for 135 Th ion production (0.4±0.1) is evidently lower than the photon order of 3.0±0.5 presented in chapter 5. This can be attributed to saturation effects. Increased fragmentation at higher laser fluence provides an additional mechanism tending to reduce the 135 Th signal and therefore the measured photon order. Indeed at pulse energies >500 μJ (248 nm, focused, 15 ns pulses), Lin et al.[325] observed a negative photon order for adenine$^+$ production and attributed this to the latter effect.

Fig. 7.2 shows that α(28 Th) = 1.5 ± 0.1. This also indicates some level of saturation in H_2CN^+ production under the present conditions, as 3 photons at 223.8 nm (5.54 eV) are required to overcome the appearance energy from gas-phase adenine[146]. The measured photon order for the 28 Th peak is greater that for the 135 Th signal. The difference of 1 implies that 1 more photon is typically required to produce H_2CN^+ compared with non-dissociative MPI. This may be interpreted as being consistent with the assumption that 28^+ is produced through 135^+ by absorption of additional photon, however other mechanisms are also possible (for example via neutral fragmentation).

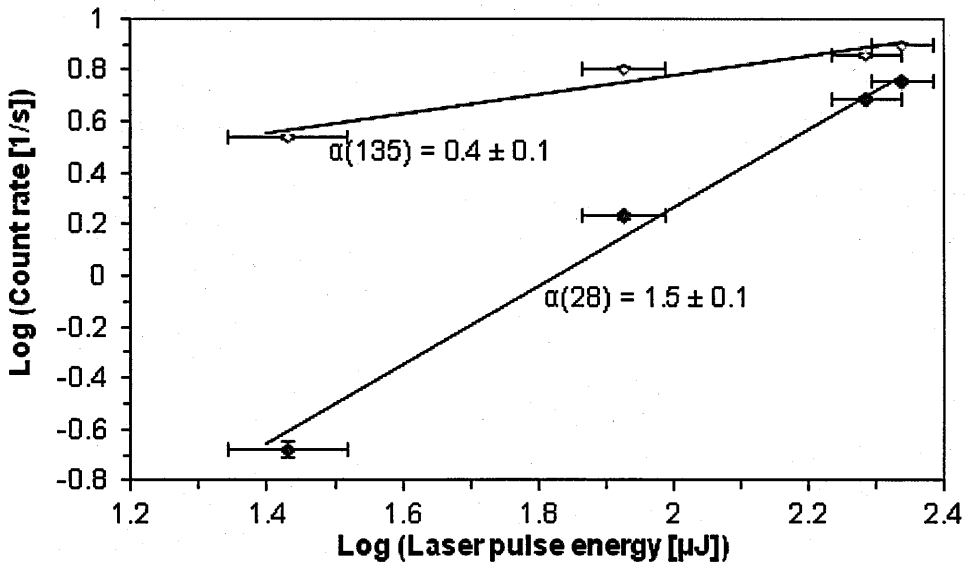

Fig. 7.2: Pulse energy dependence for the 135 and 28 Th peaks in one-color MPI (223.8 nm) mass spectra of dry adenine (235°C, 0.4 bar argon); approximate fluence range: 7.2×10^{6} - 5.8×10^{7} W/cm^2.

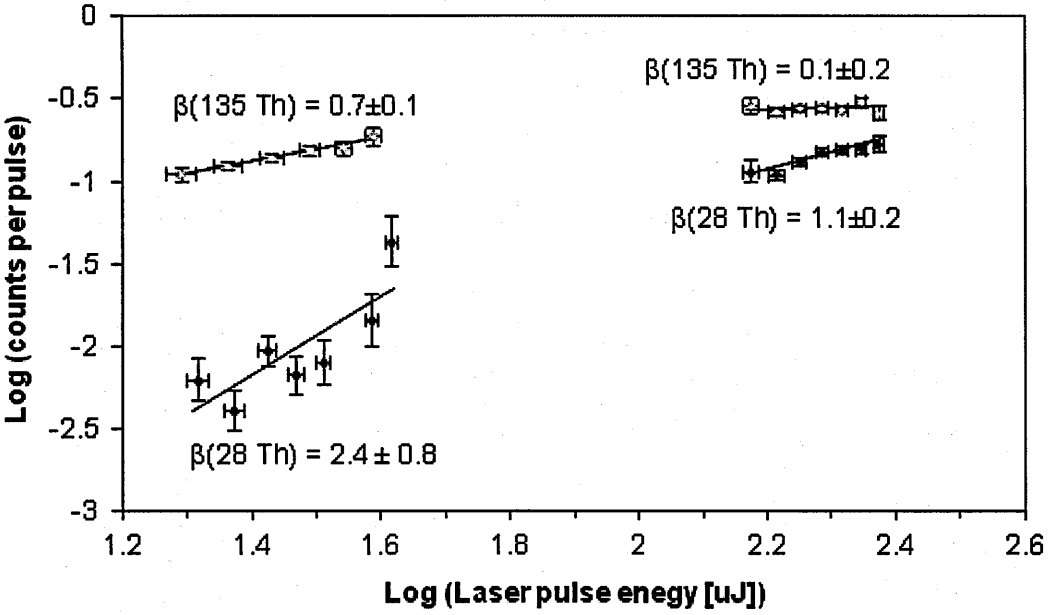

Fig. 7.3: Detailed pulse-by-pulse analysis of the data set shown in **Fig. 7.2**.

The pulse-by-pulse analysis demonstrated in **Fig. 7.3** shows increasing level of saturation (decreasing photon orders) as a function of laser pulse energy for 135 Th and 28 Th ions. The data set analyzed in **Fig. 7.3** is narrowed in relation to the data set presented in **Fig. 7.2** (points at the edges of laser pulse energy range are taken into account).

7.2.2 Fragmentation of adenine under hydrated clustering conditions

The mass spectrum presented in **Fig. 7.4** has been recorded under hydrated clustering conditions. The major difference between the mass spectra presented in **Fig. 7.1** and **Fig. 7.4** is the presence of the 108 Th fragment ion in **Fig. 7.4**. The 108 Th fragment ion has been not detected in the present measurements unless cluster ions and / or their protonated monomer fragments appear in the mass spectra.

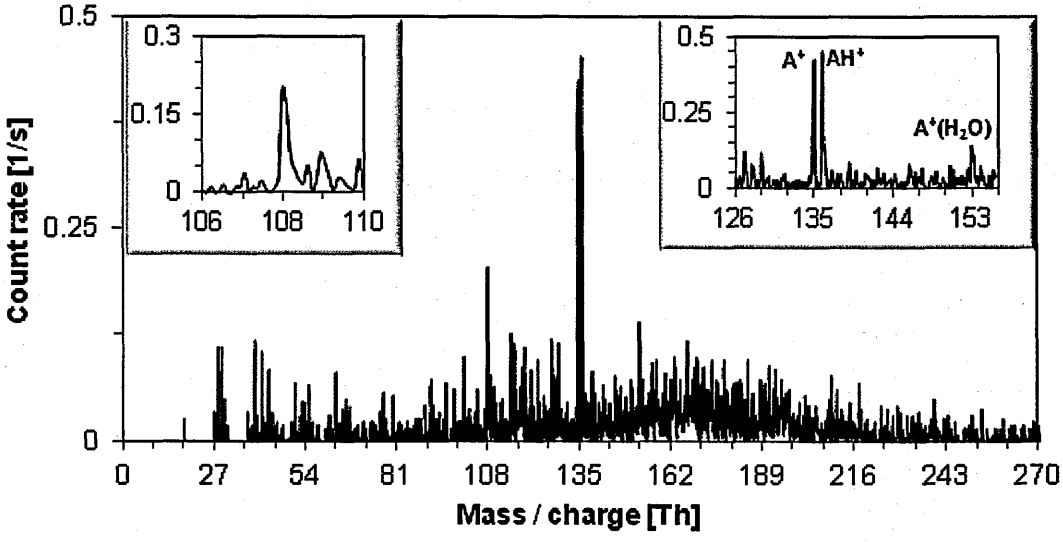

Fig. 7.4: One-colour (226 nm, ~ 2.3×10^6 W/cm^2) MPI mass spectra of hydrated adenine (240°C, 1.0 bar argon, water 80°C). At higher masses the hydrated adenine monomer peak can be found (153 Th), but dimer ions (270 Th) have not been detected.

Schlathölter et al.[415] studied adenine dissociative ionization in clusters for 50 keV O_5^+ impact on pure adenine complexes. Clear differences were observed in fragment ion production compared with equivalent measurements on adenine monomers, notably major enhancement of the $C_5H_3N_4^+$ channel (119^+, NH_2 loss). No detailed explanation has been proposed for Schlathölter et al.'s[415] observation of $C_5H_3N_4^+$ enhancement for collision-induced dissociative ionization of dry adenine clusters.

Cheong et al.'s[419] measurements of AH^+ fragmentation following photoexcitation at 266 and 263 nm revealed intense fragment ion production at 119 (NH_3 loss), 109 (HCN loss), and 18 (NH_4^+) Th, with additional signals at 94 (NH_2CN loss), 82 ($H_2C_2N_2$ loss), 67 (HCN-NH_2CN loss), 55 ($H_3C_3N_3$ loss), and 28 ($HCNH^+$) Th. Weak features of 119^+ and 18^+ fragment ions attributed to AH^+ fragmentation which can be noticed in **Fig. 7.4** suggest that

AH^+ fragmentation is only a small contribution to the mass spectrum. Further studies with more intense laser beams are required in order to confirm this.

7.3 Thymine fragment ions

7.3.1 Fragmentation of non-hydrated thymine

Fig. 7.5 shows a multi-photon ionization mass spectrum of thymine fragment ions recorded at 226 nm. Fragments attributed to thymine in previous measurements (**Table 7.2**) are found at 27, 28, 54 and 55 Th, but not at 83 Th, while 27 Th is accompanied by a relatively strong background contribution, very little background can be found at 54, 55 and 28 Th. It is unlikely that the large signal/background (S/B) ratio in the latter case is caused by laser fluence difference in **Fig. 7.5**. No other peaks featuring similarly high S/B ratio have been found in this mass spectrum, only those attributed to the most intense thymine fragments in electron impact and single photon ionization experiments (**Table 7.2**).

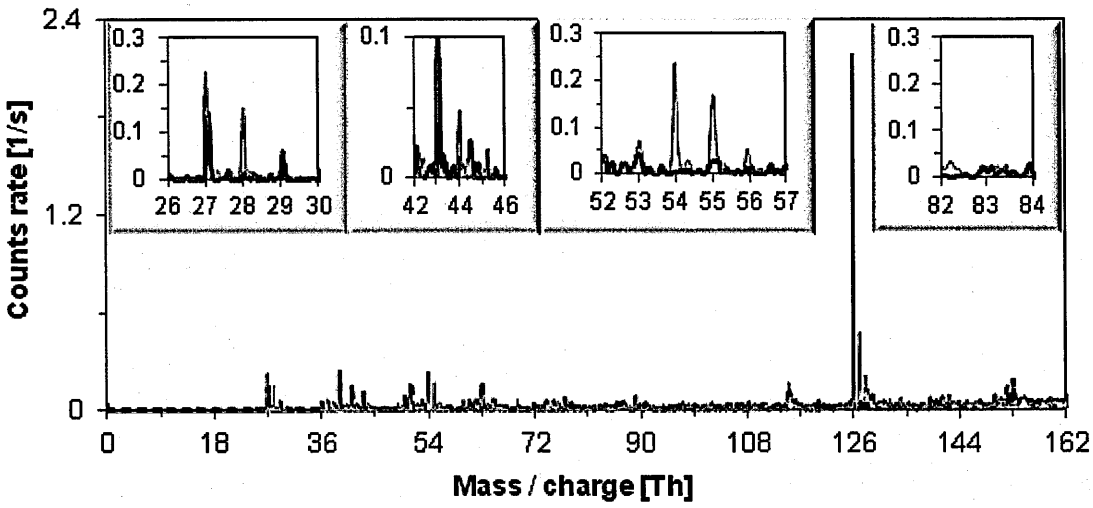

Fig. 7.5: Black line: one-colour (226 nm, ~ 4.7×10^6 W/cm^2) MPI mass spectra of background (110°C, 0.4 bar argon). Red line: one-colour (226 nm, ~1.7×10^7 W/cm^2) MPI mass spectrum of thymine (217°C, 0.5 bar argon).

Jochims et al.[146] indicated that the principal fragmentation pathways of the thymine parent cation involve sequential loss of HNCO (isocyanic acid). One unit loss gives rise to the 83 Th (AE = 10.7 eV) which is the precursor to the subsequent fragmentation steps. A weak signal of 83 Th has been detected in present work, but only in strong clustering conditions –

see section **7.3.2** (**Fig. 7.9**). The fragment ion detected with the highest intensity in previous single photon absorption and electron impact experiments is 55 Th; its peak was at least two times stronger than that of the 54 Th fragment ion in the electron impact and photon ionization data (**Table 7.2**). 55 Th has been assigned to the CH_3CCHNH^+ ion (AE = 11.7 eV), and has been attributed to CO loss by the 83 Th ion[146]. The difference in intensity between 54 Th and 55 Th shown in **Fig. 7.5** is not very significant. In the case of the summed mass spectrum for laser pulses energies within the range of 10 – 550 μJ the ratio of intensities 54 Th/55 Th is ~ 1.

Table 7.2: Up to nine most intense fragment ions in 70 and 20 eV electron impact[420] and 20 eV photoionization[146] mass spectra of thymine. Fragment ions which can be clearly traced to thymine (as opposed to background) in the present experiments (**Fig. 7.5**, **Fig. 7.7** - **Fig. 7.9**) are highlighted in red bold text.

70 eV electron impact		20 eV electron impact		20 eV photon absorption	
Fragment ion	Relative intensity	Fragment ion	Relative intensity	Fragment ion	Relative intensity
55^+	100%	**55^+**	47 %	**55^+**	100 %
28^+	59 %	**83^+**†	17 %	**28^+**	67 %
54^+	44 %	**54^+**	11 %	**54^+**	42 %
27^+	36 %	**28^+**	6 %	27^+	11 %
52^+	14 %	82^+	4 %	82^+	10 %
26^+	13 %	84^+	2 %	56^+	9 %
39^+	12 %	56^+	2 %	**44^+**	9 %
82^+	7 %	other ions	0 %	39^+	9 %
56^+	7 %			**83^+**†	8 %

† In the present measurements, the peak at 83 Th was only observed in hydrated conditions.

54 Th is produced with significant intensity, as shown in **Fig. 7.5**. It was considered[146] that 83 Th can lose a hydrogen atom to give 82 Th, a further loss of a CO group could be responsible for the formation of the strong 54 Th fragment ion $C_3H_4N^+$. However the ion yield measurements[146] show that the AE of 54 Th (~12.9 eV) is smaller than that of 82 Th (13.2 eV), hence 54 Th formation via hydrogen loss from from the 55 Th has been

proposed[146].

The strong ion signal that can be traced exclusively to thymine fragmentation in the present measurements has m/z = 28 Th. Jochims et al.[146] assigned this ion to $HCNH^+$ and proposed five different possible pathways via the respective precursors 126, 83, 82, 55 and 54 Th. The pathways via 82, 55 and 54 Th involve the rupture of only one further carbon-carbon bond to form $HCNH^+$. De Souza et al.[421] and Jochims et al.[146] have demonstrated that 55 and 28 Th thymine fragments dominate the spectrum in single photon ionization at photon energies of 21 eV and 20 eV, respectively. These results are in agreement with Jochims et al.[146] for 20 eV photon impact. A weak signal at 44 Th in **Fig. 7.5** can be also attributed to a thymine fragment ($HCNOH^+$), while Jochims et al. assigned this peak to CO_2 impurity in the 20 eV single photon ionization experiment[146].

Using respective femtosecond-timescale pump and probe wavelengths of 267 nm and 400 nm, Samoylova et al.[422] identified the following fragments of thymine: 28 Th, 55 Th (the strongest), and 83 Th. 83 Th ions have not been observed in the present MPI measurements of non-hydrated thymine-argon beams.

Fig. 7.6 shows photon orders for 126 Th and 28 Th ion production to be $\alpha(126) = 0.9\pm0.1$ and $\alpha(28) = 2.4\pm0.2$. Both values are clearly affected by partial saturation. A photon order difference of 1.5±0.2 is observed between 28 Th fragments and thymine ions. This indicates that at least one more photon is required to produce the 28 Th fragment ion. The difference of 1.5±0.2 suggests that there may be more than one pathway leading to the production of 28 Th ions, and the MPI pathways may be different in terms of the number of photons absorbed. A contribution to the observed difference of 1.5 may also originate from the detector saturation (non-specific to physical phenomenon responsible for photon orders) having larger impact on the characteristic of the 126 Th ion lowering its α value more than $\alpha(28)$. This can happen since the total signal of the 126 Th is stronger and the detector response in this situation is more prone to saturation.

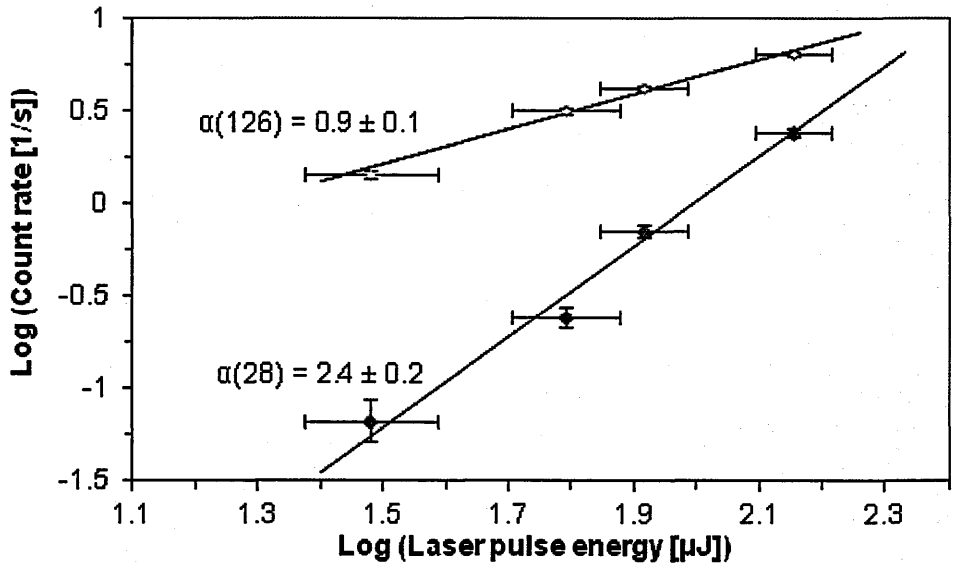

Fig. 7.6: Count rate of 28 Th fragment ions as a function of pulse energy (thymine temperature 219±1°C, argon pressure 0.49 bar, wavelength 226 nm, and approximate fluence range 7.4×10^{6} - 2.2×10^{8} W/cm^{2}). The figure also shows the equivalent data for thymine^{+} (126 Th) production over the same pulse energy range.

7.3.2 Fragmentation of thymine under hydrated clustering conditions

The clustering conditions of the target supersonic beam affect the present MPI fragmentation patterns of thymine. In particular, **Fig. 7.7** demonstrates the 55 Th / 54 Th fragment ion ratio is significantly greater under hydrated cluster conditions. Indeed strong production of 55 Th ions is demonstrated for three different wavelengths (222, 226 and 229 nm) and fluences in the mass spectra presented in **Fig. 7.7**, **Fig. 7.8** and **Fig. 7.9**. This apparent effect is broadly consistent with MPI observations regarding 108 Th fragment ion production from isolated and hydrated clustered adenine. Heavier fragment ions with lower appearance energies tend to be detected with higher intensity in hydrated clustering conditions.

A small increase in intensity of the 83 Th ion (the first intermediate stage on the fragmentation pathway) has been observed due to hydration (**Fig. 7.7**, **Fig. 7.9**). This appears to be consistent with the fact that the intensity of the 83 Th fragment ion was observed to be low for single photon and electron impact ionization. The low 83 Th has been attributed to the methyl group weakening the carbon-carbon bond to which the

oxygen atom is attached, via hyperconjugation that affects the π electron distribution[146].

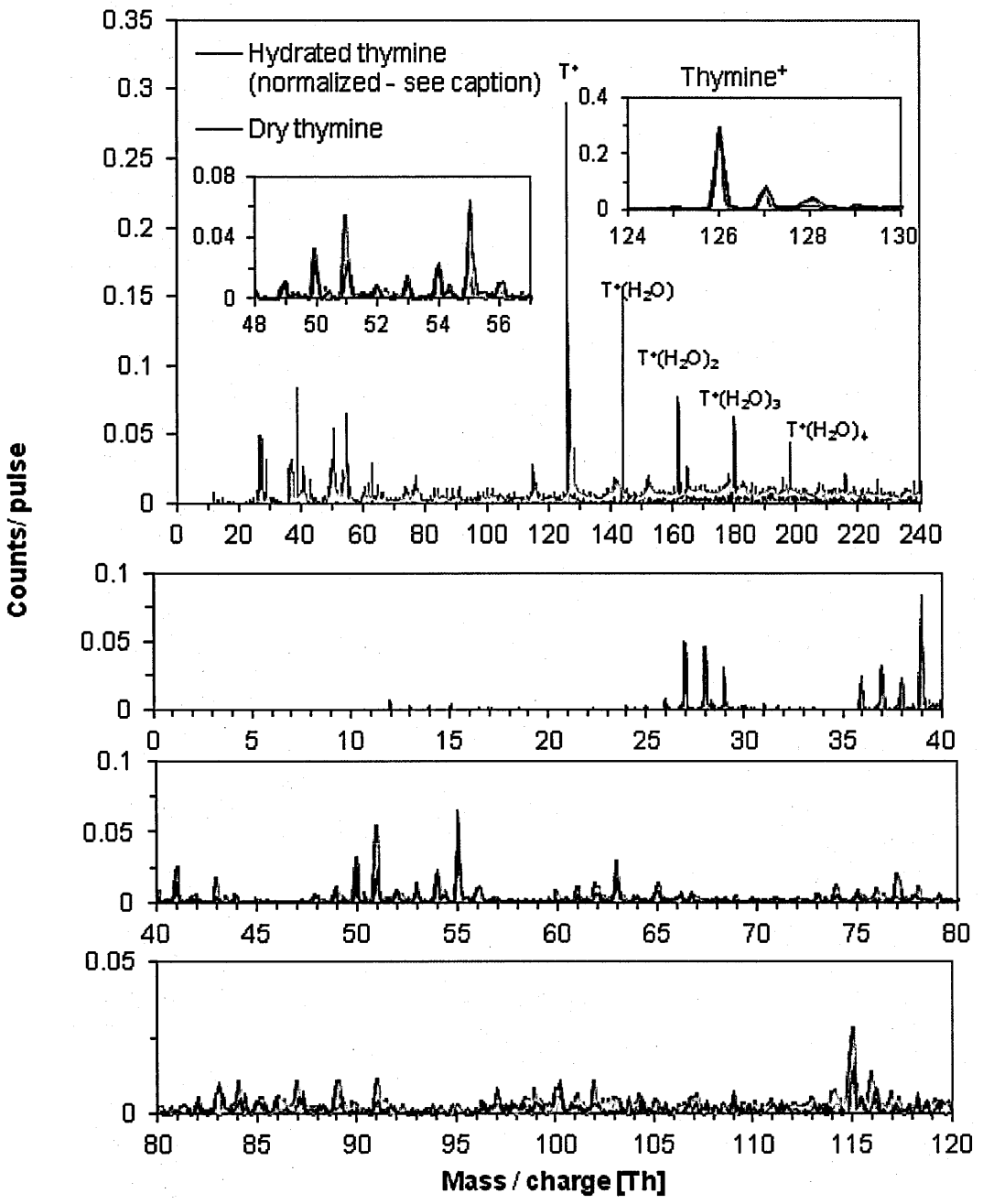

Fig. 7.7: Comparison of MPI (226 nm, ~ 4.0×10^{7} W/cm^2) mass spectra of thymine in dry (thymine 217°C, argon 0.5 bar) and hydrated conditions (thymine 230 - 235°C, water 90°C, argon 1.6 bar). Inserts show detailed parts of the mass spectra. Normalization: to enable easier relative comparisons, the hydrated thymine signal has been multiplied by a constant (1.74) in order to match the intensity of the peak at 126 Th in the dry thymine measurement.

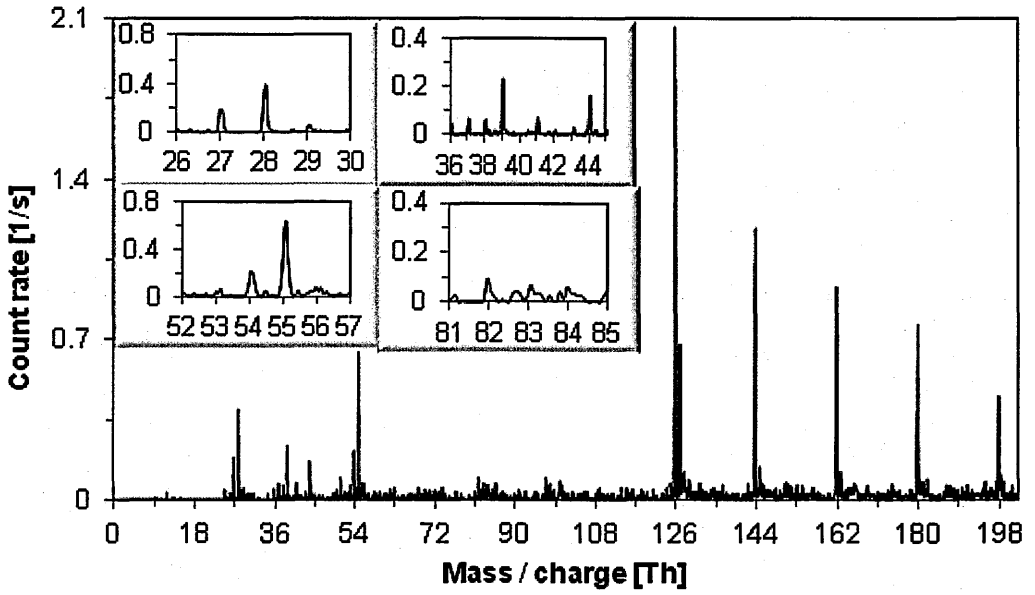

Fig. 7.8: One-colour (222 nm, ~ 2.7×10^{7} W/cm^2) MPI mass spectrum of thymine (230°C, 1.8 bar argon, water 90°C).

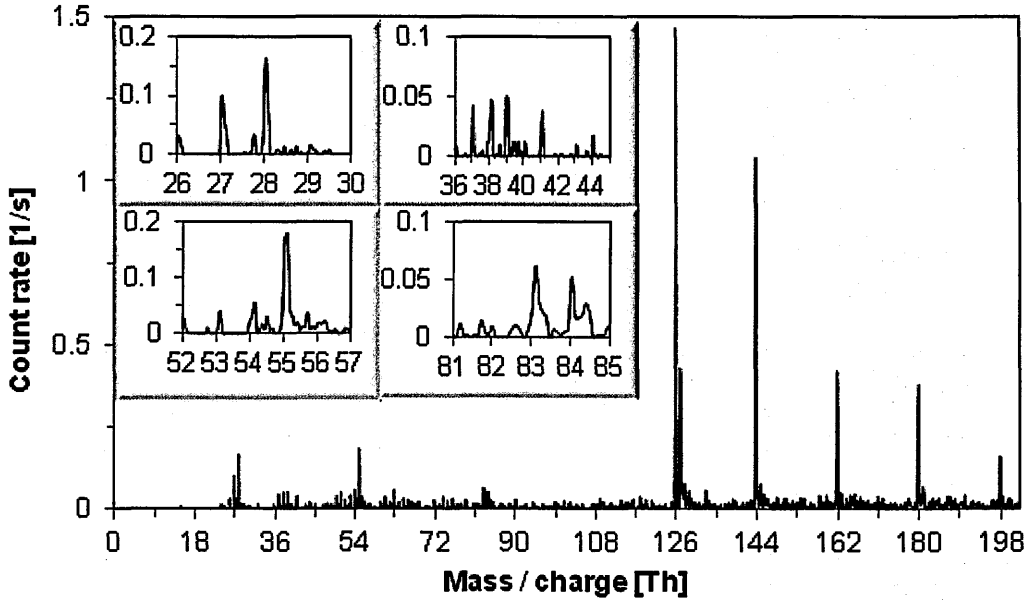

Fig. 7.9: One-colour (229 nm, ~ 7.4×10^{5} W/cm^2) MPI mass spectrum of thymine (230°C, 1.8 bar argon, water 90°C).

7.4 Uracil fragment ions

7.4.1 Fragmentation of non-hydrated uracil

The mass spectrum recorded in this work for non-hydrated uracil is presented in **Fig. 7.10**. A clear peak due to uracil fragmentation can be distinguished at 28 Th with negligible background contribution. Although weaker and less conclusive, the peaks at 42 and 69 Th

do not coincide with clear background peaks, suggesting products of uracil dissociative MPI. These three fragment ions have been identified in single photon absorption and electron impact experiments[146] as having the strongest yields.

Table 7.3 presents the relative intensities of the fragment ion peaks in the mass spectrum obtained by 20 eV single photon ionization by Jochims[146], 70 eV electron impact by Rice et al.[420], and 20 eV electron impact by Hecht et al.[423]. The fourth peak in terms of intensity in the 70 eV electron and 20 eV photon impact experiments is 40 Th fragment ion (**Table 7.3**). This fragment ion has been also identified in the mass spectrum shown in and **Fig. 7.10**. Additional ionic fragments at 53 Th and 55 Th have been found over the background signal, however their origin is unclear.

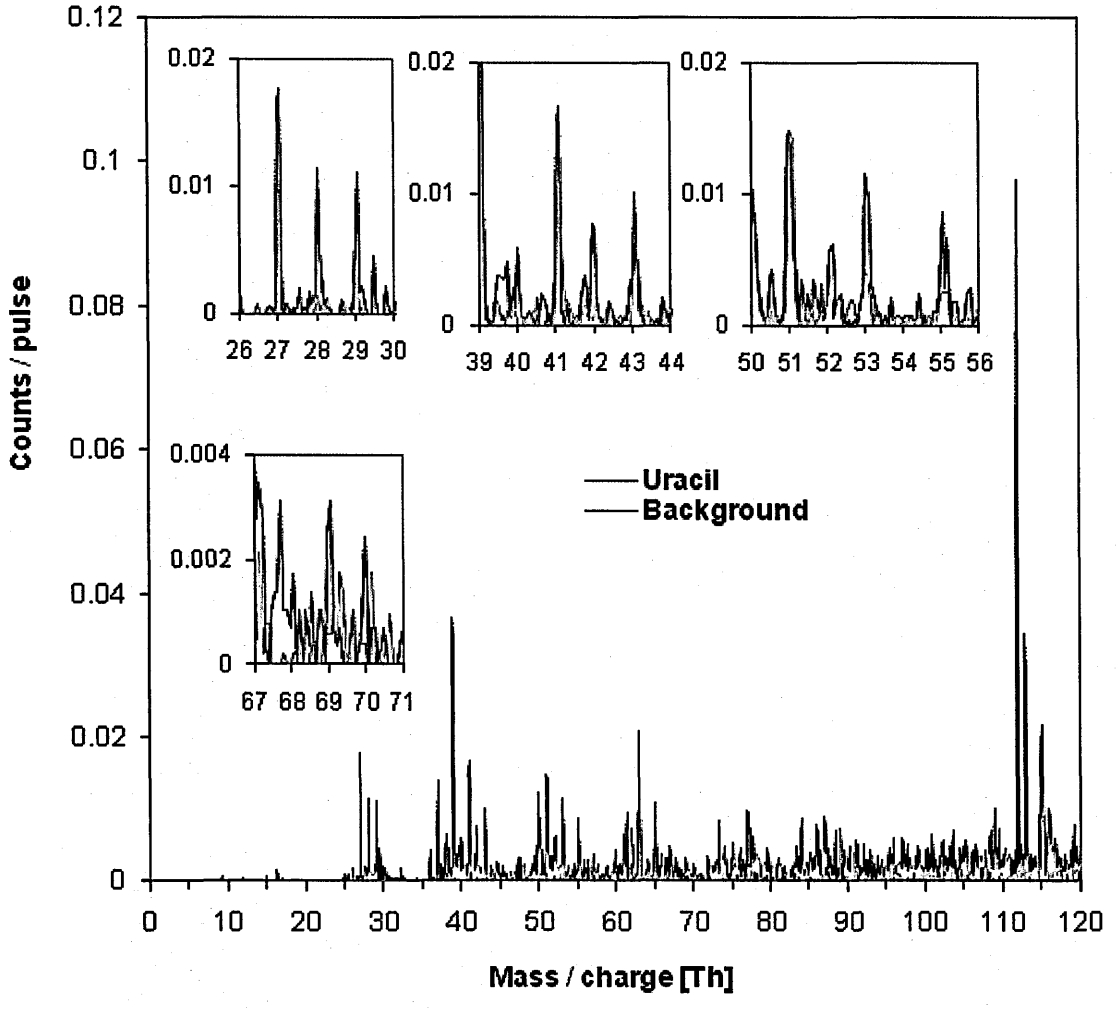

Fig. 7.10: MPI (223.8 nm, ~ 7.5×10^6 W/cm^2) of uracil (249°C, 0.6 bar argon,) compared with a background measurement at laser fluence ~ 4.7×10^6 W/cm^2.

The principal fragmentation pathways of the uracil parent cation involve HNCO loss, which gives rise to the 69 Th ion, $C_3H_3NO^+$ (AE = 10.95)[146]. The charge switch reaction produces the 43 Th ion, $HNCO^+$ (AE=13.6 eV)[146]. The 69 Th fragment ion can further fragment by a number of different pathways. Many of these pathways in uracil are similar to pathways in the fragmentation of the 83 Th ion of thymine. Jochims[146] proposed that in the 83 Th ion of thymine, loss of a CO molecule forms the 55 Th ion (the most abundant ion in the thymine mass spectrum for single photon ionization and electron impact ionization). In uracil, CO loss from 69 Th gives rise to the 41 Th fragment ion, which is not a major fragment ion in the present uracil mass spectrum.

Table 7.3: The most intense (>5% of the maximum product ion) molecular and fragment ions in 70 and 20 eV electron impact[420, 423] and 20 eV photoionization[146] mass spectra of uracil. Fragment ions which can be clearly traced to uracil (as opposed to background) MPI in the present experiments (**Fig. 7.10** and **Fig. 7.11**) are highlighted in red bold text.

70 eV electron impact		20 eV electron impact		20 eV photon impact	
Fragment ion	Relative intensity	Fragment ion	Relative intensity	Fragment ion	Relative intensity
42^+	100%	**28^+**	74 %	**42^+**	100 %
28^+	78 %	**69^+**	69 %	**28^+**	86 %
69^+	63 %	**42^+**	59 %	**69^+**	52%
40^+	57 %	**40^+**	21 %	41^+	50 %
41^+	48 %	41^+	21 %	68^+	33 %
68^+	33 %	68^+	15 %	**40^+**	25 %
43^+	15 %	43^+	6 %	43^+	10 %
39^+	15 %	39^+	5 %	27^+	4 %

The 42 Th fragment ion (AE = 13.41 eV) in uracil is assigned to $HC{=}COH^+$ formed by a rearrangement reaction (1,5 H-shift) and subsequent loss of HCN from the 69 Th precursor ion[146]. Another fragmentation pathway from the 69 Th precursor leads to formation of $HCNH^+$ (28 Th, AE = 13.75 eV), via rupture of the central carbon-carbon bond and loss of

the ketene radical HC=C=O[146]. It has been noted that the charge switch ion $HC=C=O^+$ (41 Th) can contribute to the total signal. The second mechanism for producing $HCNH^+$ (28 Th) involves direct formation from the parent ion (112 Th), which requires rupture of two bonds, the C5-C6 double bond and the C2-N1 bond. In contrast to thymine, for which five different possible pathways for forming the $HCNH^+$ ion have been suggested[146], in the case of uracil there appear to be only two viable pathways to the formation of $HCNH^+$.

The 69 Th ion can also lose a hydrogen atom to give 68 Th, which is a strong ion in photon and electron impact experiments (**Table 7.3**), with AE = 13.40 eV. It has been proposed that the 40 Th fragment ion can be formed via loss of CO group and hydrogen atom from 69 Th[146].

The most prominent uracil fragments detected in fs multiphoton dissociative ionization experiments (260+780 nm) are 28, 41 , 42 , and 69 Th[424], all observed in the present ns MPI data. Calculations indicated that most fragments observed in uracil are generated from fragment 69 Th, i.e. through sequential fragmentation. The 69 Th fragment is generated from an ionic ground state when ~ 2 eV of vibrational energy exists in the cation. However, if ionization occurs on a higher ionic state and then nonadiabatic transitions move the population to D_0 (ionic ground state) then there will be more energy available to further break fragment 69 Th to form the smaller observed fragments[424]. The same explanation can be applied to adenine and thymine fragmentation mechanisms via precursor fragment ions, i.e. 108 Th and 83 Th, respectively.

7.4.2 Fragmentation of uracil under hydrated clustering conditions

A different picture of multiphoton fragmentation can be found for hydrated clusters of uracil (**Fig. 7.11**) compared to non-hydrated conditions (**Fig. 7.10**). In particular the 69 Th fragment ion dominates the spectrum in the range below 112 Th. This observation is broadly consistent with our interpretations of the earlier findings for adenine and thymine: clustering shifts the mass distribution of molecular fragment ions towards heavier species, towards the initial precursor of any sequential fragmentation series.

In addition, photon order measurements have been performed on the uracil 69 Th fragment ion (**Fig. 7.12**). The photon order of the 69 Th fragment ion is equal to 4.2±0.7. It is reasonable to assume that one more (the fourth) photon absorbed by ionic cluster fragments U^+ or UH^+ leads to the observed 69 Th fragment ion in the present experiments. The photon order of UH^+ equal to 3.0±0.1 has been presented in section **6.6.2**, while some contribution from a 3-photon process to the production of U^+ has been confirmed by the photon order value of 2.4±0.2. The "U^+" mechanism would lead through photon absorption by the hydrated cluster ions $U^+(H_2O)_n$, the photon order measurements indicated that 2 photons are required to produce these ions and absorption of a third photon is the next step (possibly leading to U^+). Fourth photon absorbed by U^+ being an ionic cluster fragment could result in the 69 Th fragment ion production. Due to the one proton excess in the UH^+ cluster fragment ion, the direct precursor of 69 Th could be the 70 Th fragment ion produced after absorption of a fourth photon by UH^+, the 70 Th fragment ion may subsequently lose one proton due to a vibrational energy excess.

Similar mechanisms (through ionic cluster fragments) may lead to the enhanced signal of 108 Th in experiments on hydrated adenine, as well as 83 Th and 55 Th fragment ions in experiments on hydrated thymine.

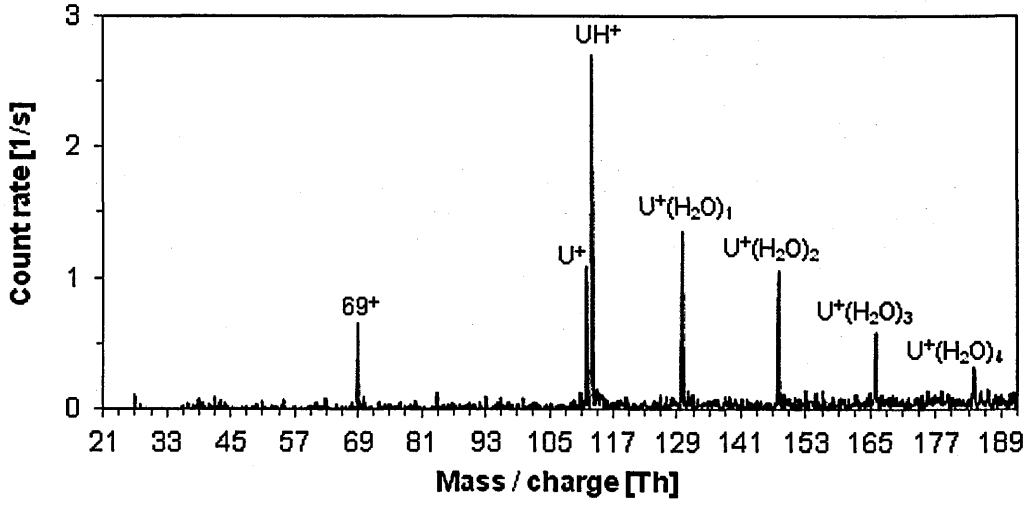

Fig. 7.11: One-colour (224 nm, ~ 3.3 ×10^6 W/cm^2) MPI mass spectra of hydrated uracil (250°C, ~1.2 bar argon, water 80 - 100°C).

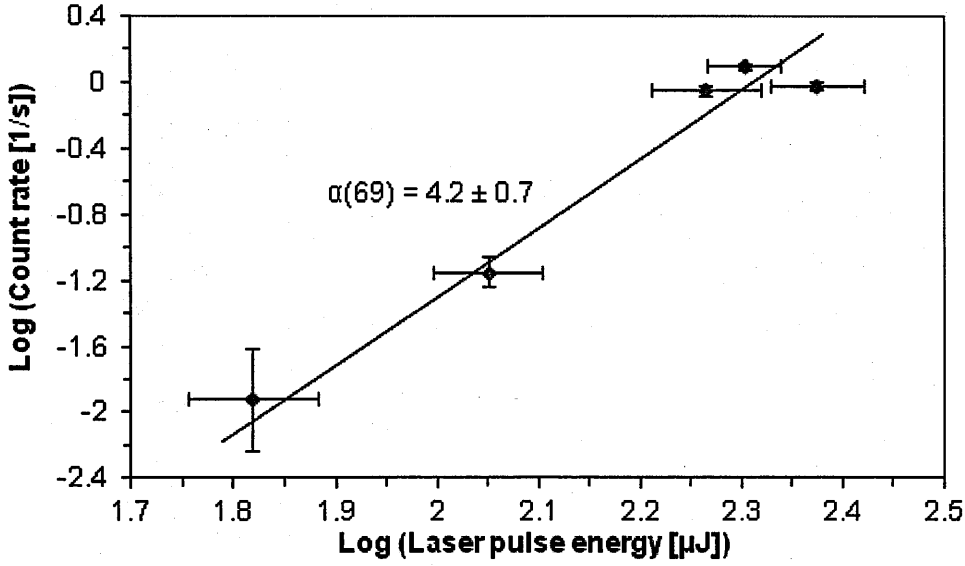

Fig. 7.12: Photon order of the uracil 69 Th fragment ion (224 nm, approximate fluence range: 1×10^6 - 4×10^6 W/cm^2; Ar pressure 1.1 - 1.2 bar; powder temperature 250°C; water 80 - 100°C).

7.5 5-fluorouracil (5-FU) fragment ions

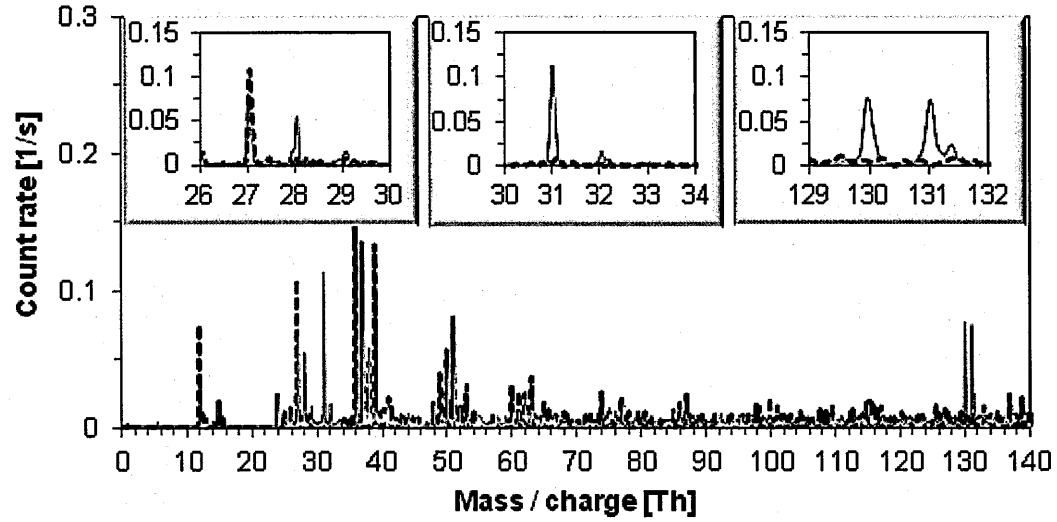

Fig. 7.13: One-colour (223.8 nm) MPI mass spectrum of background (140°C, 0.5 bar argon) (black dotted line), and one-colour (223.8 nm) MPI mass spectra of 5-fluorouracil (powder 250°C, 0.5 bar argon) (red line). Both recorded at a fluence of ~ 6.2×10^7 W/cm^2.

Fig. 7.13 shows multiphoton dissociative ionization of 5-FU clusters. As discussed in chapter 6, 5-FU ($C_4H_3FN_2O_2$) exhibits strong clustering confirmed by the presence of protonated monomer (131 Th) in the mass spectrum. 31 Th (CF^+) is the strongest fragment

ion from 5-FU. Fragmentation is an efficient process in the case of 5-FU: the 31 Th fragment ion signal exceeding that of the monomer ion. Although 28 Th ($HNCH^+$) is also present at significant levels, it does not exceed the monomer ion peak. No other fragment ions which can be clearly assigned to 5-FU have been identified. Further experiments on hydrated 5-FU with lower laser fluences could provide information to help characterise 5-FU precursor ion(s) in the dissociative ionization pathways leading to CF^+ and $HNCH^+$. Assuming that the analogy with thymine and uracil is conserved, the precursor fragment ion created by HNCO loss from the 5-FU parent cation is expected at 87 Th. Indeed, the electron impact mass spectra of several N-substituted derivatives of 5-fluorouracil showed decomposition of the 5-fluorouracil skeleton leading to the creation of $[RN=CHCF=C=O]^+$ fragment ions from N-1 substituted derivatives, which in the case of non-substituted molecule, i.e. R=H would have mass/charge ratio equal to 87 Th[425].

7.6 Fragmentation results - summary

The dominant fragment ions detected in multiphoton dissociative ionization of dry and hydrated adenine, thymine and uracil agree with fragment ions detected in single photon and electron impact ionization of dry samples. The strongest fragments of adenine ($H_5C_5N_5^+$) in the present experiments have been found at 28 ($HNCH^+$), 54, 66 ($H_2C_3N_2^+$), 70, 81, and 108 Th. Detailed fragmentation mechanisms upon different kinds of radiation have been proposed and discussed in the literature[146, 416, 424, 426]. The successive loss of neutral HCN (m = 27 a.m.u.) groups, leads to the creation of 108 ($H_4C_4N_4^+$), 81 ($H_3C_3N_3^+$), 54 ($H_2C_2N_2^+$) Th fragment ions.

Adenine fragmentation takes place predominantly via the 108 Th precursor fragment ion, created by the initial lost of the neutral HCN fragment[146]. The large energy excess in the ionic state of adenine monomer ion accumulated due to absorption of the following photon induces extended fragmentation, stronger than the loss of single HCN group only, and 108 Th cannot be observed in the present mass spectra under dry conditions.

A similar situation occurs in the thymine precursor fragment ion 83 Th formed by the loss of HNCO group from the thymine parent cation ($C_5H_6N_2O_2^+$); further loss of the CO group

leads to the 55 Th (CH_3CCHNH^+) fragment ion[146]. In the case of uracil, the precursor fragment ion 69 Th is formed by the loss of HNCO group from the uracil parent cation ($C_4H_4N_2O_2^+$) and its further fragmentation leads to 28 Th, 41 Th, and 42 Th fragment ions[424]. Again the energy excess in the uracil parent cation plays the crucial role in this process. The present mass spectra recorded in dry conditions have not revealed the 83 Th thymine precursor fragment ion. However a weak signal has been found for 69 Th uracil precursor fragment ion under dry conditions.

Very strong fragmentation of 5-fluorouracil has been observed in the present experiments, two small fragments at 31 and 28 Th (CF^+ and $HNCH^+$) have been assigned to 5-FU. No measurements on hydrated 5-FU have been carried out, which potentially could help to identify its larger (precursor) fragments.

Differences in fragmentation patterns for dry DNA/RNA bases and their hydrated clusters have been observed in the present project. The 108 Th fragment ion of adenine appears when hydrated clusters are multiphoton ionized. An analogous effect has been observed for thymine, where the 55 Th fragment ion intensity significantly increases in relation to the 54 Th fragment ion due to clustering, and a low signal is tentatively observed at 83 Th. In the case of uracil, the 69 Th fragment ion has been detected with significantly higher intensity than all other fragment ions in clustering hydrated conditions. In general, production of larger fragment ions is enhanced in the case of multiphoton dissociative ionization of clusters. This can be explained by the fact that absorption of a photon in the monomer ion leads to significant energy excess and stronger fragmentation, diminishing precursor ions (108, 83 and 69 Th), while photo-absorption in a cluster ion leads to cluster dissociation and subsequent molecular fragmentation. In particular, cluster fragments (protonated or non-protonated monomers) are created with lower vibrational energy excess than non-protonated monomer ions in non-hydrated conditions, and their photofragmentation leads to larger species.

The mechanism of the creation of fragment ions through absorption of at least one more photon than for the production of monomer cations is supported by photon order measurements for adenine and thymine molecular ions and their respective 28 Th fragment

ions. These measurements indicated that at least one additional photon absorbed by monomer ions A^+ and T^+, or their fragments (ionic or neutral) > 28 (Th or AMU), leads to fragmentation resulting in the formation of 28 Th fragment ions. The following values of photon orders have been obtained for adenine molecular ion $\alpha(135)=0.4\pm0.1$ and its fragment $\alpha(28)=1.5\pm0.1$, as well as for thymine molecular ion $\alpha(126)=0.9\pm0.1$ and its fragment $\alpha(28)=2.4\pm0.2$.

8 Conclusions

The major results described in this thesis can be split into two groups: results that show the development of a new experimental facility, and results that show the new insights into MPI processes in DNA and RNA bases and their hydrated clusters. These are summarised in the following sections **8.1** and **8.2** together with a discussion of future work in section **8.3**.

8.1 Development of a new experimental facility and methods

In this thesis an experimental system to study radiation damage induced in isolated and clustered biomolecules by multiphoton UV absorption has been developed. A new molecular beam source has been designed and constructed allowing a molecular beam to be delivered to a diagnostic chamber, where MPI takes place and the resultant ions are accelerated into a mass spectrometer flight tube for mass analysis. The design has the practical advantages of simplicity, compactness, and low cost.

The initial part of the project focused on the system design, construction and optimization. The major technical challenges which have been overcome during this stage of the work are as follows:

- The mass spectrometer and the gate valve support frames were designed and constructed.

- The vacuum system was modified by introducing a by-pass between expansion and diagnostic chambers to avoid a differential pressure damaging the skimmer during pump-down or venting of the chambers.

- The PC computer control system was designed, configured and programmed using graphical LabView platform. This system enables ion flight times with their corresponding laser pulse energies to be recorded. This feature provides opportunities to correct measurements from fluctuations in other experimental conditions such as changes in temperature and pressure. The pulse-by-pulse system has been demonstrated to work very effectively; the photon orders (slopes of the curves showing signal intensity as a function of laser pulse fluence in the

logarithmic scale) β derived using the pulse-by-pulse system match α photon orders derived using the method of recording separate mass spectra with different average laser pulse energies.

- The triggering scheme of the lasers, the mass spectrometer, and data acquisition electronics has been accomplished by use of a pulse generator.

- Insertion of a thermocouple directly into the heated gas mixture immediately above the expansion orifice provided improved control of the sample and expansion conditions than the earlier designs using the temperatures of the heater or the nozzle wall as references.

- A water reservoir was designed and attached to the argon gas tube as a source of water vapour for experiments with hydrated clusters.

- Operational procedures leading to the production of monomer and cluster ions were developed, optimized and successfully applied. The new molecular beam source has been demonstrated to produce several cluster targets that, to our knowledge, have not previously been observed in any supersonic expansion system. Most notably, adenine-uracil-water clusters have been produced for the first time. These can provide analogues for sites on cellular RNA and open opportunities for future experiments.

8.2 New insights into MPI processes in DNA/RNA related molecules and their hydrated clusters at 220-230 nm

In the second part of the project, nucleic acid bases and related chromophores (adenine, thymine, uracil, 5-fluorouracil, hypoxanthine) as well as their hydrated clusters were investigated in multiphoton ionization experiments.

8.2.1 Experiments on DNA / RNA bases multiphoton ionization (MPI) in dry argon beams with low backing pressures

In this set of experiments MPI was explored for DNA/RNA bases seeded in dry argon at low backing pressures. Under these conditions cluster formation is expected to be minimized. The major results of these experiments were:

- Strong signals were observed for adenine and thymine MPI.
- Markedly weaker signal was observed for uracil.
- Photon order measurements were applied as a tool to determine the number of photons absorbed in multiphoton ionization processes for monomer ions. They confirm that MPI of thymine (1.4±0.1) and uracil (1.9±0.3) are at least 2 photon processes.
- In the case of adenine, measurements were performed for lower laser pulse fluence delivered by unfocused beams. The photon order measured in this way equals 3±0.5 and suggests three-photon ionization. Further measurements are planned to confirm this result (see the future work section of this chapter).
- The following issues in using photon orders as an indicator of number of photons absorbed in photoionization process should be examined in further studies:
  - applicability of the perturbation theory expression for non-resonant multiphoton ionization in the case of resonant MPI;
  - saturation at the excitation or ionization step;
  - non-linearity of the electron multiplier (detector) response;
  - fluctuations of laser beam spatial and temporal characteristics.
- The significant 136/135 Th, 127/126 Th and 113/112 Th ratios in the respective mass spectra of adenine, thymine and uracil provide evidence for neutral clusters in the supersonic beams of these molecules. In the case of adenine cluster origin of some AH^+ ions is supported by the 136 Th peak shape.

- MPI signals have been obtained for all the molecules studied, except hypoxanthine. The short excited state lifetime of hypoxanthine may be responsible for no MPI being observed; time-resolved experiments are necessary to verify this interpretation.

- The discussion of the MPI pathways of DNA/RNA bases has been based on the assumption that the laser pulse has an approximately rectangular temporal profile. The experimental evidences taken from the literature and presented in this thesis show that application of ns laser pulses very often diminishes ionic signals (MPI efficiency) for molecules having very short (fs – ps time scale) lifetimes, i.e. deviations from a rectangular temporal profile (locally increased photon densities) are not large enough to sufficiently ionize short-lived excited states. Since adenine, thymine and uracil molecular ions were efficiently detected in the present research, long-lived triplet states are presented as likely candidates for intermediate excited states in the multiphoton ionization process of these non-hydrated nucleic acid bases. The possible contribution to monomer ion signals from clusters dissociated in a neutral excited state has also been discussed.

8.2.2 MPI of DNA / RNA bases in clusters

By changing the source conditions a set of MPI experiments were performed in which DNA/RNA bases formed clusters. Mass distributions of cluster ions and cluster fragment ions produced by MPI as well as the photon orders for solvated ions and their fragments were recorded. The results can be summarised as follows:

- Low signal levels of dimer ions (compared to monomer ions) were observed in the present dry experimental conditions for homogenous (adenine) and heterogeneous (adenine-uracil, adenine-thymine) molecular beams.

- The order of monomer ions intensities $A^+ > T^+ > U^+$ was derived on the basis of MPI measurements of mixed systems (adenine-thymine and adenine-uracil). In principle these differences could be attributed to vapour pressures, gas transport in the nozzle, and/or the efficiency of multiphoton ionization process. However, the lowest

signal levels have been observed for uracil (U^+), despite the literature[206, 360] indicating that uracil has the lowest sublimation enthalpy. This suggests a higher MPI efficiency of adenine and thymine.

- The first MPI measurement of 5-fluorouracil (5-FU) has been carried out. Unlike the present experiments on DNA/RNA bases (adenine, thymine and uracil), clear cluster ion signals were observed for 5-FU in dry low backing pressure conditions.

By adding water to the cluster source hydrated DNA/RNA base clusters were formed. The following results were obtained in hydrated conditions:

- Since signal suppression upon hydration has been observed for hydrated adenine molecular beam, it has been difficult to obtain cluster ions signal for hydrated adenine. However hydrated adenine cluster ions have been observed in certain expansion conditions.

- Adenine cluster ions with up to 4 water molecules attached to a single base have been observed. $A^+(H_2O)_n$ signals were relatively strong for n=1-4 and negligible for n>4. It has been demonstrated that the signal intensities of $A_2(H_2O)_n^+$ cluster ions greater than the signal intensities of $A_1(H_2O)_n^+$ cluster ions can be obtained for the excitation wavelength of 224 nm by the optimization of expansion conditions to favour the production of large hydrated adenine clusters and by applying relatively low laser fluence.

- Uracil cluster ions $U^+(H_2O)_n$ have been observed up to a maximum of n=7. The largest hydrated thymine cluster ion $T^+(H_2O)_n$ could not be identified since it is not possible to distinguish $T_m(H_2O)_n^+$ from $T_{m+1}(H_2O)_{n-7}$ ($n \geq 7$, $m \geq 1$).

- The largest hydrated adenine-uracil base pair ions $AU^+(H_2O)_n$ have been observed at n=7.

- The weak $A^+(H_2O)_n$ signals for n>4 and the negligible $U^+(H_2O)_n$ and $AU^+(H_2O)_n$ signals for n>7 may be related to hydration shell structures in the neutral or ionic clusters.

- Two types of clusters size distributions have been observed under hydrated conditions: one smoothly decreasing and another with irregularly distributed intensities. The shape of hydrated cluster ions mass distribution mainly depends on the clustering conditions, in particular varying content of water vapour in the expansion.

- Multiphoton ionization of clusters is likely to be mediated by different excited state dynamics than non-clustered molecules. Theoretical and experimental studies reported in the literature and discussed in this thesis provide evidence for the significant impact of hydration on excited state energetic levels and relaxation dynamics. Intra-cluster tautomeric transitions are likely to play a role in MPI processes in hydrated nucleic acid bases, although direct experimental evidence to validate this hypothesis could not be obtained with the present experimental setup. Theoretical studies in the literature showed that excited state tautomeric transitions are plausible in cluster environments. The lifetimes of tautomeric excited states may be longer compared to excited state lifetimes of natural nucleic acid bases (the lowest energy tautomers). Excited state tautomeric transitions are favoured over triplet states in effective ns MPI process since the latter are considered to be populated through $^1n\pi^*$ states which are destabilised in hydrogen bonding environments, therefore the triplet pathway in water clusters seems less likely to occur. Time-resolved experiments on a ns timescale could clarify excited states dynamics of hydrated clusters.

- In hydrated conditions photon order measurements indicate two-photon ionization of uracil-water and adenine-water clusters. The measured photon order is equal to 2.1±0.4 for $A^+(H_2O)_1$ and varies within the range of 1.3 – 1.9 for $U^+(H_2O)_{1\text{-}4}$ cluster ions. Higher values of photon orders have been measured for cluster fragments in hydrated conditions, i.e. $\alpha(UH^+)$=3.0±0.1, $\alpha(AH^+)$=3.2±0.4, $\alpha(U^+)$=2.4±0.2 and $\alpha(A^+)$=2.4±0.2. These increased values are consistent with a significant contribution in the cluster ion yield due to dissociative ionization in two-photon process or their photofragmentation induced by a third photon.

8.2.3 Fragment ions from DNA / RNA base molecules

Molecular fragment ions have been observed in the present MPI experiments and compared with the results of single photon and electron impact dissociative ionization reported in the literature.

- Molecular fragmentation has been observed when operating at higher laser pulse fluences using focused laser beams. The fragment ions observed from adenine, thymine, and uracil MPI are generally consistent with those observed previously in other dissociative ionization processes, notably electron impact and single-photon ionization.

- Photon orders for fragment ions of adenine and thymine have been measured. For adenine, the photon order of the strongest fragment ion peak (CNH_2^+) is approximately one greater than that for dry A+. A difference of 1.5±0.2 has been observed for thymine and its CNH_2^+ fragment.

- Differences in fragmentation patterns in dry and hydrated conditions have been identified. No 108 Th adenine fragment ions have been detected in dry conditions in contrast to single photon and electron impact ionization experiments reported in the literature, as well to the multiphoton dissociative ionization experiments carried out on adenine clusters in the present work. The absence of this fragment suggests strong vibrational excitation resulting from IC and ICS processes in MPI. In clustering conditions, heavier fragments are also recorded more strongly in the mass spectra of uracil (69 Th fragment ion) and thymine (83 Th and 55 Th fragment ions). This can be explained by photofragmentation of relatively cold ionic fragments of clusters, i.e. protonated and non-protonated monomer ions. In contrast, monomer ions that do not originate from clusters are vibrationally hot and experience more extensive fragmentation.

- The evidence obtained for uracil 69 Th fragment ions [α(69 Th)=4.2±0.7] indicating a four photon process supports the mechanism in which photoabsorption by protonated and/or non-protonated monomer ions (cluster fragments) leads to the

production of monomer fragment ions. Indeed heavier fragments like 108 Th (adenine fragment), 83 and 55 Th (thymine fragments) and 69 Th (uracil fragment) are likely to be the result of such a sequential multiphoton ionization and fragmentation processes.

- Regularly increasing photon order values from cluster though monomer ions to fragment ions in hydrated conditions have been observed. It is proposed that sequential MPI processes with 2, 3, and 4 photon absorption lead to production of cluster ions, cluster fragment ions (including protonated monomers), and molecular fragment ions, respectively.

8.3 Outlook

A new experimental system developed in this work was successfully applied in the research on radiation damage in DNA/RNA bases and related chromophores. The present results can be a starting point for further investigations; some of which are listed below:

1. Verify the 3-photon ionization of adenine. Further experimental work is required to confirm this result by excluding factors related to a laser beam spatial profile stability, which may more strongly influence the characteristic in this case than in the measurements with a focused laser beam. Unlike focused laser beam measurements, when using an unfocused beam only a part of laser beam crosses the molecular beam.

2. Measure photon orders of thymine and uracil at lower fluence to check for possible 3-photon ionization in these molecules.

3. Carry out measurements at low background levels (achieved by baking the system and using a dry backing pump). This should provide more detailed information on hydrated clustering effects on fragment ion production (e.g. improved analysis of peaks with background contributions in the present data).

4. Change the laser wavelength to explore the effects of accessing different vibrational levels of the initially populated bright $^1\pi\pi^*$ states.

5. Measurements with (partially) deuterated DNA / RNA bases to verify fragment ion assignments and to help elucidate proton / hydrogen transfer pathways and the maximum size of hydrated thymine cluster ions.

9 Appendix

9.1 Construction of the molecular cluster beam source

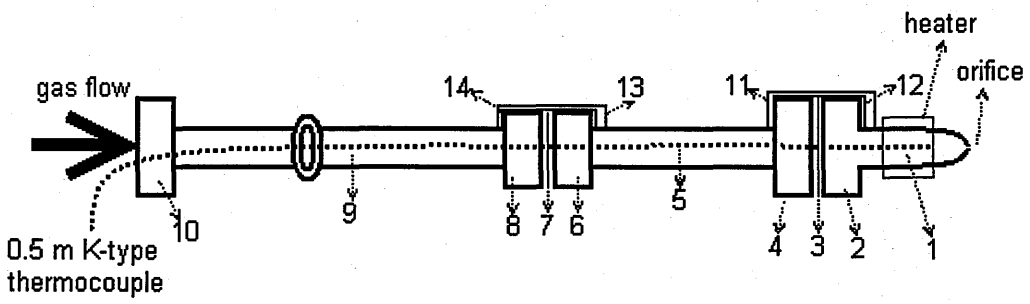

Fig. 9.1: The design of the molecular beam source.

Fig. 9.1 shows the design of the molecular cluster beam source. A VCR TBW Short Tube Butt Weld Gland **[2]** (1/2 in. VCR x 1/2 x 0.049 in., 6LV-8-VCR-3S-8TB2) has been welded to SS ½" orifice tubing **[1]**. An adapter extension has been prepared using ¼" SS tube **[5]** welded to a VCR Reducing Socket Weld Gland **[4]** (½" VCR x ¼" Tube Socket, SS-8-VCR-3-4TSW) at one end and to a VCR Socket Weld Gland **[6]** (¼" VCR x ¼" Tube Socket, SS-4-VCR-3) at the other end. This extension is connected at one end to the SS ½" orifice tubing **[1]** (through the welded gland) using a VCR ½" Male Nut **[12]** (SS-8-VCR-4), VCR ½" Female Nut **[11]** (SS-8-VCR-1) and VCR Gasket ½" **[3]** (Silver-Plated Gasket, NI-8-VCR-2). At the other end the extension is connected to the DN16KF LN FEEDTHROUGH **[9]** (¼" TUBE with VCR FITTINGS) using a VCR ¼"Female Nut **[13]** (SS-4-VCR-1), the ¼" Male Nut of the feedthrough **[14]** and a VCR Gasket **[7]** (¼" Silver-Plated Gasket, NI-4-VCR-2). Outside the vacuum chamber, the feedthrough is connected to the argon supply line by a VCR Tube fitting Female Connector **[10]** (¼" WVCR x 6mm Tube Fitting, SS-4-WVCR-6-6M0). Above this connection Swagelok Union Cross (SS-16M0-4), Caps (SS-16M0-C), Plugs (SS-16M0-P), Swagelok 6 mm Plug Valves, as well as 16 mm and ¼" tubing have been used in construction of the "in-line" water vapour reservoir (see **Fig. 3.1**).

9.2 LabView programming

A number of LabView structures have been used to prepare the data acquisition program.

A while loop (executing the sub-diagram until the conditional terminal) has been applied in the block of software responsible for the temperature control (**Fig. 9.2**). User action in the form of a mouse click has been used by the LabView event structure embedded inside the while loop to control ON/OFF function of the pulse generator (**Fig. 9.3**). When the operating system detects the user action, it notifies applications so they can react by executing any code written especially for that event. The next LabView structure which has been applied in the data acquisition system is LabView case structure. This structure executes a block of code based on the value of a certain variable; a case selector located on the case structure is wired to a data source. The value fed into the case selector determines what the case executes. The case structures together with a while loop have been applied in the block of software responsible for reading of the buffer gas pressure (**Fig. 9.5**).

A For Loop has been applied in the laser energy/pulse counting block of the software (**Fig. 9.4**). This executes a subdiagram a set number of times. N is the value in the count terminal (an input terminal) that indicates how many times to repeat the subdiagram. I is the iteration terminal (an output terminal), it contains the number of completed iterations. The iteration count always starts at zero. During the first iteration, the iteration terminal returns 0.

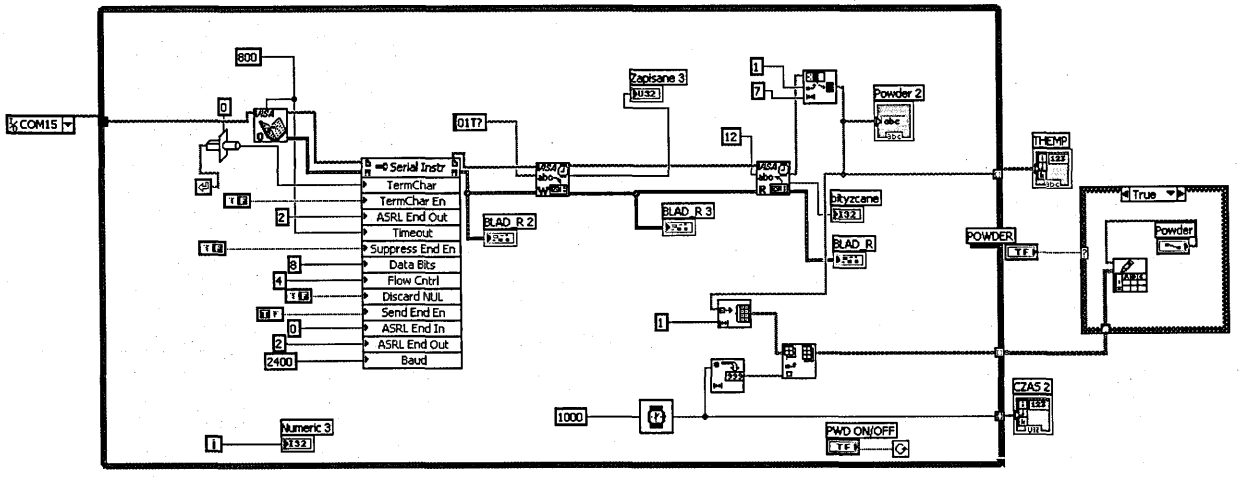

Fig. 9.2: LabView control software for the temperature controllers.

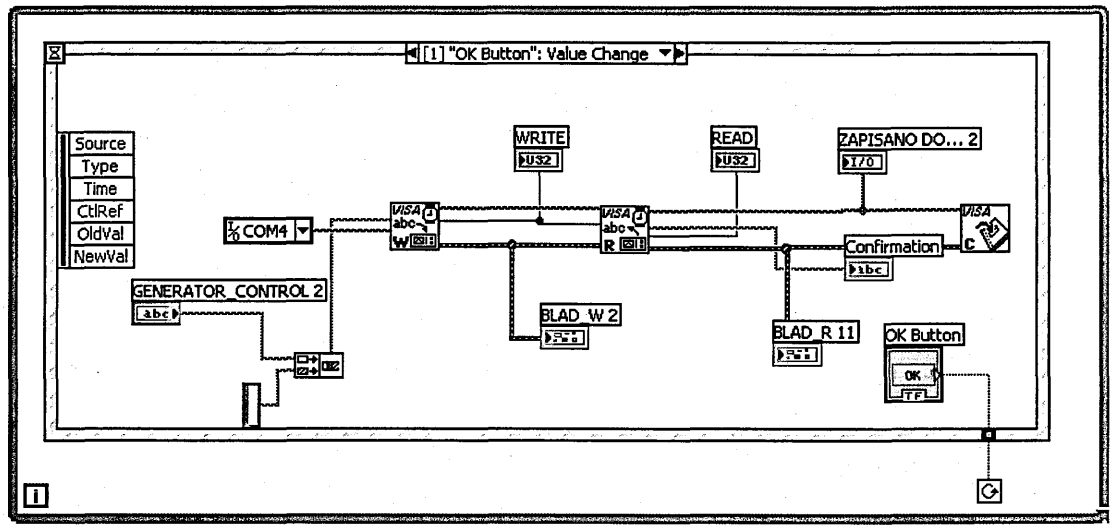

Fig. 9.3: LabView control software for the pulse generator.

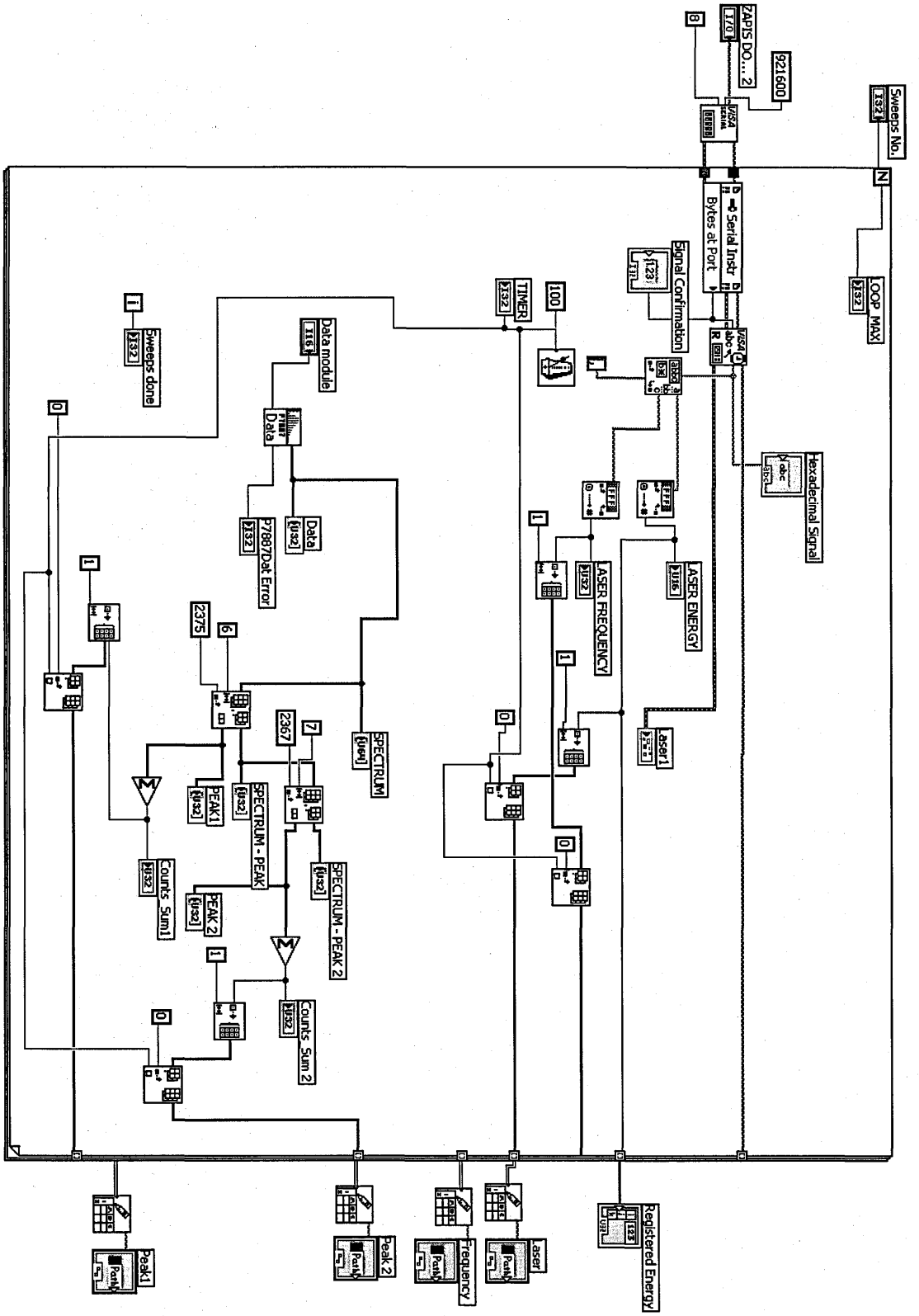

Fig. 9.4: The LabView control software for simultaneous recording of the laser pulse energy and number of ions produced by this pulse.

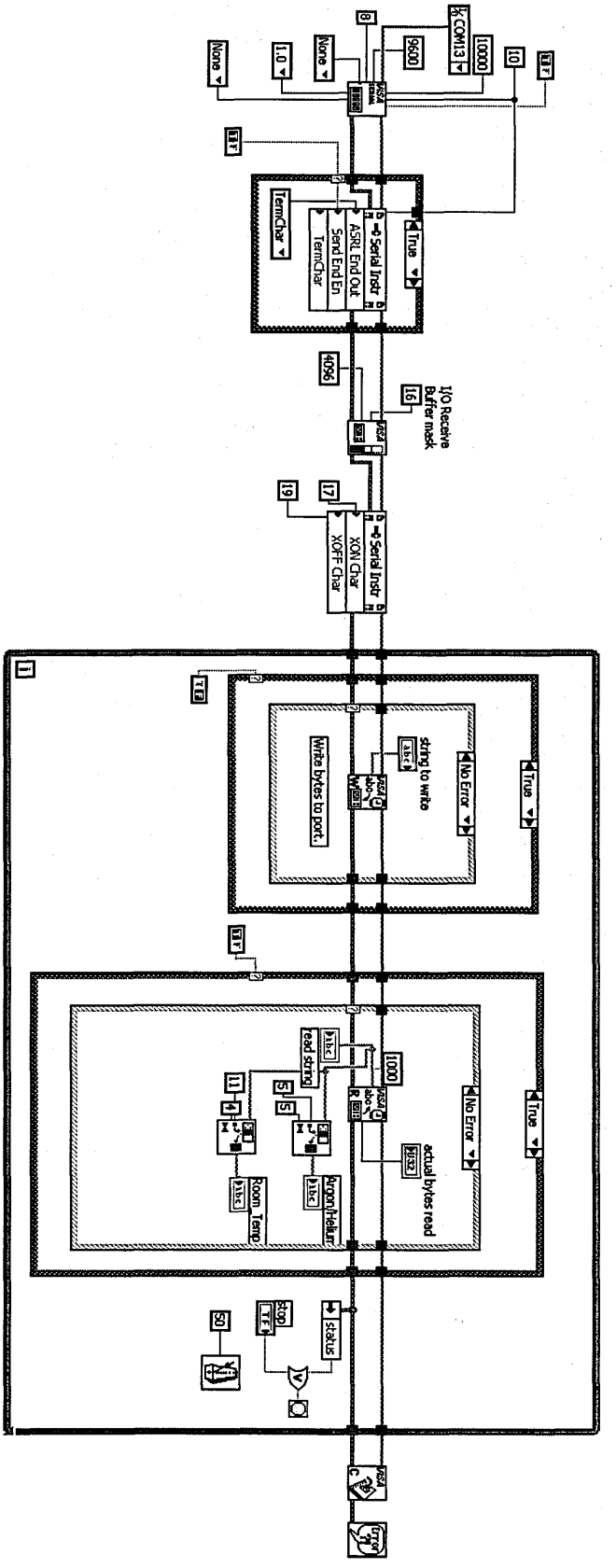

Fig. 9.5: The LabView control software for reading of the buffer (argon) gas pressure, taken from the LabView examples and modified.

To access the spectrum P7887 data directly from LabView via the DLL (dynamic link library), the LabView VI ("Virtual Instrument") P7887Dat.vi (**Fig. 9.6**) has been used within the block of the program presented in **Fig. 9.4**. P7887Dat.vi provides a 32 bit integer as an error code and the spectrum as a [U32] (unsigned long number). Data[nDisplay].s0 points to a block memory of unsigned long numbers containing the data. This Virtual Instrument has been provided by the P7887 multiscaler supplier – FastComtec.

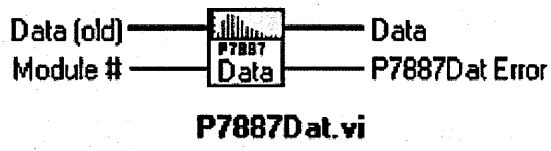

Fig. 9.6: LabView VI (Virtual Instrument) gets a copy of the P7887 Data as [U32] array.

The data access is actually performed by the code written originally in C language and then accessed by LabView using Code Interface Node (CIN), which is a block diagram node that links C/C++ source code to LabVIEW (**Fig. 9.7**).

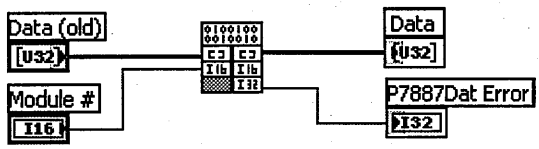

Fig. 9.7: The LabView Code Interface Nodes.

9.3 Signal intensity correction to remove the effect of small temperature variations

Small differences in average temperature have been found between the mass spectra shown in **Fig. 5.3**: 233.6, 234.2, and 234.8 °C for A, B, and C respectively. A correction for this effect has been introduced. Taking into account the dependence between vapour pressure and temperature[206]:

$$P(T) = A\exp\left[-\frac{\Delta H_{sub}}{RT}\right] \qquad \textbf{(9-1)}$$

and assuming ΔH_{sub} for adenine equal to 153.1 kJ/mol[206] (with negligible temperature dependence), A - constant, R = 8.31 J/mol*K, the expected increase of adenine vapour pressure in the nozzle can be calculated for temperatures present in the experiment. For a temperature T increase from 233.6°C (506.75 K) to 234.8°C (507.95K), the vapour pressure is expected to increase ~9%; and for a temperature increase from 233.6°C (506.75K) to 233.9°C (507.05 K), the vapour pressure is expected to increase ~2.2%. Signal intensities in **Fig. 5.4** are corrected using these percentages.

9.4 Electron impact ionization

Preliminary electron impact (EI) ionization experiments have been carried out on thymine under dry conditions, the results are presented in **Fig. 9.8** together with the MPI spectrum of adenine recorded in similar temperature and pressure in dry conditions.

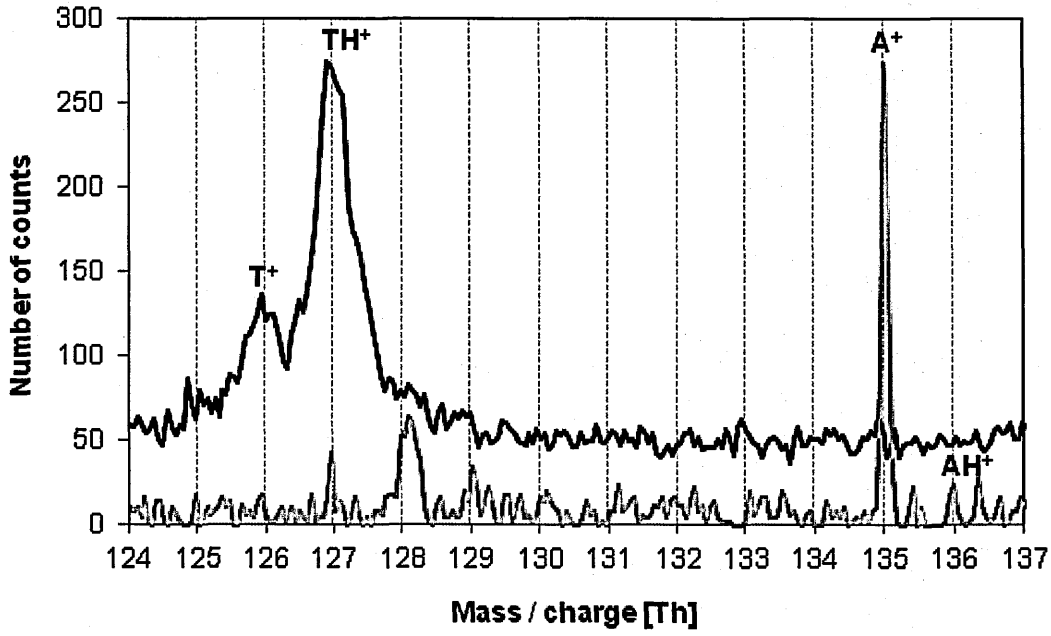

Fig. 9.8: Black line - electron impact ionization mass spectrum of thymine in non-hydrated molecular beam. Red line - a typical MPI mass spectrum of adenine in non-hydrated conditions. The powder temperature in both measurements was within the range of 310-330°C, Ar pressure ~ 1.6 bar.

The EI measurement was carried out using a diffuse electron beam from the Kimball Physics electron gun (ELG-2/EGPS-1022) installed on the diagnostic chamber. The e^- beam was passed between the pulse-out and backplate electrodes of the mass

spectrometer ion source (**Fig. 3.15**), perpendicularly to the pulsed extraction field direction. The electron energy was set to 490 eV.

The results of separate MPI and EI experiments carried in identical molecular beam conditions may help to clarify the potential role of clusters dissociating in neutral states in the present MPI experiments. These clusters could be effectively ionized in the EI experiment, contributing to the signal in a cluster or protonated monomer ion channel. The results presented in **Fig. 9.8** show that for thymine in dry conditions (black line), the cluster fragment signal at m/z = 127 Th dominates over the non-protonated thymine ion at m/z = 126 Th. Significant contributions of protonated monomers in mass spectra of hydrated adenine clusters have been observed in MPI experiments. However in dry conditions, represented by the black line in **Fig. 9.8**, the 136 / 135 Th ratio is often close to the ratio of 8% expected due to adenine isotopomers[21, 329]. The significantly higher ratio (> 100 %) detected in the EI experiment carried out on the same molecular beam in dry conditions could be the evidence for neutral dissociation of clusters. Further experimental effort is required to investigate this issue, since it can be crucial for the understanding of the production mechanism for the non-protonated monomer ions.

Acknowledgements

I would like to thank my supervisors **Nigel Mason** and **Samuel Eden** for their support and guidance throughout the project. I am grateful for the expert technical support provided by **Fraser Robertson, Roger Bence** and **Martin Percy**; **Mark Bowden** for laser trainings; **Sandra Mills** and **Beverly Bishop** for dealing with orders, deliveries and laboratory support. I wish to thank the OU postgraduate tutors **Glenn White** and **Jimena Gorfinkiel**. Thanks to **Patrick Cahillane**, **Ziad El Otell** and **Penny Thorn** for co-operation in the laboratory, I would also like to thank **Sylwia Ptasinska** for the electron gun support and colleagues from the OU **Plasma Lab** for making some research tools accessible. I am also grateful to **Paulo Limão-Vieira** and **Thomas Schlathölter** for hosting me in external laboratories in Lisbon and Groningen.

I acknowledge the Open University and European Commission (Marie Curie Intra-European Reintegration Grant MERG-CT-2007-207292) for my co-funded PhD studentship. Equipment for the new experimental system was purchased using funding from the EPSRC (Post-doctoral fellowship at the Life Sciences Interface EP/E039618/1), the European Commission, and the Open University. I am grateful to the IOP and the ITS-LEIF EU network for travel grants to attend conferences and visit external laboratories.

Milton Keynes, March 2012

Bartłomiej Barć

Bibliography

[1] RADAM 2004 in Lyon, http://costp9-radam.in2p3.fr/.

[2] RADAM 2005 in Potsdam, http://www.isa.au.dk/meetings/radam05/intro.html.

[3] RADAM 2006 in Groningen, http://radiation-chemistry.org/meeting/20060606.html.

[4] K. G. McGuigan *Journal of Physics: Conference Series*. **2007**, 101, 011001.

[5] RADAM 2008 in Debrecen, http://www.isa.au.dk/meetings/radam2008/overview.html.

[6] RADAM, COST Action P9, 2004-2008, http://www.isa.au.dk/networks/cost/.

[7] N. J. Mason in *Radiation Damage in Biomolecular Systems: Proceedings of the 5-th International Conference (RADAM 2008), Vol. 1080* (Eds.: K. Tokesi, B. Sulik), AIP Conference Proceedings, Debrecen, **2008**, pp.3-20.

[8] RADAM 2009 in Frankfurt am Main, www.fias.uni-frankfurt.de/radam2009.

[9] I. Baccarelli, F. A. Gianturco, E. Scifoni, A. V. Solov'yov, E. Surdutovich *European Physical Journal D*. **2010**, 60, 1-10.

[10] RADAM 2010 in Madrid, http://www.uned.es/074150/radam10/index.htm.

[11] 10-th International Workshop on Radiation Damage to DNA in Urabandai (2008), http://www.a-tech.co.jp/radiationdna2008/index.html.

[12] 11-th International Workshop on Radiation Damage to DNA in Atlanta (2010), http://www.biochem.emory.edu/conferences/radiationdamage2010/.

[13] 12-th International Workshop on Radiation Damage to DNA in Prague (2012), http://radamdna.odz.ujf.cas.cz/.

[14] E. M. Fielden, B. D. Michael, K. M. Prise *Radiation Research*. **1997**, 148, 481-481.

[15] M. Dizdaroglu *International Journal of Radiation Biology*. **1992**, 61, 175-183.

[16] M. S. Shukla, J. Leszczynski, *Radiation Induced Molecular Phenomena in Nucleic Acids*, Springer Science+Business Media B. V., Jackson, **2008**.

[17] N. J. Kim, Y. S. Kim, G. Jeong, T. K. Ahn, S. K. Kim *International Journal of Mass Spectrometry*. **2002**, 219, 11-21.

[18] S. K. Kim, W. Lee, D. R. Herschbach *Journal of Physical Chemistry*. **1996**, 100, 7933-7937.

[19] H. Kang, K. T. Lee, S. K. Kim *Chemical Physics Letters*. **2002**, 359, 213-219.

[20] A. Abo-Riziq, L. Grace, E. Nir, M. Kabelac, P. Hobza, M. S. de Vries *Proceedings of the National Academy of Sciences of the United States of America*. **2005**, 102, 20-23.

[21] N. Gador, E. Samoylova, V. R. Smith, A. Stolow, D. M. Rayner, W. G. Radloff, I. V. Hertel, T. Schultz *Journal of Physical Chemistry A*. **2007**, 111, 11743-11749.

[22] I. Bald, J. Langer, P. Tegeder, O. Ingolfsson *International Journal of Mass Spectrometry*. **2008**, 277, 4-25.

[23] E. Cauet, J. Lievin in *Radical cations of the nucleic bases and radiation damage to DNA: Ab initio study, Vol. 52*, **2007**, pp.121-147.

[24] J.-P. Schermann, *Spectroscopy and Modelling of Biomolecular Building Blocks*, Elsevier, Amsterdam, **2008**.

[25] K. F. Baverstock, R. B. Cundall *Radiation Protection Dosimetry*. **1990**, 31, 63-66.

[26] K. F. Baverstock, R. B. Cundall *Radiation Physics and Chemistry*. **1988**, 32, 553-556.

[27] A. W. Castleman, K. H. Bowen *Journal of Physical Chemistry*. **1996**, 100, 12911-12944.

[28] Z. Bacic, R. E. Miller *Journal of Physical Chemistry*. **1996**, 100, 12945-12959.

[29] A. J. Stace, *Commentary on: Haberland, H.; Kornmeier, H.; Langosch, H.; Oschwald, M.; Tanner, G. J. Chem. Soc. Faraday Trans. 1990, 86, 2473-2481.*, **1990**.

[30] B. Qiu, J. Liu, Z. Qin, G. B. Wang, H. Luo *Chemical Communications*. **2009**, 2863-2865.

[31] I. K. Yanson, A. B. Teplitsky, L. F. Sukhodub *Biopolymers*. **1979**, 18, 1149-1170.

[32] K. Rajabi, K. Theel, E. A. L. Gillis, G. Beran, T. D. Fridgen *Journal of Physical Chemistry A*. **2009**, 113, 8099-8107.

[33] L. Belau, K. R. Wilson, S. R. Leone, M. Ahmed *Journal of Physical Chemistry A*. **2007**, 111, 7562-7568.

[34] D. M. Close, C. E. Crespo-Hernandez, L. Gorb, J. Leszczynski *Journal of Physical Chemistry A*. **2008**, 112, 12702-12706.

[35] E. Cauet, M. Valiev, J. H. Weare *Journal of Physical Chemistry B*. **2010**, 114, 5886-5894.

[36] Z. G. Lan, L. M. Frutos, A. L. Sobolewski, W. Domcke *Proceedings of the National Academy of Sciences of the United States of America*. **2008**, 105, 12707-12712.

[37] M. F. Hineman, D. F. Kelley, E. R. Bernstein *Journal of Chemical Physics*. **1993**, 99, 4533-4538.

[38] G. Gregoire, C. Dedonder-Lardeux, C. Jouvet, S. Martrenchard, D. Solgadi *Journal of Physical Chemistry A*. **2001**, 105, 5971-5976.

[39] J. M. Mayer *Annual Review of Physical Chemistry*. **2004**, 55, 363-390.

[40] O. David, C. Dedonder-Lardeux, C. Jouvet *International Reviews in Physical Chemistry*. **2002**, 21, 499-523.

[41] R. Knochenmuss, I. Fischer *International Journal of Mass Spectrometry*. **2002**, 220, 343-357.

[42] S. S. Kim, M. Kim, H. Kang *Bulletin of the Korean Chemical Society*. **2009**, 30, 1481-1484.

[43] R. I. Cukier *Journal of Physical Chemistry B*. **2002**, 106, 1746-1757.

[44] I. V. Stasyuk, R. Y. Stetsiv, Y. V. Sizonenko *Condensed Matter Physics*. **2002**, 5, 685-706.

[45] J. R. Gord, A. W. Garrett, R. E. Bandy, T. S. Zwier *Chemical Physics Letters*. **1990**, 171, 443-450.

[46] M. Mons, I. Dimicoli, F. Piuzzi *International Reviews in Physical Chemistry*. **2002**, 21, 101-135.

[47] S. A. Claridge, A. W. Castleman, S. N. Khanna, C. B. Murray, A. Sen, P. S. Weiss *Acs Nano*. **2009**, 3, 244-255.

[48] P. Jena, A. W. Castleman *Proceedings of the National Academy of Sciences of the United States of America*. **2006**, 103, 10560-10569.

[49] A. P. Alivisatos *Acs Nano*. **2008**, 2, 1514-1516.

[50] A. W. Castleman, S. Wei *Annual Review of Physical Chemistry*. **1994**, 45, 685-719.

[51] V. Malka, J. Faure, Y. A. Gauduel *Mutation Research-Reviews in Mutation Research*. **2010**, 704, 142-151.

[52] Z. W. Deng, I. Bald, E. Illenberger, M. A. Huels *Physical Review Letters*. **2005**, 95.

[53] H. Saigusa *Journal of Photochemistry and Photobiology C-Photochemistry Reviews*. **2006**, 7, 197-210.

[54] C. T. Middleton, K. de La Harpe, C. Su, Y. K. Law, C. E. Crespo-Hernandez, B. Kohler *Annual Review of Physical Chemistry*. **2009**, 60, 217-239.

[55] M. G. D. Nix, A. L. Devine, B. Cronin, M. N. R. Ashfold *Journal of Chemical Physics*. **2007**, 126.

[56] M. Schneider, C. Schon, I. Fischer, L. Rubio-Lago, T. Kitsopoulos *Physical Chemistry Chemical Physics*. **2007**, 9, 6021-6026.

[57] D. Markovitsi, N. Chouini-Lalanne, P. Clivio, T. Douki, T. Gustavsson, E. Lazzarotto, S. Marguet, D. Onidas, J. L. Ravanat, K. Steenkeste, F. Talbot, M. P. Teulade-Fichou *Actualite Chimique*. **2007**, 8-14.

[58] R. P. Sinha, D. P. Hader *Photochemical & Photobiological Sciences*. **2002**, 1, 225-236.

[59] SET, *ISO 21348 Process for Determining Solar Irradiances*, Space Environment Technologies, http://www.spacewx.com/solar_spectrum.html.

[60] C. Honsberg, S. Bowden, *Standard Solar Spectra*, pveducation.org, http://pveducation.org/pvcdrom/appendicies/standard-solar-spectra.

[61] J. S. D'Souza, J. A. Dharmadhikari, A. K. Dharmadhikari, B. J. Rao, D. Mathur *Physical Review Letters*. **2011**, 106.

[62] D. Trautlein, M. Deibler, A. Leitenstorfer, E. Ferrando-May *Nucleic Acids Research*. **2010**, 38.

[63] M. A. Tycon, A. Chakraborty, C. J. Fecko *Journal of Photochemistry and Photobiology B-Biology*. **2011**, 102, 161-168.

[64] R. A. Meldrum, S. W. Botchway, C. W. Wharton, G. J. Hirst *Embo Reports*. **2003**, 4, 1144-1149.

[65] Y. Hatano *Radiation Physics and Chemistry*. **2003**, 67, 187-198.

[66] Y. Hatano *Radiation Physics and Chemistry*. **2009**, 78, 1021-1025.

[67] Z. L. Cai, P. Cloutier, D. Hunting, L. Sanche *Radiation Research*. **2006**, 165, 365-371.

[68] H. Yamada, K. Hieda *Photochemistry and Photobiology*. **1992**, 55, 541-548.

[69] Z. J. Li, P. Cloutier, L. Sanche, J. R. Wagner *Journal of the American Chemical Society*. **2010**, 132, 5422-5427.

[70] T. Solomun, H. Seitz, H. Sturm *Journal of Physical Chemistry B*. **2009**, 113, 11557-11559.

[71] H. Abdoul-Carime, L. Sanche *International Journal of Radiation Biology*. **2002**, 78, 89-99.

[72] S. V. Jovanovic, M. G. Simic *Journal of the American Chemical Society*. **1986**, 108, 5968-5972.

[73] T. Ito, S. Kuno, T. Uchida, S. Fujita, S. Nishimoto *Journal of Physical Chemistry B*. **2009**, 113, 389-394.

[74] J. Schmidt, W. Snipes *International Journal of Radiation Biology*. **1968**, 13, 101-109.

[75] K. Sieber, J. Huttermann *International Journal of Radiation Biology*. **1989**, 55, 331-345.

[76] A. Adhikary, D. Khanduri, V. Pottiboyina, C. T. Rice, M. D. Sevilla *Journal of Physical Chemistry B*. **2010**, 114, 9289-9299.

[77] Y. Razskazovskiy, M. G. Debije, W. A. Bernhard *Radiation Research*. **2000**, 153, 436-441.

[78] A. D. Meade, H. J. Byrne, F. M. Lyng *Mutation Research-Reviews in Mutation Research*. **2010**, 704, 108-114.

[79] B. Stenerlow, E. Hoglund, J. Carlsson, E. Blomquist *International Journal of Radiation Biology*. **2000**, 76, 549-557.

[80] R. M. Anderson, S. J. Marsden, E. G. Wright, M. A. Kadhim, D. T. Goodhead, C. S. Griffin *International Journal of Radiation Biology*. **2000**, 76, 31-42.

[81] D. Boucher, I. Testard, D. Averbeck *Radiation and Environmental Biophysics*. **2006**, 45, 267-276.

[82] A. P. Schuch, C. F. M. Menck *Journal of Photochemistry and Photobiology B-Biology*. **2010**, 99, 111-116.

[83] M. Folkard, K. M. Prise, B. Vojnovic, B. Brocklehurst, B. D. Michael *International Journal of Radiation Biology*. **2000**, 76, 763-771.

[84] P. K. Agrawala, A. Eschenbrenner, M. A. H. Du Penhoat, A. Boissiere, M. F. Politis, A. Touati, E. Sage, A. Chetioui *International Journal of Radiation Biology*. **2008**, 84, 1093-1103.

[85] L. Sellami, S. Lacombe, D. Hunting, R. J. Wagner, M. A. Huels *Review of Scientific Instruments*. **2007**, 78, 085111.

[86] W. Z. Ke, D. F. Zhou, J. Z. Wu *Journal of Raman Spectroscopy*. **2005**, 36, 39-44.

[87] Q. Miao, J.-N. Lai, J.-M. Xue, H.-L. Qin, W.-D. Wang, G.-Y. Qin, Y.-G. Wang *Nuclear Science and Techniques*. **2006**, 17, 272-275.

[88] A. Yokoya, K. Fuji, N. Shikazono, K. Akamatsu, A. Urushibara, R. Watanabe *International Journal of Radiation Biology*. **2008**, 84, 1069-1081.

[89] J. D. Watson, F. H. C. Crick *Nature*. **1953**, 171, 964-967.

[90] J. D. Watson, F. H. C. Crick *Nature*. **1953**, 171, 737-738.

[91] S. K. Pal, A. H. Zewail *Chemical Reviews*. **2004**, 104, 2099-2123.

[92] M. Chaplin, *Nucleic Acid Hydration*, Creative Commons Attribution

-Noncommercial-No Derivative Works 2.0 UK: England & Wales License, http://www.lsbu.ac.uk/water/nucleic.html.

[93] F. Lee, *Molecular Biology - Web Book*, web-books.com, http://www.web-books.com/MoBio/.

[94] S. Purkayastha, W. A. Bernhard *Journal of Physical Chemistry B*. **2004**, 108, 18377-18382.

[95] T. Douki, J. L. Ravanat, J. P. Pouget, I. Testard, J. Cadet *International Journal of Radiation Biology*. **2006**, 82, 119-127.

[96] R. Roots, S. Okada *International Journal of Radiation Biology and Related Studies in Physics Chemistry and Medicine*. **1972**, 21, 329-342.

[97] J. D. Chapman, A. P. Reuvers, J. Borsa, Greensto.Cl *Radiation Research*. **1973**, 56, 291-306.

[98] W. A. Bernhard, S. Purkayastha, J. R. Milligan *Dose-Response*. **2008**, 6, 184-195.

[99] R. Roots, G. Kraft, E. Gosschalk *International Journal of Radiation Oncology Biology Physics*. **1985**, 11, 259-265.

[100] K. F. Baverstock, S. Will *International Journal of Radiation Biology*. **1989**, 55, 563-568.

[101] R. E. Krisch, M. B. Flick, C. N. Trumbore *Radiation Research*. **1991**, 126, 251-259.

[102] J. Cadet, M. Berger *International Journal of Radiation Biology*. **1985**, 47, 127-143.

[103] M. K. Kuimova, A. J. Cowan, P. Matousek, A. W. Parker, X. Z. Sun, M. Towrie, M. W. George *Proceedings of the National Academy of Sciences of the United States of America*. **2006**, 103, 2150-2153.

[104] H. T. Kim *Journal of Molecular Structure-Theochem*. **2004**, 673, 121-126.

[105] R. N. Casaes, J. B. Paul, R. P. McLaughlin, R. J. Saykally, T. van Mourik *Journal of Physical Chemistry A*. **2004**, 108, 10989-10996.

[106] A. Singh, H. Singh *Progress in Biophysics & Molecular Biology*. **1982**, 39, 69-107.

[107] H. Nikjoo *Iranian Journal of Radiation Research*. **2003**, 1, 3-16.

[108] N. Tuteja, M. B. Singh, M. K. Misra, P. L. Bhalla, R. Tuteja *Critical Reviews in Biochemistry and Molecular Biology*. **2001**, 36, 337-397.

[109] D. T. Goodhead *International Journal of Radiation Biology*. **1989**, 56, 623-634.

[110] F. Hutchinson *Progress in Nucleic Acid Research and Molecular Biology*. **1985**, 32, 115-154.

[111] D. T. Goodhead *International Journal of Radiation Biology*. **1994**, 65, 7-17.

[112] A. Yokoya, N. Shikazono, K. Fujii, A. Urushibara, K. Akamatsu, R. Watanabe *Radiation Physics and Chemistry*. **2008**, 77, 1280-1285.

[113] U. Hagen *Radiation and Environmental Biophysics*. **1994**, 33, 45-61.

[114] A. R. Peoples, K. R. Mercer, W. A. Bernhard *Journal of Physical Chemistry B*. **2010**, 114, 9283-9288.

[115] S. W. Englander, N. R. Kallenbach, A. J. Heeger, J. A. Krumhansl, S. Litwin *Proceedings of the National Academy of Sciences of the United States of America-Biological Sciences*. **1980**, 77, 7222-7226.

[116] J. R. Milligan, J. Y. Y. Ng, C. C. L. Wu, J. A. Aguilera, R. C. Fahey, J. F. Ward *Radiation Research*. **1995**, 143, 273-280.

[117] K. M. Prise, N. E. Gillies, B. D. Michael *Radiation Research*. **1999**, 151, 635-641.

[118] B. Paap, D. M. Wilson, B. M. Sutherland *Nucleic Acids Research*. **2008**, 36, 2717-2727.

[119] B. M. Sutherland, P. V. Bennett, O. Sidorkina, J. Laval *Proceedings of the National Academy of Sciences of the United States of America*. **2000**, 97, 103-108.

[120] K. Psonka, E. Gudowska-Nowak, S. Brons, T. Elsasser, M. Heiss, G. Taucher-Scholz *Advances in Space Research*. **2007**, 39, 1043-1049.

[121] K. Magnander, R. Hultborn, K. Claesson, K. Elmroth *Radiation Research*. **2010**, 173, 272-282.

[122] J. H. Miller, A. Aceves-Gaona, M. B. Ernst, M. Haranczyk, M. Gutowski, E. R. Vorpagel, M. Dupuis *Radiation Research*. **2005**, 164, 582-585.

[123] S. Nowsheen, R. L. Wukovich, K. Aziz, P. T. Kalogerinis, C. C. Richardson, M. I. Panayiotidis, W. M. Bonner, O. A. Sedelnikova, A. G. Georgakilas *Mutation Research-Genetic Toxicology and Environmental Mutagenesis*. **2009**, 674, 131-136.

[124] G. Garty, R. Schulte, S. Shchemelinin, C. Leloup, G. Assaf, A. Breskin, R. Chechik, V. Bashkirov, J. Milligan, B. Grosswendt *Physics in Medicine and Biology*. **2010**, 55, 761-781.

[125] W. Friedland, P. Jacob, P. Kundrat *Radiation Research*. **2010**, 173, 677-688.

[126] A. Munoz, F. Blanco, G. Garcia, P. Thorn, M. Brunger, J. Sullivan, S. Buckman *International Journal of Mass Spectrometry*. **2008**, 277, 175-179.

[127] J. N. Harvey, J. O. Jung, R. B. Gerber *Journal of Chemical Physics*. **1998**, 109, 8747-8750.

[128] A. Ito, T. Ito *Photochemistry and Photobiology*. **1986**, 44, 355-358.

[129] W. A. Franklin, P. W. Doetsch, W. A. Haseltine *Nucleic Acids Research*. **1985**, 13, 5317-5325.

[130] K. Kawai, H. Kodera, Y. Osakada, T. Majima *Nature Chemistry*. **2009**, 1, 156-159.

[131] A. Kumar, M. D. Sevilla *Chemical Reviews*. **2010**, 110, 7002-7023.

[132] K. Kawai, H. Kodera, T. Majima *Journal of the American Chemical Society*. **2010**, 132, 627-630.

[133] T. Takada, M. Fujitsuka, T. Majima *Proceedings of the National Academy of Sciences of the United States of America*. **2007**, 104, 11179-11183.

[134] K. K. K. Sharma, R. Tyagi, S. Purkayastha, W. A. Bernhard *Journal of Physical Chemistry B*. **2010**, 114, 7672-7680.

[135] J. Rejnek, M. Hanus, M. Labelac, F. Ryjacek, P. Hobza *Physical Chemistry Chemical Physics*. **2005**, 7, 2006-2017.

[136] P. Colarusso, K. Q. Zhang, B. J. Guo, P. F. Bernath *Chemical Physics Letters*. **1997**, 269, 39-48.

[137] A. Les, L. Adamowicz *Journal of Physical Chemistry*. **1989**, 93, 7078-7081.

[138] C. F. Guerra, F. M. Bickelhaupt, S. Saha, F. Wang *Journal of Physical Chemistry A*. **2006**, 110, 4012-4020.

[139] D. C. Luhrs, J. Viallon, I. Fischer *Physical Chemistry Chemical Physics*. **2001**, 3, 1827-1831.

[140] M. Hanus, M. Kabelac, J. Rejnek, F. Ryjacek, P. Hobza *Journal of Physical Chemistry B*. **2004**, 108, 2087-2097.

[141] J. Zhou, O. Kostko, C. Nicolas, X. N. Tang, L. Belau, M. S. de Vries, M. Ahmed *Journal of Physical Chemistry A*. **2009**, 113, 4829-4832.

[142] J. C. Fan, Z. C. Shang, J. Liang, X. H. Liu, H. Jin *Journal of Molecular Structure-Theochem*. **2010**, 939, 106-111.

[143] M. Fernandez-Quejo, A. de la Fuente, R. Navarro *Journal of Molecular Structure*. **2005**, 744, 749-757.

[144] B. Z. Li *Acta Chimica Sinica*. **2005**, 63, 1495-1499.

[145] C. Plutzer, K. Kleinermanns *Physical Chemistry Chemical Physics*. **2002**, 4, 4877-4882.

[146] H. W. Jochims, M. Schwell, H. Baumgartel, S. Leach *Chemical Physics*. **2005**, 314, 263-282.

[147] X. H. Chen, E. A. Syrstad, M. T. Nguyen, P. Gerbaux, F. Turek *Journal of Physical Chemistry A*. **2004**, 108, 9283-9293.

[148] K. B. Bravaya, O. Kostko, S. Dolgikh, A. Landau, M. Ahmed, A. I. Krylov *Journal of Physical Chemistry A*. **2010**, 114, 12305-12317.

[149] K. W. Choi, J. H. Lee, S. K. Kim *Journal of the American Chemical Society*. **2005**, 127, 15674-15675.

[150] K. W. Choi, J. H. Lee, S. K. Kim *Chemical Communications*. **2006**, 78-79.

[151] S. Denifl, B. Sonnweber, G. Hanel, P. Scheier, T. D. Mark *International Journal of Mass Spectrometry*. **2004**, 238, 47-53.

[152] A. A. Golubeva, A. I. Krylov *Physical Chemistry Chemical Physics*. **2009**, 11, 1303-1311.

[153] F. A. Carey, R. J. Sundberg, *Advanced Organic Chemistry - Part A: Structure and Mechanisms*, Springer, New York, **2000**.

[154] W. Demtroder, *Atoms, Molecules and Photons*, Springer-Verlag, Berlin Heidleberg, **2006**.

[155] M. Orchin, H. Jaffe, *The importance of antibonding orbitals*, Houghton Mifflin, Boston, **1967**.

[156] M. B. Smith, *Organic Chemistry: An Acid-Base Approach*, CRC Press, Taylor & Francis Group, Boca Raton, **2011**.

[157] S. N. Vinogradov, R. H. Linnell, *Hydrogen bonding*, Van Nostrand Reinhold, New York, **1971**.

[158] A. Stone, *Intermolecular Forces*, University of Cambridge, Cambridge, **2004**.

[159] M. Chaplin, *Water's Hydrogen Bond Strength*, Cornell University Library, http://arxiv.org/abs/0706.1355, **2007**.

[160] K. Modig, B. G. Pfrommer, B. Halle *Physical Review Letters*. **2003**, 90, 4.

[161] I. C. Hayes, A. J. Stone *Molecular Physics*. **1984**, 53, 83-105.

[162] T. Cwiok, B. Jeziorski, W. Kolos, R. Moszynski, K. Szalewicz *Theochem-Journal of Molecular Structure*. **1994**, 113, 135-151.

[163] H. S. Park, S. H. Nam, J. K. Song, S. M. Park, S. Ryu *Journal of Physical Chemistry A*. **2008**, 112, 9023-9030.

[164] M. C. Heaven *Annual Review of Physical Chemistry*. **1992**, 43, 283-310.

[165] V. A. Venturo, P. M. Felker *Journal of Chemical Physics*. **1993**, 99, 748-751.

[166] B. K. Mishra, J. S. Arey, N. Sathyamurthy *Journal of Physical Chemistry A*. **2010**, 114, 9606-9616.

[167] A. A. Zadorozhnaya, A. I. Krylov *Journal of Physical Chemistry A*. **2010**, 114, 2001-2009.

[168] J. A. Barltrop, J. D. Coyle, *Excited States in Organic Chemistry*, John Wiley & Sons Ltd., London and New York, **1975**.

[169] M. Houde, Martin Houde's Home Page: Molecular Symmetry and Spectroscopy Lecture Notes - The rotation-vibration hamiltonian, http://www.astro.uwo.ca/~houde/courses/astro9701/Hamiltonian.pdf.

[170] B. L. Tembe, Molecular Partition Functions, http://www.chem.iitb.ac.in/~bltembe/pdfs/ch_3.pdf.

[171] K. A. Kistler, S. Matsika in *Multi-scale Quantum Models for Biocatalysis, Vol. 7* (Eds.: D. M. York, T.-S. Lee), Springer Science+Business Media B.V., Dordrecht, Heidelberg, New York, London, **2009**, pp.285-339.

[172] P. Atkins, R. Friedman, *Molecular Quantum Mechanics*, Oxford University Press, New York, **2005**.

[173] J. M. Gingell, *PhD Thesis: A Spectroscopic Study of Selected Atmospheric and Astrophysical Molecules*, University of London, London, **1998**.

[174] J. B. Birks, *Photophysics of aromatic molecules*, Wiley-Interscience, London, **1970**.

[175] T. Hirata, H. Ikeda, H. Saigusa *Journal of Physical Chemistry A*. **1999**, 103, 1014-1024.

[176] J. H. Yeh, T. L. Shen, D. G. Nocera, G. E. Leroi, I. Suzuka, H. Ozawa, Y. Namuta *Journal of Physical Chemistry*. **1996**, 100, 4385-4389.

[177] H. Saigusa, E. C. Lim *Accounts of Chemical Research*. **1996**, 29, 171-178.

[178] C. M. Marian, F. Schneider, M. Kleinschmidt, J. Tatchen *European Physical Journal D*. **2002**, 20, 357-367.

[179] D. W. Ball, *Field Guide to Spectroscopy*, SPIE - The International Society for Optical Engineering, Bellingham, Washington USA, **2006**.

[180] A. C. Vutha *European Journal of Physics*. **2010**, 31, 389-392.

[181] C. E. Tyner, H. G. Drickamer *Journal of Chemical Physics*. **1977**, 67, 4103-4115.

[182] W. Fuss, W. E. Schmid, S. A. Trushin *Journal of Chemical Physics*. **2000**, 112, 8347-8362.

[183] E. E. Nikitin *Annual Review of Physical Chemistry*. **1999**, 50, 1-21.

[184] M. A. El-Sayed *Accounts of Chemical Research*. **1968**, 1, 8-16.

[185] T. Yatsuhashi, N. Nakashima *Bulletin of the Chemical Society of Japan*. **2001**, 74, 579-593.

[186] R. Schinke, *Photodissociation Dynamics*, Cambridge University Press, Cambridge, **1993**.

[187] T. Climent, I. Gonzalez-Ramirez, R. Gonzalez-Luque, M. Merchan, L. Serrano-Andres *Journal of Physical Chemistry Letters*. **2010**, 1, 2072-2076.

[188] W. M. Kwok, C. Ma, D. L. Phillips *Journal of the American Chemical Society*. **2008**, 130, 5131-5139.

[189] N. J. Kim, H. Kang, G. Jeong, Y. S. Kim, K. T. Lee, S. K. Kim *Proceedings of the National Academy of Sciences of the United States of America*. **2001**, 98, 4841-4843.

[190] N. J. Kim, H. Kang, G. Jeong, Y. S. Kim, K. T. Lee, S. K. Kim *Journal of Chemical Physics*. **2001**, 115, 7002-7005.

[191] M. N. Khattak, S. Y. Wang, Hauswirt.W *Biochemical and Biophysical Research Communications*. **1972**, 48, 1622-1629.

[192] H. Gorner *Journal of Photochemistry and Photobiology B-Biology*. **1991**, 10, 91-110.

[193] B. Brutschy *Journal of Physical Chemistry*. **1990**, 94, 8637-8647.

[194] B. Brutschy, J. Eggert, C. Janes, H. Baumgartel *Journal of Physical Chemistry*. **1991**, 95, 5041-5050.

[195] D. R. Miller, *Atomic and Molecular Beam Methods*, Oxford University Press, Oxford, **1988**.

[196] H. R. Murphy, D. R. Miller *Journal of Physical Chemistry*. **1984**, 88, 4474-4478.

[197] A. Nass, E. Steffens *Nuclear Instruments & Methods in Physics Research Section A - Accelerators Spectrometers Detectors and Associated Equipment*. **2009**, 598, 653-666.

[198] G. Sanna, G. Tomassetti, *Introduction to molecular beams gas dynamics*, Imperial College Press, London, **2005**.

[199] W. Christen, K. Rademann *Physical Review A*. **2008**, 77, 012702.

[200] J. P. Bucher, D. C. Douglass, P. Xia, L. A. Bloomfield *Review of Scientific Instruments*. **1990**, 61, 2374-2377.

[201] D. M. Lubman, C. T. Rettner, R. N. Zare *Journal of Physical Chemistry*. **1982**, 86, 1129-1135.

[202] J. Koperski, E. S. Fry *Journal of Physics B - Atomic Molecular and Optical Physics*. **2006**, 39, S1125-S1150.

[203] X. B. Zou, X. X. Wang, C. M. Luo, M. Han *IEEE Transactions on Plasma Science*. **2002**, 30, 482-487.

[204] M. Beychok, *Chemical Process Engineering FAQ*, Tecumseh Group, Inc., http://www.eng-tips.com/faqs.cfm?fid=1196, **1998-2012**.

[205] D. P. Glavin, M. Schubert, J. L. Bada *Analytical Chemistry*. **2002**, 74, 6408-6412.

[206] J. Tabet, S. Eden, S. Feil, H. Abdoul-Carime, B. Farizon, M. Farizon, S. Ouaskit, T. D. Mark *Nuclear Instruments & Methods in Physics Research Section B-Beam Interactions with Materials and Atoms*. **2010**, 268, 2458-2466.

[207] M. Hillenkamp, S. Keinan, U. Even *Journal of Chemical Physics*. **2003**, 118, 8699-8705.

[208] S. H. Yang, L. Philippe, M. Chatelet *International Journal of Mass Spectrometry*. **2007**, 263, 190-194.

[209] A. Pelc, L. Michalak *Rapid Communications in Mass Spectrometry*. **2000**, 14, 1455-1461.

[210] Molecular Beam Skimmers, Beam Dynamics, Inc., http://www.beamdynamicsinc.com/skimmer_specs.htm, **2012**.

[211] W. C. Wiley, I. H. McLaren *Review of Scientific Instruments*. **1955**, 26, 1150-1157.

[212] A. P. L. Wang, L. Li *Applied Spectroscopy*. **1991**, 45, 969-976.

[213] S. G. Alikhanov *Soviet Physics Jetp-Ussr*. **1957**, 4, 452-453.

[214] C. Weickhardt, F. Moritz, J. Grotemeyer *Mass Spectrometry Reviews*. **1996**, 15, 139-162.

[215] B. A. Mamyrin, V. I. Karataev, D. V. Shmikk, V. A. Zagulin *Zhurnal Eksperimentalnoi I Teoreticheskoi Fiziki*. **1973**, 64, 82-89.

[216] Continuum, *Laser Manual - Powerlite Precision II Scientific Laser System*, Continuum, Santa Clara, **2002**.

[217] U. Brackmann, *LambdaChrome Laser Dyes*, Lambda Physik AG, Goettingen, Germany, **2000**.

[218] D. M. Guthals, J. W. Nibler *Optics Communications*. **1979**, 29, 322-324.

[219] S. A. Ahmad, S. G. Nakhate in *Proceedings of the XII National Conference on Atomic and Molecular Physics, Vol. 4* (Eds.: K. K. Sud, U. N. Upadhyaya), Kluwer Academic / Plenum Publishers, Udaipur, **1999**, pp.353-396.

[220] G. Mainfray *Journal De Physique*. **1982**, 43, 367-386.

[221] J. Morellec, D. Normand, G. Petite *Physical Review A*. **1976**, 14, 300-312.

[222] S. I. Chu, D. A. Telnov *Physics Reports-Review Section of Physics Letters*. **2004**, 390, 1-131.

[223] M. Crance *Journal of Physics B-Atomic Molecular and Optical Physics*. **1980**, 13, 101-113.

[224] P. M. Johnson, C. E. Otis *Annual Review of Physical Chemistry*. **1981**, 32, 139-157.

[225] M. Crance *Journal of Physics B-Atomic Molecular and Optical Physics*. **1981**, 14, 4301-4306.

[226] C. E. Otis, P. M. Johnson *Chemical Physics Letters*. **1981**, 83, 73-77.

[227] K. L. Wells, G. M. Roberts, V. G. Stavros *Chemical Physics Letters*. **2007**, 446, 20-24.

[228] S. H. Nam, H. S. Park, J. K. Song, S. M. Park *Journal of Physical Chemistry A*. **2007**, 111, 3480-3484.

[229] L. Li, B. X. Yang, P. M. Johnson *Journal of the Optical Society of America B-Optical Physics*. **1985**, 2, 748-752.

[230] J. Grotemeyer, E. W. Schlag *Angewandte Chemie-International Edition in English*. **1988**, 27, 447-459.

[231] R. A. Morgan, M. A. Baldwin, D. Ascenz, A. J. OrrEwing, M. N. R. Ashfold, W. J. Buma, J. B. Milan, C. R. Scheper, C. A. deLange *International Journal of Mass Spectrometry and Ion Processes*. **1996**, 159, 1-11.

[232] I. Conti, M. Garavelli, G. Orlandi *Journal of the American Chemical Society*. **2009**, 131, 16108-16118.

[233] W. M. I. Hassan, W. C. Chung, N. Shimakura, S. Koseki, H. Kono, Y. Fujimura *Physical Chemistry Chemical Physics*. **2010**, 12, 5317-5328.

[234] T. Gustavsson, R. Improta, D. Markovitsi *Journal of Physical Chemistry Letters*. **2010**, 1, 2025-2030.

[235] D. Nachtigallova, T. Zeleny, M. Ruckenbauer, T. Muller, M. Barbatti, P. Hobza, H. Lischka *Journal of the American Chemical Society*. **2010**, 132, 8261-8263.

[236] C. Z. Bisgaard, H. Satzger, S. Ullrich, A. Stolow *Chemphyschem*. **2009**, 10, 101-110.

[237] H. Kang, K. T. Lee, B. Jung, Y. J. Ko, S. K. Kim *Journal of the American Chemical Society*. **2002**, 124, 12958-12959.

[238] N. J. Kim, H. Kang, Y. D. Park, S. K. Kim *Physical Chemistry Chemical Physics*. **2004**, 6, 2802-2805.

[239] N. J. Kim, G. Jeong, Y. S. Kim, J. Sung, S. K. Kim, Y. D. Park *Journal of Chemical Physics*. **2000**, 113, 10051-10055.

[240] L. B. Clark, G. G. Peschel, I. Tinoco *Journal of Physical Chemistry*. **1965**, 69, 3615-3618.

[241] L. Li, D. M. Lubman *Analytical Chemistry*. **1987**, 59, 2538-2541.

[242] M. Barbatti, A. J. A. Aquino, H. Lischka *Physical Chemistry Chemical Physics*. **2010**, 12, 4959-4967.

[243] A. L. Sobolewski, W. Domcke *European Physical Journal D*. **2002**, 20, 369-374.

[244] K. L. Wells, D. J. Hadden, M. G. D. Nix, V. G. Stavros *Journal of Physical Chemistry Letters*. **2010**, 1, 993-996.

[245] S. Perun, A. L. Sobolewski, W. Domcke *Journal of the American Chemical Society*. **2005**, 127, 6257-6265.

[246] H. Kang, B. Jung, S. K. Kim *Journal of Chemical Physics*. **2003**, 118, 6717-6719.

[247] H. Y. Kang, B. Y. Jung, S. K. Kim *Journal of Chemical Physics*. **2003**, 118, 11336-11336.

[248] H. Satzger, D. Townsend, M. Z. Zgierski, S. Patchkovskii, S. Ullrich, A. Stolow *Proceedings of the National Academy of Sciences of the United States of America*. **2006**, 103, 10196-10201.

[249] H. H. Ritze, H. Lippert, E. Samoylova, V. R. Smith, I. V. Hertel, W. Radloff, T. Schultz *Journal of Chemical Physics*. **2005**, 122.

[250] M. Z. Zgierski, S. Patchkovskii, E. C. Lim *Canadian Journal of Chemistry-Revue Canadienne De Chimie*. **2007**, 85, 124-134.

[251] Y. B. Lei, S. A. Yuan, Y. S. Dou, Y. B. Wang, Z. Y. Wen *Journal of Physical Chemistry A*. **2008**, 112, 8497-8504.

[252] S. Perun, A. L. Sobolewski, W. Domcke *Chemical Physics*. **2005**, 313, 107-112.

[253] M. Barbatti, H. Lischka *Journal of the American Chemical Society*. **2008**, 130, 6831-6839.

[254] L. Serrano-Andres, M. Merchan, A. C. Borin *Proceedings of the National Academy of Sciences of the United States of America*. **2006**, 103, 8691-8696.

[255] A. C. Borin, L. Serrano-Andres, V. Ludwig, K. Coutinho, S. Canuto *International Journal of Quantum Chemistry*. **2006**, 106, 2564-2577.

[256] R. Gonzalez-Luque, T. Climent, I. Gonzalez-Ramirez, M. Merchan, L. Serrano-Andres *Journal of Chemical Theory and Computation*. **2010**, 6, 2103-2114.

[257] H. Du, R. C. A. Fuh, J. Z. Li, L. A. Corkan, J. S. Lindsey *Photochemistry and Photobiology*. **1998**, 68, 141-142.

[258] J. J. Szymczak, M. Barbatti, J. T. S. Hoo, J. A. Adkins, T. L. Windus, D. Nachtigallova, H. Lischka *Journal of Physical Chemistry A*. **2009**, 113, 12686-12693.

[259] M. Barbatti, A. J. A. Aquino, J. J. Szymczak, D. Nachtigallova, P. Hobza, H. Lischka *Proceedings of the National Academy of Sciences of the United States of America*. **2010**, 107, 21453-21458.

[260] G. Zechmann, M. Barbatti *Journal of Physical Chemistry A*. **2008**, 112, 8273-8279.

[261] H. R. Hudock, B. G. Levine, A. L. Thompson, H. Satzger, D. Townsend, N. Gador, S. Ullrich, A. Stolow, T. J. Martinez *Journal of Physical Chemistry A*. **2007**, 111, 8500-8508.

[262] D. Asturiol, B. Lasorne, G. A. Worth, M. A. Robb, L. Blancafort *Physical Chemistry Chemical Physics*. **2010**, 12, 4949-4958.

[263] D. Picconi, V. Barone, A. Lami, F. Santoro, R. Improta *Chemphyschem*. **2011**, 12, 1957-1968.

[264] M. Merchan, R. Gonzalez-Luque, T. Climent, L. Serrano-Andres, E. Rodriuguez, M. Reguero, D. Pelaez *Journal of Physical Chemistry B*. **2006**, 110, 26471-26476.

[265] A. M. Rasmussen, M. C. Lind, S. Kim, H. F. Schaefer *Journal of Chemical Theory and Computation*. **2010**, 6, 930-939.

[266] S. Lobsiger, H. M. Frey, S. Leutwyler *Physical Chemistry Chemical Physics*. **2010**, 12, 5032-5040.

[267] B. B. Brady, L. A. Peteanu, D. H. Levy *Chemical Physics Letters*. **1988**, 147, 538-543.

[268] Y. Tsuchiya, T. Tamura, M. Fujii, M. Ito *Journal of Physical Chemistry*. **1988**, 92, 1760-1765.

[269] V. B. Delchev, A. L. Sobolewski, W. Domcke *Physical Chemistry Chemical Physics*. **2010**, 12, 5007-5015.

[270] J. Lorentzon, M. P. Fulscher, B. O. Roos *Journal of the American Chemical Society*. **1995**, 117, 9265-9273.

[271] Z. G. Lan, E. Fabiano, W. Thiel *Journal of Physical Chemistry B*. **2009**, 113, 3548-3555.

[272] A. Banyasz, S. Karpati, Y. Mercier, M. Reguero, T. Gustavsson, D. Markovitsi, R. Improta *Journal of Physical Chemistry B*. **2010**, 114, 12708-12719.

[273] D. Nachtigallova, A. J. A. Aquino, J. J. Szymczak, M. Barbatti, P. Hobza, H. Lischka *Journal of Physical Chemistry A*. **2011**, 115, 5247-5255.

[274] S. Matsika *Journal of Physical Chemistry A*. **2004**, 108, 7584-7590.

[275] H. Nieber, N. L. Doltsinis *Chemical Physics*. **2008**, 347, 405-412.

[276] T. Kobayashi, H. Kuramochi, Y. Harada, T. Suzuki, T. Ichimura *Journal of Physical Chemistry A*. **2009**, 113, 12088-12093.

[277] T. Kobayashi, Y. Harada, T. Suzuki, T. Ichimura *Journal of Physical Chemistry A*. **2008**, 112, 13308-13315.

[278] M. Z. Zgierski, S. Patchkovskii, T. Fujiwara, E. C. Lim *Journal of Physical Chemistry A*. **2005**, 109, 9384-9387.

[279] Y. Mercier, M. Reguero *International Journal of Quantum Chemistry*. **2011**, 111, 3405-3415.

[280] S. Yamazaki, T. Taketsugu *Journal of Physical Chemistry A*. **2012**, 116, 491-503.

[281] D. Nachtigallova, H. Lischka, J. J. Szymczak, M. Barbatti, P. Hobza, Z. Gengeliczki, G. Pino, M. P. Callahan, M. S. de Vries *Physical Chemistry Chemical Physics*. **2010**, 12, 4924-4933.

[282] E. Epifanovsky, K. Kowalski, P. D. Fan, M. Valiev, S. Matsika, A. I. Krylov *Journal of Physical Chemistry A*. **2008**, 112, 9983-9992.

[283] P. M. Hare, C. E. Crespo-Hernandez, B. Kohler *Proceedings of the National Academy of Sciences of the United States of America*. **2007**, 104, 435-440.

[284] T. Gustavsson, A. Banyasz, E. Lazzarotto, D. Markovitsi, G. Scalmani, M. J. Frisch, V. Barone, R. Improta *Journal of the American Chemical Society*. **2006**, 128, 607-619.

[285] V. Ludwig, Z. M. da Costa, M. S. do Amaral, A. C. Borin, S. Canuto, L. Serrano-Andres *Chemical Physics Letters*. **2010**, 492, 164-169.

[286] T. Gustavsson, N. Sarkar, E. Lazzarotto, D. Markovitsi, R. Improta *Chemical Physics Letters*. **2006**, 429, 551-557.

[287] D. M. Close, C. E. Crespo-Hernandez, L. Gorb, J. Leszczynski *Journal of Physical Chemistry A*. **2005**, 109, 9279-9283.

[288] D. M. Close, C. E. Crespo-Hernandez, L. Gorb, J. Leszczynski *Journal of Physical Chemistry A*. **2006**, 110, 7485-7490.

[289] E. Sztumpf-Kulikowska, D. Shugar, J. W. Boag *Photochemistry and Photobiology*. **1967**, 6, 41-54.

[290] X. J. Hou, M. T. Nguyen *Chemical Physics*. **2005**, 310, 1-9.

[291] J. Eisinger, R. G. Shulman *Proceedings of the National Academy of Sciences of the United States of America*. **1967**, 58, 895-900.

[292] W. J. Schreier, J. Kubon, N. Regner, K. Haiser, T. E. Schrader, W. Zinth, P. Clivio, P. Gilch *Journal of the American Chemical Society*. **2009**, 131, 5038-5039.

[293] A. Wacker *Progress in Nucleic Acid Research and Molecular Biology*. **1963**, 1, 369-399.

[294] P. J. Wagner, D. J. Bucheck *Journal of the American Chemical Society*. **1970**, 92, 181-185.

[295] W. Fuchtbauer, P. Mazur *Photochemistry and Photobiology*. **1966**, 5, 323-335.

[296] S. Y. Wang *Nature*. **1961**, 190, 690-694.

[297] I. H. Brown, H. E. Johns *Photochemistry and Photobiology*. **1968**, 8, 273-286.

[298] C. Fenselau, S. Y. Wang *Tetrahedron*. **1969**, 25, 2853-2863.

[299] R. L. Hettich, M. V. Buchanan, C. H. Ho *Biomedical and Environmental Mass Spectrometry*. **1990**, 19, 55-62.

[300] V. I. Danilov, J. J. P. Stewart, A. Les, J. L. Alderfer *Chemical Physics Letters*. **2000**, 328, 75-82.

[301] H. Gorner *Journal of Photochemistry and Photobiology B-Biology*. **1994**, 26, 117-139.

[302] J. G. Burr, B. R. Gordon, E. H. Park *Photochemistry and Photobiology*. **1968**, 8, 73-78.

[303] L. Kittler, G. Lober *Photochemistry and Photobiology*. **1969**, 10, 35-44.

[304] P. W. Doetsch, T. H. Zastawny, A. M. Martin, M. Dizdaroglu *Biochemistry*. **1995**, 34, 737-742.

[305] C. Desnous, D. Guillaume, P. Clivio *Chemical Reviews*. **2010**, 110, 1213-1232.

[306] J. L. Ravanat, T. Douki, J. Cadet *Journal of Photochemistry and Photobiology B-Biology.* **2001**, 63, 88-102.

[307] C. Ponnamperuma, M. Calvin, R. M. Lemmon *Radiation Research.* **1963**, 18, 540-551.

[308] S. Matsika, P. Krause *Annual Review of Physical Chemistry, Vol 62.* **2011**, 62, 621-643.

[309] N. L. Evans, S. Ullrich *Journal of Physical Chemistry A.* **2010**, 114, 11225-11230.

[310] A. N. Brouillette, N. L. Evans, W. M. Potter, S. Ullrich. **2009**, March 4, 1-11.

[311] S. Ullrich, T. Schultz, M. Z. Zgierski, A. Stolow *Journal of the American Chemical Society.* **2004**, 126, 2262-2263.

[312] S. Ullrich, T. Schultz, M. Z. Zgierski, A. Stolow *Physical Chemistry Chemical Physics.* **2004**, 6, 2796-2801.

[313] E. Nir, K. Kleinermanns, L. Grace, M. S. de Vries *Journal of Physical Chemistry A.* **2001**, 105, 5106-5110.

[314] J. Hofstein, H. F. Xu, T. Sears, P. Johnson *Journal of Physical Chemistry A.* **2008**, 112, 1195-1201.

[315] A. Li, T. Uchimura, Y. Watanabe-Ezoe, T. Imasaka *Analytical Chemistry.* **2011**, 83, 60-66.

[316] D. Kim, H. M. Kim, K. Y. Yang, S. K. Kim, N. J. Kim *Journal of Chemical Physics.* **2008**, 128.

[317] C. Weickhardt, C. Grun, R. Heinicke, A. Meffert, J. Grotemeyer *Rapid Communications in Mass Spectrometry.* **1997**, 11, 745-748.

[318] R. L. Whetten, K. J. Fu, E. R. Grant *Journal of Chemical Physics.* **1983**, 79, 4899-4911.

[319] J. Matsumoto, C. H. Lin, T. Imasaka *Analytical Chemistry.* **1997**, 69, 4524-4529.

[320] K. W. D. Ledingham, H. S. Kilic, C. Kosmidis, R. M. Deas, A. Marshall, T. McCanny, R. P. Singhal, A. J. Langley, W. Shaikh *Rapid Communications in Mass Spectrometry.* **1995**, 9, 1522-1527.

[321] R. Weinkauf, P. Aicher, G. Wesley, J. Grotemeyer, E. W. Schlag *Journal of Physical Chemistry.* **1994**, 98, 8381-8391.

[322] J. Matsumoto, C. H. Lin, T. Imasaka *Analytica Chimica Acta.* **1997**, 343, 129-133.

[323] M. P. Callahan, B. Crews, A. Abo-Riziq, L. Grace, M. S. de Vries, Z. Gengeliczki, T. M. Holmes, G. A. Hill *Physical Chemistry Chemical Physics.* **2007**, 9, 4587-4591.

[324] A. L. Sobolewski, W. Domcke, C. Hattig *Proceedings of the National Academy of Sciences of the United States of America*. **2005**, 102, 17903-17906.

[325] C. H. Lin, J. Matsumoto, S. Ohtake, T. Imasaka *Talanta*. **1996**, 43, 1925-1929.

[326] J. H. Hahn, R. Zenobi, R. N. Zare *Journal of the American Chemical Society*. **1987**, 109, 2842-2843.

[327] R. Tembreull, D. M. Lubman *Analytical Chemistry*. **1987**, 59, 1082-1088.

[328] T. Streibel, K. Hafner, F. Muhlberger, T. Adam, R. Zimmermann *Applied Spectroscopy*. **2006**, 60, 72-79.

[329] Y. J. Hu, R. C. Lu, Y. Cai, X. Y. Wang *Journal of Mass Spectrometry*. **2001**, 36, 329-335.

[330] C. B. Reed *Physics Education*. **2010**, 45, 93-96.

[331] E. Samoylova, T. Schultz, I. V. Hertel, W. Radloff *Chemical Physics*. **2008**, 347, 376-382.

[332] J. Gonzalez-Vazquez, L. Gonzalez, E. Samoylova, T. Schultz *Physical Chemistry Chemical Physics*. **2009**, 11, 3927-3934.

[333] C. Canuel, M. Mons, F. Piuzzi, B. Tardivel, I. Dimicoli, M. Elhanine *Journal of Chemical Physics*. **2005**, 122.

[334] M. Schneider, R. Maksimenka, F. J. Buback, T. Kitsopoulos, L. R. Lago, I. Fischer *Physical Chemistry Chemical Physics*. **2006**, 8, 3017-3021.

[335] Y. G. He, C. Y. Wu, W. Kong *Journal of Physical Chemistry A*. **2003**, 107, 5145-5148.

[336] Y. G. He, C. Y. Wu, W. Kong *Journal of Physical Chemistry A*. **2004**, 108, 943-949.

[337] M. Etinski, T. Fleig, C. A. Marian *Journal of Physical Chemistry A*. **2009**, 113, 11809-11816.

[338] M. Etinski, C. M. Marian *Physical Chemistry Chemical Physics*. **2010**, 12, 4915-4923.

[339] R. A. Marcus *Laser Chemistry*. **1983**, 2, 203-217.

[340] F. F. Crim *Annual Review of Physical Chemistry*. **1984**, 35, 657-691.

[341] N. Nakashima, K. Yoshihara *Journal of Physical Chemistry*. **1989**, 93, 7763-7771.

[342] R. Montero, F. Castano, R. Martinez, A. Longarte *Journal of Physical Chemistry A*. **2009**, 113, 952-958.

[343] L. A. Pinnaduwage, Y. F. Zhu *Chemical Physics Letters*. **1997**, 277, 147-152.

[344] J. D. Petke, G. M. Maggiora, R. E. Christoffersen *Journal of the American Chemical Society*. **1990**, 112, 5452-5460.

[345] S. A. Betterton, A. S. Berka, P. E. Fleming *Journal of Theoretical & Computational Chemistry*. **2010**, 9, 189-200.

[346] M. Barbatti, S. Ullrich *Physical Chemistry Chemical Physics*. **2011**, 13, 15492-15500.

[347] R. L. Platzman *Radiation Research*. **1962**, 16, 419-425.

[348] R. S. Becker, G. Kogan *Photochemistry and Photobiology*. **1980**, 31, 5-13.

[349] G. Alagona, C. Ghio, S. Monti *International Journal of Quantum Chemistry*. **2001**, 83, 128-142.

[350] M. A. Palafox, V. K. Rastogi, H. Kumar, I. Kostova, J. K. Vats *Spectroscopy Letters*. **2011**, 44, 300-306.

[351] L. R. Rutledge, C. A. Wheaton, S. D. Wetmore *Physical Chemistry Chemical Physics*. **2007**, 9, 497-509.

[352] H. Y. Zheng, F. C. Meng *Structural Chemistry*. **2009**, 20, 943-949.

[353] A. H. Zhang, B. H. Yang, Z. H. Li *Journal of Molecular Structure-Theochem*. **2007**, 819, 95-101.

[354] E. Fort, B. Lescop, A. De Martino, H. Vach, M. Chatelet, F. Pradere *European Physical Journal D*. **2001**, 15, 331-334.

[355] M. Dey, F. Moritz, J. Grotemeyer, E. W. Schag *Journal of the American Chemical Society*. **1994**, 116, 9211-9215.

[356] J. Sponer, J. Leszczynski, P. Hobza *Journal of Physical Chemistry*. **1996**, 100, 1965-1974.

[357] P. Hobza, J. Sponer *Chemical Physics Letters*. **1996**, 261, 379-384.

[358] K. Müller-Dethlefs, M. Riese, *Molecular Clusters and Noncovalent Bonds Probed by Photoionization and Photoelectron Spectroscopy - Handbook of High-resolution Spectroscopy*, Wiley Online Library, Zurich, **2011**.

[359] C. Plutzer, I. Hunig, K. Kleinermanns, E. Nir, M. S. de Vries *Chemphyschem*. **2003**, 4, 838-842.

[360] A. L. F. de Barros, A. Medina, F. Zappa, J. M. Pereira, E. Bessa, M. H. P. Martins, L. F. S. Coelho, W. Wolff, N. V. de Castro Faria *Nuclear Instruments & Methods in Physics Research A: Accelerators Spectrometers Detectors and Associated Equipment*. **2006**, 560, 219-223.

[361] O. Kostko, K. Bravaya, A. Krylov, M. Ahmed *Physical Chemistry Chemical Physics*. **2010**, 12, 2860-2872.

[362] V. Poterya, O. Tkac, J. Fedor, M. Farnik, P. Slavicek, U. Buck *International Journal of Mass Spectrometry*. **2010**, 290, 85-93.

[363] N. J. Kim, H. Kang, G. Jeong, Y. S. Kim, K. T. Lee, S. K. Kim *Journal of Physical Chemistry A*. **2000**, 104, 6552-6557.

[364] Z. L. Cai, J. R. Reimers *Journal of Physical Chemistry A*. **2007**, 111, 954-962.

[365] V. Periquet, A. Moreau, S. Carles, J. P. Schermann, C. Desfrancois *Journal of Electron Spectroscopy and Related Phenomena*. **2000**, 106, 141-151.

[366] M. Busker, M. Nispel, T. Haber, K. Kleinermanns, M. Etinski, T. Fleig *Chemphyschem*. **2008**, 9, 1570-1577.

[367] S. Kim, S. E. Wheeler, H. F. Schaefer *Journal of Chemical Physics*. **2006**, 124.

[368] V. I. Danilov, T. van Mourik, V. I. Poltev *Chemical Physics Letters*. **2006**, 429, 255-260.

[369] S. R. Gadre, K. Babu, A. P. Rendell *Journal of Physical Chemistry A*. **2000**, 104, 8976-8982.

[370] F. F. Wang, D. X. Zhao, Z. Z. Yang *Chemical Physics*. **2009**, 360, 141-149.

[371] T. van Mourik, S. L. Price, D. C. Clary *Journal of Physical Chemistry A*. **1999**, 103, 1611-1618.

[372] T. van Mourik, D. M. Benoit, S. L. Price, D. C. Clary *Physical Chemistry Chemical Physics*. **2000**, 2, 1281-1290.

[373] V. B. Delchev, I. G. Shterev, H. Mikosch *Monatshefte Fur Chemie*. **2008**, 139, 349-362.

[374] T. van Mourik, V. I. Danilov, V. V. Dailidonis, N. Kurita, H. Wakabayashi, T. Tsukamoto *Theoretical Chemistry Accounts*. **2010**, 125, 233-244.

[375] S. M. Bachrach, M. W. Dzierlenga *Journal of Physical Chemistry A*. **2011**, 115, 5674-5683.

[376] M. Kabelac, P. Hobza *Physical Chemistry Chemical Physics*. **2007**, 9, 903-917.

[377] V. R. Smith, E. Samoylova, H. H. Ritze, W. Radloff, T. Schultz *Physical Chemistry Chemical Physics*. **2010**, 12, 9632-9636.

[378] N. U. Zhanpeisov, J. Leszczynski *Journal of Physical Chemistry A*. **1998**, 102, 6167-6172.

[379] S. G. Lias, *Ionization Energy Evaluation, NIST Standard Reference Database Number 69*, National Institute of Standards and Technology, Gathersburg MD, **1998**.

[380] C. T. Hwang, C. L. Stumpf, Y. Q. Yu, H. I. Kenttamaa *International Journal of Mass Spectrometry*. **1999**, 182, 253-259.

[381] M. Liu, T. T. Li, F. S. Amegayibor, D. S. Cardoso, Y. L. Fu, J. K. Lee *Journal of Organic Chemistry*. **2008**, 73, 9283-9291.

[382] C. L. Stumpf, *PhD Thesis: Application of Fourier transform ion cyclotron resonance mass spectrometry to a mechanistic study, examination of the properties of nucleobase radical cations, and chemical ionization reagent development*, Purdue University, Indiana, **2000**.

[383] M. A. Kurinovich, L. M. Phillips, S. Sharma, J. K. Lee *Chemical Communications*. **2002**, 2354-2355.

[384] F. Turecek, J. K. Wolken *Journal of Physical Chemistry A*. **2001**, 105, 8740-8747.

[385] I. Hunig, C. Plutzer, K. A. Seefeld, D. Lowenich, M. Nispel, K. Kleinermanns *Chemphyschem*. **2004**, 5, 1427-1431.

[386] X. H. Chen, E. A. Syrstad, M. T. Nguyen, P. Gerbaux, F. Turecek *Journal of Physical Chemistry A*. **2005**, 109, 8121-8132.

[387] E. Samoylova, V. R. Smith, H. H. Ritze, W. Radloff, M. Kabelac, T. Schultz *Journal of the American Chemical Society*. **2006**, 128, 15652-15656.

[388] T. Schultz, E. Samoylova, W. Radloff, I. V. Hertel, A. L. Sobolewski, W. Domcke *Science*. **2004**, 306, 1765-1768.

[389] S. H. Nam, H. S. Park, S. Ryu, J. K. Song, S. M. Park *Chemical Physics Letters*. **2008**, 450, 236-242.

[390] C. E. Crespo-Hernandez, B. Kohler *Journal of Physical Chemistry B*. **2004**, 108, 11182-11188.

[391] Y. Nosenko, M. Kunitski, C. Riehn, P. H. P. Harbach, A. Dreuw, B. Brutschy *Physical Chemistry Chemical Physics*. **2010**, 12, 863-870.

[392] L. M. Salter, G. M. Chaban *Journal of Physical Chemistry A*. **2002**, 106, 4251-4256.

[393] H. S. Kim, D. S. Ahn, S. Y. Chung, S. K. Kim, S. Lee *Journal of Physical Chemistry A*. **2007**, 111, 8007-8012.

[394] S. K. Mishra, M. K. Shukla, P. C. Mishra *Spectrochimica Acta Part A - Molecular and Biomolecular Spectroscopy*. **2000**, 56, 1355-1384.

[395] C. E. Crespo-Hernandez, B. Cohen, B. Kohler *Nature*. **2005**, 436, 1141-1144.

[396] M. K. Shukla, J. Leszczynski *Journal of Physical Chemistry A*. **2002**, 106, 8642-8650.

[397] Y. Mercier, F. Santoro, M. Reguero, R. Improta *Journal of Physical Chemistry B*. **2008**, 112, 10769-10772.

[398] M. A. Morsy, A. M. Al-Somali, A. Suwaiyan *Journal of Physical Chemistry B*. **1999**, 103, 11205-11210.

[399] Y. Nosenko, M. Kunitski, B. Brutschy *Journal of Physical Chemistry A*. **2011**, 115, 9429-9439.

[400] M. Kunitski, Y. Nosenko, B. Brutschy *Chemphyschem*. **2011**, 12, 2024-2030.

[401] M. K. Shukla, J. Leszczynski *Journal of Physical Chemistry A*. **2003**, 107, 5538-5543.

[402] T. Hupp, C. Sturm, E. M. B. Janke, M. P. Cabre, K. Weisz, B. Engels *Journal of Physical Chemistry A*. **2005**, 109, 1703-1712.

[403] X. J. Sun, J. K. Lee *Journal of Organic Chemistry*. **2007**, 72, 6548-6555.

[404] M. De Vries in *Radiation Induced Molecular Phenomena in Nucleic Acids, Vol. 5* (Eds.: M. Shukla, J. Leszczynski), Springer Science+Business Media B.V., Jackson, **2008**, pp.323-342.

[405] M. K. Shukla, J. Leszczynski *International Journal of Quantum Chemistry*. **2005**, 105, 387-395.

[406] C. Grun, C. Weickhardt, J. Grotemeyer *European Mass Spectrometry*. **1996**, 2, 197-202.

[407] S. Takeuchi, T. Tahara *Chemical Physics Letters*. **1997**, 277, 340-346.

[408] S. Takeuchi, T. Tahara *Journal of Physical Chemistry A*. **1998**, 102, 7740-7753.

[409] P. Share, M. Pereira, M. Sarisky, S. Repinec, R. M. Hochstrasser *Journal of Luminescence*. **1991**, 48-9, 204-208.

[410] A. Douhal, S. K. Kim, A. H. Zewail *Nature*. **1995**, 378, 260-263.

[411] K. Sakota, A. Hara, H. Sekiya *Physical Chemistry Chemical Physics*. **2004**, 6, 32-36.

[412] M. Kratochvil, O. Engkvist, J. Sponer, P. Jungwirth, P. Hobza *Journal of Physical Chemistry A*. **1998**, 102, 6921-6926.

[413] M. Kabelac, P. Hobza *Journal of Physical Chemistry B*. **2001**, 105, 5804-5817.

[414] B. A. Huber, L. Adoui, V. Bernigaud, B. Manil, L. Maunoury, J. Rangama, P. Rousseau, N. Haag, H. Johansson, H. T. Schmidt, H. Cederquist, S. B. Nielsen, B. Liu, H. Zettergren, P.

Hvelplund, F. Alvarado, S. Bari, R. Hoekstra, J. Postma, T. Schlatholter in *Fragmentation of isolated and nanosolvated biomolecular systems, Vol. 1080* (Eds.: K. Tokesi, B. Sulik), **2008**, pp.21-29.

[415] T. Schlatholter, F. Alvarado, S. Bari, A. Lecointre, R. Hoekstra, V. Bernigaud, B. Manil, J. Rangama, B. Huber *Chemphyschem.* **2006**, 7, 2339-2345.

[416] R. Bredy, J. Bernard, L. Chen, G. Montagne, B. Li, S. Martin *Journal of Chemical Physics.* **2009**, 130, 114305.

[417] O. Plekan, V. Feyer, R. Richter, M. Coreno, M. de Simone, K. C. Prince *Chemical Physics.* **2007**, 334, 53-63.

[418] J. M. Rice, G. O. Dudek *Journal of the American Chemical Society.* **1967**, 89, 2719-2725.

[419] N. R. Cheong, S. H. Nam, H. S. Park, S. Ryu, J. K. Song, S. M. Park, M. Perot, B. Lucas, M. Barat, J. A. Fayeton, C. Jouvet *Physical Chemistry Chemical Physics.* **2011**, 13, 291-295.

[420] J. M. Rice, G. O. Dudek, M. Barber *Journal of the American Chemical Society.* **1965**, 87, 4569-4576.

[421] G. G. B. de Souza, L. H. Coutinho, C. Nunez, R. Bernini, R. B. Castilho, A. F. Lago in *Excitation and ionic fragmentation of gas-phase biomolecules using electrons and synchrotron radiation, Vol. 88* (Eds.: U. Becker, R. Moshammer, P. Mokler, J. Ullrich), **2007**, pp.12005.

[422] E. Samoylova, *PhD Thesis: Excited state dynamics of isolated DNA base pairs and related chromophore clusters*, Freie Universitat Berlin, Berlin, **2009**.

[423] S. M. Hecht, A. S. Gupta, N. J. Leonard *Biochimica Et Biophysica Acta.* **1969**, 182, 444-448.

[424] S. Matsika, C. Y. Zhou, M. Kotur, T. C. Weinacht *Faraday Discussions.* **2011**, 153, 247-260.

[425] T. Marunaka *Biomedical Mass Spectrometry.* **1981**, 8, 105-110.

[426] L. Chen, R. Bredy, J. Bernard, G. Montagne, A. R. Allouche, S. Martin *Journal of Chemical Physics.* **2011**, 135.